2018

EVALUATION, IMPROVEMENT, AND APPLICATION OF MODELS OF ENVIRONMENTAL FATE AND TRANSPORT OF ATMOSPHERE-SURFACE EXCHANGEABLE POLLUTANTS (ASEPs)

Tanvir Khan
Michigan Technological University, trkhan@mtu.edu

EVALUATION, IMPROVEMENT, AND APPLICATION OF MODELS OF ENVIRONMENTAL FATE AND TRANSPORT OF ATMOSPHERE-SURFACE EXCHANGEABLE POLLUTANTS (ASEPs)

By

Tanvir R. Khan

A DISSERTATION

Submitted in partial fulfillment of the requirements for the degree of

DOCTOR OF PHILOSOPHY

In Environmental Engineering

MICHIGAN TECHNOLOGICAL UNIVERSITY

2018

This dissertation has been approved in partial fulfillment of the requirements for the Degree of DOCTOR OF PHILOSOPHY in Environmental Engineering.

Department of Civil and Environmental Engineering

Dissertation Advisor:	*Dr. Judith Perlinger*
Committee Member:	*Dr. Hugh Gorman*
Committee Member:	*Dr. Daniel Obrist*
Committee Member:	*Dr. Noelle Selin*
Committee Member:	*Dr. Noel Urban*
Committee Member:	*Dr. Shiliang Wu*
Department Chair:	*Dr. Audra Morse*

Table of Contents

Preface

Chapter 1 was published in a journal and is republished in its entirety as a chapter in this dissertation. My advisor, Dr. Judith Perlinger supported this research with ideas and made the corrections. The citation for this chapter publication is provided below:

Khan, T. R. and Perlinger, J. A.: Evaluation of five dry particle deposition parameterizations for incorporation into atmospheric transport models, *Geoscientific Model Development*, 10, 3861-3888, https://doi.org/10.5194/gmd-10-3861-2017, 2017.

Chapter 2 is unpublished work and will be submitted to the journal *Atmospheric Environment* for publication. Drs. Daniel Obrist and Judith Perlinger supported this research with ideas and made corrections. Dr. Yannick Agnan participated in preparation of monthly averaged micrometeorological data sets used for model evaluation.

Chapter 3 is unpublished work and will be submitted to a journal for publication in the future.

Acknowledgements

First and foremost, I would like to express my sincere gratitude to my mentor and advisor Dr. Judith Perlinger for her guidance, patience, and intellectual support throughout my doctoral study at Michigan Tech. Her mentorship enabled me to develop scientific thinking and provided me the courage to pursue challenging research topics. This dissertation would not have been possible without her immense support.

I would like to thank Dr. Noel Urban, and Dr. Daniel Obrist (University of Massachusetts-Lowell) for their invaluable guidance and sharing vast knowledge, and also for the hard questions, which provoked me to think beneath the surface, to be logical, and objective.

I also thank Dr. Hugh Gorman, Dr. Shiliang Wu, and Dr. Noelle Selin (Massachusetts Institute of Technology) for their insightful comments, which widened my research from various perspectives.

I am grateful to the National Science Foundation Dynamics of Coupled Natural and Human Systems Program Grant, #1313755 and the Civil & Environmental Engineering Department at Michigan Tech for providing funding to support my doctoral studies at Michigan Tech.

I am thankful to the Urban-Perlinger research group members: Dr. Bo Zhang, Ankita Mandelia, Emily Sokol, Hongyi Lin, Hang Wang, Mugdha Priyadarshini, Ashley Hendricks, and Emily Shaw, for stimulating discussions in group meetings. I also thank every member of the ASEP project; they helped me to gather knowledge outside my area of expertise.

I am forever grateful to my family: my parents and my brother for their support from 7,544 miles away (23.81° N, 90.41° E) during my Ph.D. endeavor in Houghton, Michigan (47.12° N, 88.57° W). Last but not the least, I am thankful to my wife, Momita, for her strong support and encouragement at all times.

Abstract

Certain toxic, semivolatile chemicals, also known as atmosphere-surface exchangeable pollutants (ASEPs) are emitted into the environment from anthropogenic activities and natural sources. This dissertation focused on the (i) evaluation and improvement of dry particle deposition and atmosphere-surface exchange parameterizations of ASEPs for use in chemical transport models (CTMs), and (ii) application of a dynamic multimedia model to examine recovery of Lake Superior from historical inputs of polychlorinated biphenyl (PCB) compounds (a class of ASEPs) contamination.

Current knowledge has been inadequate to propose quantitative measures of the relative performance of available dry particle deposition parameterizations. In Chapter 1 of this dissertation, five dry deposition parameterizations were evaluated against field observations across five land use categories, in terms their ability to reproduce observed deposition velocities, V_d (*accuracy*), the influence of imprecision in input parameter values on the modeled V_d (*uncertainty*), identification of the most influential parameter(s) (*sensitivity*), and complexity. Based on the evaluation, a recommendation for the superior parameterization for use in CTMs is made.

In most CTMs, current parameterizations of atmosphere-terrestrial surface exchange of elemental mercury (Hg^0) lack critical evaluation against field measurements. In Chapter 2 of this dissertation, an extensive evaluation of most commonly used resistance-based dry gaseous deposition and soil re-emission parameterizations (base model) of Hg^0 was performed using a direct comparison to micrometeorological flux measurements from two ecosystems. This evaluation elucidated two major shortcomings of the base model: significant overestimation of leaf Hg uptake in summer month and an inability of capture measured nighttime net depositions. A step-wise model calibration was performed to adjust certain stomatal, non-stomatal, and soil re-emission parameters of the base model, which enabled an improved prediction of measured net exchange fluxes and growing-season leaf Hg accumulation. Based on the evaluation, generic recommendations for improvement in modeling Hg^0 exchange for CTMs were made.

Despite the U.S. production ban on PCBs in 1979, the measured concentrations in Lake Superior fish exhibited only a slow decline over the last 20 years. Sediment recycling of PCBs is often invoked to explain this slow recovery in fish PCB concentrations. In Chapter 3 of this dissertation, a dynamic multimedia model was applied to investigate the observed leveling-off of fish PCB concentrations in Lake Superior. Using historical to present-day PCB emissions (1930-2013) as the primary input in the multimedia model, the long-term trends in predicted PCB concentrations in different environmental media (water, sediment, and biota) were compared with available measurements for Lake Superior. The model-predicted half-life of total PCBs in fish was not consistent with the observations, suggesting that food web changes in the lake may be affecting trajectories of PCB concentrations in fish.

Introduction

Certain toxic, semivolatile chemicals (sub-cooled liquid vapor pressure in the range from 10^{-9} to 10^{-2} kPa) are emitted into the environment from anthropogenic activities and natural sources. These chemicals can be termed atmosphere-surface exchangeable pollutants (ASEPs) because they cycle between surface reservoirs (e.g., soils, vegetation, lakes, and oceans) and the atmosphere (Perlinger et al., 2016). From regional to global scales, certain ASEPs such as mercury (Hg) and a class of persistent, bioaccumulative, toxic chemicals, polychlorinated biphenyl (PCB) compounds are of interest because of concerns over human exposure, negative ecosystem impacts, and discovery in remote areas far from primary sources. At present, Hg and PCBs can be found in virtually all environmental compartments (e.g., air, soil, water, sediment, and food chains) around the globe. Methylmercury, a toxic form of organic Hg, has been routinely found in the Arctic marine food web (Brown et al., 2018; Dietz et al., 2013). In addition, there has been increasing evidence that the Arctic environment has been contaminated by PCBs (Friedman and Selin, 2016; Borgå et al., 2005). Even in some remote locations in the Laurentian Great Lakes region, these chemicals have been found at levels that pose a threat to biota and ecosystems (Henry et al., 1998; Swackhamer and Hites, 1988).

Efforts to reduce primary emissions of these two classes of ASEPs through regulations and management as exemplified by the Minamata (mercury; Giang et al., 2015) and Stockholm (PCBs; Lallas, 2001) Conventions are ongoing. Nevertheless, assessing the effectiveness of such efforts to mitigate impacts requires a thorough understanding of ASEP behavior in

the multimedia environment. Environmental fate and transport models are key tools for elucidating the complex pathways of ASEPs from their initial release (e.g., emission into the air) to their ultimate fate (e.g., sequestration in soils and sediments) in the environment. Between these two endpoints (i.e., releases and sinks), models enable an understanding of the ASEP distributions among multiple environmental compartments and their dynamic inter-compartmental exchange (e.g., air-water; air-soil, air-vegetation).

Of the many types of models of environmental fate and transport of ASEPs, 3-D atmospheric or chemical transport models (CTMs) are used to simulate four general processes: emissions, atmospheric transport, chemistry, and deposition (Brasseur and Jacob, 2017). CTMs such as GEOS-Chem have been used to simulate ASEPs such as Hg (Selin et al. 2008), PCBs (Friedman and Selin, 2016), and polycyclic aromatic hydrocarbons (PAHs; Friedman and Selin, 2012). Collectively, these applications of CTMs enhance our knowledge of ASEP environmental processing in terms of ability to, e.g., predict future atmospheric concentrations under various climate, policy, and land-use/land-cover change scenarios (Kumar et al., 2018), and understand source-receptor relationships (Song et al., 2016), and responses of deposition and bioaccumulation in the Great Lakes to policy and other large-scale drivers of emissions (Perlinger et al., 2018). Multimedia environmental models of chemicals are commonly applied to establish a link between chemical properties, emissions, and concentrations, providing insights into the processes that determine fate and transport in a defined environment (Macleod et al., 2011; Macleod et al., 2005). For PCBs, a suite of multimedia mass balance models of varying complexity has been developed with the objective to investigate the relationship between sources of

PCBs and their concentrations in air, water, sediments, and biota (Meijer et al., 2006; Shen et al., 2012; Guo et al., 2017; Zhang et al., 2008; Rashleigh et al., 2009; Rowe, 2009). CTMs and multimedia environmental models are important decision-support tools for developing emission reduction strategies and monitoring progress toward targeted-reductions and/or eliminating environmental impacts of ASEPs. Improved performance of these models largely depends upon the accuracy of emission estimates, chemical reactions and pathways (reactivity; partitioning; degradation), and parameterization of physical processes (dry and wet deposition; re-emission).

Currently, there exist substantial knowledge gaps in regards to the performance of parameterizations of atmosphere-surface exchange processes of ASEPs in CTMs. In CTMs, the accuracy of estimates of dry deposition of particle-bound ASEPs such as Hg and PCBs, and other pollutants largely depends on the performance of the dry deposition parameterization. Many dry deposition models have been developed for scientific research and operational purposes (see review by Petroff et al., 2008). Despite considerable efforts to develop dry deposition parameterizations of varying complexity, there remain few gaps in systematic performance evaluation of existing schemes with reliable field measurements. More specifically, information regarding the accuracy, uncertainty, and sensitivity of a suite of dry particle deposition parameterizations has been lacking. In addition, the complexity of dry deposition model formulation is another issue given incomplete knowledge of particle deposition processes. It is currently unknown whether complex models perform better than simple models. **Chapter 1** of this dissertation presents

a comprehensive evaluation of five dry deposition parameterizations in terms of their accuracy, uncertainty, sensitivity, and complexity.

Understanding the global biogeochemical cycling of Hg using CTMs largely depends on how the atmosphere–surface exchange fluxes of elementary mercury (Hg^0) are constrained in the models (Mason et al., 2012; Pirrone et al., 2010). Thus far, the parameterization of atmosphere-surface (e.g., air-soil) exchange has been developed based on a limited understanding of the processes that govern the deposition and emission from surfaces such as soils and leaves. An improved knowledge of exchange fluxes is necessary to assess the negative impact of mercury on humans and the effectiveness of policy actions to reduce the burden of anthropogenic mercury emissions (Selin, 2014). In addition, because mercury can undergo frequent deposition and re-emission cycles, it is of importance to better parameterize the secondary emission from natural reservoirs such as surface soils and vegetation in global CTMs such GEOS-Chem. The existing surface-atmosphere exchange parameterization of Hg^0 in GEOS-Chem is yet to be tested against field measurements. **Chapter 2** of this dissertation presents a study on improvement of dry gaseous deposition and soil re-emission parameterizations of Hg^0 for use in CTMs.

Following the ban on production in the U.S. in 1979, atmospheric concentrations of PCBs above Lake Superior, the largest of the five Laurentian Great Lakes, decreased rapidly. Subsequently, PCB concentrations in the lake surface water also approached equilibrium as the atmospheric levels of PCBs declined. PCBs are of great concern in Lake Superior because these compounds tend to bioaccumulate in the aquatic food chain (Swackhamer and Hites, 1988) causing risks to predator wildlife and humans through fish consumption

(Stow, 1995; Humphrey et al., 2000). Previous studies (Chang et al., 2012; Bhavsar et al., 2007) on long-term PCB levels and trends in fish suggested that the initial rate of decline of PCB concentrations in fish has leveled off in Lake Superior. It is currently unknown what factor(s) control the current observed PCB levels in Lake Superior fish. However, recycling from sediments has often been proposed to explain this slow recovery in fish (Smith, 2000). **Chapter 3** of this dissertation presents application of a dynamic multimedia model developed in this chapter to investigate the slow decrease in PCB concentrations in fish resulting from legacy PCB inputs to Lake Superior.

References

Bhavsar, S.P., Jackson, D.A., Hayton, A., Reiner, E.J., Chen, T., Bodnar, J., 2007. Are PCB levels in fish from the Canadian Great Lakes still declining? Journal of Great Lakes Research 33, 592-605.

Borgå, K., Fisk, A.T., Hargrave, B., Hoekstra, P.F., Swackhamer, D., Muir, D.C., 2005. Bioaccumulation factors for PCBs revisited. Environmental science & technology 39, 4523-4532.

Brasseur, G.P., Jacob, D.J., 2017. Modeling of Atmospheric Chemistry. Cambridge University Press.

Brown, T.M., Macdonald, R.W., Muir, D.C., Letcher, R.J., 2018. The distribution and trends of persistent organic pollutants and mercury in marine mammals from Canada's Eastern Arctic. Science of The Total Environment 618, 500-517.

Chang, F., Pagano, J.J., Crimmins, B.S., Milligan, M.S., Xia, X., Hopke, P.K., Holsen, T.M., 2012. Temporal trends of polychlorinated biphenyls and organochlorine pesticides in Great Lakes fish, 1999–2009. Science of the total environment 439, 284-290.

Dietz, R., Sonne, C., Basu, N., Braune, B., O'Hara, T., Letcher, R.J., Scheuhammer, T., Andersen, M., Andreasen, C., Andriashek, D., 2013. What are the toxicological effects of mercury in Arctic biota? Science of the Total Environment 443, 775-790.

Friedman, C.L., Selin, N.E., 2012. Long-range atmospheric transport of polycyclic aromatic hydrocarbons: a global 3-D model analysis including evaluation of Arctic sources. Environmental science & technology 46, 9501-9510.

Friedman, C.L., Selin, N.E., 2016. PCBs in the Arctic atmosphere: determining important driving forces using a global atmospheric transport model. Atmospheric Chemistry and Physics 16, 3433-3448.

Giang, A., Stokes, L.C., Streets, D.G., Corbitt, E.S., Selin, N.E., 2015. Impacts of the minamata convention on mercury emissions and global deposition from coal-fired power generation in Asia. Environmental science & technology 49, 5326-5335.

Guo, J., Romanak, K., Westenbroek, S., Li, A., Kreis Jr, R.G., Hites, R.A., Venier, M., 2017. Updated Polychlorinated Biphenyl Mass Budget for Lake Michigan. Environmental science & technology 51, 12455-12465.

Henry, K., Kannan, K., Nagy, B., Kevern, N., Zabik, M., Giesy, J., 1998. Concentrations and hazard assessment of organochlorine contaminants and mercury in smallmouth bass

from a remote lake in the Upper Peninsula of Michigan. Archives of environmental contamination and toxicology 34, 81-86.

Humphrey, H., Gardiner, J.C., Pandya, J.R., Sweeney, A.M., Gasior, D.M., McCaffrey, R.J., Schantz, S.L., 2000. PCB congener profile in the serum of humans consuming Great Lakes fish. Environmental health perspectives 108, 167.

Kumar, A., Wu, S., Huang, Y., Liao, H., Kaplan, J.O., 2018. Mercury from wildfires: Global emission inventories and sensitivity to 2000–2050 global change. Atmospheric Environment 173, 6-15.

Lallas, P.L., 2001. The Stockholm Convention on persistent organic pollutants. American Journal of International Law 95, 692-708.

MacLeod, M., Riley, W.J., Mckone, T.E., 2005. Assessing the influence of climate variability on atmospheric concentrations of polychlorinated biphenyls using a global-scale mass balance model (BETR-Global). Environmental science & technology 39, 6749-6756.

MacLeod, M., von Waldow, H., Tay, P., Armitage, J.M., Wöhrnschimmel, H., Riley, W.J., McKone, T.E., Hungerbuhler, K., 2011. BETR global–A geographically-explicit global-scale multimedia contaminant fate model. Environmental pollution 159, 1442-1445.

Mason, R.P., Choi, A.L., Fitzgerald, W.F., Hammerschmidt, C.R., Lamborg, C.H., Soerensen, A.L., Sunderland, E.M., 2012. Mercury biogeochemical cycling in the ocean and policy implications. Environmental research 119, 101-117.

Meijer, S.N., Dachs, J., Fernandez, P., Camarero, L., Catalan, J., Del Vento, S., Van Drooge, B., Jurado, E., Grimalt, J.O., 2006. Modelling the dynamic air–water–sediment coupled fluxes and occurrence of polychlorinated biphenyls in a high altitude lake. Environmental pollution 140, 546-560.

Perlinger, J., Urban, N., Giang, A., Selin, N., Hendricks, A., Zhang, H., Kumar, A., Wu, S., Gagnon, V., Gorman, H., 2018. Responses of deposition and bioaccumulation in the Great Lakes region to policy and other large-scale drivers of mercury emissions. Environmental Science: Processes & Impacts 20, 195-209.

Perlinger, J.A., Gorman, H.S., Norman, E.S., Obrist, D., Selin, N.E., Urban, N.R., Wu, S., 2016. Measurement and Modeling of Atmosphere-Surface Exchangeable Pollutants (ASEPs) To Better Understand their Environmental Cycling and Planetary Boundaries. ACS Publications.

Petroff, A., Mailliat, A., Amielh, M., Anselmet, F., 2008. Aerosol dry deposition on vegetative canopies. Part I: review of present knowledge. Atmospheric Environment 42, 3625-3653.

Pirrone, N., Cinnirella, S., Feng, X., Finkelman, R.B., Friedli, H.R., Leaner, J., Mason, R., Mukherjee, A.B., Stracher, G., Streets, D.G., 2010. Global mercury emissions to the atmosphere from anthropogenic and natural sources. Atmospheric Chemistry and Physics 10, 5951-5964.

Rashleigh, B., Barber, M.C., Walters, D.M., 2009. Foodweb modeling for polychlorinated biphenyls (PCBs) in the Twelvemile Creek arm of Lake Hartwell, South Carolina, USA. ecological modelling 220, 254-264.

Rowe, M.D., 2009. Modeling contaminant behavior in Lake Superior: a comparison of PCBs, PBDEs, and mercury.

Selin, N.E., 2014. Global change and mercury cycling: Challenges for implementing a global mercury treaty. Environmental toxicology and chemistry 33, 1202-1210.

Selin, N.E., Jacob, D.J., Yantosca, R.M., Strode, S., Jaeglé, L., Sunderland, E.M., 2008. Global 3-D land-ocean-atmosphere model for mercury: Present-day versus preindustrial cycles and anthropogenic enrichment factors for deposition. Global Biogeochemical Cycles 22, n/a-n/a.

Shen, J., Hong, B., Schugam, L., Zhao, Y., White, J., 2012. Modeling of polychlorinated biphenyls (PCBs) in the Baltimore Harbor. Ecological modelling 242, 54-68.

Song, S., Selin, N.E., Gratz, L.E., Ambrose, J.L., Jaffe, D.A., Shah, V., Jaeglé, L., Giang, A., Yuan, B., Kaser, L., Apel, E.C., Hornbrook, R.S., Blake, N.J., Weinheimer, A.J., Mauldin Iii, R.L., Cantrell, C.A., Castro, M.S., Conley, G., Holsen, T.M., Luke, W.T., Talbot, R., 2016. Constraints from observations and modeling on atmosphere–surface exchange of mercury in eastern North America. Elementa: Science of the Anthropocene 4, 000100.

Stow, C.A., 1995. Factors associated with PCB concentrations in Lake Michigan fish. Environmental science & technology 29, 522-527.

Swackhamer, D.L., Hites, R.A., 1988. Occurrence and bioaccumulation of organochlorine compounds in fishes from Siskiwit Lake, Isle Royale, Lake Superior. Environmental science & technology 22, 543-548.

Zhang, X., Rygwelski, K.R., Rossmann, R., Pauer, J.J., Kreis Jr, R.G., 2008. Model construct and calibration of an integrated water quality model (LM2-Toxic) for the Lake Michigan Mass Balance Project. ecological modelling 219, 92-106.

1 CHAPTER 1: Evaluation of five dry particle deposition parameterizations for atmospheric transport models

Abstract

Despite considerable effort to develop mechanistic dry particle deposition parameterizations for atmospheric transport models, current knowledge has been inadequate to propose quantitative measures of the relative performance of available parameterizations. In this study, we evaluated the performance of five dry particle deposition parameterizations developed by Zhang et al. (2001) (*Z01*), Petroff and Zhang (2010) (*PZ10*), Kouznetsov and Sofiev (2012) (*KS12*), Zhang and He (2014) (*ZH14*), and Zhang and Shao (2014) (*ZS14*), respectively. The evaluation was performed in three dimensions: model ability to reproduce observed deposition velocities, V_d (*accuracy*), the influence of imprecision in input parameter values on the modeled V_d (*uncertainty*), and identification of the most influential parameter(s) (*sensitivity*). The accuracy of the modeled V_d was evaluated using observations obtained from five land use categories (LUCs): grass, coniferous and deciduous forests, natural water, and ice/snow. To ascertain the uncertainty in modeled V_d, and quantify the influence of imprecision in key model input parameters, a Monte Carlo uncertainty analysis was performed. The Sobol' sensitivity analysis was conducted with the objective to determine the parameter ranking, from the most to the least influential. Comparing the normalized mean bias factors (indicator of accuracy), we find that the *ZH14* parameterization is the most accurate for all LUCs except for coniferous forest, for which it is second most accurate. From Monte Carlo simulations, the estimated mean normalized uncertainties in the modeled V_d obtained for seven particle sizes (ranging from 0.005 to 2.5 μm) for the five LUCs are 17%, 12%, 13%, 16%, and 27% for the *Z01*, *PZ10*, *KS12*, *ZH14*, and *ZS14* parameterizations, respectively. From the Sobol' sensitivity results, we suggest that the parameter rankings vary by particle size and LUC for a given parameterization. Overall, for d_p = 0.001 to 1.0 μm, friction velocity was one of the three most influential parameters in all parameterizations. For giant particles (d_p = 10 μm), relative humidity was the most influential parameter. Because it is the least complex of the five parameterizations, and it has the greatest accuracy and least uncertainty, we propose that the *ZH14* parameterization is currently superior for incorporation into atmospheric transport models.

1.1 Introduction

Dry deposition is a complex process that is influenced by the chemical properties of aerosols and their sources, meteorological conditions, and surface characteristic features. The transference of particles from the atmosphere to the earth's surface is controlled by forcings such as frictional drag and terrain induced flow modification (Giorgi, 1986; Stull, 1988). Understanding the processes and factors controlling dry deposition is necessary to estimate the residence time of atmospheric particles, which governs their atmospheric transport distance, trans-boundary fluxes, and potential climate effects (IPCC, 2001; Nemitz et al., 2002; Pryor et al., 2008). An accurate estimation of dry deposition is also needed to quantify the atmospheric loads of particles containing sulfate, nitrate, and ammonium that contribute to acidification and eutrophication of ecosystems, toxic elements such as Pb, Zn, and Cd, and base cations such as Na^+, K^+, Ca^{2+}, and Mg^{2+} that alter the nutrient cycling in soil (Ruijgrok et al., 1995; Petroff et al., 2008a).

Over the last three decades, several indirect and direct methods were developed to measure dry particle deposition (hereinafter referred to as dry deposition) flux to ecosystems (McMahon and Denisot, 1979; Sehmel, 1980; Gallagher et al., 1997; Zhang and Vet, 2006; Pryor et al., 2008). Dry deposition velocity V_d at height z is defined as the ratio of the total flux $F(z)$ divided by the particle concentration at the same height $C(z)$ (Pryor et al., 2013; Rannik et al., 2016) and is mathematically expressed as:

$$V_d = -\frac{F(z)}{C(z)} \quad (1)$$

One of the major limitations of direct flux measurement is limited spatial coverage because the measurement stations are confined to only a limited number of sites (Nemitz et al., 2002). The application of spatially and temporally resolved 3-D atmospheric transport models, from regional to global scale, can produce estimates of dry deposition fluxes for a suite of atmospheric species over various natural surfaces such as bare soil, grass, forest canopies, water, and ice/snow. To predict the dry deposition fluxes using atmospheric transport models, a parameterization/scheme that can adequately account for the major physical processes of particle deposition (e.g., turbulent diffusion, gravitational settling, interception, impaction, and Brownian diffusion) must be embedded in the host model.

Many dry deposition models have been developed for scientific research and operational purposes (see model review by Petroff et al., 2008a). Significant advances in understanding the governing mechanisms of dry deposition were made through use of experimental deposition data on walls of vertical pipes in the developments of size-resolved parameterizations for atmospheric particle deposition on ground surface (Muyshondt et al., 1998; Noll et al., 2001; Feng, 2008). In mechanistic or process-based dry deposition models, an electrical resistance based approach is widely used to parameterize the dry deposition velocity (Venkatram and Pleim, 1999). In this approach, dry deposition occurs via two parallel pathways: turbulent diffusion (expressed as aerodynamic resistance) and gravitational settling (expressed as resistance due to gravitation). In addition, particle collection by surfaces via Brownian diffusion, interception, and impaction are represented using separate surface resistance terms (Slinn, 1982; Hicks et al., 1987; Wesely and Hicks, 2000; Zhang et al., 2001; Seinfeld and Pandis, 2006; Petroff and Zhang, 2010; Zhang and

He, 2014). In all these models, the conventional resistance-based approach does not consider surface inhomogeneity or terrain complexity (i.e., deposition over flat terrain is assumed). However, Hicks (2008) argued about the importance of considering terrain complexity in dry deposition models because the assumption of surface homogeneity in existing deposition models limits the accuracy of pollutant load estimation in sensitive ecosystems that are located in complex terrain (e.g., on mountaintops or hills).

Despite considerable efforts in developing dry deposition parameterizations of varying complexity, there remain considerable gaps in systematic performance evaluation of existing schemes with reliable field measurements. We note that the evaluation of dry deposition parameterizations with field measurements is very limited and not up to date. Van Aalst (1986) evaluated the performance of six dry deposition parameterizations against field measurements, and reported large discrepancies in terms of the modeled deposition velocities. He reported that over water surfaces the modeled deposition velocities for 1.0-μm particles by the Williams (1982) scheme were factors of 10 to 50 higher than those predicted by the Sehmel and Hodgson (1978) scheme. For forest canopy, the Wiman and Agren (1985) model over-predicted the deposition velocities of the Slinn (1982) model by a factor of five. In a recent study, Hicks et al. (2016) compared five deposition models with measurements conducted over forests. They found that for particle sizes less than ca. 0.2 μm, the modeled deposition velocities agreed fairly well with measured velocities. The largest discrepancy was observed for particle sizes of 0.3 to ca. 5.0 μm. Studies also suggest that in many dry deposition parameterizations, the largest uncertainty exists for 0.1-1.0 μm particles because of the differing treatments of some key

particle deposition processes such as Brownian diffusion (Van Aalst, 1986; Petroff and Zhang, 2010; Zhang and Shao, 2014).

Uncertainty in modeled dry deposition velocities is an area that requires a thorough investigation. Only a few studies have been conducted in quantifying the uncertainties in dry deposition parameterizations. Ruijgrok (1992) performed an uncertainty evaluation of the Slinn (1982) model by assessing the variabilities in nine input parameters to the model outputs. Using Slinn's model, Gould and Davidson (1992) determined the influence of uncertainties in the size of the collection elements, roughness length, canopy wind profile and wind speed on the modeled deposition velocities. As far as we know, a detailed uncertainty analysis to address the influence of varying particle size, meteorological conditions, and surface features has not been performed on existing dry deposition parameterizations. The results from an uncertainty analysis could be used as one of the model's performance indicators, and help guide the modeling community to adequately account for uncertainties in the modeled deposition fluxes of pollutants to ecosystems.

Sensitivity analysis is often performed to determine the most influential parameters to the model outputs. Typically, a dry deposition model incorporates a large number of input parameters, which are subject to variability. In addition to identifying the most sensitive parameter(s), a sensitivity analysis can provide important insight as to the processes that control the overall deposition process, and identify those that may require further improvement. However, a detailed sensitivity test that encompasses exploring the entire parameter spaces of the input parameters of a dry deposition parameterization has not yet been performed. Some researchers conducted one-at-a-time (OAT) sensitivity analysis

(SA) (Ruijgrok et al., 1997; Zhang et al., 2001) of dry deposition models. In OAT-SA, the effect of varying one model input parameter is tested at a time while keeping all others fixed (Salteli and Annoni, 2010). Because in reality the variabilities in a set of model input parameters are expected to occur simultaneously, an OAT-SA is not a useful tool to determine the most influential parameter(s) in the deposition models. Rather, a variance-based global sensitivity test approach is needed. In global sensitivity analysis, the potential effects from simultaneous variabilities of model input parameters over their plausible range is considered (Lilburne and Tarantola, 2008).

In the present study, five dry deposition parameterizations, developed by Zhang et al. (2001), Petroff and Zhang (2010), Kouznetsov and Sofiev (2012), Zhang and He (2014), and Zhang and Shao (2014), are selected for an intercomparison of performance in terms of accuracy, uncertainty, and sensitivity. Throughout this paper, these models are referred to as *Z01*, *PZ10*, *KS12*, *ZH14*, and *ZS14*, respectively. The objectives of this study are threefold. The first objective is to evaluate the accuracy of five dry deposition parameterizations using measured dry deposition velocities obtained from field observations. Data of measured deposition velocities were collected from the literature, which comprised of measurements conducted over land use categories (LUCs) including grass, coniferous and deciduous forests, natural water, and ice/snow. The second objective is to perform an uncertainty analysis of the modeled dry deposition velocities related to imprecision in model input parameter values. The third objective is to quantify the most influential parameters in the modeled dry deposition velocities by applying a global variance-based sensitivity analysis.

1.2 Background

1.2.1 Zhang et al. (2001) (*Z01*) scheme

The *Z01* scheme estimates dry deposition velocity as a function of particle size and density, meteorological variables, and surface properties. In the *Z01* scheme, the dry deposition velocity (V_d) is expressed as:

$$V_d = V_g + \frac{1}{R_a + R_s}, \tag{2}$$

where V_g is the gravitational settling velocity, R_a is the aerodynamic resistance above the canopy, and R_s is the surface resistance. The expression for gravitational settling velocity (V_g) is given as:

$$V_g = \frac{\rho d_p^2 g C}{18\eta_V}, \tag{3}$$

where ρ is the dry density of the particle, d_p is the particle aerodynamic diameter, g is the gravitational acceleration, C is the Cunningham correction factor, and η_V is the temperature dependent viscosity coefficient of air. The correction factor C is applied to account for the molecular structure of the air and is expressed as:

$$C = 1 + \frac{2\lambda}{d_p}\left(1.257 + 0.4e^{-\frac{0.55 d_p}{\lambda}}\right), \tag{4}$$

where λ is the mean free path of air molecules.

The aerodynamic resistance (R_a) is calculated as:

$$R_a = \frac{\ln\left(\frac{z_R}{z_0}\right) - \psi_H}{\kappa u_*}, \tag{5}$$

where z_R is the reference height where V_d is typically computed, z_0 is the roughness height, κ is the von Kármán constant, u_* is the friction velocity, and ψ_H is the stability function for heat. The expression for ψ_H is: $\psi_H = 2ln[0.5(1 + (1 - 16x)^{0.5}]$ when $x \in [-2; 0]$, and $\psi_H = -5x$ when $x \in [0; 1]$. Here, $x = z/L_O$, where z is the measurement height and L_O is the Monin-Obukhov length.

The surface resistance term, R_s in Eq. 2, is a function of particle collection efficiencies due to Brownian diffusion (E_B), impaction (E_{IM}), and interception (E_{IN}). Accordingly, R_s is parameterized as:

$$R_s = \frac{1}{\varepsilon_0 u_* (E_B + E_{IM} + E_{IN}) R_1}, \quad (6)$$

where ε_0 is an empirical constant and its value is taken as 3 for all LUCs, and R_1 is the correction factor for particle rebound, which is included to modify the collection efficiencies at the surface. R_1 is parameterized as a function of Stokes number (St) as:

$$R_1 = \exp(-St^{-0.5}). \quad (7)$$

The parameterizations for E_B, E_{IM}, and E_{IN} are expressed by Eqs. (8), (10), and (14), respectively. The particle collection efficiency (E_B) is parameterized as a function of Schmidt number (Sc) as:

$$E_B = Sc^{-\gamma}, \quad (8)$$

where Sc is the ratio of kinematic viscosity of air (ν) to the particle Brownian diffusivity (D). γ is a LUC dependent variable, and the typical values of γ range from 0.54 to 0.56 for

rough surfaces and from 0.50 to 0.56 for smooth surfaces. Brownian diffusivity (D) is calculated as:

$$D = \frac{Ck_BT}{3\pi\mu d_p}, \tag{9}$$

where C is the Cunningham correction factor as expressed by Eq. (4), k_B is the Boltzmann's constant (1.38×10^{-23} J K^{-1}), and μ is the dynamic viscosity of air at temperature T.

For smooth surfaces, particle collection efficiency by impaction (E_{IM}) is parameterized as:

$$E_{IM} = 10^{-\frac{3}{St}}. \tag{10}$$

And, for rough surfaces,

$$E_{IM} = \left(\frac{St}{\alpha+St}\right)^{\beta}, \tag{11}$$

where α and β are constants; values of α are LUC dependent, and β is taken as 2. In Eqs. (10-11), the Stokes number (St) is expressed as:

$$St = \frac{V_g u_*}{gA} \quad \text{(for vegetative surfaces)}, \tag{12}$$

$$St = \frac{V_g u_*^2}{\nu} \quad \text{(for smooth surfaces)}, \tag{13}$$

where A is the characteristic radius of the surface collector elements. The values of A are given for different LUCs for various seasons by Zhang et al. (2001).

Collection efficiency by interception (E_{IN}) is calculated as:

$$E_{IN} = \frac{1}{2}\left(\frac{d_p}{A}\right)^2. \quad (14)$$

Growth of particles under humid conditions is considered in the *Z01* scheme by replacing the d_p with a wet particle diameter (d_w), which is calculated as:

$$d_w = \left[\frac{C_1\left(\frac{d_p}{2}\right)^{C_2}}{C_3\left(\frac{d_p}{2}\right)^{C_4} - logRH} + \left(\frac{d_p}{2}\right)^{C_3}\right]^{1/3}, \quad (15)$$

where C_1, C_2, C_3, and C_4 are the empirical constants (values given in Table 1 of Zhang et al., 2001), and RH is the relative humidity.

1.2.2 Petroff and Zhang (2010) (*PZ10*) scheme

Petroff and Zhang (2010) parameterized dry deposition velocity using an expression similar to Eq. (2) with some improvements of the surface resistance and collection efficiency terms. In the *PZ10* scheme, the effect of gravity and drift forces (e.g., phoretic effects) were taken into account by introducing the term drift velocity $\left(V_{drift}\right)$. Thus, dry deposition velocity (V_d) at a reference height (z_R) is given as:

$$V_d = V_{drift} + \frac{1}{R_a + R_s}. \quad (16)$$

Here, the drift velocity V_{drift} is equal to the sum of gravitational settling velocity and phoretic velocity, and the expression of V_{drift} is:

$$V_{drift} = V_g + V_{phor}. \quad (17)$$

V_g is calculated using Eq. (3). The LUC dependent values of V_{phor} were given by Petroff and Zhang (2010).

Surface resistance (R_s) is commonly expressed as an inverse of the surface deposition velocity, V_{ds} (i.e., $R_s = 1/V_{ds}$). In the *PZ10* scheme, V_{ds} is parameterized as:

$$\frac{V_{ds}}{u_*} = E_g \frac{1+\left[\frac{Q}{Q_g}-\frac{\alpha}{2}\right]\frac{\tanh(\eta)}{\eta}}{1+\left[\frac{Q}{Q_g}+\alpha\right]\frac{\tanh(\eta)}{\eta}}. \quad (18)$$

The parameters (e.g., Q, Q_g, α, and η) used in Eq. (18) are dependent on the aerodynamic and surface characteristic features. The parameterization of the total particle collection efficiency on the ground below the vegetation (E_g) has two components: (i) collection by Brownian diffusion (E_{gb}) and (ii) collection by turbulent impaction (E_{gt}). In the *PZ10* scheme, formulation of E_{gb} is expressed as:

$$E_{gb} = \frac{Sc^{-2/3}}{14.5}\left[\frac{1}{6} ln\frac{(1+F)^2}{1-F+F^2} + \frac{1}{\sqrt{3}} Arctan\frac{2F-1}{\sqrt{3}} + \frac{\pi}{6\sqrt{3}}\right]^{-1}, \quad (19)$$

where F is a function of the Schmidt number (Sc) and is expressed as $F = Sc^{\frac{1}{3}}/2.9$.

Collection efficiency by turbulent impaction, E_{gt}, is a function of dimensionless particle relaxation time (τ_{ph}^{+}) and a coefficient C_{IT} (taken as 0.14). In the *PZ10* scheme, E_{gt} is parameterized as:

$$E_{gt} = 2.5 \times 10^{-3} C_{IT} \tau_{ph}^{+2}. \quad (20)$$

τ_{ph}^{+} is calculated as $\tau_{ph}^{+} = \tau_p u_f^2 / \nu$. The local friction velocity (u_f) is expressed as:

$$u_f = u_* e^{-\alpha}, \tag{21}$$

where α is the aerodynamic extinction coefficient and is expressed as:

$$\alpha = \left(\frac{k_x LAI}{12\kappa^2(1-\frac{d}{h})^2}\right)^{1/3} \Phi_m^{2/3}\left(\frac{h-d}{L_O}\right). \tag{22}$$

In Eq. (20), k_x is the inclination coefficient of canopy elements, LAI is the leaf area index, d is the zero-plane displacement height, h is the height of the canopy, L_O is the Monin-Obukhov length, and Φ_m is the non-dimensional stability function for momentum. The expressions for Φ_m is, $\Phi_m(x) = (1-16x)^{-1/4}$ when $x \in [-2{:}\,0]$ and $\Phi_m(x) = (1+5x)^{-1/4}$ when $x \in [0{:}\,1]$.

In Eq. (18), the non-dimensional time-scale parameter, Q, is defined as the ratio the turbulent transport time scale to the vegetation collection time scale. The magnitude of Q can be used to characterize the dominant mechanism of the vertical transport of particles to the surface. For particle deposition over a canopy, $Q \ll 1$ describes a condition in which homogeneous concentration of Aitken and accumulation mode particles prevails throughout the canopy. This condition occurs when turbulent mixing is very efficient and transfer of particles is limited by the collection efficiency on leaves. In contrast, $Q \gg 1$ characterizes a situation in which an inhomogeneous particle concentration within the canopy prevails, which is typical for coarse mode particles. Under such conditions, efficient collection of particles by leaves takes place and transfer to the surface is usually limited by the turbulent transport.

In the *PZ10* scheme, Q and Q_g are parameterized using Eqs. (23) and (24), respectively:

$$Q = \frac{LAIE_T h}{l_{mp}(h)}, \tag{23}$$

$$Q_g = \frac{E_g h}{l_{mp}(h)}, \tag{24}$$

where E_T is the total particle collection efficiency by various physical processes and $l_{mp}(h)$ is the mixing height for the particles. The mixing height for particles, $l_{mp}(h)$, is calculated as:

$$l_{mp}(h) = \frac{\kappa(h-d)}{\Phi_h\left(\frac{h-d}{L_O}\right)}, \tag{25}$$

where Φ_h is the stability function for heat and expressed as: $\Phi_h(x) = (1-16x)^{-1/2}$ when $x \in [-2; 0]$ and $\Phi_h(x) = 1 + 5x$ when $x \in [0; 1]$.

The total collection efficiency (E_T) is expressed as:

$$E_T = \frac{U_h}{u_*}(E_B + E_{IN} + E_{IM}) + E_{IT}, \tag{26}$$

where U_h is the horizontal wind speed at canopy height h, and E_B, E_{IN}, E_{IM}, and E_{IT} are the collection efficiencies by Brownian diffusion, interception, impaction, and turbulent impaction, respectively. Note that the physical meaning of the first three efficiency terms are similar to those of the *Z01* scheme. However, the parameterizations of these terms differ from the *Z01* scheme. The term describing turbulent impaction efficiency (E_{IT}) is absent in the *Z01* scheme.

Parameterization of deposition efficiencies (i.e., E_B, E_{IN}, E_{IM}, and E_{IT}) are given below according to the *PZ10* scheme:

Particle collection efficiency by Brownian diffusion (E_B):

$$E_B = C_B Sc^{-2/3} Re_h^{-1/2}. \quad (27)$$

In Eq. (27), C_B is the LUC dependent coefficient, Re_h is the Reynolds number of the horizontal air flow calculated at top of the canopy height h as $Re_h = \frac{U_h L}{\nu}$. Here, L is the LUC dependent characteristic length of the canopy obstacle elements.

Particle collection efficiency by interception (E_{IN}):

$$E_{IN} = C_B \frac{d_p}{L} \ (for\ needle-like\ obstacle), \quad (28)$$

$$E_{IN} = C_B \frac{d_p}{L}\left[2 + ln\frac{4L}{d_p}\right] \ (for\ leaf\ of\ plane\ obstacle). \quad (29)$$

In Eqs. 28-29, C_B is the LUC dependent coefficient.

Particle collection efficiency by impaction (E_{IM}):

$$E_{IM} = C_{IM}\left(\frac{St_h}{St_h+\beta_{IM}}\right)^2. \quad (30)$$

In Eq. (30), St_h is the Stokes number on top of the canopy, which is calculated as $St_h = \frac{\tau_p U_h}{L}$. τ_p is the particle relaxation time calculated as $\tau_p = V_g/g$. C_{IM} and β_{IM} are LUC dependent coefficients.

Particle collection efficiency by turbulent impaction (E_{IT}) is parameterized as:

$$E_{IT} = 2.5 \times 10^{-3} C_{IT} \tau_{ph}^{+2} \qquad if\ \tau_{ph}^{+} \leq 20, \tag{31}$$

$$E_{IT} = C_{IT} \qquad if\ \tau_{ph}^{+} \geq 20, \tag{32}$$

In Eqs. (31-32), the dimensionless particle relaxation time, $\tau_{ph}^{+} = \tau_p u_*^2/\nu$.

The term η in Eq. (18) is taken as:

$$\eta = \sqrt{\frac{\alpha^2}{4}} + Q. \tag{33}$$

For non-vegetative surfaces, such as bare soil, natural water and ice/snow, a modified form of Eq. (16) is used in the form of Eq. (34), which is expressed as:

$$V_d = V_{drift} + \frac{1}{R_a + 1/(E_{gb} u*)}. \tag{34}$$

1.2.3 Kouznetsov and Sofiev (2012) (*KS12*) scheme

Kouznetsov and Sofiev (2012) developed a dry deposition parameterization by extending the conventional resistance-based analogy using the exact solution of the steady-state equation for aerosol flux. According to the *KS12* scheme, for rough surfaces, dry deposition velocity (V_d) is computed as:

$$V_d = V_{diff} + V_{int} + V_{imp} + V_g, \tag{35}$$

where V_{diff}, V_{int}, V_{imp}, and V_g are the velocities for the depositing particles due to Brownian diffusion, interception, impaction, and gravitational settling, respectively. The parameterizations for these terms are provided below.

V_{diff} was parameterized as:

$$V_{diff} = 2u_* Re_*^{-1/2} Sc^{-2/3}, \tag{36}$$

where Re_* is the canopy Reynolds number given by

$$Re_* = \frac{u_* a}{\nu}, \tag{37}$$

where a is the length scale for different LUCs.

V_{int} is parameterized as:

$$V_{int} = u_* Re_*^{1/2} \left(\frac{d_p}{a}\right)^2, \tag{38}$$

V_{imp} is parameterized as:

$$V_{imp} = \frac{2u_*^2}{U_{top}} \eta_{imp} \left(St - \frac{u_*}{U_{top}} Re_*^{-1/2}\right), \tag{39}$$

where U_{top} is the mean horizontal wind speed on top of the canopy, η_{imp} is the particle collection efficiency due to impaction, and St is the Stokes number. Kouznetsov and Sofiev (2012) used Eq. (40) to parameterize $\frac{u_*}{U_{top}}$ as:

$$\frac{u_*}{U_{top}} = min\left[(C_s + C_R LAI/2)^2, \left(\frac{u_*}{U_{top}}\right)_{max}\right], \quad (40)$$

where C_s = 0.003, C_R = 0.3, and $\left(\frac{u_*}{U_{top}}\right)_{max}$ = 0.3 are constants.

The Stokes number St is expressed as:

$$St = \frac{\tau_p u_*}{a}, \quad (41)$$

where τ_p is the particle relaxation time calculated as $\tau_p = V_g/\mathrm{g}$.

The expression for η_{imp} is given as:

$$\eta_{imp} = exp\left\{\frac{-0.1}{St_e - 0.15} - \frac{1}{\sqrt{St_e - 0.15}}\right\} \qquad if\ St_e > 0.15, \quad (42)$$

$$\eta_{imp} = 0 \qquad if\ St_e \leq 0.15, \quad (43)$$

where St_e is the effective Stokes number calculated as:

$$St_e = St - Re_c^{-\frac{1}{2}}, \quad (44)$$

where Re_c is the critical Reynolds number calculated as:

$$Re_c = \left(\frac{U_{top}}{u_*}\right)^2 Re_*. \quad (45)$$

The term V_g in Eq. (35) is parameterized using Eq. (3).

Note that in the *KS12* scheme, the parameterization of V_d over smooth surfaces requires solving the universal velocity profiles (either numerically or analytically) described by Kouznetsov and Sofiev (2012). We exclude the details of the solution procedure in this paper. We used the analytical solutions of the velocity profile obtained from the authors of the *KS12* scheme through personal communication.

1.2.4 Zhang and He (2014) (*ZH14*) scheme

Zhang and He (2014) developed an empirical resistance-based parameterization for dry deposition by modifying the *Z01* scheme. The overall structure of the *ZH14* scheme is similar to that of the *Z01* scheme (i.e., V_d is calculated using Eq. (2)). In the *ZH14* scheme, the parameterizations of R_a and R_g are similar to those of the *Z01* scheme. However, in the *ZH14* scheme, parameterization for the surface resistance term R_s were modified for three bulk particle sizes (i.e., $PM_{2.5}$, $PM_{2.5\text{-}10}$, and PM_{10+}). Recalling, $R_s = 1/V_{ds}$, the parameterizations of V_{ds} are given below.

For particle sizes less than or equal to 2.5 μm ($PM_{2.5}$), V_{ds} is expressed as:

$$V_{ds(PM2.5)} = a_1 u_*, \tag{46}$$

where a_1 is an empirical constant derived by regression analysis. Values of a_1 are given by Zhang and He (2014) for five groups of 26 LUCs.

For particle sizes between 2.5 and 10 μm ($PM_{2.5\text{-}10}$), V_{ds} is expressed as:

$$V_{ds(PM2.5-10)} = (b_1 u_* + b_2 u_*^2 + b_3 u_*^3) e^{k1\left(\frac{LAI}{LAI_{max}} - 1\right)}, \tag{47}$$

where b_1, b_2, and b_3 are LUC dependent constants, LAI_{max} is the maximum leaf area index for a given LUC, and $k1$ is a constant, which is a function of u_*, and expressed as:

$$k1 = c_1 u_* + c_2 u_*^2 + c_3 u_*^3, \tag{48}$$

where c_1, c_2, and c_3 are the LUC dependent constants.

For particle sizes larger than 10 μm (PM_{10+}), V_{ds} is expressed as:

$$V_{ds(PM10+)} = (d_1 u_* + d_2 u_*^2 + d_3 u_*^3) e^{k2\left(\frac{LAI}{LAI_{max}} - 1\right)}, \tag{49}$$

where d_1, d_2, and d_3 are the LUC dependent constants, and LAI_{max} is the maximum leaf area index for a given LUC. The parameter $k2$ is a constant, which is a function of u_*, and is expressed as:

$$k2 = f_1 u_* + f_2 u_*^2 + f_3 u_*^3, \tag{50}$$

where f_1, f_2, and f_3 are the LUC dependent constants.

1.2.5 Zhang and Shao (2014) (*ZS14*) scheme

Zhang and Shao (2014) used an analytical solution of the steady-state flux equation to derive an expression to compute dry deposition velocity V_d as:

$$V_d = \left(R_g + \frac{R_s - R_g}{\exp(\frac{R_a}{R_g})} \right)^{-1}, \tag{51}$$

For neutral atmospheric stability conditions, the parameterizations of R_a for rough and smooth surfaces are given in Eqs. (52), and (53), respectively:

$$R_a = \frac{Sc_T}{\kappa u_*} ln\left(\frac{z-d}{h_c-d}\right), \qquad (rough\ surfaces) \tag{52}$$

$$R_a = \frac{B_1 Sc_T}{\kappa u_*} ln\left(\frac{z}{z_0}\right), \qquad (smooth\ surfaces) \tag{53}$$

where B_1 is an empirical constant (0.45), and Sc_T is the turbulent Schmidt number expressed as:

$$Sc_T = \left(1 + \frac{\alpha^2 V_g^2}{u_*^2}\right), \tag{54}$$

where α is a dimensionless coefficient taken as 1.

The gravitational resistance term R_g is calculated as $R_g = 1/V_g$. The parameterization of the surface resistance term R_s is given by Zhang and Shao (2014) as follows:

$$R_s = \left\{ RV_{dm} \left[\frac{E}{C_d} \frac{\tau_c}{\tau} + \left(1 + \frac{\tau_c}{\tau}\right) Sc^{-1} + 10^{\frac{-3}{T_{p,\delta}^+}} \right] + V_{g,w} \right\}^{-1}, \tag{55}$$

where $R = \exp(-b\sqrt{St})$ and where b is an empirical constant, E is the total collection efficiency, C_d is the drag partition coefficient, Sc is the Schmidt number, $T_{p,\delta}^+$ is the dimensionless particle relaxation time near the surface, and $V_{g,w}$ is the gravitational settling velocity of particle after humidity correction. $\frac{\tau_c}{\tau}$ is the ratio of the drag on the roof of the roughness element (τ_c) to the total shear stress (τ) and is calculated as:

$$\frac{\tau_c}{\tau} = \frac{\beta \lambda_e}{1+\beta \lambda_e}, \tag{56}$$

where β is the ratio of the pressure-drag coefficient to friction-drag coefficient, and λ_e is the effective frontal area index. The parameter λ_e is a function of frontal area index or roughness density (λ), and plane area index (η). The expression of λ_e is

$$\lambda_e = \frac{\lambda}{(1-\eta)^{c_2}} exp\left(-\frac{c_1\lambda}{(1-\eta)^{c_2}}\right), \tag{57}$$

where $c_1 = 6$ and $c_2 = 0.1$.

Eq. (56) is used to compute $T_{p,\delta}^+$ as:

$$T_{p,\delta}^+ = \frac{T_{p,\delta}u_*^2}{\nu}, \tag{58}$$

where $T_{p,\delta}$ is the particle relaxation time near the surface ($T_{p,\delta} = V_g/g$).

V_{dm} is calculated using two separate expressions for rough and smooth surfaces, as expressed in Eqs. (59) and (60), respectively:

$$V_{dm} = \frac{u_*}{u_a h_c} \quad (for \text{ rough surfaces}), \tag{59}$$

where u_a is the horizontal air speed and h_c is the height of the roughness element.

$$V_{dm} = B_2 u_* \quad (\text{for smooth surfaces}), \tag{60}$$

where B_2 is an empirical constant taken as 3.

In Eq. (55), the total collection efficiency (E) is comprised of collection efficiencies by Brownian diffusion (E_B), impaction (E_{IM}), and interception (E_{IN}). The parameterizations for each of these three terms are given below:

$$E_B = C_B Sc^{-2/3} Re^{n_B - 1}, \tag{61}$$

where C_B and n_B are empirical parameters function of flow regimes, and are given by Zhang and Shao (2014).

$$E_{IM} = \left(\frac{St}{0.6+St}\right)^2, \tag{62}$$

where St is the Stokes number and is expressed as $St = \tau_p u_* / d_c$. Here, d_c is the diameter of the surface collection element. Values of d_c are given by Zhang and Shao (2014) for various surfaces.

$$E_{IN} = A_{in} u_* 10^{-St \frac{2d_{p,w}}{d_c}}, \tag{63}$$

where A_{in} is a surface dependent micro-roughness characteristic element, and $d_{p,w}$ is the wet diameter of the particle.

1.3 Methods

1.3.1 An evaluation of the dry deposition parameterizations

To assess the accuracy of the five parameterizations, the modeled dry deposition velocities were compared with field measurements from both rough and smooth surfaces. The measurement studies conducted on various natural surfaces were collected from the

literature. More specifically, the studies citied in the review article on particle flux measurements by Pryor et al. (2008) were collected to acquire the meta-data on particle deposition. The availability of the measured and/or reported parameters (e.g., particle size and density, air temperature, relative humidity, horizontal wind speed, friction velocity, atmospheric stability parameter, canopy height, roughness height, zero-plane displacement height, and leaf area index) from these measurement studies was thoroughly investigated and compiled. It was found that many (ca. 50%) of the studies citied by Pryor et al. (2008) did not report most of the aforementioned parameters necessary to run the parameterizations to perform a valid comparison between the model output and measurements. To reduce uncertainty, those studies were excluded from the parameterization accuracy evaluation. In addition, a literature search was performed in Web of Science® to find measurement studies published after 2008, and those studies were thoroughly assessed to determine the availability of required input parameters to run the dry deposition models. Finally, 29 measurement studies covering five land use categories (LUCs) were selected to evaluate the accuracy of the five parameterizations. The five LUCs include grass, deciduous, and coniferous forests (rough surfaces), and natural water and ice/snow (smooth surfaces). Table 1 summarizes information related to sampling location, latitude, longitude, elevation above mean sea level (AMSL), sampling periods, and particle sizes reported in the measurement studies. The global spatial distribution of these measurement studies is shown in Figure 1 according to the five LUCs.

Table 1. Measurement studies used to evaluate the five parameterizations.

Land use category	No.	Title	Authors	Location	Latitude	Longitude	Elevation a.m.s.l. (m)	Sampling dates	Particle size (μm)
Grass	1	Dry deposition of fine aerosol to a grass surface	Allen et al. (1991)	UK	51.88° N	0.94° E	28	June 1988–June 1989	0.48
	2	An eddy-correlation measurement of particulate deposition from the atmosphere	Wesely et al. (1977)	US	38.84° N	90.06° W	225	February–March 1976	0.075
	3	Eddy correlation measurements of atmospheric fluxes of ozone, sulfur, and particulates during the Champaign intercomparison study	Neumann and den Hartog (1985)	US	40.11° N	88.27° W	225	June 1982	0.10–2.28
	4	Micrometeorological measurements of particle deposition velocities to moorland vegetation	Nemitz et al. (2002)	UK	55.79° N	3.23° W	109	May–October 1999	0.12–0.45
	5	Eddy correlation measurements of aerosol deposition to grass	Vong et al. (2004)	US	44.46° N	123.11° W	81	May–June 2000	0.52
Coniferous forest	6	The Landes experiment: biosphere–atmosphere exchanges of ozone and aerosol particles above a pine forest	Lamaud et al. (1994)	France	44.84° N	0.58° W	58	June 1992	0.04
	7	Micrometeorological measurement of the dry deposition flux of sulfate and nitrate aerosols to coniferous forest	Wyers and Duyzers (1997)	the Netherlands	52.27° N	5.71° E	26	April–December 1993	0.6
	8	Atmospheric particles and their interactions with natural surfaces	Gallagher et al. (1997)	the Netherlands	52.27° N	5.71° E	26	June–July 1993	0.1–0.50
	9	The dry deposition of particles to a forest canopy: a comparison of model and experimental results	Ruijgrok et al. (1997)	the Netherlands	52.27° N	5.71° E	26	June–July 1993	0.35–0.60
	10	Deposition velocities of nucleation mode particles into a Scots pine forest	Rannik et al. (2000)	Finland	61.85° N	24.28° E	181	September 2000	0.015–0.35
	11	Vertical aerosol fluxes measured by the eddy-covariance method and deposition of nucleation mode particles above a Scots pine forest in southern Finland	Buzorious et al. (2000)	Finland	61.85° N	24.28° E	181	March–May 1997	0.015
	12	Relaxed eddy accumulation system for size-resolved aerosol particle flux measurements	Gaman et al. (2004)	Finland	61.85° N	24.28° E	181	September–October 2001	0.05
	13	Analyses of flux methods and functional dependencies	Pryor et al. (2007)	Finland	61.85° N	24.28° E	181	January–December 2004	0.01–0.07
Deciduous forest	14	Aerosol particle dry deposition to canopy and forest floor measured by two-layer eddy-covariance system	Grönholm et al. (2009)	Finland	61.85° N	24.28° E	181	March 2003	0.01–0.05
	15	Fluxes of gases and particles above a deciduous forest in wintertime	Wesely et al. (1983)	US	35.98° N	78.91° W	77	January–February 1981	0.48
	16	Size-resolved particle deposition velocities of sub-100 nm diameter particles over a forest	Pryor (2006)	Denmark	55.48° N	11.64° E	40	May–June 2004	0.025–0.065
	17	Deposition velocity of $PM_{2.5}$ sulfate in the summer above a deciduous forest in central Japan	Matsuda et al. (2010)	Japan	36.40° N	138.58° E	1380	July 2009	2.5
Water	18	Mechanisms of transport from the atmosphere to the Earth's surface	Möller and Schumann (1970)	(Wind tunnel)	–	–	–	–	0.03–1.13
	19	Particle deposition rates on a water surface as a function of particle diameter and air velocity	Sehmel et al. (1974)	(Wind tunnel)	–	–	–	–	0.25–29
	20	Airborne concentrations and dry deposition fluxes of particulate species to surrogate surfaces deployed in southern Lake Michigan	Zufall et al. (1998)	US	44.00° N	87.00° W	–	July 1994; January 1995	0.4–24.0
	21	Determination of size-dependent dry particle deposition velocities with multiple intrinsic elemental tracers	Caffrey et al. (1998)	US	44.00° N	87.00° W	–	July 1994	0.05–48.0
Ice/snow	22	Aerosol dry deposition measured with eddy-covariance technique at Wasa and Aboa, Dronning Maud Land, Antarctica	Gronlund et al. (2002)	Antarctica	73.00° S	13.41° W	584	January 2000	0.02–0.2
	23	Deposition velocity of ultrafine particles measured with the eddy-correlation method over the Nansen Ice Sheet (Antarctica)	Contini et al. (2010)	Antarctica	74.88° S	163.17° W	84.7	December 2006	0.06–0.070
	24	On the potential contribution of open lead particle emissions to the central Arctic aerosol concentration	Held et al. (2011a)	Arctic Ocean	87.00° N	6.00° W	–	August–September 2008	0.045
	25	Near-surface profiles of aerosol number concentration and temperature over the Arctic Ocean	Held et al. (2011b)	Arctic Ocean	87.00° N	6.00° W	–	August–September 2008	0.045
	26	Correlation of dry deposition velocity and friction velocity over different surfaces for $PM_{2.5}$ and particle number concentrations	Donateo and Contini (2014)	Antarctica	74.88° S	163.17° W	–	December 2006	0.015, 0.13
	27	An experimental and theoretical investigation of the dry deposition of particles to snow, pine trees and artificial collectors	Ibrahim et al. (1983)	Canada	51.25° N	85.32° W	450	February 1980; March 1981	0.7, 0.8, 7.0
	28	Eddy correlation measurements of the dry deposition of particles in wintertime	Duan et al. (1988)	US	40.70° N	77.96° W	177	December 1985	0.22, 0.73
	29	Turbulent aerosol fluxes over the Arctic Ocean 1. Dry deposition over sea and pack ice	Nilsson and Rannik (2001)	Arctic Ocean	88.00° N	15.00° E	–	August 1999	0.02, 0.05

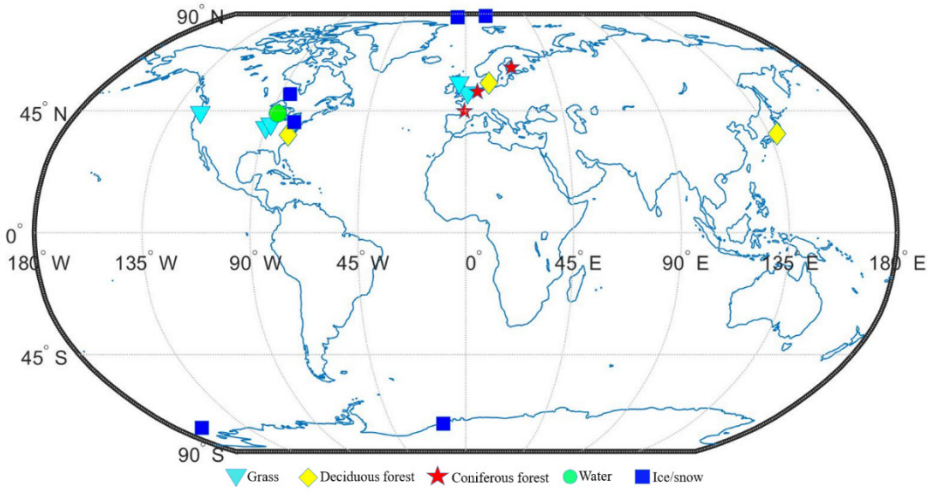

Figure 1. Global distribution of dry deposition measurement locations (listed in Table 1) used to evaluate the *Z01*, *PZ10*, *KS12*, *ZH14*, and *ZS14* parameterizations. Note that for multiple measurement campaigns conducted in one location, only one data point is shown. Two wind tunnel studies on water surfaces are not shown.

Measurements conducted over grass by Wesely et al. (1977), Neumann and den Hartog (1985), Allen et al. (1991), Nemitz et al. (2002), and Vong et al. (2004) were used to evaluate the performance of the five parameterizations. For coniferous forest, modeled deposition velocities were compared with measurements from Lamaud et al. (1994), Wyzers and Duyzer (1996), Gallagher et al. (1997), Ruijgrok et al. (1997), Buzorius et al. (2000), Rannik et al. (2000), Gaman et al. (2004), Pryor et al. (2007), and Grönholm et al. (2009). Experiments conducted over deciduous forest are limited, and only three studies (Wesely et al., 1983; Pryor, 2006; Matsuda et al., 2010) were used in the present paper.

To evaluate the performance of the parameterizations over water surfaces, studies by Möller and Schumann (1970), Sehmel et al. (1974), Zufall et al. (1998) and Caffrey et al. (1998) were used. We note that the studies by Möller and Schumann, and Sehmel et al. were conducted in the wind tunnels, and thus the observed deposition does not necessarily

reflect deposition under natural conditions. Particle deposition measurements on ice/snow pack were collected from eight studies: Ibrahim (1983); Duan et al. (1988); Nilsson and Rannik (2001); Gronlund et al. (2002); Contini et al. (2010); Held et al. (2011a); Held et al. (2011b); and Donateo and Contini (2014). The parameterizations were fed using reported values of particle properties (diameter and density), meteorological conditions (stability parameter, temperature, wind speed, etc.), and surface properties (canopy height, roughness length, leaf area index, etc.). However, reasonable values of the missing parameters were used when needed.

In the present study, the accuracy of the dry deposition parameterizations was evaluated using the normalized mean bias factor (B_{NMBF}). The B_{NMBF} provides a statistically robust and unbiased symmetric measure of the factor by which the modeled dry deposition velocities differ from the measured ones, and the sense of that factor (i.e., the positive and negative values imply the ovepredictiion and underprediction by models, respectively). The interpretation of the B_{NMBF} is simple (i.e., average amount by which the ratio of modeled and measured quantities differ from unity), and it avoids any inflation that may be caused by low values of measured quantities (Yu et al., 2006).

To quantify the disagreement between the modeled and observed quantities, the normalized mean bias factors were calculated for the pairs of modeled ($V_{d(modeled),i}$) and measured dry deposition velocities ($V_{d(measured),i}$), respectively. In this study, the expressions for computing B_{NMBF} used in two different forms, which are:

For the $V_{d(modeled),i} > V_{d(measured),i}$ case (i.e., overestimation):

$$B_{NMBF} = \frac{\sum V_{d(modeled),i}}{\sum V_{d(measured),i}} - 1 \tag{64}$$

For the $V_{d(modeled),i} < V_{d(measured),i}$ case (i.e., underestimation):

$$B_{NMBF} = 1 - \frac{\sum V_{d(measured),i}}{\sum V_{d(modeled),i}} \tag{65}$$

The step-wise derivation of the Eqs. (64-65) and their application on training air quality data sets are illustrated by Yu et al. (2006).

1.3.2 Uncertainty analysis

To quantify the influence of imprecision in the model input parameter values on the modeled velocities, a classical Monte Carlo uncertainty analysis was applied. The Monte Carlo techniques have been widely used to evaluate the propagated uncertainty in the modeled outputs in many geophysical models (e.g., Alcamo and Bartnickj, 1987; Derwent and Hov, 1988; Chen et al., 1997; Tatang et al., 1997; Hanna et al., 1998, 2001; Bergin et al., 1999; Bergin and Milford, 2000; Beekman et al., 2003; Mallet and Sportisse, 2006). Monte Carlo uncertainty evaluation techniques are relatively straightforward and flexible means for incorporating probabilistic values in the modeled dry deposition velocities. Indeed, the techniques are less reliant on assumptions about distributions of the input parameters (Hanna et al., 2001).

In this study, we define uncertainty in the parameterizations as the inability to confidently specify single-valued quantities because of the imprecision in the model input parameters. A classical Monte Carlo uncertainty method was applied to assess the overall uncertainty of a dry deposition parameterization with regard to the uncertainties in the following input parameters: RH, h, z_0, d, LAI, U, u_*, and L_O. The uncertainty estimates for those input parameters were obtained from the literature and are presented in Table 2. Using the uncertainty ranges for each of these parameters, uniform probability distribution functions were assigned since information on their actual distributions are lacking. It is noted that a constant dry particle density of 1500 kg m^{-3} (Petroff and Zhang 2010) was used in all Monte Carlo simulations. Because of the inhomogeneous nature of ambient particles, accurate measurement of particle density is challenging. In their work, Oskouie et al. (2003) developed methods using a time-of-flight instrument to minimize the effect of uncertainties in density estimation in particle size characterization.

Table 2. Parameter values and associated uncertainties in Monte Carlo simulation.

Parameter	Base value (assumed)		Uncertainty	Reference*
Relative humidity, *RH* (%)	80	(all LUCs)	±5%	Heinonen (2002)
Wind speed, *U* (m/s)	4	(all LUCs)	±3%	Högström and Smedman (2004)
Friction velocity, u_* (m/s)	0.3	(all LUCs)	±10%	Andreas (1992)
Monin-Obukhov length, L_O (m)	50	(all LUCs)	±10%	Weidinger et al. (2000)
Roughness length, z_0 (m)	0.04	(Grass)	±25%	Su et al. (2001)
	1.2	(Coniferous forest)		
	1.5	(Deciduous forest)		
	0.001	(Ice/snow)		
Canopy height, *h* (m)	0.5	(Grass)	±5%	Larjavaara and Muller-Landau (2013)
	15	(Coniferous forest)		
	25	(Deciduous forest)		
Zero-plane displacement height, *d* (m)	0.3	(Grass)	±25%	Su et al. (2001)
	7	(Coniferous forest)		
	16	(Deciduous forest)		
Leaf area index (one-sided), *LAI* (m^2/m^2)	4	(Grass)	±5%	Richardson et al. (2011)
	10	(Coniferous forest)		
	10	(Deciduous forest)		

* The references are for the uncertainty values (in percentage).

The Monte Carlo simulations were performed using R statistical software (version 3.2.4). Each simulation was run by randomly drawing 100 samples from the assigned uniform probability density function (PDF). The simulations were repeated 10,000 times. Frequency distributions or the PDFs of the modeled dry deposition velocity are the basic

results of the Monte Carlo simulations. These PDFs were approximated assuming normal distributions, and then the 5th, 50th, and 95th percentile dry deposition velocities were computed. We use the range of the central 90% (the difference between 95^{th} and 5^{th} percentiles) of the PDFs as a convenient measure of uncertainty in the modeled deposition velocity. These steps were repeated for all five parameterizations using seven different particle sizes: 0.005, 0.05, 0.5, 1.0, 1.5, 2.0, and 2.5 μm on the selected five LUCs (i.e., grass, deciduous and coniferous forests, water, and ice/snow). These particle sizes were selected to represent four distinct particle modes: nucleation (<0.01 μm), Aitken (0.01-0.1 μm), accumulation (0.1-1.0 μm), and coarse (>1.0 μm), respectively.

1.3.3 Sensitivity analysis

In this study, the Sobol' sensitivity method (Sobol' 1990) was applied to identify the most influential input parameter or the set of parameters of a dry deposition parameterization, and to characterize the relative contribution of the parameters to the overall variability in the modeled V_d. As opposed to the local sensitivity analysis (e.g., OAT approach), the Sobol' method is a global sensitivity approach, in which a set of input parameters of a model can be varied simultaneously over their entire parameter value space to identify their relative contributions to the overall model output variance. The Sobol' method has been applied in environmental modeling applications (Tang et al., 2007; Pappenberger et al., 2008; van Werkhoven et al., 2008; Yang, 2011), but has not yet been applied in dry deposition modeling research. Given that in most of the dry deposition parameterizations, model inputs can span a wide range within their physical realms, the application of a global

sensitivity analysis used in this study should be viewed as a critical step toward the understanding of different sub-physical processes of particle deposition.

In the Sobol' method, the variance contributions to the total output variance of individual parameters and parameter interactions can be determined. These contributions are characterized by the ratio of the partial variance (V_i) to the total variance (V) as expressed in Eq. 66. This ratio is commonly termed as Sobol' first order index (S_i) (Saltelli et al., 2010; Nossent et al., 2011). The first order indices represent the fractions of the unconditional model output variance. In this study, Sobol' first order sensitivity indices were calculated as:

$$S_i = \frac{V_i}{V} = \frac{V_{X_i}(E_{\boldsymbol{X}_{\sim i}}(V_d|X_i))}{V(V_d)}, \tag{66}$$

where X_i is the *i*-th input parameter and $\boldsymbol{X}_{\sim i}$ denotes the matrix of all input parameters but X_i. The meaning of the inner expectation operator is that the mean of V_d is taken over all possible values of $X_{\sim i}$ while keeping X_i fixed. The outer variance is taken over all possible values of X_i. The variance $V(V_d)$ in the denominator is the total (unconditional) variance.

The numerator in Eq. (66) can be interpreted as follows: $V_{X_i}(E_{\boldsymbol{X}_{\sim i}}(V_d|X_i))$ is the expected reduction in variance that would be obtained if X_i could be fixed. In regard to the variability of the model input parameters in dry deposition schemes, S_i provides a means to quantity the effect of parameter X_i by itself. A higher order (S_{ij}) or total order (S_{Ti}) can be computed when the total effect of a parameter, inclusive of all its interaction with other

model input parameters, are of interest. In this paper, we confine the sensitivity analysis to Sobol' first order indices only.

For each of the five parameterizations evaluated here, four to nine input parameters were selected for determining the first order Sobol' sensitivity indices. An exception to applying the Sobol' method was made for the *KS12* parameterization while evaluating the parameter sensitivity for smooth surfaces. Due to the complex nature of *KS12* smooth surface parameterization, it was not computationally feasible to apply the Sobol' method. Instead, the OAT approach was applied for water and ice/snow surfaces. Note that the total number of input parameters that go into each model varies between parameterizations, and LUC types. For each parameterization, five particle sizes (d_p = 0.001, 0.01, 0.1, 1.0, and 10 μm) were assessed for Sobol' analysis. The sensitivity of each parameterization was tested for the following three sets of input parameters for five LUCs: (i) particle properties, (ii) aerodynamic parameters, and (iii) surface characteristics of particle deposition. First, the sensitivity of particle deposition to particle properties (aerodynamic diameter and density) was tested. Sensitivity indices were calculated for the particle size range of 0.001 μm to 10 μm. Second, the sensitivity of the schemes was tested for aerodynamic parameters (friction velocity, wind speed, and stability condition) for different particle sizes one-at-a-time. Third, the sensitivity of the schemes to surface characteristics was tested. Surface characteristics include h, z_0, d, and LAI. The sensitivity ranges for the parameter values used for Sobol' analysis are reported in Table 3.

Table 3. Input parameter ranges for Sobol' sensitivity analysis.

Parameter	Range		Reference
Relative humidity, RH (%)	10-100	(all LUCs)	Assumed
Dry particle density, ρ (kg m^{-3})	1500-2000	(all LUCs)	Studies # 1-29
Wind speed, U (m/s)	1-5	(all LUCs)	Studies # 1-29
Friction velocity, u_* (m/s)	0.1-0.5	(all LUCs)	Studies # 1-29
Monin-Obukhov length, L_O (m)	10-100	(all LUCs)	Studies # 1-29
Roughness length, z_0 (m)	0.02-.0.10	(Grass)	Studies # 1-5
	0.9-3.0	(Coniferous forest)	Studies # 6-14
	0.5-1.5	(Deciduous forest)	Studies # 15-17
	0.00002-0.0066	(Ice/snow)	Studies # 22-29
Canopy height, h (m)	0.15-0.77	(Grass)	Studies # 1-5
	14-20	(Coniferous forest)	Studies # 6-14
	20-25	(Deciduous forest)	Studies # 15-17
Zero-plane displacement height, d (m)	0.10-0.49	(Grass)	Studies # 1-5
	7-12	(Coniferous forest)	Studies # 6-14
	8-16	(Deciduous forest)	Studies # 15-17
Leaf area index (one-sided), LAI (m^2/m^2)	1-4	(Grass)	Studies # 1-5
	0.2-10	(Coniferous forest)	Studies # 6-14
	0.2-10	(Deciduous forest)	Studies # 15-17

The Sobol 2007 package in R statistical software package (version 3.2.4) was used to perform the Sobol' sensitivity analysis. In the Sobol' method, the Monte Carlo simulations were performed by drawing samples from the assigned parameter value distribution. In this study, all the selected parameters were approximated using uniform PDFs. To assert uncertainty in the simulations, bootstrapping (Efron and Tibshirani, 1994) with re-sampling was used to achieve 95% confidence intervals on the Sobol' first order indices. For a fixed particle size, the simulations were run 100,000 times and samples were bootstrapped 1,000 times. To identify the most important parameters in each of the five dry deposition models with respect to particle size and LUC, a parameter ranking (e.g., from most to least influential) was conducted.

The results section is organized in the following manner. First, the accuracy of five dry deposition parameterizations (i.e., *Z01*, *PZ10*, *KS12*, *ZH14*, and *ZS14*) are compared with measured dry deposition velocities obtained from five LUCs. Second, the uncertainties in modeled dry deposition velocities due to the imprecision in the model input parameter values quantified using Monte Carlo simulation techniques are presented. Third, the sensitivity analysis results for modeled dry deposition velocities by the five parameterizations are presented.

1.4 Results

1.4.1 Evaluation of the dry deposition parameterizations

Field measurements conducted on five LUCs: grass, coniferous forest, deciduous forest, water surfaces, and ice/snow were used to evaluate the agreement between measured and

modeled dry deposition velocity (V_d). The parameterizations were run using reported values of the meteorological (e.g., U, u_*, T, RH, and L_O) and canopy (e.g., h, z_0, d, and LAI) parameters, and particle properties (e.g., d_p and ρ) from the measurement studies. Reasonable parameter values were assumed for any missing or unreported parameters. Normalized mean bias factors (B_{NMBF}) were used as an indicator of the agreement between measured and modeled V_d. B_{NMBF} is a signed quantity-its magnitude indicates the factor by which the modeled and observed V_d differ from each other, and its sign provides an indicator as to whether the modeled V_d is greater or less than the measured V_d. It is to be noted that uncertainties in the measured dry deposition velocities were not considered while evaluating the performance of the five parameterizations in terms of accuracy.

1.4.1.1 *Evaluation of dry deposition to grass*

Five measurement studies conducted on grass (Wesely et al., 1977; Allen et al., 1991; Neumann and den Hartog, 1985; Nemitz et al., 2002; and Vong et al., 2004) were used to evaluate the accuracy of the parameterizations. In those studies, reported values of meteorological parameters, canopy properties, and particle size vary widely. For example, the u_* varies from 0.05 to 0.70 m/s, wind speed (U) varies from 0.67 to 6.20 m/s, particle size (d_p) varies from 0.05 to 2.28 μm, and LAI varies from 2 to 4 m^2/m^2. The parameterizations were fed with reported values from each of the studies to reduce any uncertainty in the accuracy comparison; however, for any missing parameter value(s), the assumed input parameter values typically fell within the aforementioned ranges.

Table 4 summarizes the B_{NMBF} for modeled V_d computed against five measurement studies on grass. The B_{NMBF} is interpreted as follows: for example, if B_{NMBF} is positive, the parameterization overestimates the measured V_d by a factor of B_{NMBF}+1. If B_{NMBF} is negative, the model underestimates the measured V_d by a factor of 1-B_{NMBF}. For the case using the observations from Allen et al. (1991), the B_{NMBF} values of -17.61, -18.12, -0.55, and -5.13 indicate that the *Z01*, *KS12*, *ZH14*, and *ZS14* parameterizations underestimated the measured V_d by factors of 18.61, 19.12, 1.55, and 6.13, respectively, whereas, the B_{NMBF} value of +15.96 indicates that the *PZ10* parameterization overestimated the observations by a factor of 16.96.

Table 4. Results of the normalized mean bias factors for grass (boldfaced value indicates the most accurate parameterization).

	Dry particle deposition parameterization				
Study	Z01	PZ10	KS12	ZH14	ZS14
Allen et al. (1991)	-17.61	15.96	-18.12	-0.55	-5.13
Wesely et al. (1977)	-2.78	-28.78	-7.56	-10.62	-102.92
Neumann and den Hartog (1985)	0.96	-0.12	-0.50	4.79	0.56
Nemitz et al. (2002)	5.15	1.12	-3.82	2.17	-0.10
Vong et al. (2004)	-4.55	-4.55	-25.71	-2.12	-4.03
Five studies	5.45	-1.80	-9.37	**-0.54**	-4.30

These results provide means for a relative comparison of the parameterizations' accuracy. For instance, the B_{NMBF} values corresponding to the Allen et al. study suggest that the *ZH14* parameterization is the most accurate and the *KS12* parameterization is least accurate. Similar comparison between the modeled and observed V_d can be made using the B_{NMBF} values for the remaining four studies in Table 4. Nonetheless, it is evident that none of the parameterizations performed best in terms of accuracy for all of the five studies since the B_{NMBF} values show high variability both in terms of the magnitude and direction of the bias (i.e., positive or negative) when assessed against all the five studies listed in Table 4.

The characteristics of a parameterization (e.g., *Z01*) to simultaneously over-predict (i.e., the positive B_{NMBF} for Neumann and den Hartog, and Nemitz et al.) and under-predict (i.e., the negative B_{NMBF} for Allen et al. 1991, Wesely et al. 1977, and Vong et al., 2004) the measurements could be misleading, resulting in erroneous judgement of the performance of the parameterizations. To address this limitation, an ensemble approach was taken, in which B_{NMBF} was calculated for each of the parameterizations using all the observations reported in the five studies. The results from this ensemble analysis indicate that, except for the *Z01* parameterization, the other four parameterizations underestimated the measured V_d by factors ranging from 1.54 to 10.37. In contrast, the *Z01* parameterization overestimated the observation by a factor of 6.45 (Table 4). Overall, these results indicate that the *ZH14* parameterization provided the best agreement between the measured and modeled V_d of the five parameterizations.

1.4.1.2 *Evaluation of dry deposition to coniferous forest*

Nine studies conducted on coniferous forest (Lamaud et al., 1994; Wyers and Duyzers, 1997; Gallagher et al., 1997; Ruijgrok et al., 1997; Rannik et al., 2000; Buzorious et al., 2000; Gaman et al., 2004; Pryor et al., 2007; and Grönholm et al., 2009) were used to evaluate the accuracy of the parameterizations. In these studies, the largest variations (ranges are given in the parentheses) were associated with u_* (0.06-1.30 m/s), U (0.60-6.19 m/s), LAI (6-10 m^2/m^2), and d_p (0.01-0.60 μm). For any missing parameter value(s), the assumed input parameter values typically fell within the aforementioned ranges.

Comparison of the computed B_{NMBF} values for coniferous forest (Table 5) shows that the majority of the simulations performed using the five parameterizations underestimated the measured V_d. For example, the *PZ10* parameterization underestimated observed V_d by factors ranged from 1.51 to 27.98 (B_{NMBF} values varied from -0.51 to -26.98) for eight of the nine studies on coniferous forest. Table 5 also illustrates that both the magnitude and sign of the B_{NMBF} values varied widely when the accuracy of the five parameterizations was evaluated against only one study (e.g., Pryor et al., 2007). Of the B_{NMBF} values associated with the Rannik et al. (2000) study, the *Z01* and *KS12* parameterizations overestimated the measured V_d by factors of 4.16 and 1.51, respectively, whereas the *PZ10*, *ZH14*, and *ZS14* parameterizations underestimated the measured V_d by factors of 3.54, 2.13, and 19.75, respectively. The bias factors for the *Z01* parameterization for the following studies: Lamaud et al. (1994), Gallagher et al. (1997), Buzorious et al. (2000), and Gaman et al. (2004), were +0.77, -1.74, +0.75, and -0.90, respectively. Comparing these values with the corresponding B_{NMBF} values of the other four parameterizations, it can be deduced that the *Z01* parameterization is the most accurate against those observations reported in these four studies. However, the accuracy of the *Z01* parameterization is not the best for the other five studies, as can be seen from Table 5.

Table 5. Results of the normalized mean bias factors for coniferous forest (boldfaced value indicates the most accurate parameterization).

	Dry particle deposition parameterization				
Study	Z01	PZ10	KS12	ZH14	ZS14
Lamaud et al. (1994)	0.77	-12.75	-1.91	-2.14	-16.71
Wyers and Duyzers (1996)	-25.98	-26.98	-81.39	-13.57	-4.51
Gallagher et al. (1997)	-1.74	-6.34	-19.83	-1.90	-2.39
Ruijgrok et al. (1997)	-5.70	-0.51	-0.93	-2.58	-0.48
Rannik et al. (2000)	3.16	-2.54	0.51	-1.13	-18.75
Buzorious et al. (2000)	0.75	-6.65	-2.91	-4.53	-67.41
Gaman et al. (2004)	-0.90	-13.00	-6.12	-1.84	-17.45
Pryor et al. (2007)	0.69	-5.37	-0.26	-0.84	-12.22
Grönholm et al. (2009)	0.95	0.13	1.55	1.72	-1.90
Nine studies	-2.35	-3.93	**-1.75**	-2.31	-3.67

An ensemble approach similar to the one described in the previous section was used to determine the most and the least accurate parameterizations. From this analysis, the bias factors for the *Z01*, *PZ10*, *KS12*, *ZH14*, and *ZS14* parameterizations are -2.35, -3.93, -1.75, -2.31, and -3.67, respectively, suggesting that the *KS12* is the most accurate parameterization (i.e., under-predicted the observations by a factor of 2.75), and the *PZ10* is the least accurate parameterization (i.e., under-predicted the observations by a factor of 4.93) for coniferous forest. It can be noted that the performance of the *Z01* and *ZH14* parameterizations are nearly identical, while the *ZH14* is the second most accurate (i.e., under-predicted the observations by a factor of 3.31).

1.4.1.3 *Evaluation of dry deposition to deciduous forest*

A similar comparison between measured and modeled V_d was performed using three studies (Wesely et al., 1983; Pryor, 2006; and Matsuda et al., 2010) for deciduous forest. In these studies, the largest variations (ranges are given in the parentheses) were associated

with u_* (0.12-1.13 m/s), U (1.20-6.00 m/s), LAI (0.20-10 m^2/m^2), and d_p (0.05-2.50 μm). For any missing parameter value(s), the assumed input parameter values typically fell within the aforementioned ranges.

Computed B_{NMBF} values for deciduous forest are presented in Table 6. For the Wesely et al. (1983) study, comparison of the B_{NMBF} values between the parameterizations show that the performance of the *ZS14* parameterization was the most accurate (i.e., B_{NMBF} = -2.28; under-predicted the observations by a factor of 3.28). The B_{NMBF} values associated with the *PZ10* parameterization showed strong variation between the studies (e.g., two orders of magnitude discrepancy between the Wesely et al. (1983) and Pryor (2006) or Matsuda et al. (2010) studies).

Table 6. Results of the normalized mean bias factors for deciduous forest (boldfaced value indicates the most accurate parameterization).

	Dry particle deposition parameterization				
Study	Z01	PZ10	KS12	ZH14	ZS14
Wesely et al. (1983)	-9.25	-130.30	-34.58	-5.27	-2.28
Pryor (2006)	1.55	-2.42	-2.42	-0.90	-13.62
Matsuda et al. (2010)	-5.19	-1.34	-1.91	-2.37	-0.15
Three studies	-8.11	-4.51	-4.96	**-3.75**	-10.93

Evidently, none of the parameterizations performed consistently better for all the three studies. Overall, the results from the ensemble approach show that all the parameterizations overestimated the observations reported in three studies. Considering the B_{NMBF} values obtained by this approach, it is apparent that the *ZH14* is the most accurate parameterization (i.e., B_{NMBF} = -3.75, underestimated the observed V_d by a factor of 4.75), and the *ZS14* is the least accurate of the five parameterizations (i.e., B_{NMBF} = -10.93, underestimated the observed V_d by a factor of 11.93) for deciduous forest.

1.4.1.4 *Evaluation of dry deposition to water surfaces*

Only a limited number of measurement studies on size-segregated dry deposition over natural water surfaces are available in the literature. In this research, four studies (Möller and Schumann, 1970; Sehmel et al., 1974; Zuffal et al., 1998; and Caffery et al., 1998) conducted over water surfaces were used to evaluate the parameterizations' accuracy. From these studies, the reported values of the parameters that show the largest variations (ranges are given in the parentheses) are u_* (0.11-0.40 m/s) and d_p (0.03 to 48 μm).

Table 7 shows that the *PZ10* parameterization performed best for two studies (i.e., Möller and Schumann, 1970; and Caffery et al., 1998), in which B_{NMBF} values were -1.65 and +0.35, respectively. Comparison of the B_{NMBF} values between the *Z01* and *ZH14* parameterizations reveal that the accuracy of the two parameterizations varied widely among the studies (e.g., B_{NMBF} ranged from -0.144 to +18.87 and -0.33 to +10.28, respectively). Nevertheless, none of the five parameterizations was able to reproduce the measured V_d satisfactorily for all the four studies. Comparison of the B_{NMBF} values obtained by the ensemble approach showed that the *ZH14* parameterization is the most accurate, which underestimated the measured V_d by a factor of 1.25 (i.e., B_{NMBF} = -0.25), and the *PZ10* is the least accurate parameterization (i.e., B_{NMBF} = -0.89).

Table 7. Results of the normalized mean bias factors for water surfaces (boldfaced value indicates the most accurate parameterization).

	Dry particle deposition parameterization				
Study	Z01	PZ10	KS12	ZH14	ZS14
Möller and Schumann (1970)	18.87	-1.65	-2.51	10.28	106.00
Sehmel et al. (1974)	0.44	0.45	-0.59	1.51	3.65
Zufall et al. (1998)	-0.144	-0.39	-0.47	-0.33	5.14
Caffrey et al. (1998)	0.75	0.35	-0.85	0.70	3.61
Four studies	0.52	-0.89	-0.64	**-0.25**	4.22

1.4.1.5 *Evaluation of dry deposition to snow and ice surfaces*

Two studies over snow (Ibrahim, 1983; and Duan et al., 1987), and six studies over ice surfaces (Nilsson and Rannik, 2001; Gronlund et al., 2002; Contini et al., 2010; Held et al., 2011a; Held et al., 2011b; and Donateo and Contini, 2014) were used to evaluate the accuracy of the four parameterizations (*Z01*, *PZ10*, *KS12*, and *ZH14*) for smooth surfaces. The *ZS14* parameterization was not included here because it does not allow prediction of deposition over ice/snow surfaces. The B_{NMFB} values for the parameterizations are presented in Table 8.

Table 8. Results of the normalized mean bias factors for ice/snow surfaces (boldfaced value indicates the most accurate parameterization).

	Dry particle deposition parameterization			
Study	Z01	PZ10	KS12	ZH14
Gronlund et al. (2002)	-1.22	-271.73	-105.92	-2.58
Contini et al. (2010)	5.68	-57.22	-24.96	0.62
Held et al. (2011a)	2.96	-38.66	-15.58	0.67
Held et al. (2011b)	2.78	-42.93	-16.71	0.52
Donateo and Contini (2014)	1.62	-35.26	-12.57	-0.32
Ibrahim (1983)	4.14	-6.72	-7.72	3.98
Duan et al. (1987)	0.22	-12.09	-15.49	0.42
Nilsson and Rannik (2001)	1.69	-37.78	-13.46	-0.74
Eight studies	1.98	-53.03	-21.80	**0.26**

Of the four parameterizations, agreement between the modeled and measured V_d is not satisfactory for the *PZ10* and *KS12* parameterizations because they significantly underestimated the measured V_d (e.g., the bias factors from ensemble approach are -53.03 and -21.80, respectively). In contrast, the *Z01* and *ZH14* parameterizations predicted the measured V_d with reasonable accuracy (e.g., the bias factors from ensemble approach were +1.98 and +0.26, respectively). Table 8 also shows that the *ZH14* parameterization performed best for six of the eight measurements in which the B_{NMBF} varied between -0.74 to 3.98. Overall, for the nine studies combined (i.e., ensemble measurements), the *ZH14* parameterization is the most accurate (overestimated the measured V_d by a factor of 1.26), and the *PZ10* is the least accurate parameterization (underestimated the measured V_d by a factor of 54.03).

To summarize, the results from the ensemble evaluation of the parameterizations are graphically shown in Figs. 2(A-B) for the five LUCs. The horizontal dotted-dashed line in the plots indicates 100% agreement between modeled and measured V_d, whereas any dispersion from this line either above (i.e., over-estimation) or below (i.e., under-estimation) indicates the degree of the model's accuracy.

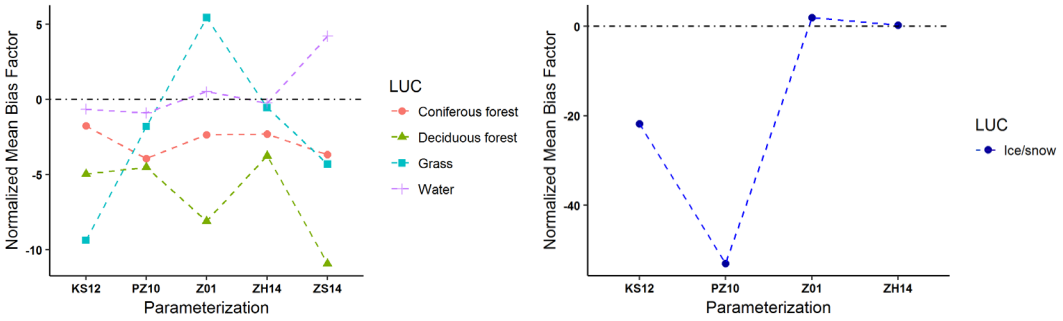

Figure 2. Ensemble averaged, normalized mean bias factors for the five parameterizations: a) three rough surfaces and water, b) Ice/snow.

1.4.2 Uncertainty analysis results from the Monte Carlo simulations

The overall uncertainty in the modeled V_d due to imprecision in the model inputs was assessed by performing a set of Monte Carlo simulations on the five dry deposition parameterizations. Uncertainties (in terms of imprecision) in the following model input parameters: *RH*, *U*, u_*, L_O, *h*, z_0, *d*, and *LAI* were approximated using uniform distributions. Note that not all of the five parameterizations require an identical number of input parameters. For example, Monte Carlo simulations performed on rough surfaces (i.e., grass, coniferous, and deciduous forests) for the *Z01*, *PZ10*, *KS12*, *ZH14*, and *ZS14* parameterizations, imprecision in four (*RH*, *L*, u_*, and z_0), eight (*RH*, *L*, u_*, *U*, z_0, *h*, *d*, and *LAI*), four (*RH*, u_*, *U*, and *LAI*), four (*RH*, *L*, u_*, and z_0), and two (*RH*, u_*) input parameters, respectively, were assessed to evaluate the overall uncertainty in modeled dry deposition velocities.

The results from the Monte Carlo simulations are summarized in Table 9 and are presented and discussed in two steps. First, the uncertainty estimates that are shown in Table 9 for five parameterizations on five LUCs are used to elucidate the models' precision, which is one of the indicators of overall performance of the parameterization. Second, the size-dependent uncertainty ranges (i.e., the difference between the 95th and 5th percentiles) was divided by the 50th percentile V_d, which can be treated as a normalized measure of uncertainty. This approach was taken to make reasonable comparison between different particle sizes for different parameterizations. Note that the *ZS14* parameterization does not treat different vegetative covers separately; therefore, inter-comparison of the Monte Carlo simulation results is confined to the first four parameterizations listed in Table 9.

Table 9. Median (50th percentile) values of the simulated dry deposition velocities ($m\,s^{-1}$) with 5th and 95th percentiles of distribution indicating the range of uncertainty.

Land use	Particle	Z01			PZ10			KS12			ZH14			ZS14*		
category	size (μm)	5th	50th	95th	5th	50th	95th	5th	50th	95th	5th	50th	95th	5th	50th	95th
Grass	0.005	1.72×10^{-2}	1.9×10^{-2}	2.1×10^{-2}	9.0×10^{-3}	9.5×10^{-3}	1.0×10^{-2}	1.7×10^{-2}	1.77×10^{-2}	1.86×10^{-2}	1.4×10^{-3}	1.5×10^{-3}	1.7×10^{-3}	4.0×10^{-4}	5.0×10^{-4}	5.0×10^{-4}
	0.05	5.2×10^{-3}	5.7×10^{-3}	6.2×10^{-3}	8.0×10^{-4}	8.0×10^{-4}	9.0×10^{-4}	9.0×10^{-4}	9.0×10^{-4}	9.0×10^{-4}	1.4×10^{-3}	1.5×10^{-3}	1.7×10^{-3}	1.0×10^{-4}	1.0×10^{-4}	1.0×10^{-4}
	0.5	9.0×10^{-4}	9.0×10^{-4}	1.1×10^{-3}	9.0×10^{-4}	9.0×10^{-4}	9.0×10^{-4}	1.0×10^{-4}	1.0×10^{-4}	1.0×10^{-4}	1.4×10^{-3}	1.5×10^{-3}	1.7×10^{-3}	7.0×10^{-4}	9.0×10^{-4}	1.0×10^{-3}
	1.0	6.15×10^{-4}	6.7×10^{-4}	7.25×10^{-4}	1.7×10^{-3}	1.8×10^{-3}	1.9×10^{-3}	1.45×10^{-4}	1.49×10^{-4}	1.55×10^{-4}	1.45×10^{-3}	1.58×10^{-3}	1.72×10^{-3}	1.47×10^{-3}	1.75×10^{-3}	2.06×10^{-3}
	1.5	5.72×10^{-4}	6.16×10^{-4}	6.59×10^{-4}	2.71×10^{-3}	2.87×10^{-3}	3.04×10^{-3}	2.59×10^{-4}	2.74×10^{-4}	2.91×10^{-4}	1.52×10^{-3}	1.66×10^{-3}	1.8×10^{-3}	2.20×10^{-3}	2.61×10^{-3}	3.06×10^{-3}
	2.0	6.16×10^{-4}	6.55×10^{-4}	6.93×10^{-4}	3.97×10^{-3}	4.23×10^{-3}	4.5×10^{-3}	4.3×10^{-4}	4.6×10^{-4}	4.94×10^{-4}	1.63×10^{-3}	1.77×10^{-3}	1.9×10^{-3}	2.91×10^{-3}	3.44×10^{-3}	4.10×10^{-3}
	2.5	7.0×10^{-4}	7.0×10^{-4}	8.0×10^{-4}	5.6×10^{-3}	6.0×10^{-3}	6.4×10^{-3}	7.0×10^{-4}	7.0×10^{-4}	8.0×10^{-4}	1.8×10^{-3}	1.9×10^{-3}	2.0×10^{-3}	3.6×10^{-3}	4.2×10^{-3}	4.9×10^{-3}
Coniferous Forest	0.005	1.62×10^{-2}	1.8×10^{-2}	1.98×10^{-2}	2.31×10^{-2}	2.46×10^{-2}	2.62×10^{-2}	2.87×10^{-2}	2.99×10^{-2}	3.14×10^{-2}	1.1×10^{-3}	1.2×10^{-3}	1.3×10^{-3}			
	0.05	4.4×10^{-3}	4.9×10^{-3}	5.3×10^{-3}	2.6×10^{-3}	2.7×10^{-3}	2.9×10^{-3}	1.4×10^{-3}	1.5×10^{-3}	1.6×10^{-3}	1.1×10^{-3}	1.2×10^{-3}	1.3×10^{-3}			
	0.5	7.0×10^{-4}	8.0×10^{-4}	8.0×10^{-4}	4.7×10^{-3}	4.9×10^{-3}	5.1×10^{-3}	2.0×10^{-4}	2.0×10^{-4}	2.0×10^{-4}	1.1×10^{-3}	1.2×10^{-3}	1.3×10^{-3}			
	1.0	4.87×10^{-4}	5.29×10^{-4}	5.71×10^{-4}	9.28×10^{-3}	9.76×10^{-3}	1.03×10^{-2}	3.24×10^{-4}	3.5×10^{-4}	3.79×10^{-4}	1.16×10^{-3}	1.27×10^{-3}	1.38×10^{-3}			
	1.5	4.7×10^{-4}	5.03×10^{-4}	5.73×10^{-4}	1.48×10^{-2}	1.57×10^{-2}	1.66×10^{-2}	6.27×10^{-4}	6.96×10^{-4}	7.7×10^{-4}	1.23×10^{-3}	1.34×10^{-3}	1.45×10^{-3}			
	2.0	5.29×10^{-4}	5.6×10^{-4}	5.92×10^{-4}	2.11×10^{-2}	2.26×10^{-2}	2.41×10^{-2}	1.07×10^{-3}	1.20×10^{-3}	1.34×10^{-3}	1.34×10^{-3}	1.45×10^{-3}	1.56×10^{-3}			
	2.5	6.0×10^{-4}	7.0×10^{-4}	7.0×10^{-4}	2.72×10^{-2}	2.93×10^{-2}	3.15×10^{-2}	1.7×10^{-3}	1.9×10^{-3}	2.1×10^{-3}	1.5×10^{-3}	1.6×10^{-3}	1.7×10^{-3}			
Deciduous Forest	0.005	1.28×10^{-2}	1.42×10^{-2}	1.58×10^{-2}	9.7×10^{-3}	1.08×10^{-2}	1.2×10^{-2}	2.87×10^{-2}	3.0×10^{-2}	3.14×10^{-2}	2.2×10^{-3}	2.2×10^{-3}	2.6×10^{-3}			
	0.05	4.10×10^{-3}	4.6×10^{-3}	5.0×10^{-3}	9.0×10^{-4}	1.0×10^{-3}	1.1×10^{-3}	1.4×10^{-3}	1.5×10^{-3}	1.6×10^{-3}	2.2×10^{-3}	2.2×10^{-3}	2.6×10^{-3}			
	0.5	7.0×10^{-4}	8.0×10^{-4}	8.0×10^{-4}	9.0×10^{-4}	1.1×10^{-3}	1.2×10^{-3}	2.0×10^{-4}	2.0×10^{-4}	2.0×10^{-4}	2.2×10^{-3}	2.2×10^{-3}	2.6×10^{-3}			
	1.0	4.84×10^{-4}	5.25×10^{-4}	5.67×10^{-4}	1.68×10^{-3}	1.96×10^{-3}	2.25×10^{-3}	9.02×10^{-5}	9.16×10^{-5}	9.35×10^{-5}	2.25×10^{-3}	2.46×10^{-3}	2.68×10^{-3}			
	1.5	4.65×10^{-4}	4.98×10^{-4}	5.31×10^{-4}	2.46×10^{-3}	2.86×10^{-3}	3.28×10^{-3}	1.66×10^{-4}	1.71×10^{-4}	1.77×10^{-4}	2.33×10^{-3}	2.54×10^{-3}	2.76×10^{-3}			
	2.0	5.2×10^{-4}	5.49×10^{-4}	5.78×10^{-4}	3.29×10^{-3}	3.81×10^{-3}	4.35×10^{-3}	2.77×10^{-4}	2.87×10^{-4}	3.0×10^{-4}	2.43×10^{-3}	2.65×10^{-3}	2.86×10^{-3}			
	2.5	6.0×10^{-4}	7.0×10^{-4}	7.0×10^{-4}	4.2×10^{-3}	4.8×10^{-3}	5.5×10^{-3}	1.7×10^{-3}	1.9×10^{-3}	2.1×10^{-3}	2.6×10^{-3}	2.6×10^{-3}	3.0×10^{-3}			
Water	0.005	8.9×10^{-3}	9.9×10^{-3}	1.1×10^{-2}	4.0×10^{-4}	4.0×10^{-4}	5.0×10^{-4}	4.66×10^{-4}	5.12×10^{-4}	5.58×10^{-4}	1.6×10^{-3}	1.8×10^{-3}	1.9×10^{-3}	1.04×10^{-2}	1.14×10^{-2}	1.24×10^{-2}
	0.05	4.0×10^{-3}	4.4×10^{-3}	4.8×10^{-3}	1.0×10^{-4}	1.0×10^{-4}	1.0×10^{-4}	5.06×10^{-5}	6.06×10^{-5}	6.06×10^{-5}	1.6×10^{-3}	1.8×10^{-3}	1.9×10^{-3}	2.3×10^{-3}	2.8×10^{-3}	3.3×10^{-3}
	0.5	9.0×10^{-4}	1.0×10^{-3}	1.1×10^{-3}	1.0×10^{-4}	1.0×10^{-4}	1.0×10^{-4}	1.49×10^{-5}	1.64×10^{-5}	1.79×10^{-5}	1.6×10^{-3}	1.8×10^{-3}	1.9×10^{-3}	2.19×10^{-2}	2.62×10^{-2}	3.06×10^{-2}
	1.0	6.82×10^{-4}	7.44×10^{-4}	8.07×10^{-4}	1.11×10^{-4}	1.13×10^{-4}	1.15×10^{-4}	5.0×10^{-5}	5.5×10^{-5}	5.99×10^{-5}	1.66×10^{-3}	1.82×10^{-3}	1.98×10^{-3}	4.32×10^{-2}	5.08×10^{-2}	5.87×10^{-2}
	1.5	6.39×10^{-4}	6.92×10^{-4}	7.47×10^{-4}	1.85×10^{-4}	1.89×10^{-4}	1.94×10^{-4}	1.08×10^{-4}	1.19×10^{-4}	1.3×10^{-4}	1.73×10^{-3}	1.9×10^{-3}	2.06×10^{-3}	6.26×10^{-2}	7.29×10^{-2}	8.31×10^{-2}
	2.0	6.88×10^{-4}	7.42×10^{-4}	8.0×10^{-4}	2.87×10^{-4}	2.95×10^{-4}	3.06×10^{-4}	1.90×10^{-4}	2.09×10^{-4}	2.27×10^{-4}	1.84×10^{-3}	2.0×10^{-3}	2.17×10^{-3}	8.02×10^{-2}	9.25×10^{-2}	1.04×10^{-1}
	2.5	8.0×10^{-4}	9.0×10^{-4}	9.0×10^{-4}	4.0×10^{-4}	4.0×10^{-4}	5.0×10^{-5}	2.96×10^{-4}	3.25×10^{-4}	3.55×10^{-4}	2.0×10^{-3}	2.1×10^{-3}	2.3×10^{-3}	9.63×10^{-2}	1.1×10^{-1}	1.23×10^{-1}
Ice/snow	0.005	1.15×10^{-2}	1.26×10^{-2}	1.38×10^{-2}	4.0×10^{-4}	4.0×10^{-4}	4.0×10^{-4}	2.8×10^{-2}	2.93×10^{-2}	3.07×10^{-2}	1.1×10^{-3}	1.2×10^{-3}	1.3×10^{-2}			
	0.05	3.4×10^{-3}	3.7×10^{-3}	4.0×10^{-3}	2.0×10^{-5}	2.0×10^{-5}	2.0×10^{-5}	1.4×10^{-3}	1.5×10^{-3}	1.5×10^{-3}	1.1×10^{-3}	1.2×10^{-3}	1.3×10^{-2}			
	0.5	6.0×10^{-4}	7.0×10^{-4}	7.0×10^{-4}	2.0×10^{-5}	2.0×10^{-5}	2.0×10^{-5}	2.0×10^{-4}	2.0×10^{-4}	2.0×10^{-4}	1.1×10^{-3}	1.2×10^{-3}	1.3×10^{-2}			
	1.0	4.41×10^{-4}	4.81×10^{-4}	5.23×10^{-4}	6.71×10^{-5}	6.86×10^{-5}	7.06×10^{-5}	4.38×10^{-4}	4.85×10^{-4}	5.37×10^{-4}	1.15×10^{-3}	1.26×10^{-3}	1.37×10^{-3}			
	1.5	4.67×10^{-4}	5.14×10^{-4}	5.69×10^{-4}	1.45×10^{-4}	1.49×10^{-4}	1.55×10^{-4}	9.14×10^{-4}	1.04×10^{-3}	1.17×10^{-3}	1.24×10^{-3}	1.34×10^{-3}	1.45×10^{-3}			
	2.0	6.0×10^{-4}	6.84×10^{-4}	7.92×10^{-4}	2.54×10^{-4}	2.63×10^{-4}	2.75×10^{-4}	1.61×10^{-3}	1.84×10^{-3}	2.1×10^{-3}	1.35×10^{-3}	1.46×10^{-3}	1.57×10^{-3}			
	2.5	9.0×10^{-4}	1.0×10^{-3}	1.2×10^{-3}	4.0×10^{-4}	4.0×10^{-4}	4.0×10^{-4}	2.5×10^{-3}	2.9×10^{-3}	3.3×10^{-3}	1.5×10^{-3}	1.6×10^{-3}	1.7×10^{-3}			

* The parameterization does not categorize rough or vegetative surfaces into different LUCs. In this analysis, grass is used to represent a rough surface.

1.4.2.1 *Uncertainties in the modeled V_d for grass*

The uncertainties in simulated V_d (i.e., differences between 95th and 5th percentiles of distribution) for the given range of d_p (i.e., 0.005-2.5 μm) on grass varied widely (Table 9). In the *Z01* parameterization, the estimated uncertainty for nucleation mode particles (0.0038 m s^{-1} for d_p = 0.005 μm) was larger than that of coarse mode particles (0.0001 m s^{-1} for d_p > 1.0 μm). Overall, in the *Z01* parameterization, the trend was that as the particle size increased from 0.005 to 2.5 μm, uncertainties in modeled V_d decreased considerably. In the *PZ10* parameterization, the range of uncertainty for the simulated particle sizes is narrower as compared to those of the *Z01* parameterization. Although not consistent, a decreasing trend in uncertainties can be seen for all the particle sizes in the *PZ10* parameterization. Of the simulated particle sizes, the uncertainty for d_p = 0.005 μm is the largest (0.0016 m s^{-1}) in the *KS12* parameterization. As particle size increased from 0.005 to 2.5 μm, significant decrease in uncertainties is observed. For d_p = 0.05 to 1.5 μm, the 5th and 95th percentile V_d were nearly identical (Table 9), suggesting that the *KS12* parameterization is the most precise of five parameterizations specifically for those particle sizes. From Table 9, it can be deduced that the uncertainties associated with the *ZH14* parameterization, which is an improved and simplified version of the *Z01* parameterization, were fairly constant (ca. 0.0003 m s^{-1}) for the seven particle sizes simulated here for grass.

1.4.2.2 *Uncertainties in the modeled V_d for coniferous forest*

For nucleation mode particles (i.e., d_p = 0.005 μm), the largest uncertainty (0.0036 m s^{-1}, median V_d = 0.0180 m s^{-1}) was associated with the *Z01* parameterization (Table 9).

Overall, the uncertainties in the *Z01* parameterization showed a decreasing trend as the particle size increased from 0.005 to 2.5 μm. We note that in the *PZ10* parameterization, the relative magnitude of the uncertainties associated with 0.005, 1.0, 1.5, 2.0, and 2.5 μm particles were of the same order (i.e., varied between 0.0010 to 0.0031 m s^{-1}). In comparison, uncertainties in modeled V_d for 0.05 and 0.5 μm particles were smaller by factors of ca. 10. In the *KS12* parameterization, the largest uncertainty was found for the nucleation mode particles (i.e., 0.0027 m s^{-1}; median V_d = 0.0299 m s^{-1}), and the uncertainties in modeled V_d decreased substantially as d_p increased. The uncertainties in modeled V_d in the *ZH14* parameterization were constant (0.0002 m s^{-1}) for all seven particle sizes indicating the model's ability to reproduce dry deposition velocities with high precision.

1.4.2.3 *Uncertainties in the modeled V_d for deciduous forest*

A similar comparison of the uncertainties in modeled V_d can be made for deciduous forest. It is seen from Table 9 that, for all the parameterizations except for *ZH14*, the largest uncertainties were associated with nucleation mode particles. That is, *Z01* and *KS12* parameterizations showed substantially greater uncertainties for d_p = 0.005 μm (0.0030 and 0.0027 m s^{-1}, respectively) as compared to the Aitken or coarse mode particles, for which the relative magnitude of the uncertainties were smaller by factors of ca. 13-30. In the *KS12* parameterization, the identical values of the 5th and 95th percentile V_d resulted in uncertainty values of zero for each simulated particle size of 0.5 to 2.0 μm, which indicates that it is the most precise of all four parameterizations. In addition, the uncertainties in the

modeled V_d in the *ZH14* parameterization were constant (0.0004 m s^{-1}) for all seven particle sizes.

1.4.2.4 *Uncertainties in the modeled V_d for water surface*

For water surfaces, the uncertainties in modeled V_d varied largely for the *Z01* parameterization (Table 9). That is, the largest uncertainty (0.0021 m s^{-1}) was associated with d_p = 0.005 μm (median V_d = 0.0099 m s^{-1}), and as d_p increased to 2.5 μm, the uncertainty decreased to 0.0001 m s^{-1} (for 2.5 μm particles, median V_d = 0.0009 m s^{-1}). Relatively narrower ranges in the uncertainties in modeled V_d for the *PZ10* and *KS12*, and constant uncertainties in the *ZH1*4 parameterizations with regard to changes in particle size suggest their higher precision as compared to the *Z01* parameterization under similar model input parameter uncertainties. Overall, as compared to the simulated uncertainties in the modeled V_d by the *Z01*, *PZ10*, *KS12*, and *ZH14* parameterizations, uncertainties in the *ZS14* parameterization are larger for d_p = 0.05 to 2.5 μm.

1.4.2.5 *Uncertainties in the modeled V_d for ice/snow surfaces*

Comparison between the simulated uncertainties in modeled V_d revealed that the uncertainties vary significantly for the *Z01* and *KS12* parameterizations as d_p changes. For example, uncertainties estimated from Table 9 for these two parameterizations decreased from 0.0023 to 0.0003 m s^{-1} and 0.0027 to 0.0008 m s^{-1}, respectively, as particle size increased from 0.005 to 2.5 μm. Note that the median V_d by the *PZ10* parameterization is an order of magnitude lower than that of other three parameterizations, which results in

close to zero uncertainties for all seven particle sizes. Also revealed in Table 9, the uncertainties in the *ZH14* parameterization are constant (0.0002 m s^{-1}) with regard to changes in the particle size.

1.4.2.6 *Normalized uncertainties in the modeled V_d*

An extended analysis of the results presented in the previous sections are summarized here. The normalized uncertainties presented in the Table 10 can be interpreted as follows: any value that is closer to zero indicates higher model precision (i.e., less uncertainty). As shown in Table 10, the normalized uncertainties for grass and d_p = 0.005 μm associated with the *Z01*, *PZ10*, *KS12*, *ZH14*, and *ZS14* parameterizations are 0.20, 0.11, 0.09, 0.20, and 0.20, respectively. These results suggest that *KS12* is the least uncertain (i.e., most precise) parameterization for nucleation mode particles, whereas, the *Z01*, *ZH14*, and *ZS14* are the most uncertain (i.e., least precise) parameterizations. Similar comparisons can be made for other particle sizes, as well as between the different LUCs. For example, the uncertainties associated with d_p = 0.05 μm is greater for the *PZ10* parameterization for deciduous forest as compared to grass (0.20 > 0.13).

Table 10. Normalized uncertainties in modeled dry deposition velocities.

		Dry particle deposition parameterization				
Land use category	Particle size, d_p (μm)	Z01	PZ10	KS12	ZH14	ZS14
Grass	0.005	0.20	0.11	0.09	0.20	0.20
	0.05	0.18	0.13	0.00	0.20	0.00
	0.5	0.22	0.00	0.00	0.20	0.33
	1.0	0.16	0.11	0.07	0.17	0.34
	1.5	0.14	0.11	0.12	0.17	0.33
	2.0	0.12	0.12	0.14	0.16	0.32
	2.5	0.14	0.13	0.14	0.11	0.31
Coniferous forest	0.005	0.20	0.13	0.09	0.17	
	0.05	0.18	0.11	0.13	0.17	
	0.5	0.13	0.08	0.00	0.17	
	1.0	0.16	0.10	0.16	0.17	
	1.5	0.13	0.11	0.20	0.16	
	2.0	0.11	0.13	0.22	0.15	
	2.5	0.14	0.15	0.21	0.13	
Deciduous forest	0.005	0.21	0.21	0.09	0.18	
	0.05	0.20	0.20	0.13	0.18	
	0.5	0.13	0.27	0.00	0.18	
	1.0	0.16	0.29	0.04	0.18	
	1.5	0.13	0.28	0.06	0.17	
	2.0	0.10	0.28	0.08	0.16	
	2.5	0.14	0.27	0.21	0.15	
Water	0.005	0.21	0.25	0.18	0.17	0.18
	0.05	0.18	0.00	0.18	0.17	0.36
	0.5	0.20	0.00	0.18	0.17	0.33
	1.0	0.17	0.03	0.18	0.18	0.31
	1.5	0.15	0.05	0.18	0.17	0.28
	2.0	0.15	0.07	0.18	0.16	0.26
	2.5	0.11	0.25	0.18	0.14	0.24
Ice/snow	0.005	0.18	0.00	0.09	0.17	
	0.05	0.16	0.00	0.07	0.17	
	0.5	0.14	0.00	0.00	0.17	
	1.0	0.17	0.05	0.20	0.17	
	1.5	0.20	0.07	0.25	0.16	
	2.0	0.28	0.08	0.27	0.15	
	2.5	0.30	0.00	0.28	0.13	

Note: a normalized uncertainty value of zero indicates that the 95th and 5th percentile V_d are of equal magnitude.

Comparison of the normalized uncertainties in modeled V_d over smooth surfaces (i.e., water and ice/snow) also reveals interesting findings. For example, for d_p = 0.5 μm, the normalized uncertainties over water surfaces for the *Z01*, *PZ10*, *KS12*, and *ZH14* parameterizations are 0.20, 0.00, 0.50, and 0.17, respectively. These results suggest that the *PZ10* parameterization is the least uncertain (i.e., most precise), whereas, the *KS12* is the most uncertain (i.e., least precise) parameterization for accumulation mode particles. Over ice/snow surfaces, with d_p = 0.005 μm, both the *Z01* and *ZH14* parameterizations have large uncertainties (normalized uncertainties are 0.18 and 0.17). In contrast, *PZ10* is the most precise parameterization with close to zero normalized uncertainty value.

The normalized uncertainties presented in Table 10 also reveal interesting findings about the relative magnitude of imprecision for a given particle size on various LUCs by one parameterization. For example, with d_p = 0.005 μm, the range in normalized uncertainties varies from 0.18-0.20 and 0.09-0.20 for all the five LUCs for the *Z01* and *KS12* parameterizations, respectively.

Figs. 3(A-E) show the relative comparison between uncertainties in modeled V_d by five parameterization for seven particle sizes across five LUCs. For LUC grass, Fig. 3A shows that in the uncertainties in the *Z01* and *ZH14* parameterizations show nearly identical trends, which are relatively narrow. That is, the uncertainties for particle sizes from 0.005 to 2.5 μm varied from 12-22% and 11-20% in the *Z01* and *ZH14* parameterizations, respectively. In contrast, uncertainties in the *PZ10* and *KS12* parameterizations exhibit large dispersion (i.e., uncertainty ranges from ~0-13% in the *PZ10*, and ~0-14% in the *KS12* parameterizations). The largest uncertainties in the simulated V_d are associated with

the *ZS14* parameterization, in which the range of uncertainty varied from ~0-34% for the seven particle sizes. We note that the minimum V_d produced by the *KS12* parameterization is at d_p = 0.5 µm for grass, coniferous and deciduous forest, and ice/snow surfaces, which can be confirmed from the Fig. 3(A-C and E). In addition, Fig. 3(D-E) show that the position of this minimum V_d in the *PZ10* parameterization ranged from d_p = 0.5-1.0 µm for water and ice/snow surfaces.

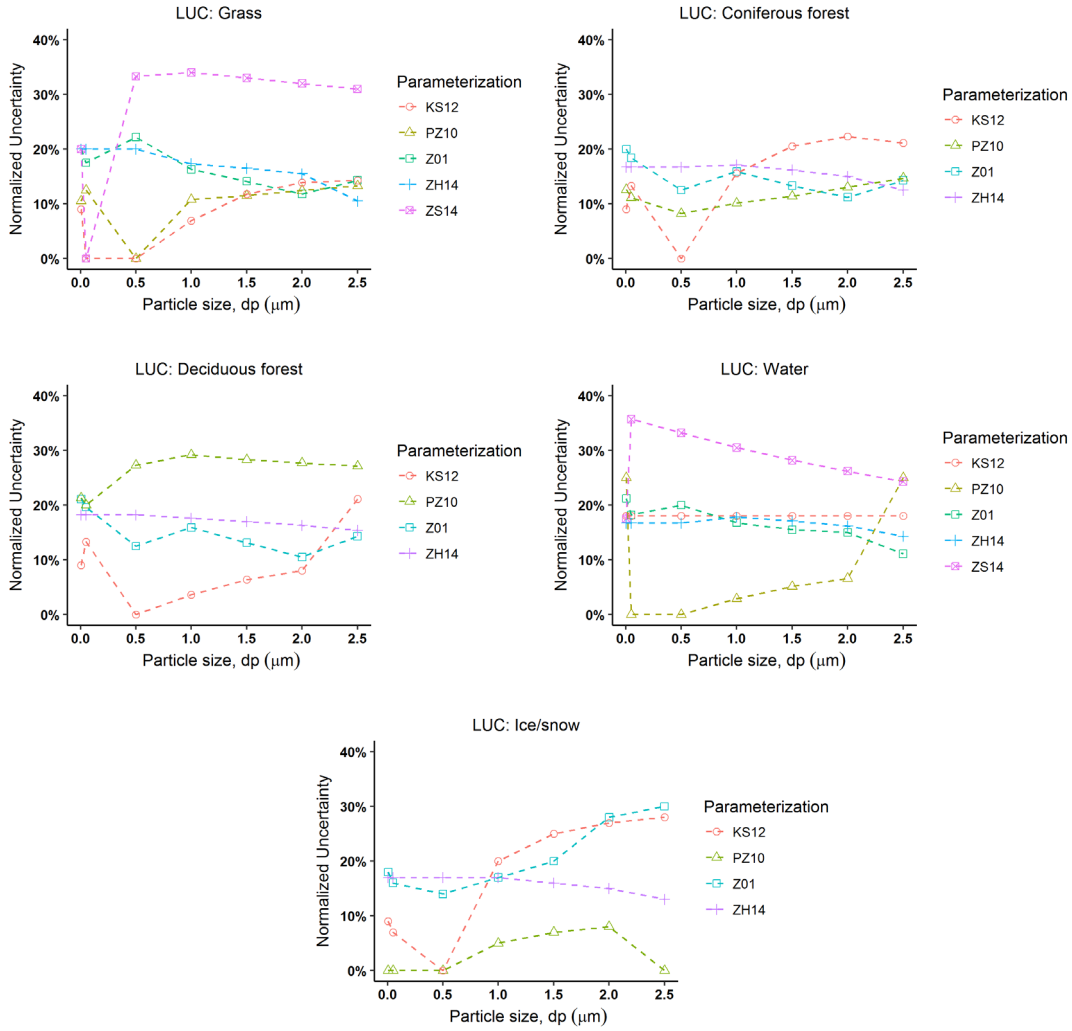

Figure 3. Comparison of the simulated uncertainties in the modeled dry deposition velocities as a function of particle size in five parameterizations for five LUCs.

1.4.3 Sensitivity analysis results: Sobol' first order sensitivity index

For Sobol' first order sensitivity analysis, five particle sizes (i.e., d_p = 0.001, 0.01, 0.1, 1.0, and 10 μm) were selected. A sample size (n) of 100,000 was used for model evaluations for each of the five particle sizes. To assess the confidence intervals for the first order Sobol' sensitivity index, bootstrapping resampling was used. In the bootstrapping method, the n samples used for the sensitivity simulations were sampled 1,000 times with replacement. In the following sections, the results from the Sobol' sensitivity analysis, and evolution of the parameter rankings are presented.

The Sobol' sensitivity analysis performed here is used to achieve a ranking of the model input parameters. The ranking of the parameters from most to least sensitive of the five particle sizes for the five parameterizations is shown in Table 11. Tables S1-S5 show the first order Sobol' indices of the various input parameters used in five dry deposition parameterizations for five LUCs. In these tables, particle size-dependent first order Sobol' index (S_i) for different model input parameters are presented with 95% confidence intervals (CI) obtained by bootstrap sampling. For example, the results of the first order Sobol' indices for the *Z01* parameterization on five LUCs are presented in Table S1. It is important to note that the number of parameters tested for Sobol' analysis varied between different LUCs, mainly because the number of parameters required for modeling V_d for one LUC may be more or less as compared to another LUC.

Table 11. Ranking of first order Sobol' sensitivity indices for the five dry particle deposition parameterizations.

Land use category	d_P (µm)	*Z01*	*PZ10*	*KS12*	*ZH14*	*ZS14*
Grass	0.001	u_*, z_0, L_O, (RH, ρ_P)	u_*, LAI, z_0, U, L_O, (h, d, RH, ρ_P)	u_*, (RH, ρ_P, LAI)	u_*, (z_0, L_O, RH, ρ_P)	U, u_*, (RH, ρ_P)
	0.01	u_*, z_0, L_O, (RH, ρ_P)	LAI, U, u_*, (L_O, h), (z_0, d, RH, ρ_P)	u_*, (RH, ρ_P, LAI)	u_*, (z_0, L_O, RH, ρP)	U, u_*, (RH, ρ_P)
	0.1	u_*, (z_0, L_O, RH, ρ_P)	LAI, U, d, (u_*, L_O, h, z_0, RH, ρ_P)	u_*, (RH, ρ_P, LAI)	u_*, (z_0, L_O, RH, ρ_P)	u_*, U, (RH, ρ_P)
	1.0	u_*, ρ_P , RH, (z_0, L_O)	U, LAI, RH, u_*, L_O, (h, z_0, d, ρ_P)	RH, u_*, ρ_P, LAI	u_*, (z_0, L_O, RH, ρ_P)	u_*, U, RH, ρ_P
	10	RH, u_*, ρ_P, (z_0, L_O)	RH, u_*, U, LAI, (ρ_P, z_0), L_O, (h, d)	RH, u_*, LAI, ρ_P	RH, ρ_P , (u_*, L_O, z_0)	u_*, U, RH, ρ_P
Coniferous Forest	0.001	u_*, L_O, z_0, (RH, ρ_P)	u_*, L_O, z_0, LAI, h, (d, U, RH, ρ_P)	u_*, (RH, ρ_P, LAI)	u_*, L_O, (z_0, RH, ρ_P)	
	0.01	u_*, L_O, z_0, (RH, ρ_P)	L_O, LAI, u_*, U, z_0, h, (d, RH, ρ_P)	u_*, (RH, ρ_P, LAI)	u_*, L_O, (z_0, RH, ρ_P)	
	0.1	u_*, L_O, (z_0, RH, ρ_P)	L_O, LAI, U, u_*, (d, z_0, h, RH, ρ_P)	u_*, (RH, ρ_P, LAI)	u_*, (L_O, z_0, RH, ρ_P)	
	1.0	u_*, ρ_P , RH, (L_O,z_0)	L_O, U, LAI, u_*, RH, (ρ_P, d, z_0, h)	u_*, RH, ρ_P, LAI	u_*, L_O, (z_0, RH, ρ_P)	
	10	RH, u_*, ρ_P, L_O, z_0	u_*, L_O, RH, z_0, (ρ_P, U), (LAI, d, h)	RH, u_*, LAI, ρ_P	RH, u_*, L_O, z_0, ρ_P	
Deciduous Forest	0.001	u_*, z_0, L_O, (RH, ρ_P)	L_O, u_*, LAI, z_0, U, (h, d, RH, ρ_P)	u_*, (RH, ρ_P, LAI)	u_*, L_O, (z_0, RH, ρ_P)	
	0.01	u_*, z_0, L_O, (RH, ρ_P)	L_O, LAI, u_*, U, (z_0, d), (h, RH, ρ_P)	u_*, (RH, ρ_P, LAI)	u_*, L_O, (z_0, RH, ρ_P)	
	0.1	u_*, z_0, (L_O, RH, ρ_P)	L_O, LAI, U, u_*, d, (z_0, h, RH, ρ_P)	u_*, (RH, ρ_P, LAI)	u_*, L_O, (z_0, RH, ρ_P)	
	1.0	u_*, ρ_P, (L_O, z_0, RH)	L_O, LAI, U, u_*, RH, (z_0, d), (h, ρ_P)	RH, ρ_P, u_*, LAI	u_*, L_O, (z_0, RH, ρ_P)	
	10	RH, u_*, ρ_P, z_0, L_O	L_O, RH, u_*, LAI, ρ_P, U z_0, (d, h)	RH, ρ_P, u_*, LAI	RH, u_*, LAI, L_O, ρ_P, z_0	
Water	0.001	u_*, (L_O, RH, ρ_P)	u_*, (L_O, RH, ρ_P)	u_*, L_O, (ρ_P, RH)	u_*, (L_O, RH, ρ_P)	
	0.01	u_*, (L_O, RH, ρ_P)	u_*, (L_O, RH, ρ_P)	u_*, L_O, (ρ_P, RH)	u_*, (L_O, RH, ρ_P)	
	0.1	u_*, (L_O, RH, ρ_P)	u_*, ρ_P, (L_O, RH)	u_*, L_O, (ρ_P, RH)	u_*, (L_O, RH, ρ_P)	
	1.0	u_*, ρ_P , (RH, L_O)	RH, ρ_P , (u_*, L_O)	ρ_P, u_*, (RH, L)	u_*, (L_O, RH, ρ_P)	
	10	u_*, RH, (ρ_P, L_O)	RH, ρ_P , (u_*, L_O)	ρ_P, u_*, L_O, RH	u_*, RH, (L_O, ρ_P)	
Ice/snow	0.001	u_*, L_O, (z_0, RH, ρ_P)	u_*, (L_O, z_0, RH, ρ_P)	u_*, RH, ρ_P	u_*, (L_O, z_0, RH, ρ_P)	
	0.01	u_*, z_0, L_O, (RH, ρ_P)	u_*, (L_O, z_0, RH, ρ_P)	u_*, RH, ρ_P	u_*, (L_O, z_0, RH, ρ_P)	
	0.1	u_*, (L_O, z_0, RH, ρ_P)	u_*, (L_O, z_0, RH, ρ_P)	u_*, RH, ρ_P	u_*, (L_O, z_0, RH, ρ_P)	
	1.0	u_*, (L_O, z_0, RH, ρ_P)	RH, ρ_P, (z_0, L_O, z_0)	u_*, RH, ρ_P	u_*, (L_O, z_0, RH, ρ_P)	
	10	u_*, RH, (ρ_P, L_O, z_0)	RH, ρ_P, (z_0, L_O, z_0)	RH, u_*, ρ_P	u_*, RH, (z_0, L_O, ρ_P)	

As shown in Table S1, for the *Z01* parameterization on grass, the importance of the most influential parameters on the modeled dry deposition velocities for five particles sizes can be compared using the corresponding S_i values of the model input parameters (e.g., $i = RH$, ρ, L_O, u_*, etc.). For example, with $d_p = 0.001$ μm, it can be clearly seen that the u_* is by far the single most sensitive parameter with an S_i value of 0.918, which indicates that 91.8% of the variation in the modeled V_d can be attributed to variations in u_*. The other parameters that have significant effect on the modeled V_d are z_0 and L_O. These two parameters have S_i values of 0.044 and 0.009, respectively. As compared to the first order Sobol' value of u_*, these values are significantly smaller; however, the lower limits of the corresponding 95% C.I. intervals for z_0 and L_O are greater than zero, indicating that they have a significant effect on the modeled velocities. The S_i values for the other two parameters, *RH* and particle ρ, were approximately zero for $d_p = 0.001$ μm (Table S1), and indicate that these variables have no influence on the modeled V_d.

Comparison between the first order Sobol' indices for different particle sizes for grass shows strong variations for certain input parameters, which reveals interesting findings about the relative importance (from the most to the least) of the model input parameters to the modeled dry V_d. For example, as seen from Table S1, as d_p increases from 0.001 to 10 μm, S_i values of u_* decrease from 0.918 to 0.245, which indicates that deposition of coarse particles is not strongly influenced by variations in friction velocity. From Table S1 it is also seen that parameters that influence particle properties (i.e., *RH* and ρ_P) have higher S_i values for the coarse particles as compared to the fine or accumulation mode particles. Similar comparisons between size-dependent behavior of parameter sensitivity for other

rough surfaces (i.e., coniferous and deciduous forests) can be made using the S_i values reported in Table S1.

The results of the first order Sobol' indices for the *Z01* parameterization on two smooth surfaces: water and ice/snow are also presented in Table S1. Over liquid water surfaces, variation in $u*$ values has the largest influence modeled V_d for d_p = 0.001 to 10.0 μm. As is seen from Table S1, the S_i values of $u*$ can alone explain 98.3-99.5% of the variations in modeled V_d for particle sizes up to fine mode (i.e., 0.001-0.01 μm). For coarse mode particles (e.g., d_p = 10 μm), $u*$ is also the most influential parameter, contributing ca. 56% of the total variation in modeled V_d, while relative humidity is the second most influential/sensitive parameter with an S_i value of 0.393. The influence of $u*$ also tends to dominate the modeled V_d over ice/snow surfaces. This theory can be confirmed by comparing the size-dependent S_i values of $u*$ shown in Table S1, which suggest that $u*$ is the single most sensitive parameter (S_i = 0.978) for d_p = 1.0 μm. As the particle size increased to 10 μm, *RH* and $u*$ can explain 92.7% of the total variation in modeled V_d in the *Z01* parameterization.

The results of the first order Sobol' indices for the *PZ10* parameterization on five LUCs are presented in Table S2. The size-dependent S_i values on coniferous forest can be compared here to elucidate the contribution of different input parameters on the modeled V_d. It can be noted that, on rough surfaces, the *PZ10* parameterization was tested for the most number of input parameters (i.e., nine) among the five parameterizations. Some canopy properties such as *h*, *d*, *LAI*, and meteorological properties such as *U* were tested for their influence on modeled V_d in addition to those parameters that were tested for the

rough surfaces in the *Z01* parameterization. As seen from Table S2, for coniferous forest, for d_p = 0.001 μm, u_* and L_O are the two most influential parameters (S_i values of 0.492 and 0.462, respectively). Although *LAI* is not the most influential parameter for the range of d_p tested here, its influence on the overall variability in the modeled V_d increase from 0.5 to 31.3% as particle size increases from 0.001 to 0.1 μm. Similarly, wind speed tends to show an increasing influence as d_p increases from 0.001 to 1.0 μm (overall contribution of U in the variability in V_d shows an increase from 0.1% to 27.7%). For coarse particles (i.e., d_p = 10 μm), u_* and L_O are the two most influential parameters with S_i values of 0.372 and 0.350, respectively. Together with *RH*, the three parameters can explain 92% of the variation in the modeled V_d. Results from the first order Sobol' indices for the other LUCs for the *PZ10* parameterization presented in Table S2 can be explained in a manner similar to that used to explain the contribution of the most sensitive parameters to the modeled dry deposition velocities. For the water surface, u_* is the most influential parameter for d_p = 0.001 μm as 99.4% of the total variance on the modeled V_d is attributed to its variability. Indeed, for particle sizes up to 0.1 μm, the u_* itself is the most sensitive parameter. As seen from Table 11, *RH* becomes the most influential model parameter for d_p = 1.0 and 10.0 μm, which alone contributes to 69.5% and 95.6% of the total variabilities in the modeled V_d, respectively.

Table S3 shows the first order Sobol' indices for the *KS12* parameterization on five LUCs. For brevity, the results of the first order sensitivity indices for deciduous forest are discussed herein. It is seen that u_* is the single most influential parameter for d_p = 0.001 to 0.1 μm (e.g., total contribution on the modeled V_d attributable to u_* ranges from 94.4 to

96.7%). For d_p = 1.0 and 10 μm, *RH* is the most influential parameter with S_i values of 0.629 and 0.934, respectively.

Table S4 shows the first order Sobol' indices for the *ZH14* parameterization on five LUCs. The results show a strong influence of u_* on the modeled V_d. As shown in Table S4, the S_i values alone can explain nearly 100% of the variation in the modeled V_d for d_p = 0.001 to 1.0 μm. For large particles (e.g., d_p = 10 μm), *RH* is the most influential parameter, however, the contributions of other parameters as listed in Table S4 vary with regard to changes in LUCs.

1.5 Discussion

The accuracy of the parameterizations should be interpreted within the context of the field measurements used in this study assuming that they were accurate. In addition, the inter-comparison of the parameterizations' accuracy is subject to uncertainties with regard to the assumed values of missing meteorological parameters, particle properties, or surface features. Evidently, the normalized mean bias factors obtained using the ensemble approach is a useful measure to inter-compare the parameterizations' performance against a sub-set of field measurements for a given LUC. Extending the comparison of the normalized mean bias factors across the five LUCs for the five parameterizations investigated in this study provides a relative assessment of their accuracy. However, the *ZH14* parameterization is most accurate for all parameterizations except coniferous forest, where it is a close second to the *KS12* parameterization.

For rough surfaces, our results suggest that *ZH14* is the most accurate parameterization for grass and deciduous forest, and it is the second most accurate parameterization for coniferous forest. In contrast, *KS12*, *PZ10*, and *ZS14* are the least accurate parameterizations for grass, coniferous, and deciduous forests, respectively. It is interesting that in most cases the models under-predicted the measured dry deposition velocities (negative bias factors in Tables 4-8). Indeed, for grass, except for the *Z01* parameterization, the other four parameterizations under-predicted the measured V_d by factors of 1.54 to 10.37 (B_{NMBF} varied from -0.54 to -9.37). With regard to deciduous and coniferous forests, all of the five models (from the most to the least accurate: *ZH14*, *PZ10*, *KS12*, *Z01*, and *ZS14; KS12*, *ZH14*, *Z01, ZS14*, and *PZ10*) under-predicted the measured V_d by factors of 4.75 to 11.93, and 2.75 to 4.93, respectively.

A direct quantitative comparison of the accuracy of the five parameterizations with those reported in other studies is impossible because the metric used in the present study (B_{NMBF}) is not commonly used to evaluate the accuracy of the dry deposition models. However, qualitatively, our findings regarding the *PZ10* performance for coniferous forests are in accordance with those reported by Petroff and Zhang (2010). They reported that the *PZ10* parameterization under-predicted the measured deposition velocities for the following subset of observations that we also investigated for coniferous forest: Lamaud et al. (1994), Gallagher et al. (1997), Buzorious et al. (2000), Gaman et al. (2004), and over-predicted for Grönholm et al. (2009).

The accuracy results over smooth surfaces suggest that, for the water surface, the best agreement between the measured and modeled V_d was found for the *ZH14*

parameterization. Overall, the accuracy ranking from best to worst is as follows: *ZH14*, *Z01*, *KS12*, *PZ10*, and *ZS14*. Over ice/snow surface, the results suggest that the *ZH14* is the most accurate parameterization, and *PZ10* is the least accurate. Qualitatively, this finding is consistent with Petroff and Zhang (2010), who reported that their model significantly underestimated the measured deposition velocities over ice/snow surface for the following studies: Ibrahim (1983), Duan et al. (1987), Nilsson and Rannik (2001), and Contini et al. (2010), which were also investigated in the present study. We also note that the *Z01* parameterization overestimated the measured V_d from the aforementioned studies. This finding is consistent with Petroff and Zhang (2010), as they compared their model with *Z01* over the ice/snow surface. One possible explanation for a large discrepancy between modeled and measured V_d by *PZ10* is an incorrect magnitude of the drift velocity applied, corresponding to phoretic effects on ice and snow.

Collectively for both rough and smooth surfaces, it is found that the *ZH14* scheme is the most accurate for these LUCs: grass, deciduous forest, water, and ice/snow surfaces. *KS12* performed slightly better for coniferous forest only. The performance of the *PZ10* scheme could be viewed as moderate. This finding is interesting considering that the *ZH14* is the simplest resistance-based scheme of the five parameterizations. We emphasize that *Z01* and *ZH14* parameterizations share similar structural features, but simplifications of the particle collection processes by constant values by *ZH14* (see Eqs. (46-50)) could produce better agreement. In addition, we note that the *KS12* parameterization is based exclusively on wind tunnel measurements and its performance over forest canopies is not satisfactory, as reported by the model developers Kouznetsov and Sofiev (2012). However, we find that

KS12 performed the best over coniferous forests with the nine studies used in this research. However, Kouznetsov and Sofiev (2012) did not use the same subset of studies to evaluate the model performance as we used.

Given the complex nature and incomplete knowledge of the dry deposition process, it is of importance to account for the uncertainties in the modeled deposition velocities in atmospheric transport models (Petroff and Zhang, 2010; Zhang et al., 2012). Although there have been many dry deposition models developed over the years, the information on the model output uncertainties is meager and not up-to-date. To assert uncertainty on the modeled dry deposition velocities, Gould and Davidson (1992) adopted a step-wise uncertainty test of Slinn's (1982) model. However, in reality, the model parameters are subject to simultaneous variability, and a OAT test cannot adequately propagate the error to the overall model outputs. This limitation was partially overcome by Ruijgrok (1992), who performed a probabilistic uncertainty test of Slinn's model.

The Monte Carlo uncertainty analysis performed in this study assumes that in the five parameterizations all the major physical processes (e.g., turbulent diffusion, Brownian diffusion, impaction, interception, and gravitational settling) of dry deposition are accounted for satisfactorily. Thus, the uncertainty analysis conforms to the uncertainties in the model input variables and their overall contribution to the propagated uncertainties in the modeled dry deposition velocities. Additional uncertainties in the modeled deposition velocities may arise from inadequate model formulation and/or inappropriate use of certain micrometeorological parameters. For example, in dry deposition models (such as *PZ10*), d and z_0 are often calculated as a fraction of h, and are often taken as $d \approx 2h/3$ and $z_0 \approx 0.1$h.

These expressions are valid for dense canopies (Katul et al., 2010). If the leaf area density is highly skewed or shows a bimodal distribution, such approximations cannot be used (Katul et al., 2010). In addition, the parameter values of d and z_0 are subject to large uncertainty and are very difficult to measure in urban areas (Cherin et al., 2015). Therefore, caution must be taken when using constant d and z_0 values from lookup tables. Also, current deposition models do not consider terrain complexity in their formulations. Hicks (2008) argued that conventional use of d and z_0 for non-flat terrain such as mountains is not appropriate for modeling deposition on complex terrain. In addition, experimentally derived values of d and z_0 often represent local characteristics. Thus, it poses a challenge to scale those up in a model grid cell (Schaudt and Dickinson, 2000) in atmospheric transport models. Using remote sensing, robust scaling of these parameter values is achieved, which could be used to acquire representative values in a model grid cell (Tian et al., 2011). However, addressing the issue of a model's structural uncertainty in a detailed manner was outside the scope of this paper.

The values of the eight model parameters, covering four meteorological (U, u_*, L_O, and RH) and four canopy morphological (z_0, d, h, and LAI) properties, used in the Monte Carlo simulations were assumed to be uniformly distributed because their true distributions were unknown. It is emphasized that these parameters are not all necessarily independent; z_0 and d are functions of the surface characteristics (Zhang and Shao, 2014; Shao and Yang, 2005, 2008). Considering these underlying assumptions, the uncertainties in modeled V_d reported in this paper should be viewed as the effect of the chosen parameter PDFs on the output uncertainty. The uncertainty bounds (i.e., the central 90% values) reported in the Table 9

could be treated as a metric of the quality of the modeled outputs. The normalized uncertainties reported in this study are a useful indicator to assess the overall performance of a model for four particle modes (seven particle sizes) across five LUCs.

We applied Sobol' sensitivity analysis to identify the most influential parameter(s) of the five parameterizations. Parameter rankings achieved using the Sobol' first order indices for different models provide a robust evaluation of the models' sensitivity by varying a set of input parameters within their plausible ranges. It is emphasized that a local sensitivity analysis such as OAT could lead to incomplete or misleading inference of the parameter sensitivity on the model's output because assumptions of model linearity are not always justified for dry deposition parameterizations due to their complex formulations.

The Sobol' sensitivity rankings presented in Table 11 can be used for inter-comparison between models' parameter sensitivity. Over rough surfaces, for nucleation size particles (e.g., d_p = 0.001 μm), u_* is the most sensitive parameter for *Z01*, *PZ10*, *KS12*, and *ZH14* parameterizations. As particle size increases from 0.001 μm to 1.0 μm, except for the *PZ10* scheme and for 1.0 μm for grass in *KS12* scheme, u_* remains the most influential parameter. This finding is in accordance with previous studies (Zhang et al., 2001; Zhang and He, 2014) that show that dry deposition velocities for atmospheric particles are greatly influenced by friction velocity. We note that in the *PZ10* scheme, *LAI* and L_O are the two most commonly-found sensitive parameters for d_p = 0.001 to 1.0 μm for rough surfaces. As seen from the parameter rankings (Table 11), for d_p = 10 μm in the *Z01*, *PZ10*, *KS10*, *ZH14* schemes, *RH* is the most influential factor. We postulate that with particle growth, high humidity may have a significant effect on coarse mode particles, and as a result, other

model input parameters become less sensitive. The parameter ranking of the *PZ10* scheme for deciduous forest shows that L_O is the most influential parameter. Similarly, for coniferous forest, L_O is found to be one of the most sensitive parameters for most particle sizes. One possible reason for this finding could be the interdependency of the particle mixing length parameter and L_O in the *PZ10* scheme. Indeed, the mixing length indirectly relates to particle collection efficiencies in the *PZ10* parameterization (see Eqs. 18, 25, and 26). The rankings of the *Z01* and *ZH14* parameters are nearly identical for rough and smooth surfaces. This finding is not surprising given that these two parameterizations were developed by applying similar assumptions.

In general, dry deposition parameterizations developed for different particle size ranges and surfaces vary widely in terms of their complexity in model structure. The complexity in their numerical formulations often depends on the purpose (e.g., operational or research) of the model development (Petroff et al., 2008a). Comparing two previously developed one-dimensional aerosol deposition models for broadleaf and coniferous canopies (see details in Petroff et al., 2008b; Petroff et al., 2009) with the *PZ10* parameterization, Petroff and Zhang (2010) argued that the mathematical formulations in those models are too complex and require numerous input parameters for implementation in aerosol transport models. Following this hypothesis, we attempt to qualitatively evaluate the relative complexity of the five dry deposition parameterizations tested in this study for incorporation into atmospheric transport models.

Of the five parameterizations, we note that the model structure of the *PZ10* is relatively more complex than those of the *Z01*, *ZH14*, and *ZS14* parameterizations. The complexity

of the *KS12* parameterization tends to be different by a large degree between rough (i.e., vegetative canopies and snow) and smooth (i.e., water) surfaces. The *ZS14* formulation (Eqs. (51-63)) is of comparable complexity to the rough surface formulation in the *KS12* parameterization (Eqs. (35-45)), and these parameterizations can be viewed as moderately complex. The formulation of the *Z01* parameterization can be viewed as moderately complex as well. In this parameterization, three processes (Brownian diffusion, interception, and impaction) were parameterized using Eqs. (8-14) to describe the particle deposition at the collection surface. We claim that the *KS12* parameterization for smooth surfaces is the most complex of the five models. This is mainly because it requires solving the dimensionless dry deposition velocity profiles over smooth surfaces using an analytical approach, which can be complex and computationally-expensive.

A direct qualitative comparison of the relative complexities of the major process terms in the *PZ10* and *Z01* parameterizations is possible because both of these parameterizations are resistance-based (i.e., expressions of V_d in Eqs. 2 and 16 are of similar forms). It is evident from Eqs. (19-31) that the formulations in the *PZ10* parameterization to compute the three surface collection process terms are relatively complex as compared to those in the *Z01* parameterization. In the *ZH14* parameterization (a resistance-based scheme as well), these process terms are not explicitly parameterized. Presumably, by incorporating a large number of LUC dependent constants to compute surface deposition velocity using Eqs. (46-50), simplifications were made possible to the *ZH14* parameterization. The use of fitting parameters to account for poorly understood dry deposition processes in parameterizations is not uncommon. Due to the complex nature and inadequate

understanding of the particle collection processes to leaf surfaces, suggestions were made to treat particle deposition on vegetative surfaces in a simplified manner using empirically derived fitting parameters (Petroff et al., 2008a). Consequently, Petroff and Zhang (2010) also introduced a large number of artificial parameters to account for characteristic length and orientation of the canopy obstacle, and different LUCs to parameterize the particle collection efficiencies (e.g., due to Brownian diffusion, interception, turbulent and inertial impaction). Based on these considerations and those in the previous paragraph, we claim that the *ZH14* is the simplest of the five parameterizations.

1.6 Conclusions

In terms of overall performance for incorporation in atmospheric transport models, we suggest that parameterization accuracy and uncertainty should be considered jointly, while, based on our findings, sensitivity of the model input parameters should be treated separately for each dry deposition parameterization. The paper presents a comprehensive evaluation of the performance of five parameterizations in terms of their accuracy, model output uncertainty, and parameter sensitivity. Based on the results, it is evident that the *ZH14* parameterization is the most accurate for four of the five LUCs (grass, deciduous forest, water, and ice/snow surfaces) and second most accurate for the fifth LUC (coniferous forest). Of the five parameterizations, the uncertainty range for the *ZH14* (11-20%) has the lowest upper bound across the five LUCs for particle size ranging from 0.005-2.5 μm. In terms of the lower bound of the uncertainty range, the *ZH14* is second to the *Z01* (10-30%) parameterization. We demonstrated that the Sobol' sensitivity analysis can

be successfully applied to dry deposition models to rank the input parameters by taking into account the complex interactions between them. One could argue that, if the different models exhibited greatest sensitivities to different parameters, and those parameters were more uncertain, the models exhibiting greatest sensitivity to the least certain parameters would be the most uncertain. In this way, sensitivity plays a potential role in determining which model is better. However, because our results showed that all models were most sensitive to u_*, or, at large size, *RH*, sensitivity does not end up playing a role in assigning which model is best. We also note that accurate measurement of u_* is extremely challenging (Andreas, 1992; Weber, 1999), and there exists ambiguity in its definition in boundary-layer meteorology (Weber, 1999).

The large dispersion in the parameterizations' accuracy may indicate that despite considerable efforts in developing sophisticated process-based dry deposition models, there remain major gaps in our understanding of the dry deposition process. Another possible explanation for the large dispersion may be that it is significantly caused by measurement uncertainties, which were not addressed in this paper. However, inter-variability in modeled deposition velocities is not uncommon, as pointed out by Ruijgrok et al. (1995) in an inter-comparison study of several earlier dry deposition models. We emphasize that the accuracy results presented in this paper should be discussed in terms of the locations in which the parameterization accuracy has been evaluated against measurements for the five LUCs (Table 1; Figure 1).

The results from the uncertainty analysis using the Monte Carlo simulations on the size-segregated particles should be of interest to atmospheric transport modelers as well as to

the scientific community interested in quantifying the uncertainty bounds in the atmospheric deposition fluxes of pollutants to ecosystems using concentration data from monitoring stations. This is because until now, uncertainties in modeled V_d for size-segregated particles for a suite of currently-available dry deposition parameterizations has been unavailable. We stress that future work on probabilistic uncertainty analysis should focus on quantifying uncertainties for additional LUCs than those covered in this study. One of the major limitations of our uncertainty analysis approach is the assumption of uniform distribution of all imprecise model input parameters. To address this limitation, accurate information on the input parameter PDFs is needed.

With the help of field observations, and improved theoretical knowledge of dry deposition, the Sobol' parameter rankings could be used to fine-tune dry deposition models to better account for processes that are currently lacking or poorly parameterized. Future work should focus on estimating higher order (i.e., second order and total order) Sobol' indices. Such indices would be useful for model developers interested in understanding the joint influence of multiple input parameters on the modeled deposition velocities.

Based on the qualitative evaluation of relative complexity of the five parameterizations, we suggest that the model structure of the *ZH14* parameterization is the least complex. After reviewing over 100 air quality models, Kouznetsov and Sofiev (2012) reported that resistance-based approaches are extensively implemented in most of those models. Thus, in practice, it may be preferable to use a relatively simple parameterization over a complex (and potentially computationally expensive) one, if the accuracy and uncertainty of the model justify it. Based on these criteria (i.e., accuracy, uncertainty, and complexity), we

propose that, of the five parameterizations we tested, the *ZH14* parameterization is currently superior for incorporation into atmospheric transport models.

A supplemental information (S.I.) (section 1.8) is provided after the references. The S.I. section includes the table of first order Sobol' indices and the computer codes written in R for model accuracy, uncertainty, and Sobol' sensitivity analyses.

1.7 References

Alcamo, J. and Bartnicki, J.: A framework for error analysis of a long-range transport model with emphasis on parameter uncertainty, Atmospheric Environment (1967), 21, 2121-2131, 1987.

Allen, A., Harrison, R., and Nicholson, K.: Dry deposition of fine aerosol to a short grass surface, Atmospheric Environment. Part A. General Topics, 25, 2671-2676, 1991.

Andreas, E. L.: Uncertainty in a Path-averaged Measurement of the Friction Velocity u, Journal of Applied Meteorology, 31, 1312-1321, 1992.

Beekmann, M. and Derognat, C.: Monte Carlo uncertainty analysis of a regional-scale transport chemistry model constrained by measurements from the atmospheric pollution over the Paris area (ESQUIF) campaign, Journal of Geophysical Research: Atmospheres, 108, 2003.

Bergin, M. S. and Milford, J. B.: Application of Bayesian Monte Carlo analysis to a Lagrangian photochemical air quality model, Atmospheric Environment, 34, 781-792, 2000.

Bergin, M. S., Noblet, G. S., Petrini, K., Dhieux, J. R., Milford, J. B., and Harley, R. A.: Formal uncertainty analysis of a Lagrangian photochemical air pollution model, Environmental Science & Technology, 33, 1116-1126, 1999.

Buzorius, G., Rannik, Ü., Mäkelä, J., Keronen, P., Vesala, T., and Kulmala, M.: Vertical aerosol fluxes measured by the eddy covariance method and deposition of nucleation mode particles above a Scots pine forest in southern Finland, Journal of Geophysical Research: Atmospheres, 105, 19905-19916, 2000.

Caffrey, P. F., Ondov, J. M., Zufall, M. J., and Davidson, C. I.: Determination of size-dependent dry particle deposition velocities with multiple intrinsic elemental tracers, Environmental science & technology, 32, 1615-1622, 1998.

Chen, L., Rabitz, H., Considine, D. B., Jackman, C. H., and Shorter, J. A.: Chemical reaction rate sensitivity and uncertainty in a two-dimensional middle atmospheric ozone model, Journal of Geophysical Research: Atmospheres, 102, 16201-16214, 1997.

Cherin, N., Roustan, Y., Musson-Genon, L., and Seigneur, C.: Modelling atmospheric dry deposition in urban areas using an urban canopy approach, Geoscientific Model Development, 8, 893-910, 2015.

Contini, D., Donateo, A., Belosi, F., Grasso, F., Santachiara, G., and Prodi, F.: Deposition velocity of ultrafine particles measured with the Eddy-Correlation Method over the Nansen Ice Sheet (Antarctica), Journal of Geophysical Research: Atmospheres, 115, 2010.

Derwent, R. and Hov, Ø.: Application of sensitivity and uncertainty analysis techniques to a photochemical ozone model, Journal of Geophysical Research: Atmospheres, 93, 5185-5199, 1988.

Donateo, A. and Contini, D.: Correlation of dry deposition velocity and friction velocity over different surfaces for PM2. 5 and particle number concentrations, Advances in Meteorology, 2014, 2014.

Duan, B., Fairall, C., and Thomson, D.: Eddy correlation measurements of the dry deposition of particles in wintertime, Journal of Applied Meteorology, 27, 642-652, 1988.

Efron, B. and Tibshirani, R. J.: An introduction to the bootstrap, CRC press, 1994.

Feng, J.: A size-resolved model and a four-mode parameterization of dry deposition of atmospheric aerosols, Journal of Geophysical Research: Atmospheres, 113, 2008.

Gallagher, M., Beswick, K., Duyzer, J., Westrate, H., Choularton, T., and Hummelshøj, P.: Measurements of aerosol fluxes to Speulder forest using a micrometeorological technique, Atmospheric Environment, 31, 359-373, 1997.

Gaman, A., Rannik, Ü., Aalto, P., Pohja, T., Siivola, E., Kulmala, M., and Vesala, T.: Relaxed eddy accumulation system for size-resolved aerosol particle flux measurements, Journal of Atmospheric and Oceanic Technology, 21, 933-943, 2004.

Giorgi, F.: A particle dry-deposition parameterization scheme for use in tracer transport models, Journal of Geophysical Research: Atmospheres, 91, 9794-9806, 1986.

Gould, T. and Davidson, C.: Variability and uncertainty in particle dry deposition modelling, Precipitation Scavenging and Atmosphere–Surface Exchange Processes. Hemisphere, Publ., Washington, DC, 1992. 1125-1142, 1992.

Grönholm, T., Launiainen, S., Ahlm, L., Mårtensson, E., Kulmala, M., Vesala, T., and Nilsson, E.: Aerosol particle dry deposition to canopy and forest floor measured by two-layer eddy covariance system, Journal of Geophysical Research: Atmospheres, 114, 2009.

Gronlund, A., Nilsson, D., Koponen, I. K., Virkkula, A., and Hansson, M. E.: Aerosol dry deposition measured with eddy-covariance technique at Wasa and Aboa, Dronning Maud Land, Antarctica, Annals of Glaciology, 35, 355-361, 2002.

Hanna, S. R., Chang, J. C., and Fernau, M. E.: Monte Carlo estimates of uncertainties in predictions by a photochemical grid model (UAM-IV) due to uncertainties in input variables, Atmospheric Environment, 32, 3619-3628, 1998.

Hanna, S. R., Lu, Z., Frey, H. C., Wheeler, N., Vukovich, J., Arunachalam, S., Fernau, M., and Hansen, D. A.: Uncertainties in predicted ozone concentrations due to input uncertainties for the UAM-V photochemical grid model applied to the July 1995 OTAG domain, Atmospheric Environment, 35, 891-903, 2001.

Heinonen, M.: A comparison of humidity standards at seven European national standards laboratories, Metrologia, 39, 303, 2002.

Held, A., Brooks, I., Leck, C., and Tjernstrom, M.: On the potential contribution of open lead particle emissions to the central Arctic aerosol concentration, Atmospheric Chemistry and Physics, 11, 3093-3105, 2011a.

Held, A., Orsini, D., Vaattovaara, P., Tjernström, M., and Leck, C.: Near-surface profiles of aerosol number concentration and temperature over the Arctic Ocean, Atmospheric Measurement Techniques, 4, 1603, 2011b.

Hicks, B., Baldocchi, D., Meyers, T., Hosker, R., and Matt, D.: A preliminary multiple resistance routine for deriving dry deposition velocities from measured quantities, Water, Air, & Soil Pollution, 36, 311-330, 1987.

Hicks, B. B.: On estimating dry deposition rates in complex terrain, Journal of Applied Meteorology and Climatology, 47, 1651-1658, 2008.

Hicks, B. B., Saylor, R. D., and Baker, B. D.: Dry deposition of particles to canopies—A look back and the road forward, Journal of Geophysical Research: Atmospheres, 121, 2016.

Högström, U. and Smedman, A.-S.: Accuracy of sonic anemometers: laminar wind-tunnel calibrations compared to atmospheric in situ calibrations against a reference instrument, Boundary-Layer Meteorology, 111, 33-54, 2004.

Ibrahim, M., Barrie, L., and Fanaki, F.: An experimental and theoretical investigation of the dry deposition of particles to snow, pine trees and artificial collectors, Atmospheric Environment (1967), 17, 781-788, 1983.

IPCC third assessment report, Cambridge and New York: Cambridge University Press. Volumes I (The Scientific Basis), II (Impacts, Adaptation, and Vulnerability) and III (Mitigation), 2001. 2001.

Katul, G., Grönholm, T., Launiainen, S., and Vesala, T.: Predicting the dry deposition of aerosol-sized particles using layer-resolved canopy and pipe flow analogy models: Role of turbophoresis, Journal of Geophysical Research: Atmospheres, 115, 2010.

Kouznetsov, R. and Sofiev, M.: A methodology for evaluation of vertical dispersion and dry deposition of atmospheric aerosols, Journal of Geophysical Research: Atmospheres, 117, 2012.

Lamaud, E., Brunet, Y., Labatut, A., Lopez, A., Fontan, J., and Druilhet, A.: The Landes experiment: Biosphere-atmosphere exchanges of ozone and aerosol particles above a pine forest, Journal of Geophysical Research: Atmospheres, 99, 16511-16521, 1994.

Larjavaara, M. and Muller-Landau, H. C.: Measuring tree height: a quantitative comparison of two common field methods in a moist tropical forest, Methods in Ecology and Evolution, 4, 793-801, 2013.

Lilburne, L. and Tarantola, S.: Sensitivity analysis of spatial models, International Journal of Geographical Information Science, 23, 151-168, 2009.

McMahon, T. and Denisot, P.: Empirical atmospheric deposition-a survey, Atmospheric Environment, 13, 571-585, 1979.

Mallet, V. and Sportisse, B.: Uncertainty in a chemistry-transport model due to physical parameterizations and numerical approximations: An ensemble approach applied to ozone modeling, Journal of Geophysical Research: Atmospheres, 111, 2006.

Matsuda, K., Fujimura, Y., Hayashi, K., Takahashi, A., and Nakaya, K.: Deposition velocity of PM2. 5 sulfate in the summer above a deciduous forest in central Japan, Atmospheric Environment, 44, 4582-4587, 2010.

Möller, U. and Schumann, G.: Mechanisms of transport from the atmosphere to the Earth's surface, Journal of Geophysical Research, 75, 3013-3019, 1970.

Muyshondt, A., Anand, N., and McFarland, A. R.: Turbulent deposition of aerosol particles in large transport tubes, Aerosol Science and Technology, 24, 107-116, 1996.

Nemitz, E., Gallagher, M. W., Duyzer, J. H., and Fowler, D.: Micrometeorological measurements of particle deposition velocities to moorland vegetation, Quarterly Journal of the Royal Meteorological Society, 128, 2281-2300, 2002.

Neumann, H. and Den Hartog, G.: Eddy correlation measurements of atmospheric fluxes of ozone, sulphur, and particulates during the Champaign intercomparison study, Journal of Geophysical Research: Atmospheres, 90, 2097-2110, 1985.

Nilsson, E.D. and Rannik, Ü.: Turbulent aerosol fluxes over the Arctic Ocean 1. Dry deposition over sea and pack ice, Journal of Geophysical Research, 106, 32,125-132,137, 2001.

Noll, K. E., Jackson, M. M., and Oskouie, A. K.: Development of an atmospheric particle dry deposition model, Aerosol Science & Technology, 35, 627-636, 2001.

Nossent, J., Elsen, P., and Bauwens, W.: Sobol'sensitivity analysis of a complex environmental model, Environmental Modelling & Software, 26, 1515-1525, 2011.

Oskouie, A. K., Noll, K. E., and Wang, H.-C.: Minimizing the effect of density in determination of particle aerodynamic diameter using a time of flight instrument, Journal of aerosol science, 34, 501-506, 2003.

Pappenberger, F., Beven, K. J., Ratto, M., and Matgen, P.: Multi-method global sensitivity analysis of flood inundation models, Advances in water resources, 31, 1-14, 2008.

Petroff, A., Mailliat, A., Amielh, M., and Anselmet, F.: Aerosol dry deposition on vegetative canopies. Part I: review of present knowledge, Atmospheric Environment, 42, 3625-3653, 2008a.

Petroff, A., Mailliat, A., Amielh, M., and Anselmet, F.: Aerosol dry deposition on vegetative canopies. Part II: A new modelling approach and applications, Atmospheric Environment, 42(16), 3654-3683, 2008b.

Petroff, A., Zhang, L., Pryor, S.C. and Belot, Y.: An extended dry deposition model for aerosols onto broadleaf canopies, Journal of Aerosol Science, 40(3), 218-240, 2009.

Petroff, A. and Zhang, L.: Development and validation of a size-resolved particle dry deposition scheme for application in aerosol transport models, Geoscientific Model Development, 3, 753-769, 2010.

Pryor, S.: Size-resolved particle deposition velocities of sub-100nm diameter particles over a forest, Atmospheric Environment, 40, 6192-6200, 2006.

Pryor, S., Larsen, S. E., Sørensen, L. L., Barthelmie, R. J., Grönholm, T., Kulmala, M., Launiainen, S., Rannik, Ü., and Vesala, T.: Particle fluxes over forests: Analyses of flux methods and functional dependencies, Journal of Geophysical Research: Atmospheres, 112, 2007.

Pryor, S., Gallagher, M., Sievering, H., Larsen, S. E., Barthelmie, R. J., Birsan, F., Nemitz, E., Rinne, J., Kulmala, M., and Grönholm, T.: A review of measurement and modelling results of particle atmosphere–surface exchange, Tellus B, 60, 42-75, 2008.

Pryor, S., Barthelmie, R., and Hornsby, K.: Size-resolved particle fluxes and vertical gradients over and in a sparse pine forest, Aerosol Science and Technology, 47, 1248-1257, 2013.

Rannik, Ü., Petäjä, T., Buzorius, G., Aalto, P., Vesala, T., and Kulmala, M.: Deposition velocities of nucleation mode particles into a Scots pine forest, Environmental and Chemical Physics, 22, 97-102, 2000.

Rannik, Ü., Zhou, L., Zhou, P., Gierens, R., Mammarella, I., Sogachev, A., and Boy, M.: Aerosol dynamics within and above forest in relation to turbulent transport and dry deposition, Atmospheric Chemistry and Physics, 16, 3145-3160, 2016.

Richardson, A. D., Dail, D. B., and Hollinger, D.: Leaf area index uncertainty estimates for model–data fusion applications, Agricultural and forest meteorology, 151, 1287-1292, 2011.

Ruijgrok, W.: Uncertainty in models calculating the dry deposition of aerosols to forests, Nucleation and atmospheric aerosols. Deepak Publ., Hampton, 1992. 481-485, 1992.

Ruijgrok, W., Davidson, C. I., and Nicholson, K. W.: Dry deposition of particles: Implications and recommendations for mapping of deposition over Europe, Tellus B: Chemical and Physical Meteorology, 48, 710-710, 1995.

Ruijgrok, W., Tieben, H., and Eisinga, P.: The dry deposition of particles to a forest canopy: a comparison of model and experimental results, Atmospheric Environment, 31, 399-415, 1997.

Saltelli, A. and Annoni, P.: How to avoid a perfunctory sensitivity analysis, Environmental Modelling & Software, 25, 1508-1517, 2010.

Saltelli, A., Annoni, P., Azzini, I., Campolongo, F., Ratto, M., and Tarantola, S.: Variance based sensitivity analysis of model output. Design and estimator for the total sensitivity index, Computer Physics Communications, 181, 259-270, 2010.

Schaudt, K. and Dickinson, R.: An approach to deriving roughness length and zero-plane displacement height from satellite data, prototyped with BOREAS data, Agricultural and Forest Meteorology, 104, 143-155, 2000.

Sehmel, G. and Hodgson, W.: Model for predicting dry deposition of particles and gases to environmental surfaces, Battelle Pacific Northwest Labs., Richland, WA (USA), 1978.

Sehmel, G., Sutter, S., and Simpson, C.: Particle deposition rates on a water surface as a function of particle diameter and air velocity, Battelle Pacific Northwest Labs., Richland, Wash.(USA), 1974.

Sehmel, G. A.: Particle and gas dry deposition: a review, Atmospheric Environment (1967), 14, 983-1011, 1980.

Seinfeld, J. and Pandis, S.: Atmospheric chemistry and physics: from air pollution to climate change, 2006. 2006.

Shao, Y. and Yang, Y.: A scheme for drag partition over rough surfaces, Atmospheric Environment, 39, 7351-7361, 2005.

Shao, Y. and Yang, Y.: A theory for drag partition over rough surfaces, Journal of Geophysical Research: Earth Surface, 113, 2008.

Slinn, W.: Predictions for particle deposition to vegetative canopies, Atmospheric Environment (1967), 16, 1785-1794, 1982.

Sobol', I. M.: Sensitivity estimates for nonlinear mathematical models, Mathematical Modelling and Computational Experiments, 1, 407-414, 1993.

Stull, R. B.: An introduction to boundary layer meteorology, Springer Science & Business Media, 2012.

Su, Z., Schmugge, T., Kustas, W., and Massman, W.: An evaluation of two models for estimation of the roughness height for heat transfer between the land surface and the atmosphere, Journal of applied meteorology, 40, 1933-1951, 2001.

Tang, T., Reed, P., Wagener, T., and Van Werkhoven, K.: Comparing sensitivity analysis methods to advance lumped watershed model identification and evaluation, Hydrology and Earth System Sciences Discussions, 3, 3333-3395, 2006.

Tatang, M. A., Pan, W., Prinn, R. G., and McRae, G. J.: An efficient method for parametric uncertainty analysis of numerical geophysical models, Journal of Geophysical Research: Atmospheres, 102, 21925-21932, 1997.

Tian, X., Li, Z., Van der Tol, C., Su, Z., Li, X., He, Q., Bao, Y., Chen, E., and Li, L.: Estimating zero-plane displacement height and aerodynamic roughness length using synthesis of LiDAR and SPOT-5 data, Remote sensing of environment, 115, 2330-2341, 2011.

Van Aaslt, R.M.: Dry deposition of aerosol particles, Lee, D., Schneider, T., Grant, L. et Verkert, P., éditeurs, Aerosols, 933-949, 1986.

Van Werkhoven, K., Wagener, T., Reed, P., and Tang, Y.: Characterization of watershed model behavior across a hydroclimatic gradient, Water Resources Research, 44, 2008.

Venkatram, A. and Pleim, J.: The electrical analogy does not apply to modeling dry deposition of particles, Atmospheric Environment, 33, 3075-3076, 1999.

Vong, R. J., Vickers, D., and Covert, D. S.: Eddy correlation measurements of aerosol deposition to short grass, Tellus B, 56, 105-117, 2004.

Weber, R. O.: Remarks on the definition and estimation of friction velocity, Boundary-Layer Meteorology, 93,197-209, 1999.

Weidinger, T., Pinto, J., and Horváth, L.: Effects of uncertainties in universal functions, roughness length, and displacement height on the calculation of surface layer fluxes, Meteorologische Zeitschrift, 9, 139-154, 2000.

Wesely, M., Cook, D., and Hart, R.: Fluxes of gases and particles above a deciduous forest in wintertime, Boundary-Layer Meteorology, 27, 237-255, 1983.

Wesely, M. and Hicks, B.: A review of the current status of knowledge on dry deposition, Atmospheric environment, 34, 2261-2282, 2000.

Wesely, M., Hicks, B., Dannevik, W., Frisella, S., and Husar, R.: An eddy-correlation measurement of particulate deposition from the atmosphere, Atmospheric Environment (1967), 11, 561-563, 1977.

Williams, R. M.: A model for the dry deposition of particles to natural water surfaces, Atmospheric Environment (1967), 16, 1933-1938, 1982.

Wiman, B. L. and Ågren, G. I.: Aerosol depletion and deposition in forests—a model analysis, Atmospheric Environment (1967), 19, 335-347, 1985.

Wyers, G. and Duyzer, J.: Micrometeorological measurement of the dry deposition flux of sulphate and nitrate aerosols to coniferous forest, Atmospheric Environment, 31, 333-343, 1997.

Yang, J.: Convergence and uncertainty analyses in Monte-Carlo based sensitivity analysis, Environmental Modelling & Software, 26, 444-457, 2011.

Yu, S., Eder, B., Dennis, R., Chu, S. H., and Schwartz, S. E.: New unbiased symmetric metrics for evaluation of air quality models, Atmospheric Science Letters, 7, 26-34, 2006.

Zhang, J. and Shao, Y.: A new parameterization of particle dry deposition over rough surfaces, Atmospheric Chemistry and Physics, 14, 12429-12440, 2014.

Zhang, L., Gong, S., Padro, J., and Barrie, L.: A size-segregated particle dry deposition scheme for an atmospheric aerosol module, Atmospheric Environment, 35, 549-560, 2001.

Zhang, L. and He, Z.: Technical Note: An empirical algorithm estimating dry deposition velocity of fine, coarse and giant particles, Atmospheric Chemistry and Physics, 14, 3729-3737, 2014.

Zhang, L. and Vet, R.: A review of current knowledge concerning size-dependent aerosol removal, China Particuology, 4, 272-282, 2006.

Zhang, L., Blanchard, P., Gay, D. A., Prestbo, E. M., Risch, M. R., Johnson, D., Narayan, J., Zsolway, R., Holsen, T. M., Miller, E. K., Castro, M. S., Graydon, J. A., Louis, V. L. St., and Dalziel, J.: Estimation of speciated and total mercury dry deposition at monitoring locations in eastern and central North America, Atmos. Chem. Phys., 12, 4327–4340, https://doi.org/10.5194/acp- 12-4327-2012, 2012.

Zufall, M. J., Davidson, C. I., Caffrey, P. F., and Ondov, J. M.: Airborne concentrations and dry deposition fluxes of particulate species to surrogate surfaces deployed in southern Lake Michigan, Environmental science & technology, 32, 1623-1628, 1998.

1.8 Supplemental information

Table S1. First order sensitivity index (*Si*) with bootstrap confidence intervals (*CI*) of the modeled V_d for the *Z01* parameterization.

		d_p = 0.001 µm			d_p = 0.01 µm			d_p = 0.1 µm			d_p = 1.0 µm			d_p = 10 µm		
LUC	Parameter	*Si*	*95% CI*		*Si*	*95% CI*		*Si*	*95% CI*		*Si*	*95% CI*		*Si*	*95% CI*	
Grass	*RH*	0.000	0.000	0.000	0.000	0.000	0.000	0.000	0.000	0.000	0.001	-0.001	0.003	0.673	0.620	0.721
	ρ_P	0.000	0.000	0.000	0.000	0.000	0.000	0.000	0.000	0.000	0.002	0.000	0.003	0.019	0.016	0.022
	L_O	0.009	0.006	0.012	0.002	-0.001	0.006	0.000	0.000	0.000	0.000	0.000	0.000	0.000	0.000	0.000
	z_0	0.044	0.037	0.051	0.012	0.004	0.020	0.000	-0.001	0.001	0.000	0.000	0.000	0.000	-0.001	0.001
	u_*	0.918	0.884	0.948	0.959	0.896	1.021	0.981	0.949	1.011	0.975	0.938	1.009	0.245	0.230	0.260
Coniferous forest	*RH*	0.000	0.000	0.000	0.000	0.000	0.000	0.000	0.000	0.001	0.001	0.000	0.002	0.598	0.493	0.690
	ρ_P	0.000	0.000	0.000	0.000	0.000	0.000	0.000	0.000	0.000	0.002	0.001	0.003	0.022	0.015	0.029
	L_O	0.260	0.231	0.289	0.124	0.103	0.147	0.005	0.000	0.011	0.000	0.000	0.000	0.009	0.003	0.016
	z_0	0.012	0.003	0.019	0.003	-0.002	0.008	0.000	-0.001	0.001	0.000	0.000	0.000	0.000	-0.001	0.001
	u_*	0.674	0.624	0.723	0.836	0.778	0.893	0.972	0.906	1.036	0.984	0.964	1.004	0.311	0.275	0.344
Deciduous forest	*RH*	0.000	0.000	0.000	0.000	0.000	0.000	0.000	0.000	0.000	0.000	-0.001	0.002	0.844	0.782	0.903
	ρ_P	0.000	0.000	0.000	0.000	0.000	0.000	0.000	0.000	0.000	0.002	0.000	0.003	0.019	0.016	0.022
	z_0	0.300	0.283	0.316	0.178	0.166	0.189	0.012	0.009	0.014	0.000	0.000	0.001	0.002	0.000	0.003
	L_O	0.007	0.004	0.010	0.002	0.000	0.003	0.000	0.000	0.000	0.000	0.000	0.000	0.000	0.000	0.000
	u_*	0.671	0.643	0.698	0.791	0.762	0.817	0.972	0.947	0.996	0.979	0.950	1.009	0.092	0.084	0.098
Water	*RH*	0.000	0.000	0.000	0.000	0.000	0.000	0.000	0.000	0.000	0.000	-0.001	0.000	0.393	0.369	0.416
	ρ_P	0.000	0.000	0.000	0.000	0.000	0.000	0.000	0.000	0.000	0.002	0.000	0.003	0.008	0.006	0.009
	L_O	0.000	0.000	0.000	0.000	0.000	0.000	0.000	0.000	0.000	0.000	0.000	0.000	0.000	0.000	0.000
	u_*	0.995	0.963	1.028	0.995	0.962	1.027	0.994	0.959	1.027	0.983	0.960	1.005	0.559	0.543	0.575
Ice/snow	*RH*	0.000	0.000	0.000	0.000	0.000	0.000	0.000	0.000	0.000	0.001	-0.001	0.002	0.376	0.350	0.403
	ρ_P	0.000	0.000	0.000	0.000	0.000	0.000	0.000	0.000	0.000	0.004	0.002	0.005	0.010	0.008	0.012
	L_O	0.013	0.009	0.017	0.006	0.003	0.009	0.000	0.000	0.001	0.000	0.000	0.000	0.002	0.001	0.003
	u_*	0.926	0.893	0.959	0.963	0.928	0.996	0.982	0.956	1.007	0.978	0.949	1.005	0.551	0.531	0.569
	z_0	0.051	0.043	0.059	0.026	0.020	0.032	0.002	0.001	0.003	0.000	0.000	0.000	0.010	0.007	0.012

Table S2. First order sensitivity index with bootstrap confidence intervals (*CI*) of the modeled V_d for the *PZ10* parameterization.

		d_p = 0.001 µm			d_p = 0.01 µm			d_p = 0.1 µm			d_p = 1.0 µm			d_p = 10 µm		
LUC	Parameter	*Si*	*95% CI*		*Si*	*95% CI*		*Si*	*95% CI*		*Si*	*95% CI*		*Si*	*95% CI*	
Grass	*RH*	0.000	0.000	0.000	0.000	0.000	0.000	0.000	0.000	0.000	0.014	0.010	0.018	0.347	0.320	0.372
	ρ_P	0.000	0.000	0.000	0.000	0.000	0.000	0.000	0.000	0.000	0.000	0.000	0.001	0.012	0.010	0.015
	L_O	0.009	0.006	0.012	0.001	0.000	0.003	-0.001	-0.002	0.000	0.001	0.000	0.003	0.002	0.000	0.003
	z_0	0.034	0.027	0.041	0.000	-0.001	0.001	0.000	0.000	0.000	0.000	-0.001	0.001	0.012	0.009	0.015
	u_*	0.780	0.751	0.809	0.050	0.043	0.058	0.000	-0.001	0.001	0.006	0.004	0.009	0.244	0.229	0.258
	LAI	0.103	0.091	0.115	0.693	0.664	0.722	0.553	0.536	0.572	0.379	0.360	0.397	0.040	0.035	0.045
	h	0.000	0.000	0.001	0.001	0.000	0.002	0.000	-0.001	0.001	0.000	-0.001	0.002	0.000	-0.001	0.000
	d	0.000	0.000	0.000	0.000	-0.001	0.001	0.001	0.000	0.001	0.000	-0.001	0.002	0.000	0.000	0.001
	U	0.032	0.025	0.038	0.225	0.210	0.242	0.408	0.393	0.424	0.511	0.489	0.532	0.228	0.215	0.240
Coniferous forest	*RH*	0.000	0.000	0.000	0.000	0.000	0.000	0.000	0.000	0.000	0.009	0.007	0.011	0.198	0.179	0.215
	ρ_P	0.000	0.000	0.000	0.000	0.000	0.000	0.000	0.000	0.000	0.001	0.000	0.001	0.004	0.002	0.005
	L_O	0.462	0.440	0.483	0.493	0.468	0.514	0.375	0.357	0.393	0.358	0.347	0.368	0.350	0.334	0.366
	z_0	0.011	0.007	0.015	0.004	0.001	0.006	0.000	0.000	0.001	0.001	0.000	0.001	0.006	0.004	0.009
	u_*	0.492	0.466	0.517	0.164	0.148	0.180	0.008	0.005	0.011	0.052	0.047	0.057	0.372	0.354	0.390
	LAI	0.005	0.003	0.008	0.220	0.202	0.240	0.313	0.293	0.334	0.162	0.154	0.170	0.000	-0.001	0.001
	h	0.001	0.000	0.002	0.001	0.000	0.002	0.000	-0.001	0.001	0.001	0.000	0.001	0.000	0.000	0.001
	d	0.000	0.000	0.000	-0.001	-0.002	0.000	0.000	-0.001	0.001	0.001	0.000	0.001	0.000	0.000	0.000
	U	0.001	-0.001	0.002	0.069	0.058	0.078	0.217	0.199	0.231	0.277	0.266	0.288	0.004	0.002	0.006
Deciduous forest	*RH*	0.000	0.000	0.000	0.000	0.000	0.000	0.000	0.000	0.000	0.002	0.001	0.003	0.280	0.257	0.302
	ρ_P	0.000	0.000	0.000	0.000	0.000	0.000	0.000	0.000	0.000	0.000	0.000	0.000	0.006	0.004	0.007
	L_O	0.501	0.484	0.518	0.458	0.442	0.472	0.401	0.387	0.415	0.453	0.441	0.464	0.339	0.325	0.352
	z_0	0.004	0.002	0.005	0.001	0.000	0.002	0.000	0.000	0.000	0.001	0.000	0.001	0.002	0.001	0.004
	u_*	0.390	0.372	0.407	0.111	0.102	0.119	0.011	0.008	0.014	0.081	0.075	0.087	0.237	0.225	0.250
	LAI	0.016	0.012	0.019	0.252	0.240	0.265	0.281	0.269	0.293	0.192	0.183	0.199	0.005	0.003	0.007
	h	0.000	0.000	0.001	0.000	0.000	0.000	0.000	0.000	0.000	0.000	0.000	0.000	0.000	0.000	0.001
	d	0.000	0.000	0.001	0.001	0.000	0.002	0.002	0.001	0.003	0.001	0.000	0.002	0.000	0.000	0.000
	U	0.001	0.000	0.002	0.031	0.026	0.035	0.122	0.114	0.130	0.106	0.100	0.112	0.005	0.003	0.007
Water	*RH*	0.000	0.000	0.000	0.000	0.000	0.000	-0.001	-0.002	0.000	0.695	0.620	0.770	0.956	0.877	1.025
	ρ_P	0.000	0.000	0.000	0.000	0.000	0.000	0.013	0.003	0.023	0.241	0.194	0.285	0.016	0.013	0.019
	L_O	0.000	0.000	0.000	0.000	0.000	0.000	0.000	0.000	0.000	0.000	0.000	0.000	0.000	0.000	0.000
	u_*	0.994	0.959	1.027	0.988	0.942	1.032	0.878	0.640	1.121	-0.001	-0.003	0.002	0.000	0.000	0.000
Ice/snow	*RH*	0.000	0.000	0.000	0.000	0.000	0.000	0.000	0.000	0.000	0.703	0.654	0.750	0.974	0.912	1.034
	ρ_P	0.000	0.000	0.000	0.000	0.000	0.000	0.004	0.002	0.005	0.270	0.244	0.296	0.015	0.013	0.016
	L_O	0.002	0.001	0.003	0.000	0.000	0.000	0.000	0.000	0.000	0.000	0.000	0.000	0.000	0.000	0.000
	u_*	0.962	0.931	0.993	0.969	0.938	1.000	0.956	0.913	0.998	0.000	-0.001	0.002	0.000	0.000	0.000
	z_0	0.004	0.002	0.006	0.000	0.000	0.000	0.000	0.000	0.000	0.000	0.000	0.000	0.000	0.000	0.000

Table S3. First order sensitivity index (*Si*) with bootstrap confidence intervals (*CI*) of the modeled V_d for the *KS12* parameterization.

		d_p = 0.001 µm			d_p = 0.01 µm			d_p = 0.1 µm			d_p = 1.0 µm			d_p = 10 µm		
LUC	Parameter	*Si*	*95% CI*		*Si*	*95% CI*		*Si*	*95% CI*		*Si*	*95% CI*		*Si*	*95% CI*	
Grass	*RH*	0.000	0.000	0.000	0.000	0.000	0.000	0.000	-0.002	0.003	0.777	0.731	0.822	0.816	0.709	0.916
	ρ_P	0.000	0.000	0.000	0.000	0.000	0.000	0.000	0.000	0.000	0.039	0.031	0.047	0.000	0.000	0.001
	u_*	0.904	0.832	0.976	0.904	0.832	0.976	0.902	0.829	0.974	0.122	0.106	0.138	0.009	0.005	0.012
	LAI	0.000	0.000	0.000	0.000	0.000	0.000	0.000	0.000	0.000	0.000	0.000	0.000	0.002	-0.001	0.003
Coniferous forest	*RH*	0.000	0.000	0.000	0.000	0.000	0.000	0.000	-0.001	0.000	0.139	0.126	0.153	0.783	0.709	0.849
	ρ_P	0.000	0.000	0.000	0.000	0.000	0.000	0.000	0.000	0.000	0.004	0.002	0.007	0.002	0.001	0.003
	u_*	0.911	0.823	0.995	0.911	0.823	0.995	0.943	0.879	1.005	0.829	0.798	0.860	0.032	0.029	0.035
	LAI	0.000	0.000	0.000	0.000	0.000	0.000	0.000	0.000	0.000	0.000	0.000	0.000	0.005	0.002	0.007
Deciduous forest	*RH*	0.000	0.000	0.000	0.000	0.000	0.000	0.000	-0.001	0.000	0.629	0.571	0.686	0.934	0.856	1.004
	ρ_P	0.000	0.000	0.000	0.000	0.000	0.000	0.000	0.000	0.000	0.243	0.206	0.277	0.012	0.010	0.014
	u_*	0.944	0.880	1.005	0.944	0.880	1.005	0.967	0.929	1.005	0.054	0.037	0.072	0.002	0.000	0.004
	LAI	0.000	0.000	0.000	0.000	0.000	0.000	0.000	0.000	0.000	0.000	0.000	0.000	0.000	-0.001	0.001
Ice/snow	*RH*	0.000	0.000	0.000	0.000	0.000	0.000	0.001	-0.001	0.002	0.302	0.287	0.316	0.848	0.789	0.899
	ρ_P	0.000	0.000	0.000	0.000	0.000	0.000	0.000	0.000	0.000	0.001	0.000	0.001	0.002	0.001	0.003
	u_*	0.905	0.840	0.972	0.905	0.840	0.972	0.902	0.836	0.970	0.614	0.595	0.632	0.022	0.020	0.024

Table S4. First order sensitivity index (*Si*) with bootstrap confidence intervals (*CI*) of the modeled V_d for the *ZH14* parameterization.

		d_p = 0.001 µm			d_p = 0.01 µm			d_p = 0.1 µm			d_p = 1.0 µm			d_p = 10 µm		
LUC	Parameter	*Si*	*95% CI*		*Si*	*95% CI*		*Si*	*95% CI*		*Si*	*95% CI*		*Si*	*95% CI*	
Grass	*RH*	0.000	0.000	0.000	0.000	0.000	0.000	0.000	0.000	0.000	0.001	0.000	0.002	0.940	0.847	1.014
	ρ_P	0.000	0.000	0.000	0.000	0.000	0.000	0.000	0.000	0.000	0.001	0.000	0.001	0.006	0.004	0.008
	u_*	1.002	0.973	1.033	1.002	0.973	1.033	1.002	0.973	1.033	1.000	0.967	1.032	0.000	0.000	0.000
	L	0.000	0.000	0.000	0.000	0.000	0.000	0.000	0.000	0.000	0.000	0.000	0.000	0.000	0.000	0.000
	z_0	0.000	0.000	0.000	0.000	0.000	0.000	0.000	0.000	0.000	0.000	0.000	0.001	0.000	0.000	0.000
Coniferous forest	*RH*	0.000	0.000	0.000	0.000	0.000	0.000	0.000	0.000	0.000	0.000	0.000	0.001	0.420	0.382	0.456
	ρ_P	0.000	0.000	0.000	0.000	0.000	0.000	0.000	0.000	0.000	0.000	0.000	0.000	0.006	0.004	0.007
	u_*	0.988	0.960	1.016	0.988	0.960	1.016	0.988	0.960	1.016	0.971	0.947	0.994	0.341	0.325	0.356
	L	0.002	0.001	0.003	0.002	0.000	0.003	0.002	0.000	0.003	0.004	0.002	0.005	0.141	0.131	0.150
	z_0	0.000	0.000	0.000	0.000	0.000	0.000	0.000	0.000	0.000	0.000	0.000	0.000	0.012	0.009	0.014
Deciduous forest	*RH*	0.000	0.000	0.000	0.000	0.000	0.000	0.000	0.000	0.000	0.000	0.000	0.001	0.634	0.585	0.675
	ρ_P	0.000	0.000	0.000	0.000	0.000	0.000	0.000	0.000	0.000	0.000	0.000	0.001	0.004	0.003	0.006
	u_*	0.988	0.962	1.011	0.988	0.962	1.011	0.988	0.962	1.011	0.987	0.960	1.012	0.185	0.174	0.195
	L	0.006	0.004	0.008	0.006	0.004	0.008	0.006	0.004	0.008	0.006	0.004	0.008	0.015	0.012	0.018
	z_0	0.000	0.000	0.000	0.000	0.000	0.000	0.000	0.000	0.000	0.000	0.000	0.000	0.000	0.000	0.000
	LAI													0.053	0.048	0.057
Water	*RH*	0.000	0.000	0.000	0.000	0.000	0.000	0.000	0.000	0.000	0.000	0.000	0.001	0.465	0.429	0.499
	ρ_P	0.000	0.000	0.000	0.000	0.000	0.000	0.000	0.000	0.000	0.000	0.000	0.001	0.008	0.005	0.010
	L	0.000	0.000	0.000	0.000	0.000	0.000	0.000	0.000	0.000	0.000	0.000	0.000	0.000	0.000	0.000
	u_*	0.981	0.954	1.010	0.981	0.954	1.010	0.981	0.953	1.010	0.980	0.952	1.010	0.499	0.480	0.517
Ice/snow	*RH*	0.000	0.000	0.000	0.000	0.000	0.000	0.000	0.000	0.000	0.000	0.000	0.001	0.407	0.378	0.433
	ρ_P	0.000	0.000	0.000	0.000	0.000	0.000	0.000	0.000	0.000	0.000	0.000	0.000	0.005	0.003	0.007
	L	0.000	0.000	0.000	0.000	0.000	0.000	0.000	0.000	0.000	0.000	0.000	0.000	0.004	0.002	0.005
	u_*	0.984	0.959	1.008	0.984	0.959	1.008	0.984	0.959	1.008	0.986	0.964	1.006	0.548	0.531	0.564
	z_0	0.001	0.000	0.001	0.001	0.000	0.001	0.001	0.000	0.001	0.000	0.000	0.001	0.014	0.011	0.017

Table S5. First order sensitivity index (*Si*) with bootstrap confidence intervals (*CI*) of the modeled V_d for the *ZS14* parameterization.

		d_p = 0.001 µm			d_p = 0.01 µm			d_p = 0.1 µm			d_p = 1.0 µm			d_p = 10 µm		
LUC	Parameter	*Si*	*95% CI*		*Si*	*95% CI*		*Si*	*95% CI*		*Si*	*95% CI*		*Si*	*95% CI*	
Plant	*RH*	0.000	0.000	0.000	0.000	0.000	0.000	0.000	0.000	0.000	0.006	0.004	0.008	0.071	0.060	0.085
	ρ_P	0.000	0.000	0.000	0.000	0.000	0.000	0.000	0.000	0.000	0.000	0.000	0.000	0.000	-0.001	0.002
	u_*	0.436	0.410	0.463	0.347	0.324	0.369	0.576	0.547	0.603	0.611	0.580	0.640	0.750	0.707	0.789
	U	0.464	0.430	0.498	0.607	0.568	0.643	0.306	0.282	0.329	0.275	0.252	0.297	0.145	0.127	0.163
Water	*RH*	0.000	0.000	0.000	0.000	0.000	0.000	0.000	0.000	0.000	0.003	0.001	0.004	0.001	0.000	0.003
	ρ_P	0.000	0.000	0.000	0.000	0.000	0.000	0.000	0.000	0.000	0.000	0.000	0.000	0.000	0.000	0.001
	u_*	0.991	0.958	1.023	0.966	0.935	0.997	0.989	0.963	1.014	0.988	0.961	1.015	0.989	0.956	1.020
	U	0.000	0.000	0.001	0.027	0.022	0.032	0.000	0.000	0.000	0.000	0.000	0.000	0.000	0.000	3.180

Codes for evaluation of model accuracy using Zhang et al. (2001) parameterization

```
#Accuracy Evaluation: Grass
#Dry deposition parameterization by Zhang et al. (2001)

attach(Allen_etal_1991)  # Use separate text file to feed V1, V2,… for different studies

C1 = 0.2789

C1 = 0.2789

C2 = 3.115

C3 = 5.145*10^-11

RH = 90/100

dp_i = 0.48

dp_d = dp_i*10^-6

rd = dp_d/2

r_w = {(C1*rd^C2)/(C3*rd^C4-log10(RH))+rd^3}^(1/3)

dp = r_w*2

#Correction factor, C

k_B = 1.38*10^-23

Temp_1 = V1

Temp = 273.15+V1

P = 101325

d_air = 3.72*10^-10

lambda = (k_B*Temp)/(sqrt(2)*3.1416*P*d_air^2)

C = 1+(2*lambda/dp)*(1.257+0.4*exp(-0.55*dp/lambda))

dyn.vis = ((5*10^-8)*Temp)+4*10^-6

rho = 2000

Vg = (rho*(dp)^2*9.81*C)/(18*dyn.vis)

# Compute aerodynamic resistance Ra:

z = 2

L = V4

x = z/L

# Compute shi_H (stability function)
```

```
shi_H.1 = 2*log(0.5*{1+(1-16*x)^0.5})

shi_H.2 = -5*x

shi_H =ifelse(x <= 0, shi_H.1 , shi_H.2)

zR = 3.5

z0 = 0.01

u_star = V2                                          #Use from input text file

k_c = 0.41

Ra = (log(zR/z0)-shi_H)/(k_c*u_star)

# Compute surface resistance Rs:

e_0 = 3

R1 = 1

# Compute E_B (collection efficiency from Brownian diffusion)

kin.vis = ((9*10^-8)*Temp)+10^-5

gamma = 0.54

D = (C*k_B*Temp)/(3*3.1416*dyn.vis*dp)

Sc = (kin.vis/D)

E_B = Sc^(-gamma)

# Compute E_IM (collection efficiency from impaction)

alpha = 1.2

beta =  2

A = 2/1000

St = (Vg*u_star)/(9.81*A)

E_IM = {St/(alpha+St)}^beta

# Compute E_IN (collection efficiency from interception)

E_IN = 0.5*(dp/A)^2

Rs = 1/{(e_0*u_star)*(E_B+E_IM+E_IN)*R1}

# Compute Dry deposition velocity
```

```
#Accuracy Evaluation: Coniferous forest
#Dry deposition parameterization by Zhang et al. (2001)

attach(Rannik_etal_2000)     # Use separate text file to feed V1, V2,… for different studies

C1 = 0.2789

C2 = 3.115

C3 = 5.145*10^-11

C4 = -1.399

RH = 90/100

dp_i = V1

dp_d = dp_i*10^-6

rd = dp_d/2

r_w = {(C1*rd^C2)/(C3*rd^C4-log10(RH))+rd^3}^(1/3)

dp = r_w*2

#Correction factor, C

k_B = 1.38*10^-23

Temp = 273.15+25

P = 101325

d_air = 3.72*10^-10

lambda = (k_B*Temp)/(sqrt(2)*3.1416*P*d_air^2)

C = 1+(2*lambda/dp)*(1.257+0.4*exp(-0.55*dp/lambda))

dyn.vis = 1.891*10^-5

rho = 1500

Vg = (rho*(dp)^2*9.81*C)/(18*dyn.vis)

# Compute aerodynamic resistance Ra:

z = 23.7

L = 200

x = z/L

shi_H2 = -5*x

zR = 26

z0 = 1.2
```

```
u_star = V2

k_c = 0.41

Ra = (log(zR/z0)-shi_H2)/(k_c*u_star)

e_0 = 3

R1 =1

kin.vis = 1.683*10^-5

gamma = 0.56

D = (C*k_B*Temp)/(3*3.1416*dyn.vis*dp)

Sc = (kin.vis/D)

E_B = Sc^(-gamma)

# Compute E_IM (collection efficiency from impaction)

alpha = 1.0

beta =  2

A = 5/1000

St = (Vg*u_star)/(9.81*A)

E_IM = {St/(alpha+St)}^beta

# Compute E_IN (collection efficiency from interception)

E_IN = 0.5*(dp/A)^2

Rs = 1/{(e_0*u_star)*(E_B+E_IM+E_IN)*R1}

# Compute Dry deposition velocity

Vd =  Vg+(1/(Ra+Rs));Vd   #unit: m/s

#Accuracy Evaluation: Deciduous forest
#Dry deposition parameterization by Zhang et al. (2001)
attach(Wesely_etal_1983)        # Use separate text file to feed V1, V2,… for different studies

C1 = 0.2789

C2 = 3.115

C3 = 5.145*10^-11

C4 = -1.399

RH = 95/100

dp_i = 0.4
```

```
dp_d = dp_i*10^-6

rd = dp_d/2

r_w = {(C1*rd^C2)/(C3*rd^C4-log10(RH))+rd^3}^(1/3)

dp = r_w*2

#Correction factor, C

k_B = 1.38*10^-23

Temp = V1

P = 101325

d_air = 3.72*10^-10

lambda = (k_B*Temp)/(sqrt(2)*3.1416*P*d_air^2)

C = 1+(2*lambda/dp)*(1.257+0.4*exp(-0.55*dp/lambda))

dyn.vis = V2

rho = 2000

Vg = (rho*(dp)^2*9.81*C)/(18*dyn.vis)

# Compute aerodynamic resistance Ra:

z = 39

L = V6

x = z/L

shi_H2 = -5*x

zR = 56

z0 = 1.6

u_star = V4

k_c = 0.41

Ra = (log(zR/z0)-shi_H1)/(k_c*u_star)

# Compute surface resistance Rs:

e_0 = 3

R1 =1

kin.vis = V3

gamma = 0.56
```

```
D = (C*k_B*Temp)/(3*3.1416*dyn.vis*dp)

Sc = (kin.vis/D)

E_B = Sc^(-gamma)

# Compute E_IM (collection efficiency from impaction)

alpha = 0.80

beta =  2

A = 5/1000

St = (Vg*u_star)/(9.81*A)

E_IM = {St/(alpha+St)}^beta

# Compute E_IN (collection efficiency from interception)

E_IN = 0.5*(dp/A)^2

Rs = 1/{(e_0*u_star)*(E_B+E_IM+E_IN)*R1}

# Compute Dry deposition velocity

Vd =  Vg+(1/(Ra+Rs));Vd


#Accuracy Evaluation: Water
#Dry deposition parameterization by Zhang et al. (2001)

attach(Caffrey_etal_1998)

C1 = 0.2789

C2 = 3.115

C3 = 5.415*10^-11

C4 = -1.399

RH = 79/100

dp_i = 0.005

dp_d = dp_i*10^-6

rd = dp_d/2

r_w = {(C1*rd^C2)/(C3*rd^C4-log10(RH))+rd^3}^(1/3)

dp = r_w*2

#Correction factor, C

k_B = 1.38*10^-23
```

```
Temp = 273.15+22

P = 101325

d_air = 3.72*10^-10

lambda = (k_B*Temp)/(sqrt(2)*3.1416*P*d_air^2)

C = 1+(2*lambda/dp)*(1.257+0.4*exp(-0.55*dp/lambda))

dyn.vis = ((5*10^-8)*Temp)+4*10^-6

rho = 2000

Vg = (rho*(dp)^2*9.81*C)/(18*dyn.vis)

# Compute aerodynamic resistance Ra:

z = 8/100

L = 50

x = z/L

# Compute shi_H (stability function)

shi_H.1 = 2*log(0.5*{1+(1-16*x)^0.5})

shi_H.2 = -5*x

shi_H =ifelse(x <= 0, shi_H.1 , shi_H.2)

zR = 5

u_star = 13.5/100

z0_1 = 0.021*(u_star)^3.32

z0_2 = 0.00098*(u_star)^1.65

z0 = ifelse(u_star<= 0.16, z0_1, z0_2)

k_c = 0.41

Ra = (log(zR/z0)-shi_H)/(k_c*u_star)  # m/s

# Compute surface resistance Rs:

e_0 = 3

R1 = 1

kin.vis = ((9*10^-8)*Temp)+10^-5

gamma = 0.50

D = (C*k_B*Temp)/(3*3.1416*dyn.vis*dp)
```

```
Sc = (kin.vis/D)

E_B = Sc^(-gamma)

alpha = 100

beta =  2

A = 2/1000

St = (Vg*u_star^2)/(kin.vis)

E_IM = {St/(alpha+St)}^beta

Rs = 1/{(e_0*u_star)*(E_B+E_IM)*R1}

# Compute Dry deposition velocity

Vd =  Vg+(1/(Ra+Rs));Vd


#Accuracy Evaluation: Ice/snow

#Dry deposition parameterization by Zhang et al. (2001)

attach(Ibrahim_et_al_1983)

C1 = 0.2789

C2 = 3.115

C3 = 5.415*10^-11

C4 = -1.399

RH = 60/100

dp_i = c(0.22, 0.73)

dp_d = dp_i*10^-6

rd = dp_d/2

r_w = {(C1*rd^C2)/(C3*rd^C4-log10(RH))+rd^3}^(1/3)

dp = r_w*2

#Correction factor, C

k_B = 1.38*10^-23

Temp = 273.15+25

P = 101325

d_air = 3.72*10^-10
```

```
lambda = (k_B*Temp)/(sqrt(2)*3.1416*P*d_air^2)

C = 1+(2*lambda/dp)*(1.257+0.4*exp(-0.55*dp/lambda))

dyn.vis = ((5*10^-8)*Temp)+4*10^-6

rho = 1500

Vg = (rho*(dp)^2*9.81*C)/(18*dyn.vis)

# Compute aerodynamic resistance Ra:

#z =

#L =

#x = z/L

x = 0.2

# Compute shi_H (stability function)

shi_H.1 = 2*log(0.5*{1+(1-16*x)^0.5})

shi_H.2 = -5*x

shi_H =ifelse(x <= 0, shi_H.1 , shi_H.2)

zR = 5

u_star = 0.12

z0 = 0.1/100

k_c = 0.41

Ra = (log(zR/z0)-shi_H)/(k_c*u_star)

# Compute surface resistance Rs:

e_0 = 3

R1 = 1

kin.vis = ((9*10^-8)*Temp)+10^-5

gamma = 0.54

D = (C*k_B*Temp)/(3*3.1416*dyn.vis*dp)

Sc = (kin.vis/D)

E_B = Sc^(-gamma)

alpha = 50

beta =  2
```

```
A = 2/1000

St = (Vg*u_star^2)/(kin.vis)

E_IM = {St/(alpha+St)}^beta

Rs = 1/{(e_0*u_star)*(E_B+E_IM)*R1}

# Compute Dry deposition velocity

Vd =  Vg+(1/(Ra+Rs));Vd
```

Codes for evaluation of model accuracy using Petroff and Zhang (2010) parameterization

```
#Accuracy Evaluation: Grass

#Dry deposition velocity parameterization by Petroff and Zhang (2010)

attach(Allen_etal_1991)

C1 = 0.2789

C2 = 3.115

C3 = 5.145*10^-11

C4 = -1.399

RH = 90/100

dp_i = 0.48

dp_d = dp_i*10^-6

rd = dp_d/2

r_w = {(C1*rd^C2)/(C3*rd^C4-log10(RH))+rd^3}^(1/3)

dp = r_w*2

#Correction factor, C

k_B = 1.38*10^-23

Temp = 273.15+25

P = 101325

d_air = 3.7208*10^-10

lambda = (k_B*Temp)/(sqrt(2)*3.1416*P*d_air^2)

C = 1+(2*lambda/dp)*(1.257+0.4*exp(-0.55*dp/lambda))

dyn.vis = ((5*10^-8)*Temp)+4*10^-6
```

```
rho = 1500

Tau = (rho*(dp)^2*C)/(18*dyn.vis)

Ws = Tau*9.81

Vphor = 0

Vdrift = Ws+Vphor

# Compute aerodynamic resistance (Ra):

z = 2

L = 200

x = z/L

# Compute stability function (shi_H)

shi_H.1 = 2*log(0.5*{1+(1-16*x)^0.5})

shi_H.2 = -5*x

shi_H = ifelse(x <= 0, shi_H.1 , shi_H.2)

zR = 3.5

z0 = 0.01

u_star = 0.5

k_c = 0.41

Ra = (log(zR/z0)-shi_H)/(k_c*u_star)

# Compute surface resistance (Rs)

kin.vis = ((9*10^-8)*Temp)+10^-5

D = (C*k_B*Temp)/(3*3.1416*dyn.vis*dp)

Sc = (kin.vis/D)

FSc = (Sc^(1/3))/2.9

Egb = (Sc^(-2/3)/14.5)*{1/6*log(1+FSc)^2/(1-FSc+FSc^2)+1/sqrt(3)*atan((2*FSc-
1)/sqrt(3))+3.1416/6*sqrt(3)}^-1

cd = 1/6

kx = 0.216

LAI = 4

h =  0.07
```

```
d  = 0.04

phi_H.1 = (1-16*x)^(-0.5)

phi_H.2 = 1+5*x

phi_H = ifelse(x<=0, phi_H.1, phi_H.2)

phi_M.1 = (1-16*x)^(-0.25)

phi_M.2 = 1+5*x

phi_M = ifelse(x<=0, phi_M.1, phi_M.2)

lmp = (0.41*(z-d))/(phi_H*(z-d)/abs(L))

lmp_h = (0.41*(h-d))/(phi_M*(h-d)/abs(L))

alphaPZ = {(kx*LAI)/(12*k_c^2*(1-d/h)^2)}^(1/3)*phi_M^(2/3)*{(h-d)/abs(L)}

C_IT = 0.056

Tau_phplus.1 = (Tau*u_star^2)/kin.vis

Tau_phplus.2 = C_IT

Tau_phplus = ifelse(Tau_phplus.1<20,Tau_phplus.1, Tau_phplus.2)

E_t.1 = 2.5*10^-3*C_IT*(Tau_phplus)^2

E_t.2 = C_IT

E_t = ifelse(Tau_phplus.1<20, E_t.1, E_t.2)

u_starf = u_star*exp(-alphaPZ)

Tau_phplus.f1 = (Tau*u_star^2)/kin.vis

Tau_phplus.f2 = 0.14

Tau_phplusf = ifelse(Tau_phplus.f1<20,Tau_phplus.f1, Tau_phplus.f2)

E_gt1 = 2.5*10^-3*0.14*(Tau_phplusf)^2

E_gt2 = 0.14

Egt = ifelse(Tau_phplus.f1<20, E_gt1, E_gt2)

Eg = Egb + Egt

# Compute Qg (non-dimensional number)

Qg = Eg*h/lmp_h

# Compute Q

U_z = 2
```

```
U_h = U_z/(exp(alphaPZ*(z/h-1)))

#Compute E_B (Brownian diffusion)

L_obs = 0.01

C_B = 0.996

Re_h = (U_h*L_obs)/(kin.vis)

E_B = C_B*(Sc^(-2/3))*(Re_h^(-1/2))

#Compute E_IN (Interception)

C_IN = 0.162

E_IN = C_IN*(dp/L_obs)

#Compute E_IM (Impaction)

C_IM = 0.081

beta_IM = 0.47

St_h = (Tau*U_h)/L_obs

E_IM = C_IM*(St_h/(St_h+beta_IM))^2

E_T = (U_h/u_star)*(E_B+E_IN+E_IM)+E_t

Q  = LAI*E_T*h/(lmp_h)

# Compute etaPZ

etaPZ = (alphaPZ^2/4+Q)^0.5

Vds = u_star*Eg*{(1+Q/Qg-alphaPZ/2)*tanh(etaPZ)/etaPZ}/{(1+Q+alphaPZ/2)*tanh(etaPZ)/etaPZ}

Vd = Vdrift+1/(Ra+1/Vds);Vd

#Accuracy Evaluation: Coniferous forest

#Dry deposition velocity parameterization by Petroff and Zhang (2010)

attach(Rannik_etal_2000)

C1 = 0.2789

C2 = 3.115

C3 = 5.145*10^-11

C4 = -1.399

RH= 0.90
```

```
dp_i = V1

dp_d = dp_i*10^-6

rd = dp_d/2

r_w = {(C1*rd^C2)/(C3*rd^C4-log10(RH))+rd^3}^(1/3)

dp = r_w*2

#Correction factor, C

k_B = 1.38*10^-23

Temp =  273.15+25

P = 101325

d_air = 3.7208*10^-10

lambda = (k_B*Temp)/(sqrt(2)*3.1416*P*d_air^2)

C = 1+(2*lambda/dp)*(1.257+0.4*exp(-0.55*dp/lambda))

dyn.vis = 1.891*10^-5

rho = 1500

Tau = (rho*(dp)^2*C)/(18*dyn.vis)

Ws = Tau*9.81

Vphor = 0

Vdrift = Ws+Vphor

# Compute aerodynamic resistance (Ra):

z = 23.7

L = 200

x = z/L

# Compute stability function (shi_H)

shi_H.1 = 2*log(0.5*{1+(1-16*x)^0.5})

shi_H.2 = -5*x

shi_H =ifelse(x <= 0, shi_H.1 , shi_H.2)

zR = 26

z0 = 1.2

u_star = V2
```

```
k_c = 0.41

Ra = (log(zR/z0)-shi_H)/(k_c*u_star)

kin.vis = 1.683*10^-5

D = (C*k_B*Temp)/(3*3.1416*dyn.vis*dp)

Sc = (kin.vis/D)

FSc = (Sc^(1/3))/2.9

Egb = (Sc^(-2/3)/14.5)*{1/6*log(1+FSc)^2/(1-FSc+FSc^2)+1/sqrt(3)*atan((2*FSc-1)/sqrt(3))
        +3.1416/6*sqrt(3)}^-1

cd = 1/6

kx = 0.216

LAI = 6

h =  13

d  = 9.75

phi_H.1 = (1-16*x)^(-0.5)

phi_H.2 = 1+5*x

phi_H = ifelse(x<=0, phi_H.1, phi_H.2)

phi_M.1 = (1-16*x)^(-0.25)

phi_M.2 = 1+5*x

phi_M = ifelse(x<=0, phi_M.1, phi_M.2)

lmp = (0.41*(z-d))/(phi_H*(z-d)/abs(L))

lmp_h = (0.41*(h-d))/(phi_M*(h-d)/abs(L))

alphaPZ = {(kx*LAI)/(12*k_c^2*(1-d/h)^2)}^(1/3)*phi_M^(2/3)*{(h-d)/abs(L)}

C_IT = 0

Tau_phplus.1 = (Tau*u_star^2)/kin.vis

Tau_phplus.2 = C_IT

Tau_phplus = ifelse(Tau_phplus.1<20,Tau_phplus.1, Tau_phplus.2)

E_t.1 = 2.5*10^-3*C_IT*(Tau_phplus)^2

E_t.2 = C_IT

E_t = ifelse(Tau_phplus.1<20, E_t.1, E_t.2)
```

```
u_starf = u_star*exp(-alphaPZ)

Tau_phplus.f1 = (Tau*u_star^2)/kin.vis

Tau_phplus.f2 = 0.14

Tau_phplusf = ifelse(Tau_phplus.f1<20,Tau_phplus.f1, Tau_phplus.f2)

E_gt1 = 2.5*10^-3*0.14*(Tau_phplusf)^2

E_gt2 = 0.14

Egt = ifelse(Tau_phplus.f1<20, E_gt1, E_gt2)

Eg = Egb + Egt

# Compute Qg (non-dimensional number)

Qg = Eg*h/lmp_h

# Compute Q

U_z = V3

U_h = U_z/(exp(alphaPZ*(z/h-1)))

L_obs = 0.15

C_B = 0.887

Re_h = (U_h*L_obs)/(kin.vis)

E_B = C_B*(Sc^(-2/3))*(Re_h^(-1/2))

C_IN = 0.810

E_IN = C_IN*(dp/L_obs)

#Compute E_IM (Impaction)

C_IM = 0.162

beta_IM = 0.60

St_h = (Tau*U_h)/L_obs

E_IM = C_IM*(St_h/(St_h+beta_IM))^2

E_T = (U_h/u_star)*(E_B+E_IN+E_IM)+E_t

Q  = LAI*E_T*h/(lmp_h)

# Compute etaPZ

etaPZ = (alphaPZ^2/4+Q)^0.5

Vds = u_star*Eg*{(1+Q/Qg-alphaPZ/2)*tanh(etaPZ)/etaPZ}/{(1+Q+alphaPZ/2)*tanh(etaPZ)/etaPZ}
```

```
Vd = Vdrift+1/(Ra+1/Vds);Vd

#Accuracy Evaluation: Deciduous forest

#Dry deposition parameterization by Petroff and Zhang (2010)

attach(Wesely_etal_1983)

C1 = 0.2789

C2 = 3.115

C3 = 5.145*10^-11

C4 = -1.399

RH= 95/100

dp_i = 0.4

dp_d = dp_i*10^-6

rd = dp_d/2

r_w = {(C1*rd^C2)/(C3*rd^C4-log10(RH))+rd^3}^(1/3)

dp = r_w*2

k_B = 1.38*10^-23

Temp = V1

P = 101325

d_air = 3.7208*10^-10

lambda = (k_B*Temp)/(sqrt(2)*3.1416*P*d_air^2)

C = 1+(2*lambda/dp)*(1.257+0.4*exp(-0.55*dp/lambda))

dyn.vis = V2

rho = 2000

Tau = (rho*(dp)^2*C)/(18*dyn.vis)

Ws = Tau*9.81

Vphor = 0

Vdrift = Ws+Vphor

# Compute aerodynamic resistance (Ra):

z = 39
```

```
L = (1*V6)

x = z/L

# Compute stability function (shi_H)

shi_H.1 = 2*log(0.5*{1+(1-16*x)^0.5})

shi_H.2 = -5*x

shi_H =ifelse(x <= 0, shi_H.1 , shi_H.2)

zR = 56

z0 = 1.6

u_star = V4

k_c = 0.41

Ra = (log(zR/z0)-shi_H)/(k_c*u_star)

kin.vis = V3

D = (C*k_B*Temp)/(3*3.1416*dyn.vis*dp)

Sc = (kin.vis/D)

FSc = (Sc^(1/3))/2.9

Egb = (Sc^(-2/3)/14.5)*{1/6*log(1+FSc)^2/(1-FSc+FSc^2)+1/sqrt(3)*atan((2*FSc-1)/sqrt(3))

        +3.1416/6*sqrt(3)}^-1

cd = 1/6

kx = 0.216

LAI = 0.2

h =  28

d  = 21

phi_H.1 = (1-16*x)^(-0.5)

phi_H.2 = 1+5*x

phi_H = ifelse(x<=0, phi_H.1, phi_H.2)

phi_M.1 = (1-16*x)^(-0.25)

phi_M.2 = 1+5*x

phi_M = ifelse(x<=0, phi_M.1, phi_M.2)

lmp = (0.41*(z-d))/(phi_H*(z-d)/abs(L))
```

```
lmp_h = (0.41*(h-d))/(phi_M*(h-d)/abs(L))

alphaPZ = {(kx*LAI)/(12*k_c^2*(1-d/h)^2)}^(1/3)*phi_M^(2/3)*{(h-d)/abs(L)}

C_IT = 0.056

Tau_phplus.1 = (Tau*u_star^2)/kin.vis

Tau_phplus.2 = C_IT

Tau_phplus = ifelse(Tau_phplus.1<20,Tau_phplus.1, Tau_phplus.2)

E_t.1 = 2.5*10^-3*C_IT*(Tau_phplus)^2

E_t.2 = C_IT

E_t = ifelse(Tau_phplus.1<20, E_t.1, E_t.2)

u_starf = u_star*exp(-alphaPZ)

Tau_phplus.f1 = (Tau*u_star^2)/kin.vis

Tau_phplus.f2 = 0.14

Tau_phplusf = ifelse(Tau_phplus.f1<20,Tau_phplus.f1, Tau_phplus.f2)

E_gt1 = 2.5*10^-3*0.14*(Tau_phplusf)^2

E_gt2 = 0.14

Egt = ifelse(Tau_phplus.f1<20, E_gt1, E_gt2)

Eg = Egb + Egt

# Compute Qg (non-dimensional number)

Qg = Eg*h/lmp_h

# Compute Q

U_z = V5

U_h = U_z/(exp(alphaPZ*(z/h-1)))

L_obs = 0.03

C_B = 1.262

Re_h = (U_h*L_obs)/(kin.vis)

E_B = C_B*(Sc^(-2/3))*(Re_h^(-1/2))

C_IN = 0.216

E_IN = C_IN*(dp/L_obs)*(2+log(4*L_obs/dp))

C_IM = 0.130
```

```
beta_IM = 0.47

St_h = (Tau*U_h)/L_obs

E_IM = C_IM*(St_h/(St_h+beta_IM))^2

E_T = (U_h/u_star)*(E_B+E_IN+E_IM)+E_t

Q  = LAI*E_T*h/(lmp_h)

# Compute etaPZ

etaPZ = (alphaPZ^2/4+Q)^0.5

Vds = u_star*Eg*{(1+Q/Qg-alphaPZ/2)*tanh(etaPZ)/etaPZ}/{(1+Q+alphaPZ/2)*tanh(etaPZ)/etaPZ}

Vd = Vdrift+1/(Ra+1/Vds);Vd


#Accuracy Evaluation: Water

#Dry deposition parameterization by Petroff and Zhang (2010)

attach(Moller_Schumann_1970)

C1 = 0.2789

C2 = 3.115

C3 = 5.415*10^-11

C4 = -1.399

RH = 90/100

dp_i = V1

dp_d = dp_i*10^-6

rd = dp_d/2

r_w = {(C1*rd^C2)/(C3*rd^C4-log10(RH))+rd^3}^(1/3)

dp = r_w*2

k_B = 1.38*10^-23

Temp = 273.15+25

P = 101325

d_air = 3.7208*10^-10

lambda = (k_B*Temp)/(sqrt(2)*3.1416*P*d_air^2)

C = 1+(2*lambda/dp)*(1.257+0.4*exp(-0.55*dp/lambda))
```

```
dyn.vis = ((5*10^-8)*Temp)+4*10^-6

rho = 1500

Tau = (rho*(dp)^2*C)/(18*dyn.vis)

Ws = Tau*9.81

Vphor = (5*10^-3)/100

Vdrift = Ws+Vphor

# Compute aerodynamic resistance (Ra):

z = 8/100

L = 50

x = z/L

shi_H.1 = 2*log(0.5*{1+(1-16*x)^0.5})

shi_H.2 = -5*x

shi_H = ifelse(x <= 0, shi_H.1 , shi_H.2)

zR = 5

u_star = 0.4

z0_1 = 0.021*(u_star)^3.32

z0_2 = 0.00098*(u_star)^1.65

z0 = ifelse(u_star<= 0.16, z0_1, z0_2)

k_c = 0.41

Ra = (log(zR/z0)-shi_H)/(k_c*u_star)

# Compute surface resistance (Rs)

kin.vis = ((9*10^-8)*Temp)+10^-5

D = (C*k_B*Temp)/(3*3.1416*dyn.vis*dp)

Sc = (kin.vis/D)

FSc = (Sc^(1/3))/2.9

Egb = (Sc^(-2/3)/14.5)*{1/6*log(1+FSc)^2/(1-FSc+FSc^2)+1/sqrt(3)*atan((2*FSc-
1)/sqrt(3))+3.1416/6*sqrt(3)}^-1

Eg = Egb

Vd = Vdrift+1/(Ra+(1/(Eg*u_star)));Vd
```

```
#Accuracy Evaluation: Ice/snow
#Dry deposition velocity parameterization by Petroff and Zhang (2010)
attach(Ibrahim_1983)
C1 = 0.2789
C2 = 3.115
C3 = 5.415*10^-11
C4 = -1.399
RH = 60/100
dp_i = c(0.22, 0.73)
dp_d = dp_i*10^-6
rd = dp_d/2
r_w = {(C1*rd^C2)/(C3*rd^C4-log10(RH))+rd^3}^(1/3)
dp = r_w*2
#Correction factor, C
k_B = 1.38*10^-23
#Temp_1 = 25
Temp = 273.15+3
P = 101325
d_air = 3.7208*10^-10
lambda = (k_B*Temp)/(sqrt(2)*3.1416*P*d_air^2)
C = 1+(2*lambda/dp)*(1.257+0.4*exp(-0.55*dp/lambda))
dyn.vis = ((5*10^-8)*Temp)+4*10^-6
rho = 1500
Tau = (rho*(dp)^2*C)/(18*dyn.vis)
Ws = Tau*9.81
Vphor = (2*10^-4)/100
Vdrift = Ws+Vphor
# Compute aerodynamic resistance (Ra):
#z =
```

```
#L = z/L

#x = z/L

x = 0.2

# Compute stability function (shi_H)

shi_H.1 = 2*log(0.5*{1+(1-16*x)^0.5})

shi_H.2 = -5*x

shi_H = ifelse(x <= 0, shi_H.1 , shi_H.2)

zR = 10

u_star = 0.12

z0 = 0.1/100

k_c = 0.41

Ra = (log(zR/z0)-shi_H)/(k_c*u_star)  # m/s

# Compute surface resistance (Rs)

kin.vis = ((9*10^-8)*Temp)+10^-5

D = (C*k_B*Temp)/(3*3.1416*dyn.vis*dp)

Sc = (kin.vis/D)

FSc = (Sc^(1/3))/2.9

Egb = (Sc^(-2/3)/14.5)*{1/6*log(1+FSc)^2/(1-FSc+FSc^2)+1/sqrt(3)*atan((2*FSc-1)/sqrt(3))+3.1416/6*sqrt(3)}^-1

Eg = Egb

Vd = Vdrift+1/(Ra+(1/(Eg*u_star)));Vd
```

Codes for evaluation of model accuracy using Kouznetsov and Sofiev (2012) parameterization

```
#Accuracy Evaluation: Grass

#Dry deposition parameterization by Kouznetsov and Sofiev (2012)

attach(Allen_etal_1990)

C1 = 0.4809

C2 = 3.082

C3 = 3.110*10^-11

C4 = -1.428
```

```
RH = 90/100

dp_a = 0.48

dp_i = dp_a*10^-6

rd = dp_i/2

r_w = {(C1*rd^C2)/(C3*rd^C4-log10(RH))+rd^3}^(1/3)

dp = r_w*2

#Correction factor, C

k_B = 1.38*10^-23

Temp_1 = V1

Temp = 273.15+V1

P = 101325

d_air = 3.7208*10^-10

lambda = (k_B*Temp)/(sqrt(2)*3.1416*P*d_air^2)

C = 1+(2*lambda/dp)*(1.257+0.4*exp(-0.55*dp/lambda))

dyn.vis = ((5*10^-8)*Temp)+4*10^-6

rho =  2000

Tau = (rho*(dp)^2*C)/(18*dyn.vis)

V_s = Tau*9.81

u_star = V2

a  =  2*10^-3

kin.vis = ((9*10^-8)*Temp)+10^-5

D = (C*k_B*Temp)/(3*3.1416*dyn.vis*dp)

Sc = (kin.vis/D)

Re_star = (u_star*a)/kin.vis

# Compute V_diff (velocity for diffusion)

V_diff = 2*(Re_star^(-0.5))*Sc^(-2/3) #m/s

# Compute V_int (velocity for interception)
```

```
V_int = 80*u_star*((dp/a)^2)*(Re_star^(0.5))

# Compute V_imp

C_S = 0.003

C_R = 0.3

LAI = 4

CsCR = (C_S+C_R/LAI)^0.5

u.Uh = 0.3

u_star.by.U_h = min(u.Uh, CsCR)

#Compute Re_c

Re_c = ((u_star.by.U_h)^-1)^2*Re_star

# Calculate St

St = (Tau*u_star)/a

# Calculate St_e

St_e = St - Re_c^(-0.5)

eta_impSt.e1 = exp((-0.1/(St_e - 0.15 ) )-(1/sqrt(St_e -0.15)))

eta_impSt.e2 = 0

eta_impSt.e = ifelse(St_e>0.15,eta_impSt.e1,eta_impSt.e2)

V_imp = ((2*u_star.by.U_h)/u_star)*eta_impSt.e*(St-u_star.by.U_h*Re_star^-0.5)

# Dry deposition velocity

Vd = V_diff+V_int+V_imp+V_s;Vd

#Accuracy Evaluation: Coniferous forest

#Dry deposition parameterization by Kouznetsov and Sofiev (2012)

attach(Rannik_etal_2000)

C1 = 0.2789

C2 = 3.115

C3 = 5.145*10^-11

C4 = -1.399

RH = 0.90
```

```
dp_a = V1

dp_i = dp_a*10^-6

rd = dp_i/2

r_w = {(C1*rd^C2)/(C3*rd^C4-log10(RH))+rd^3}^(1/3)

dp = r_w*2

#Correction factor, C

k_B = 1.38*10^-23

Temp =  273.15+25

P = 101325

d_air = 3.7208*10^-10

lambda = (k_B*Temp)/(sqrt(2)*3.1416*P*d_air^2)

C = 1+(2*lambda/dp)*(1.257+0.4*exp(-0.55*dp/lambda))

dyn.vis = 1.891*10^-5

#dyn.vis = V2

rho = 1500

Tau = (rho*(dp)^2*C)/(18*dyn.vis)

V_s = Tau*9.81

# Need to compute Sc, Re_star

u_star = V2

a  =  0.7*10^-3

kin.vis = 1.683*10^-5

D = (C*k_B*Temp)/(3*3.1416*dyn.vis*dp)

Sc = (kin.vis/D)

Re_star = (u_star*a)/kin.vis

# Compute V_diff (velocity for diffusion)

V_diff = 2*(Re_star^(-0.5))*Sc^(-2/3)

# Compute V_int (velocity for interception)

V_int = 80*u_star*((dp/a)^2)*(Re_star^(0.5))

# Compute V_imp
```

```
C_S = 0.003

C_R = 0.3

LAI = 6

CsCR = (C_S+C_R/LAI)^0.5

u.Uh = 0.3

u_star.by.U_h = min(u.Uh, CsCR)

#Compute Re_c

Re_c = ((u_star.by.U_h)^-1)^2*Re_star

# Calculate St

St = (Tau*u_star)/a

# Calculate St_e

St_e = St - Re_c^(-0.5)

eta_impSt.e1 = exp((-0.1/(St_e - 0.15 ) )-(1/sqrt(St_e -0.15)))

eta_impSt.e2 = 0

eta_impSt.e = ifelse(St_e>0.15,eta_impSt.e1,eta_impSt.e2)

V_imp = ((2*u_star.by.U_h)/u_star)*eta_impSt.e*(St-u_star.by.U_h*Re_star^-0.5)

# Dry deposition velocity

Vd = V_diff+V_int+V_imp+V_s;Vd

#Accuracy Evaluation: Deciduous forest

#Dry deposition parameterization by Kouznetsov and Sofiev (2012)

attach(Wesely_etal_1983)

C1 = 0.2789

C2 = 3.115

C3 = 5.145*10^-11

C4 = -1.399

RH = 0.95

dp_a = 0.4

dp_i = dp_a*10^-6

rd = dp_i/2
```

```
r_w = {(C1*rd^C2)/(C3*rd^C4-log10(RH))+rd^3}^(1/3)

dp = r_w*2

#Correction factor, C

k_B = 1.38*10^-23

Temp = V1

P = 101325

d_air = 3.7208*10^-10

lambda = (k_B*Temp)/(sqrt(2)*3.1416*P*d_air^2)

C = 1+(2*lambda/dp)*(1.257+0.4*exp(-0.55*dp/lambda))

dyn.vis = V2

rho = 2000

Tau = (rho*(dp)^2*C)/(18*dyn.vis)

V_s = Tau*9.81

# Need to compute Sc, Re_star

u_star = V4

a  = 0.7*10^-3

kin.vis = 1.597*10^-5

D = (C*k_B*Temp)/(3*3.1416*dyn.vis*dp)

Sc = (kin.vis/D)

Re_star = (u_star*a)/kin.vis

# Compute V_diff (velocity for diffusion)

V_diff = 2*(Re_star^(-0.5))*Sc^(-2/3) #m/s

# Compute V_int (velocity for interception)

V_int = 80*u_star*((dp/a)^2)*(Re_star^(0.5))

# Compute V_imp

C_S = 0.003

C_R = 0.3

LAI = 0.2

CsCR = (C_S+C_R/LAI)^0.5
```

```
u.Uh = 0.3

u_star.by.U_h = min(u.Uh, CsCR)

#Compute Re_c

Re_c = ((u_star.by.U_h)^-1)^2*Re_star

# Calculate St

St = (Tau*u_star)/a

# Calculate St_e

St_e = St - Re_c^(-0.5)

eta_impSt.e1 = exp((-0.1/(St_e - 0.15 ) )-(1/sqrt(St_e -0.15)))

eta_impSt.e2 = 0

eta_impSt.e = ifelse(St_e>0.15,eta_impSt.e1,eta_impSt.e2)

V_imp = ((2*u_star.by.U_h)/u_star)*eta_impSt.e*(St-u_star.by.U_h*Re_star^-0.5)

#Dry deposition velocity

Vd = V_diff+V_int+V_imp+V_s;Vd

#Accuracy Evaluation: Ice/snow

#Dry deposition parameterization by Kouznetsov and Sofiev (2012)

attach(Ibrahim_1983)

C1 = 0.4809

C2 = 3.082

C3 = 3.110*10^-11

C4 = -1.428

RH = 0.90

dp_a = c(0.22, 0.73)

dp_i = dp_a*10^-6

rd = dp_i/2

r_w = {(C1*rd^C2)/(C3*rd^C4-log10(RH))+rd^3}^(1/3)

dp = r_w*2

#Correction factor, C

k_B = 1.38*10^-23
```

```
Temp = 273.15+3

P = 101325

d_air = 3.7208*10^-10

lambda = (k_B*Temp)/(sqrt(2)*3.1416*P*d_air^2)

C = 1+(2*lambda/dp)*(1.257+0.4*exp(-0.55*dp/lambda))

dyn.vis = ((5*10^-8)*Temp)+4*10^-6

rho =  1500

Tau = (rho*(dp)^2*C)/(18*dyn.vis)

V_s = Tau*9.81

u_star = 0.12

a  =  0.5*10^-3

kin.vis = ((9*10^-8)*Temp)+10^-5

D = (C*k_B*Temp)/(3*3.1416*dyn.vis*dp)

Sc = (kin.vis/D)

Re_star = (u_star*a)/kin.vis

# Compute V_diff (velocity for diffusion)

V_diff = 2*(Re_star^(-0.5))*Sc^(-2/3) #m/s

# Compute V_int (velocity for interception)

V_int = 80*u_star*((dp/a)^2)*(Re_star^(0.5))

#Compute V_imp

C_S = 0.003

C_R = 0.3

LAI = 0

CsCR = (C_S+C_R/LAI)^0.5

u.Uh = 0.3

u_star.by.U_h = min(u.Uh, CsCR)

#Compute Re_c

Re_c = ((u_star.by.U_h)^-1)^2*Re_star

# Calculate St
```

```
St = (Tau*u_star)/a

# Calculate St_e

St_e = St - Re_c^(-0.5)

eta_impSt.e1 = exp((-0.1/(St_e - 0.15 ) )-(1/sqrt(St_e -0.15)))

eta_impSt.e2 = 0

eta_impSt.e = ifelse(St_e>0.15,eta_impSt.e1,eta_impSt.e2)

#V_imp = ((2*u_star.by.U_h)/u_star)*eta_impSt.e*(St-u_star.by.U_h*Re_star^-0.5)

V_imp = (2*u_star.by.U_h*eta_impSt.e*(St-(u_star.by.U_h*Re_star^-0.5)))*u_star

# Dry deposition velocity

Vd = V_diff+V_int+V_imp+V_s;Vd

#Accuracy Evaluation: Water

#Dry deposition parameterization by Kouznetsov and Sofiev (2012)

C1 = 0.2789

C2 = 3.115

C3 = 5.415*10^-11

C4 = -1.399

dp_i = c(0.22, 0.73)

dp = dp_i*10^-6

rho = 1500

RH = 0.60

Temp = 25+273.15

u_star = 0.12

z0 =0.1/100

L = 40

kin.vis = ((9*10^-8)*Temp)+10^-5

dyn.vis = ((5*10^-8)*Temp)+4*10^-6

d_air = 3.7208*10^-10

k_B = 1.38*10^-23

P = 101325
```

```
lambda = (k_B*Temp)/(sqrt(2)*3.1416*P*d_air^2)

C = 1+((2*lambda/dp)*(1.257+0.4*exp(-0.55*dp/lambda)))

tau_p = (rho*(dp)^2*C)/(18*dyn.vis)

D = (C*k_B*Temp)/(3*3.1416*dyn.vis*dp)

v_s = 9.81*tau_p

taup = (tau_p*u_star^2)/(kin.vis)

Sc = (kin.vis/D)

vsplus = v_s/u_star

rplus = (dp*u_star)/(2*kin.vis)

R_s = 0

Rsplus = u_star*R_s

z_meas = 8

zpmax = (z_meas*u_star)/(kin.vis)

MOplus = (kin.vis)/(u_star*L)

#Fixed parameters

Zbuf = 3

Ztf = 18                              #turbophoretic sublayer height

taultf = 5                            #Lagrangian time in turbophoretic layer

Nutp_Ztf= (0.4*(Ztf)^3)/(Ztf^2+200)  #Dimensionless eddy viscosity of air

It_Ztf = (2.5*log10(Ztf ))-(100/Ztf^2)

It_Zbuf = (2.5*log10(Zbuf))-(100/Zbuf^2)

S = Sc^(1/3)

Zl = 20/S

fTmp = 2.5/Sc

fTmp1 = (fTmp^3/27+(fTmp*(100+5*sqrt(8*fTmp/27)+400)))^(1/3)

Zl_1 = fTmp1+((fTmp*fTmp)/(9*fTmp1))+(1/3)*fTmp                #Zl updated as zl_1

fTmp_1 = (Zl_1^2)/(Zl_1^2+200)                                 #fTmp updated as fTmp_1

fTmp_2 = 1.2*(fTmp_1)-0.8*fTmp_1^2                             #fTmp_1 updated as fTmp_2

fTmp1_1 = 1/(Sc*fTmp_2)                                        #fTmp1 updated as fTmp1_1
```

```
fTmp_3 = 1/Sc                                                    #ftmp_2 updated as fTmp_3

x_1 = Zl_1 - fTmp1_1

x_2 = Zl_1

x_3 = Zl_1+fTmp1_1

Nutp_x_1 = (0.4*x_1^3)/(x_1^2+200)

Nutp_x_2 = (0.4*x_2^3)/(x_2^2+200)

Nutp_x_3 = (0.4*x_3^3)/(x_3^2+200)

fIvd = Rsplus+(Zl_1-fTmp1_1)*Sc+0.3333*fTmp1_1*(1/fTmp_3+((0.4*x_1^3)/(x_1^2+200)))+

4/(fTmp_3+((0.4*x_2^3)/(x_2^2+200)))+1/(fTmp_3+((0.4*x_3^3)/(x_3^2+200)))

x_4 = zpmax

x_5 = Zl_1 + fTmp1_1

It_x_4 = 2.5*log10(x_4) - 100/(x_4^2)

It_x_5 = 2.5*log10(x_5) - 100/(x_5^2)

s = 2.35*(zpmax*MOplus+abs(zpmax*MOplus))

u1 = 0.5*(abs(zpmax*MOplus)-zpmax*MOplus)

u = -4*u1/(2.65*sqrt(u1*sqrt(u1))+1)

fu_Psi = s+u

fTmp_4 = It_x_4 - It_x_5 + 2.5*fu_Psi

fIvd_1 = fIvd+0.5*(fTmp_4+abs(fTmp_4))    #fIvd updated as fIvd_1

fu_vdplus_smooth_1 = 1/fIvd_1             #mind fu_vdplus_smooth is denoted as _1

Il_input1= Zl*S/7.92

Il_input2= rplus*S/7.92

Il_1 = -0.16667*log10(Il_input1^2-Il_input1+1)+0.57735*atan((2*Il_input1-1)*0.57735)

+0.3333*log10(Il_input1+1)

Il_2 = -0.16667*log10(Il_input2^2-Il_input2+1)+0.57735*atan((2*Il_input2-1)*0.57735)

+0.3333*log10(Il_input2+1)

R = 7.92*S^2*(Il_1-Il_2)  #laminar resistance

R_1 = 0.5*(R+abs(R))      #R updated as R_1 #should be zero if rplus > Zl

Zl_2 = 0.5*(rplus+Zl+abs(rplus-Zl))   #Zl updated as Zl_2, not to be confused
```

```
with Zl_1 as if statement is in use

It_Zbuf = 2.5*log10(Zbuf) - (100/(Zbuf^2))

It_Zl_2 = 2.5*log10(Zl_2) - (100/(Zl_2^2))

R1 = It_Zbuf - It_Zl_2

R_2 = R_1+0.5*(R1+abs(R1))                    #R_1 updated as R_2

fTmp_5 = vsplus*R_2                           #fTmp used as fTmp_5.

Not updated as previous fTmp_4 is for different condition

fTmp_6 = exp(-fTmp_5)                         #fTmp_5 updated as fTmp_6

fIvd_2  = Rsplus*fTmp_6+(1-fTmp_6)/vsplus     #fIvd denoted as fIvd_2 NOT updated

previous fIvd_1 is for different condition

fIvd_3 = Rsplus+R_2                           #fIvd_3 used; NOT updated

fIvd_23 = ifelse(abs(fTmp_5)>0.001, fIvd_2, fIvd_3 )

#Use above values for the following calculations for turbophoretic layer

V  = 0.81*taup/(Ztf-Zbuf)/(1+taup/taultf) + vsplus   #chcek for sign of vsplus

It_Ztf = 2.5*log10(Ztf) - 100/(Ztf^2)

R_3  = ((It_Ztf)-(It_Zbuf))*(1+taup/taultf)    #R_2 updated as R_3

fTmp_7 = V*R_3                                 #fTmp_6 updated as fTmp_7

fTmp_8 = exp(-fTmp_7)                          #fTmp_7 updated as fTmp_8

fIvd_4 = (fIvd_23*fTmp_8)+(1-fTmp_8)/V         #fIvd_23 updated as fIvd_4

fIvd_5 = fIvd_3+R_3                            #fIvd_5 used; NOT updated

fIvd_45 = ifelse(abs(fTmp_7)>0.001, fIvd_4, fIvd_5)

#Now calculations for the Lagrangian turbophoretic layer

Ztf2 = 2*taup

V_1 = 0.4+vsplus

R_4 = 0.1667*((1+taup/(0.5*Ztf))/(Nutp_Ztf)+4*(1+taup/(0.25*(Ztf+Ztf2)))/

((0.4*(0.5*(Ztf+Ztf2))^3)/((0.5*(Ztf+Ztf2))^2+200))+(1+taup/(0.5*Ztf2))/

((0.4*Ztf2 ^3)/(Ztf2^2+200)))*(Ztf2-Ztf)

fTmp_9 = V_1*R_4

fTmp_10 = exp(-fTmp_9)
```

```
fIvd_6 = fIvd_45*fTmp_10 + (1-fTmp_10)/V_1   #fIvd_5 or fIvd_4 (fIvd_45)

fIvd_7 = fIvd_45+R_3                        #Either fIvd_4 or fIvd_5,

R_3 used not R_4 since outside if statement

fIvd_67 = ifelse(abs(fTmp_9) > 0.001, fIvd_6, fIvd_7)

Ztf2_2 = Ztf

fIvd67_Ztf2 = ifelse(Ztf2>Ztf, fIvd_67, Ztf2_2)


#Following calculations are for aerodynamic layer

It_zpmax = 2.5*log10(zpmax) - 100/(zpmax^2)

Ztf22 = ifelse(Ztf2>Ztf, Ztf2, Ztf2_2)

It_Ztf22  = 2.5*log10(Ztf22) - 100/(Ztf22^2)       #be careful which Ztf2 to

be used here based on previous condition

R_5 = It_zpmax - It_Ztf22  + 2.5*fu_Psi            #R_5 used, NOT updated from R_4

R_6 = 0.5*(R_5+abs(R_5))                           #R_5 updated as R_6

fTmp_11  = vsplus*R_6                              #fTmp_11 used, NOT updated from fTmp_10

fTmp_12 = exp(-fTmp_11)                            #fTmp_11 updated as fTmp_12

fIvd_4567 = ifelse(Ztf2>Ztf, fIvd_67,fIvd_45)

fIvd_8 = (fIvd_4567* fTmp_12)+(1-fTmp_12)/vsplus   # Caution:fIvd_45 or fIvd_67 may be used

fIvd_9 = fIvd_4567 + R_6                           #fIvd_9 used, NOT updated.

Caution:fIvd_5 or fIvd_4 may be used

fIvd_10 = ifelse(abs(fTmp_11) > 0.001, fIvd_8, fIvd_9)

fu_vdplus_smooth_3 = 1/fIvd_10                      #fu_vdplus_smooth_3 used.

NOT updated. fIvd_8 could be used

fu_vdplus_smooth = ifelse(Zl>Zbuf, fu_vdplus_smooth_1, fu_vdplus_smooth_3)

Vd_smooth = fu_vdplus_smooth*u_star;Vd_smooth
```

Codes for evaluation of model accuracy using Zhang and He (2014) parameterization

```
#Accuracy Evaluation: Grass (code is similar for coniferous forest)

#Dry deposition parameterization by Zhang and He (2014)
```

```
attach(Allen_etal_1991)

C1 = 0.4809

C2 = 3.082

C3 = 3.110*10^-11

C4 = -1.428

RH = 90/100

dp_a = 0.48

dp_i = dp_a*10^-6

rd = dp_i/2

r_w = {(C1*rd^C2)/(C3*rd^C4-log10(RH))+rd^3}^(1/3)

dp = r_w*2

#Correction factor, C

k_B = 1.38*10^-23

Temp_1 = V1

Temp = 273.15+V1

P = 101325

d_air = 3.7208*10^-10

lambda = (k_B*Temp)/(sqrt(2)*3.1416*P*d_air^2)

C = 1+(2*lambda/dp)*(1.257+0.4*exp(-0.55*dp/lambda))

dyn.vis = ((5*10^-8)*Temp)+4*10^-6              # kg/m*s (temp. corrected viscosity coeff. of
air)

rho = 2000

Tau = (rho*(dp)^2*C)/(18*dyn.vis)

V_g = Tau*9.81

Rg = 1/V_g

u_star = V2

a1 = 4.8*10^-3

z = 2

L = V4
```

```
x = z/L

# Compute stability function (shi_H)

shi_H.1 = 2*log(0.5*{1+(1-16*x)^0.5})

shi_H.2 = -5*x

shi_H =ifelse(x <= 0, shi_H.1 , shi_H.2)

zR = 3.5

z0 = 0.01

k_c = 0.41

Ra = (log(zR/z0)-shi_H)/(k_c*u_star)

# Calculate Vds = 1/Rs

#For PM2.5

Vds_PM2.5 = (a1*u_star)

Rds_PM2.5 = (1/Vds_PM2.5)

# For PM2.5-10

#b1= -1.6*10^-1

#b2= 1.5*10^0

#b3 = 7.8*10^-1

#c1= 1.8

#c2 = -2.0*10^-1

#c3 = -5.3*10^-1

#k = c1*u_star+c2*u_star^2+c3*u_star^3

#LAI =

#LAImax =

#Vds_PM10 = (b1*u_star+b2*u_star^2+b3*u_star^3)  #*exp(k*(LAI/LAImax)-1)

#Rds_PM10 = 1/Vds_PM10

# For PM10+

#d1= -2.2

#d2= 3.9*10^1

#d3 = -6.7
```

```
#f1= 6.2

#f2 = -1.2*10^1

#f3 = 6.1

#k = f1*u_star+f2*u_star^2+f3*u_star^3

#LAI =

#LAImax =

#Vds_PM10Plus = (d1*u_star+d2*u_star^2+d3*u_star^3)*exp(k*(LAI/LAImax)-1)

#Rds_PM10Plus = (1/Vds_PM10Plus)

#Compute Vd

Vd = 1/Rg+(1/(Ra+Rds_PM2.5));Vd



#Accuracy Evaluation: Deciduous forest

#Dry deposition parameterization by Zhang and He (2014)

attach(Rannik_etal_2000)

C1 = 0.2789

C2 = 3.115

C3 = 5.145*10^-11

C4 = -1.399

RH = 90/100

dp_a = V1

dp_i = dp_a*10^-6

rd = dp_i/2

r_w = {(C1*rd^C2)/(C3*rd^C4-log10(RH))+rd^3}^(1/3)

dp = r_w*2

k_B = 1.38*10^-23

Temp = 273.15+25

P = 101325

d_air = 3.7208*10^-10
```

```
lambda = (k_B*Temp)/(sqrt(2)*3.1416*P*d_air^2)

C = 1+(2*lambda/dp)*(1.257+0.4*exp(-0.55*dp/lambda))

dyn.vis = 1.891*10^-5

rho = 1500

Tau = (rho*(dp)^2*C)/(18*dyn.vis)

V_g = Tau*9.81

Rg = 1/V_g

u_star = V2

a1 = 4.3*10^-3

z = 23.7

L = 200

x = z/L

# Compute stability function (shi_H)

shi_H.1 = 2*log(0.5*{1+(1-16*x)^0.5})

shi_H.2 = -5*x

shi_H =ifelse(x <= 0, shi_H.1 , shi_H.2)

zR = 26

z0 = 1.2

k_c = 0.41

Ra = (log(zR/z0)-shi_H)/(k_c*u_star)

# Calculate Vds = 1/Rs

#For PM2.5

Vds_PM2.5 = (a1*u_star)

Rds_PM2.5 = (1/Vds_PM2.5)

# For PM2.5-10

#b1= -1.6*10^-1

#b2= 1.5*10^0

#b3 = 7.8*10^-1

#c1= 1.8
```

```
#c2 = -2.0*10^-1

#c3 = -5.3*10^-1

k = c1*u_star+c2*u_star^2+c3*u_star^3

LAI = 12

LAImax = 12

Vds_PM10 = (b1*u_star+b2*u_star^2+b3*u_star^3)  #*exp(k*(LAI/LAImax)-1)

Rds_PM10 = 1/Vds_PM10

# For PM10+

#d1= -2.2

#d2= 3.9*10^1

#d3 = -6.7

#f1= 6.2

#f2 = -1.2*10^1

#f3 = 6.1

#k = f1*u_star+f2*u_star^2+f3*u_star^3

#LAI =

#LAImax =

#Vds_PM10Plus = (d1*u_star+d2*u_star^2+d3*u_star^3)*exp(k*(LAI/LAImax)-1)

#Rds_PM10Plus = (1/Vds_PM10Plus)

#Compute Vd

Vd = 1/Rg+(1/(Ra+Rds_PM2.5));Vd

#Accuracy Evaluation: Water

#Dry deposition parameterization by Zhang and He (2014)

attach(Caffrey_etal_1998)

C1 = 0.2789

C2 = 3.115

C3 = 5.415*10^-11

C4 = -1.399
```

```
RH = 79/100

dp_a = V1

dp_i = dp_a*10^-6

rd = dp_i/2

r_w = {(C1*rd^C2)/(C3*rd^C4-log10(RH))+rd^3}^(1/3)

dp = r_w*2

#Correction factor, C

k_B = 1.38*10^-23

Temp = 273.15+22

P = 101325

d_air = 3.7208*10^-10

lambda = (k_B*Temp)/(sqrt(2)*3.1416*P*d_air^2)

C = 1+(2*lambda/dp)*(1.257+0.4*exp(-0.55*dp/lambda))

dyn.vis = ((5*10^-8)*Temp)+4*10^-6

rho = 2000

Tau = (rho*(dp)^2*C)/(18*dyn.vis)

V_g = Tau*9.81

Rg = 1/V_g

a1 = 6.9*10^-3

z = 8/100

L = 50

x = z/L

# Compute stability function (shi_H)

shi_H.1 = 2*log(0.5*{1+(1-16*x)^0.5})

shi_H.2 = -5*x

shi_H =ifelse(x <= 0, shi_H.1 , shi_H.2)

zR = 5

u_star = 13.5/100

z0_1 = 0.021*(u_star)^3.32
```

```
z0_2 = 0.00098*(u_star)^1.65

z0 = ifelse(u_star<= 0.16, z0_1, z0_2)

k_c = 0.41

Ra = (log(zR/z0)-shi_H)/(k_c*u_star)  # m/s

# Calculate Vds = 1/Rs

#For PM2.5

Vds_PM2.5 = (a1*u_star)

Rds_PM2.5 = (1/Vds_PM2.5)

#Compute Vd

Vd = 1/Rg+(1/(Ra+Rds_PM2.5));Vd

#Accuracy Evaluation: Ice/snow

#Dry deposition parameterization by Zhang and He (2014)

#attach(Nilsson_Rannik_2001)

C1 = 0.2789

C2 = 3.115

C3 = 5.415*10^-11

C4 = -1.399

RH = 60/100

dp_a = c(0.22, 0.73)

dp_i = dp_a*10^-6

rd = dp_i/2

r_w = {(C1*rd^C2)/(C3*rd^C4-log10(RH))+rd^3}^(1/3)

dp = r_w*2

#Correction factor, C

k_B = 1.38*10^-23

Temp = 273.15+3

P = 101325

d_air = 3.7208*10^-10
```

```
lambda = (k_B*Temp)/(sqrt(2)*3.1416*P*d_air^2)

C = 1+(2*lambda/dp)*(1.257+0.4*exp(-0.55*dp/lambda))

dyn.vis = ((5*10^-8)*Temp)+4*10^-6

rho = 1500

Tau = (rho*(dp)^2*C)/(18*dyn.vis)

V_g = Tau*9.81

Rg = 1/V_g

a1 = 4.3*10^-3

#z =

#L =

#x = z/L

x = 0.2

# Compute stability function (shi_H)

shi_H.1 = 2*log(0.5*{1+(1-16*x)^0.5})

shi_H.2 = -5*x

shi_H =ifelse(x <= 0, shi_H.1 , shi_H.2)

zR = 10

u_star = 0.12

z0 = 0.1/100

k_c = 0.41

Ra = (log(zR/z0)-shi_H)/(k_c*u_star)  # m/s

# Calculate Vds = 1/Rs

#For PM2.5

Vds_PM2.5 = (a1*u_star)

Rds_PM2.5 = (1/Vds_PM2.5)

#Compute Vd

Vd = 1/Rg+(1/(Ra+Rds_PM2.5));Vd
```

Codes for evaluation of model accuracy using Zhang and Shao (2014) parameterization

```
#Accuracy Evaluation: Rough and smooth surfaces
#Dry deposition parameterization by Zhang and He (2014)

#attach(Allen_etal_1991)

C1 = 0.4809

C2 = 3.082

C3 = 3.110*10^-11

C4 = -1.428

RH_1 = 90

RH = 90/100

dp_a = 0.50

dp_i = dp_a*10^-6

rd = dp_i/2

r_w = {(C1*rd^C2)/(C3*rd^C4-log10(RH))+rd^3}^(1/3)

dp = r_w*2

#Correction factor, C

k_B = 1.38*10^-23

Temp = 273.15+25

P = 101325

d_air = 3.7208*10^-10

lambda = (k_B*Temp)/(sqrt(2)*3.1416*P*d_air^2)

C = 1+(2*lambda/dp)*(1.257+0.4*exp(-0.55*dp/lambda))

Temp = 273.15+25

dyn.vis = ((5*10^-8)*Temp)+4*10^-6

rho = 1500

Tau = (rho*(dp_i)^2*C)/(18*dyn.vis)

Tau_wet = (rho*(dp)^2*C)/(18*dyn.vis)

Wt = Tau*9.81

Vg = Wt

Vg_wet = Tau_wet*9.81
```

```
u_star = 0.5

k =  0.41

z =  1

zd = 0.20

h_c = 0.23

z0 = 0.002

B1 = 0.45

Sc_T = (1+(Vg^2/u_star^2))^0.5

Ra = (Sc_T/(k*u_star))*(log((z-zd)/(h_c-zd)))  # For rough surface

#Ra = (B1*Sc_T/k*u_star)*log(z/z0)             # For smooth surface

Rg = 1/Vg

# Calculate surface resistance (Rs)

U_h = 2

kin.vis = ((9*10^-8)*Temp)+10^-5

d_c = 0.005

D = (C*k_B*Temp)/(3*3.1416*dyn.vis*dp)

Sc = (kin.vis/D)

Re_h = (U_h*d_c)/(kin.vis)

nB = 0.5

C_B = 0.467

E_B = C_B*Sc^(-2/3)*Re_h^(nB-1)

#Compute impaction collection efficiency (E_IM)

beta_IM = 0.6

St_h = (Tau*u_star)/d_c

E_IM = (St_h/(St_h+beta_IM))^2

#Compute interception efficiency (E_IN)

Ain = 150

E_IN = Ain*u_star*(10^(-St_h))*(2*dp/d_c)

#Compute R
```

```
b = 2

R = exp(-b*sqrt(St_h))

#Compute w_dm

B2 = 3

w_dm = (u_star/U_h*h_c)       #For rough surface

#w_dm = B2*u_star             #For smooth surface

#compute Tau_c/Tau (ratio of stress)

Beta = 200

C_1 = 6

C_2 = 0.1

lambda_FAI = 0.4

n_FAI = (lambda_FAI)/(h_c*d_c)

q = (3.1416*d_c^2)/4

eta_BAI = n_FAI*q

lambda_FAIe = ((lambda_FAI)/(1-eta_BAI)^C_2)*exp((-C_1*lambda_FAI)/(1-eta_BAI)^C_2)

Tau_c_BY_Tau = (Beta*lambda_FAIe)/(1+Beta*lambda_FAIe)

#Compute Rs

E = E_B+E_IM+E_IN

Tau_wetplus = (Tau_wet*u_star^2)/kin.vis

Cd = 1/6

Rs = (R*w_dm*((E*Tau_c_BY_Tau/Cd)+(1+Tau_c_BY_Tau)*Sc^-1+10^(-3/Tau_wetplus))+Vg_wet)^-1

#Compute Vd

Vd = (Rg+((Rs-Rg)/exp(Ra/Rg)))^-1;Vd
```

Codes for Monte Carlo uncertainty evaluation for Zhang et al. (2001) parameterization

```
#Dry deposition parameterization by Zhang et al. (2001)

#Uncertainty test: Grass

set.seed(5)

C1 = 0.2789
```

```
C2 = 3.115

C3 = 5.145*10^-11

C4 = -1.399

RH = replicate(10000,runif(100,0.76,0.84))

dp_i = 2.0*10^-6

rd = dp_i/2

r_w = {(C1*rd^C2)/(C3*rd^C4-log10(RH))+rd^3}^(1/3)

dp = r_w*2

#Correction factor, C

k_B = 1.38*10^-23

Temp = (273.15+25)

P = 101325

d_air = 3.72*10^-10

lambda = (k_B*Temp)/(sqrt(2)*3.1416*P*d_air^2)

C = 1+(2*lambda/dp)*(1.257+0.4*exp(-0.55*dp/lambda))

dyn.vis = 1.8908*10^-5

rho = 1500

Vg = (rho*(dp)^2*9.81*C)/(18*dyn.vis)

# Compute aerodynamic resistance Ra:

z = 5

L = replicate(10000,runif(100,45,55))

x = z/L

# Compute shi_H (stability function)

shi_H2 = -5*x

zR = 3.5

z0 = replicate(10000,runif(100,0.03, 0.05))

u_star = replicate(10000,runif(100,0.27,0.33))

k_c = 0.41

Ra = (log(zR/z0)-shi_H2)/(k_c*u_star)
```

```
# Compute surface resistance Rs:

e_0 = 3

R1 =1

# Compute E_B (collection efficienty from Brownian diffusion)

kin.vis = 1.6834*10^-5

gamma = 0.54

D = (C*k_B*Temp)/(3*3.1416*dyn.vis*dp)

Sc = (kin.vis/D)

E_B = Sc^(-gamma)

# Compute E_IM (collection efficiency from impaction)

alpha = 1.2

beta =  2

A = 2/1000

St = (Vg*u_star)/(9.81*A)

E_IM = {St/(alpha+St)}^beta

# Compute E_IN (collection efficiency from interception)

E_IN = 0.5*(dp/A)^2

Rs = 1/{(e_0*u_star)*(E_B+E_IM+E_IN)*R1}

# Compute Dry deposition velocity

Vd <- Vg+(1/(Ra+Rs))

quantile(Vd, c(.05, 0.10, .50, 0.95))


#Dry deposition parameterization by Zhang et al. (2001)

#Uncertainty test: Coniferous forest

set.seed(5)

C1 = 0.2789

C2 = 3.115

C3 = 5.145*10^-11

C4 = -1.399
```

```
RH = replicate(10000,runif(100,0.76,0.84))

dp_i = 2.0*10^-6                #particle dia = 0.005-50 um (assumed, vary)

rd = dp_i/2

r_w = {(C1*rd^C2)/(C3*rd^C4-log10(RH))+rd^3}^(1/3)

dp = r_w*2

#Correction factor, C

k_B = 1.38*10^-23

Temp = (273.15+25)

P = 101325

d_air = 3.72*10^-10

lambda = (k_B*Temp)/(sqrt(2)*3.1416*P*d_air^2)

C = 1+(2*lambda/dp)*(1.257+0.4*exp(-0.55*dp/lambda))

dyn.vis = 1.8908*10^-5

rho = 1500

Vg = (rho*(dp)^2*9.81*C)/(18*dyn.vis)   #m/s

# Compute aerodynamic resistance Ra:

L = replicate(10000,runif(100,45,55))

x = z/L

shi_H2 = -5*x

zR = 30

z0 = replicate(10000,runif(100,0.9, 1.5))

u_star = replicate(10000,runif(100,0.27,0.33))

k_c = 0.41

Ra = (log(zR/z0)-shi_H2)/(k_c*u_star)  # m/s

# Compute surface resistance Rs:

e_0 = 3

R1 =1

# Compute E_B (collection efficiency from Brownian diffusion)

kin.vis = 1.6834*10^-5
```

```
gamma = 0.56

D = (C*k_B*Temp)/(3*3.1416*dyn.vis*dp)

Sc = (kin.vis/D)

E_B = Sc^(-gamma)

# Compute E_IM (collection efficiency from impaction)

alpha = 1.0

beta =  2

A = 2/1000

St = (Vg*u_star)/(9.81*A)

E_IM = {St/(alpha+St)}^beta

# Compute E_IN (collection efficiency from interception)

E_IN = 0.5*(dp/A)^2

Rs = 1/{(e_0*u_star)*(E_B+E_IM+E_IN)*R1}  #(m/s)

# Compute Dry deposition velocity

Vd <- Vg+(1/(Ra+Rs))

quantile(Vd, c(.05, 0.10, .50, 0.95))


#Dry deposition parameterization by Zhang et al. (2001)

#Uncertainty test: Deciduous forest

set.seed(5)

C1 = 0.2789

C2 = 3.115

C3 = 5.145*10^-11

C4 = -1.399

RH = replicate(10000,runif(100,0.76,0.84))

dp_i = 2.0*10^-6

rd = dp_i/2

r_w = {(C1*rd^C2)/(C3*rd^C4-log10(RH))+rd^3}^(1/3)

dp = r_w*2
```

```
#Correction factor, C

k_B = 1.38*10^-23

Temp = (273.15+25)

P = 101325

d_air = 3.72*10^-10

lambda = (k_B*Temp)/(sqrt(2)*3.1416*P*d_air^2)

C = 1+(2*lambda/dp)*(1.257+0.4*exp(-0.55*dp/lambda))

dyn.vis = 1.8908*10^-5

rho = 1500

Vg = (rho*(dp)^2*9.81*C)/(18*dyn.vis)

# Compute aerodynamic resistance Ra:

z = 35

L = replicate(10000,runif(100,45,55))

x = 35/L

# Compute shi_H (stability function)

shi_H2 = -5*x

zR = 50

z0 = replicate(10000,runif(100,1.125, 1.875))

u_star = replicate(10000,runif(100,0.27,0.33))

k_c = 0.41

Ra = (log(zR/z0)-shi_H2)/(k_c*u_star)

# Compute surface resistance Rs:

e_0 = 3

R1 =1

# Compute E_B (collection efficienty from Brownian diffusion)

kin.vis = 1.6834*10^-5

gamma = 0.56

D = (C*k_B*Temp)/(3*3.1416*dyn.vis*dp)

Sc = (kin.vis/D)
```

```
E_B = Sc^(-gamma)

# Compute E_IM (collection efficienty from impaction)

alpha = 0.80

beta =  2

A = 5/1000

St = (Vg*u_star)/(9.81*A)

E_IM = {St/(alpha+St)}^beta

# Compute E_IN (collection efficienty from interception)

E_IN = 0.5*(dp/A)^2

Rs = 1/{(e_0*u_star)*(E_B+E_IM+E_IN)*R1}

# Compute Dry deposition velocity

Vd <- Vg+(1/(Ra+Rs))

quantile(Vd, c(.05, 0.10, .50, 0.95))


#Dry deposition parameterization by Zhang et al. (2001)

#Uncertainty test: Water

set.seed(5)

C1 = 0.2789

C2 = 3.115

C3 = 5.415*10^-11

C4 = -1.399

RH = replicate(10000,runif(100,0.76,0.84))

dp_i = 2.0 #Parameter to vary for MCs

dp_d = dp_i*10^-6

rd = dp_d/2

r_w = {(C1*rd^C2)/(C3*rd^C4-log10(RH))+rd^3}^(1/3)

dp = r_w*2

#Correction factor, C

k_B = 1.38*10^-23
```

```
Temp = 273.15+25

P = 101325

d_air = 3.72*10^-10

lambda = (k_B*Temp)/(sqrt(2)*3.1416*P*d_air^2)

C = 1+(2*lambda/dp)*(1.257+0.4*exp(-0.55*dp/lambda))

dyn.vis = ((5*10^-8)*Temp)+4*10^-6

rho = 1500

Vg = (rho*(dp)^2*9.81*C)/(18*dyn.vis)

# Compute aerodynamic resistance Ra:

z = 8/100

L = replicate(10000,runif(100,45,55))

x = z/L

# Compute shi_H (stability function)

shi_H.1 = 2*log(0.5*{1+(1-16*x)^0.5})

shi_H.2 = -5*x

shi_H =ifelse(x <= 0, shi_H.1 , shi_H.2)

zR = 5

u_star = replicate(10000,runif(100,0.27,0.33))

z0_1 = 0.021*(u_star)^3.32

z0_2 = 0.00098*(u_star)^1.65

z0 = ifelse(u_star<= 0.16, z0_1, z0_2)

k_c = 0.41

Ra = (log(zR/z0)-shi_H)/(k_c*u_star)

# Compute surface resistance Rs:

e_0 = 3

R1 = 1

kin.vis = ((9*10^-8)*Temp)+10^-5

gamma = 0.50

D = (C*k_B*Temp)/(3*3.1416*dyn.vis*dp)
```

```
Sc = (kin.vis/D)

E_B = Sc^(-gamma)

alpha = 100

beta =  2

A = 2/1000

St = (Vg*u_star^2)/(kin.vis)

E_IM = {St/(alpha+St)}^beta

Rs = 1/{(e_0*u_star)*(E_B+E_IM)*R1}  #(m/s)

# Compute Dry deposition velocity

Vd =  Vg+(1/(Ra+Rs))

quantile(Vd, c(.05, 0.10, .50, 0.95))


#Dry deposition parameterization by Zhang et al. (2001)

#Uncertainty test: Ice/snow

set.seed(5)

C1 = 0.2789

C2 = 3.115

C3 = 5.415*10^-11

C4 = -1.399

RH = replicate(10000,runif(100,0.76,0.84))

dp_i = 2.0

dp_d = dp_i*10^-6

rd = dp_d/2

r_w = {(C1*rd^C2)/(C3*rd^C4-log10(RH))+rd^3}^(1/3)

dp = r_w*2

#Correction factor, C

k_B = 1.38*10^-23

Temp = 273.15+0

P = 101325
```

```
d_air = 3.72*10^-10

lambda = (k_B*Temp)/(sqrt(2)*3.1416*P*d_air^2)

C = 1+(2*lambda/dp)*(1.257+0.4*exp(-0.55*dp/lambda))

dyn.vis = ((5*10^-8)*Temp)+4*10^-6

rho = 1500

Vg = (rho*(dp)^2*9.81*C)/(18*dyn.vis)

# Compute aerodynamic resistance Ra:

z = 5

L = replicate(10000,runif(100,45,55))

x = z/L

# Compute shi_H (stability function)

shi_H.1 = 2*log(0.5*{1+(1-16*x)^0.5})

shi_H.2 = -5*x

shi_H =ifelse(x <= 0, shi_H.1 , shi_H.2)

zR = 10

u_star = replicate(10000,runif(100,0.27,0.33))

z0 = replicate(10000,runif(100,0.0075,0.0125))

k_c = 0.41

Ra = (log(zR/z0)-shi_H)/(k_c*u_star)

# Compute surface resistance Rs:

e_0 = 3

R1 = 1

kin.vis = ((9*10^-8)*Temp)+10^-5

gamma = 0.54

D = (C*k_B*Temp)/(3*3.1416*dyn.vis*dp)

Sc = (kin.vis/D)

E_B = Sc^(-gamma)

alpha = 50

beta =  2
```

```
A = 2/1000

St = (Vg*u_star^2)/(kin.vis)

E_IM = {St/(alpha+St)}^beta

Rs = 1/{(e_0*u_star)*(E_B+E_IM)*R1}  #(m/s)

# Compute Dry deposition velocity

Vd =  Vg+(1/(Ra+Rs))

quantile(Vd, c(.05, 0.10, .50, 0.95))
```

Codes for Monte Carlo uncertainty evaluation for Petroff and Zhang (2010) parameterization

```
#Dry deposition parameterization by Petroff and Zhang (2010)

#Uncertainty test: Grass

set.seed(5)

C1 = 0.2789

C2 = 3.115

C3 = 5.145*10^-11

C4 = -1.399

RH = replicate(10000,runif(100,0.76,0.84))

dp_a = 2.0

dp_i = dp_a*10^-6

rd = dp_i/2

r_w = {(C1*rd^C2)/(C3*rd^C4-log10(RH))+rd^3}^(1/3)

dp = r_w*2

#Correction factor, C

k_B = 1.38*10^-23

Temp = (273.15+25)

P = 101325

d_air = 3.7208*10^-10

lambda = (k_B*Temp)/(sqrt(2)*3.1416*P*d_air^2)

C = 1+(2*lambda/dp)*(1.257+0.4*exp(-0.55*dp/lambda))
```

```
dyn.vis = 1.8908*10^-5

rho = 1500

Tau = (rho*(dp)^2*C)/(18*dyn.vis)

Ws = Tau*9.81

Vphor = 0

Vdrift = Ws+Vphor

# Compute aerodynamic resistance (Ra):

z = 5

L = replicate(10000,runif(100,45,55))

x = z/L

# Compute stability function (shi_H)

shi_H.1 = 2*log(0.5*{1+(1-16*x)^0.5})

shi_H.2 = -5*x

shi_H =ifelse(x <= 0, shi_H.1 , shi_H.2)

zR = 3.5

z0 = replicate(10000,runif(100,0.03,0.05))

u_star = replicate(10000,runif(100,0.27,0.33))

k_c = 0.41

Ra = (log(zR/z0)-shi_H)/(k_c*u_star)

# Compute surface resistance (Rs)

kin.vis = 1.6834*10^-5

D = (C*k_B*Temp)/(3*3.1416*dyn.vis*dp)

Sc = (kin.vis/D)

FSc = (Sc^(1/3))/2.9

Egb = (Sc^(-2/3)/14.5)*{1/6*log(1+FSc)^2/(1-FSc+FSc^2)+1/sqrt(3)*atan((2*FSc-1)/sqrt(3))

        +3.1416/6*sqrt(3)}^-1

cd = 1/6

kx = 0.216

LAI = replicate(10000,runif(100,3.8,4.2))
```

```
h = replicate(10000,runif(100,0.475,0.525))

d = replicate(10000,runif(100,0.225,0.375))

phi_H.1 = (1-16*x)^(-0.5)

phi_H.2 = 1+5*x

phi_H = ifelse(x<=0, phi_H.1, phi_H.2)

phi_M.1 = (1-16*x)^(-0.25)

phi_M.2 = 1+5*x

phi_M = ifelse(x<=0, phi_M.1, phi_M.2)

lmp = (0.41*(z-d))/(phi_H*(z-d)/abs(L))

lmp_h = (0.41*(h-d))/(phi_M*(h-d)/abs(L))

alphaPZ = {(kx*LAI)/(12*k_c^2*(1-d/h)^2)}^(1/3)*phi_M^(2/3)*{(h-d)/abs(L)}

C_IT = 0.042

Tau_phplus.1 = (Tau*u_star^2)/kin.vis

Tau_phplus.2 = C_IT

Tau_phplus = ifelse(Tau_phplus.1<20,Tau_phplus.1, Tau_phplus.2)

E_t.1 = 2.5*10^-3*C_IT*(Tau_phplus)^2

E_t.2 = C_IT

E_t = ifelse(Tau_phplus.1<20, E_t.1, E_t.2)

u_starf = u_star*exp(-alphaPZ)

Tau_phplus.f1 = (Tau*u_star^2)/kin.vis

Tau_phplus.f2 = 0.14

Tau_phplusf = ifelse(Tau_phplus.f1<20,Tau_phplus.f1, Tau_phplus.f2)

E_gt1 = 2.5*10^-3*0.14*(Tau_phplusf)^2

E_gt2 = 0.14

Egt = ifelse(Tau_phplus.f1<20, E_gt1, E_gt2)

Eg = Egb + Egt

Qg = Eg*h/lmp_h

U_z = replicate(10000,runif(100,2.91,3.09))

U_h = U_z/(exp(alphaPZ*(z/h-1)))
```

```
L_obs = 0.005

C_B = 0.7

Re_h = (U_h*L_obs)/(kin.vis)

E_B = C_B*(Sc^(-2/3))*(Re_h^(-1/2))

C_IN = 0.7

E_IN = C_IN*(dp/L_obs)

C_IM = 0.191

beta_IM = 0.60

St_h = (Tau*U_h)/L_obs

E_IM = C_IM*(St_h/(St_h+beta_IM))^2

E_T = (U_h/u_star)*(E_B+E_IN+E_IM)+E_t

Q  = LAI*E_T*h/(lmp_h)

etaPZ = (alphaPZ^2/4+Q)^0.5

Vds = u_star*Eg*{(1+Q/Qg-alphaPZ/2)*tanh(etaPZ)/etaPZ}/{(1+Q+alphaPZ/2)*tanh(etaPZ)/etaPZ}

Vd = Vdrift+1/(Ra+1/Vds)

quantile(Vd, c(.05, 0.10, .50, 0.95))


#Dry deposition parameterization by Petroff and Zhang (2010)

#Uncertainty test: Coniferous forest

set.seed(5)

C1 = 0.2789

C2 = 3.115

C3 = 5.145*10^-11

C4 = -1.399

RH = replicate(10000,runif(100,0.76,0.84))

dp_a = 50

dp_i = dp_a*10^-6

rd = dp_i/2

r_w = {(C1*rd^C2)/(C3*rd^C4-log10(RH))+rd^3}^(1/3)
```

```
dp = r_w*2

#Correction factor, C

k_B = 1.38*10^-23

Temp = (273.15+25)

P = 101325

d_air = 3.7208*10^-10

lambda = (k_B*Temp)/(sqrt(2)*3.1416*P*d_air^2)

C = 1+(2*lambda/dp)*(1.257+0.4*exp(-0.55*dp/lambda))

dyn.vis = 1.8908*10^-5

rho = 1500

Tau = (rho*(dp)^2*C)/(18*dyn.vis)

Ws = Tau*9.81

Vphor = 0

Vdrift = Ws+Vphor

# Compute aerodynamic resistance (Ra):

z = 35

L = replicate(10000,runif(100,180,200))

x = z/L

# Compute stability function (shi_H)

shi_H.1 = 2*log(0.5*{1+(1-16*x)^0.5})

shi_H.2 = -5*x

shi_H =ifelse(x <= 0, shi_H.1 , shi_H.2)

zR = 30

z0 = replicate(10000,runif(100,0.9,1.5))

u_star = replicate(10000,runif(100,0.27,0.33))

k_c = 0.41

Ra = (log(zR/z0)-shi_H)/(k_c*u_star)

# Compute surface resistance (Rs)

kin.vis = 1.6834*10^-5
```

```
D = (C*k_B*Temp)/(3*3.1416*dyn.vis*dp)

Sc = (kin.vis/D)

FSc = (Sc^(1/3))/2.9

Egb = (Sc^(-2/3)/14.5)*{1/6*log(1+FSc)^2/(1-FSc+FSc^2)+1/sqrt(3)*atan((2*FSc-1)/sqrt(3))
        +3.1416/6*sqrt(3)}^-1

cd = 1/6

kx = 0.216

LAI = replicate(10000,runif(100,9.5,10.5))

h = replicate(10000,runif(100,14.25,15.75))

d = replicate(10000,runif(100,5.25,8.75))

phi_H.1 = (1-16*x)^(-0.5)

phi_H.2 = 1+5*x

phi_H = ifelse(x<=0, phi_H.1, phi_H.2)

phi_M.1 = (1-16*x)^(-0.25)

phi_M.2 = 1+5*x

phi_M = ifelse(x<=0, phi_M.1, phi_M.2)

lmp = (0.41*(z-d))/(phi_H*(z-d)/abs(L))

lmp_h = (0.41*(h-d))/(phi_M*(h-d)/abs(L))

alphaPZ = {(kx*LAI)/(12*k_c^2*(1-d/h)^2)}^(1/3)*phi_M^(2/3)*{(h-d)/abs(L)}

C_IT = 0

Tau_phplus.1 = (Tau*u_star^2)/kin.vis

Tau_phplus.2 = C_IT

Tau_phplus = ifelse(Tau_phplus.1<20,Tau_phplus.1, Tau_phplus.2)

E_t.1 = 2.5*10^-3*C_IT*(Tau_phplus)^2

E_t.2 = C_IT

E_t = ifelse(Tau_phplus.1<20, E_t.1, E_t.2)

u_starf = u_star*exp(-alphaPZ)

Tau_phplus.f1 = (Tau*u_star^2)/kin.vis

Tau_phplus.f2 = 0.14
```

```
Tau_phplusf = ifelse(Tau_phplus.f1<20,Tau_phplus.f1, Tau_phplus.f2)

E_gt1 = 2.5*10^-3*0.14*(Tau_phplusf)^2

E_gt2 = 0.14

Egt = ifelse(Tau_phplus.f1<20, E_gt1, E_gt2)

Eg = Egb + Egt

# Compute Qg (non-dimensional number)

Qg = Eg*h/lmp_h

# Compute Q

U_z = replicate(10000,runif(100,3.88,4.12))

U_h = U_z/(exp(alphaPZ*(z/h-1)))

#Compute E_B (Brownian diffusion)

L_obs = 0.0015

C_B = 0.887

Re_h = (U_h*L_obs)/(kin.vis)

E_B = C_B*(Sc^(-2/3))*(Re_h^(-1/2))

#Compute E_IN (Interception)

C_IN = 0.810

E_IN = C_IN*(dp/L_obs)

#Compute E_IM (Impaction)

C_IM = 0.162

beta_IM = 0.60

St_h = (Tau*U_h)/L_obs

E_IM = C_IM*(St_h/(St_h+beta_IM))^2

E_T = (U_h/u_star)*(E_B+E_IN+E_IM)+E_t

Q  = LAI*E_T*h/(lmp_h)

# Compute etaPZ

etaPZ = (alphaPZ^2/4+Q)^0.5

Vds = u_star*Eg*{(1+Q/Qg-alphaPZ/2)*tanh(etaPZ)/etaPZ}/{(1+Q+alphaPZ/2)*tanh(etaPZ)/etaPZ}

Vd = Vdrift+1/(Ra+1/Vds)
```

```
quantile(Vd, c(.05, 0.10, .50, 0.95))


#Dry deposition parameterization by Petroff and Zhang (2010)

#Uncertainty test: Deciduous forest

set.seed(5)

C1 = 0.2789

C2 = 3.115

C3 = 5.145*10^-11

C4 = -1.399

RH = replicate(10000,runif(100,0.76,0.84))

dp_a = 2.0

dp_i = dp_a*10^-6

rd = dp_i/2

r_w = {(C1*rd^C2)/(C3*rd^C4-log10(RH))+rd^3}^(1/3)

dp = r_w*2

#Correction factor, C

k_B = 1.38*10^-23

Temp = (273.15+25)

P = 101325

d_air = 3.7208*10^-10

lambda = (k_B*Temp)/(sqrt(2)*3.1416*P*d_air^2)

C = 1+(2*lambda/dp)*(1.257+0.4*exp(-0.55*dp/lambda))

dyn.vis = 1.8908*10^-5

rho = 1500

Tau = (rho*(dp)^2*C)/(18*dyn.vis)

Ws = Tau*9.81

Vphor = 0

Vdrift = Ws+Vphor

# Compute aerodynamic resistance (Ra):
```

```
z = 35

L = replicate(10000,runif(100,45,55))

x = z/L

# Compute stability function (shi_H)

shi_H.1 = 2*log(0.5*{1+(1-16*x)^0.5})

shi_H.2 = -5*x

shi_H =ifelse(x <= 0, shi_H.1 , shi_H.2)

zR = 50

z0 = replicate(10000,runif(100,1.125, 1.875))

u_star = replicate(10000,runif(100,0.54,0.66))

k_c = 0.41

Ra = (log(zR/z0)-shi_H)/(k_c*u_star)

# Compute surface resistance (Rs)

kin.vis = 1.6834*10^-5

D = (C*k_B*Temp)/(3*3.1416*dyn.vis*dp)

Sc = (kin.vis/D)

FSc = (Sc^(1/3))/2.9

Egb = (Sc^(-2/3)/14.5)*{1/6*log(1+FSc)^2/(1-FSc+FSc^2)+1/sqrt(3)*atan((2*FSc-1)/sqrt(3))
        +3.1416/6*sqrt(3)}^-1

cd = 1/6

kx = 0.216

LAI = replicate(10000,runif(100,9.5,10.5))

h = replicate(10000,runif(100,23.75,26.25))

d = replicate(10000,runif(100,12,20))

phi_H.1 = (1-16*x)^(-0.5)

phi_H.2 = 1+5*x

phi_H = ifelse(x<=0, phi_H.1, phi_H.2)

phi_M.1 = (1-16*x)^(-0.25)

phi_M.2 = 1+5*x
```

```
phi_M = ifelse(x<=0, phi_M.1, phi_M.2)

lmp = (0.41*(z-d))/(phi_H*(z-d)/abs(L))

lmp_h = (0.41*(h-d))/(phi_M*(h-d)/abs(L))

alphaPZ = {(kx*LAI)/(12*k_c^2*(1-d/h)^2)}^(1/3)*phi_M^(2/3)*{(h-d)/abs(L)}

C_IT = 0.056

Tau_phplus.1 = (Tau*u_star^2)/kin.vis

Tau_phplus.2 = C_IT

Tau_phplus = ifelse(Tau_phplus.1<20,Tau_phplus.1, Tau_phplus.2)

E_t.1 = 2.5*10^-3*C_IT*(Tau_phplus)^2

E_t.2 = C_IT

E_t = ifelse(Tau_phplus.1<20, E_t.1, E_t.2)

u_starf = u_star*exp(-alphaPZ)

Tau_phplus.f1 = (Tau*u_star^2)/kin.vis

Tau_phplus.f2 = 0.14

Tau_phplusf = ifelse(Tau_phplus.f1<20,Tau_phplus.f1, Tau_phplus.f2)

E_gt1 = 2.5*10^-3*0.14*(Tau_phplusf)^2

E_gt2 = 0.14

Egt = ifelse(Tau_phplus.f1<20, E_gt1, E_gt2)

Eg = Egb + Egt

# Compute Qg (non-dimensional number)

Qg = Eg*h/lmp_h

U_z = replicate(10000,runif(100,3.88,4.12))

U_h = U_z/(exp(alphaPZ*(z/h-1)))

#Compute E_B (Brownian diffusion)

L_obs = 0.03

C_B = 1.262

Re_h = (U_h*L_obs)/(kin.vis)

E_B = C_B*(Sc^(-2/3))*(Re_h^(-1/2))

#Compute E_IN (Interception)
```

```
C_IN = 0.216

E_IN = C_IN*(dp/L_obs)*(2+log(4*L_obs/dp))

#Compute E_IM (Impaction)

C_IM = 0.130

beta_IM = 0.47

St_h = (Tau*U_h)/L_obs

E_IM = C_IM*(St_h/(St_h+beta_IM))^2

E_T = (U_h/u_star)*(E_B+E_IN+E_IM)+E_t

Q  = LAI*E_T*h/(lmp_h)

# Compute etaPZ

etaPZ = (alphaPZ^2/4+Q)^0.5

Vds = u_star*Eg*{(1+Q/Qg-alphaPZ/2)*tanh(etaPZ)/etaPZ}/{(1+Q+alphaPZ/2)*tanh(etaPZ)/etaPZ}

Vd = Vdrift+1/(Ra+1/Vds)

quantile(Vd, c(.05, 0.10, .50, 0.95))


#Dry deposition parameterization by Petroff and Zhang (2010)

#Uncertainty test: Water

set.seed(5)

C1 = 0.2789

C2 = 3.115

C3 = 5.415*10^-11

C4 = -1.399

RH = replicate(10000,runif(100,0.76,0.84))

dp_i = 2.0

dp_d = dp_i*10^-6

rd = dp_d/2

r_w = {(C1*rd^C2)/(C3*rd^C4-log10(RH))+rd^3}^(1/3)

dp = r_w*2

k_B = 1.38*10^-23
```

```
Temp = 273.15+25

P = 101325

d_air = 3.7208*10^-10

lambda = (k_B*Temp)/(sqrt(2)*3.1416*P*d_air^2)

C = 1+(2*lambda/dp)*(1.257+0.4*exp(-0.55*dp/lambda))

dyn.vis = ((5*10^-8)*Temp)+4*10^-6

rho = 1500

Tau = (rho*(dp)^2*C)/(18*dyn.vis)

Ws = Tau*9.81

Vphor = (5*10^-3)/100

Vdrift = Ws+Vphor

# Compute aerodynamic resistance (Ra):

z = 8/100

L = replicate(10000,runif(100,45,55))

x = z/L

# Compute stability function (shi_H)

shi_H.1 = 2*log(0.5*{1+(1-16*x)^0.5})

shi_H.2 = -5*x

shi_H = ifelse(x <= 0, shi_H.1 , shi_H.2)

zR = 5

u_star = replicate(10000,runif(100,0.27,0.33))

z0_1 = 0.021*(u_star)^3.32

z0_2 = 0.00098*(u_star)^1.65

z0 = ifelse(u_star<= 0.16, z0_1, z0_2)

k_c = 0.41

Ra = (log(zR/z0)-shi_H)/(k_c*u_star)

# Compute surface resistance (Rs)

kin.vis = ((9*10^-8)*Temp)+10^-5

D = (C*k_B*Temp)/(3*3.1416*dyn.vis*dp)
```

```
Sc = (kin.vis/D)

FSc = (Sc^(1/3))/2.9

Egb = (Sc^(-2/3)/14.5)*{1/6*log(1+FSc)^2/(1-FSc+FSc^2)+1/sqrt(3)*atan((2*FSc-
1)/sqrt(3))+3.1416/6*sqrt(3)}^-1

Eg = Egb

Vd = Vdrift+1/(Ra+(1/(Eg*u_star)))

quantile(Vd, c(.05, 0.10, .50, 0.95))



#Dry deposition parameterization by Petroff and Zhang (2010)

#Uncertainty test: Ice/snow

set.seed(5)

C1 = 0.2789

C2 = 3.115

C3 = 5.415*10^-11

C4 = -1.399

RH = replicate(10000,runif(100,0.76,0.84))

dp_i = 2.0

dp_d = dp_i*10^-6

rd = dp_d/2

r_w = {(C1*rd^C2)/(C3*rd^C4-log10(RH))+rd^3}^(1/3)

dp = r_w*2

#Correction factor, C

k_B = 1.38*10^-23

Temp = 273.15+0

P = 101325

d_air = 3.7208*10^-10

lambda = (k_B*Temp)/(sqrt(2)*3.1416*P*d_air^2)

C = 1+(2*lambda/dp)*(1.257+0.4*exp(-0.55*dp/lambda))

dyn.vis = ((5*10^-8)*Temp)+4*10^-6
```

```
rho = 1500

Tau = (rho*(dp)^2*C)/(18*dyn.vis)

Ws = Tau*9.81

Vphor = (2*10^-4)/100

Vdrift = Ws+Vphor

# Compute aerodynamic resistance (Ra)

z = 5

L = replicate(10000,runif(100,45,55))

x = z/L

# Compute stability function (shi_H)

shi_H.1 = 2*log(0.5*{1+(1-16*x)^0.5})

shi_H.2 = -5*x

shi_H = ifelse(x <= 0, shi_H.1 , shi_H.2)

zR = 10

u_star = replicate(10000,runif(100,0.27,0.33))

z0 = replicate(10000,runif(100,0.0075,0.0125))

k_c = 0.41

Ra = (log(zR/z0)-shi_H)/(k_c*u_star)

# Compute surface resistance (Rs)

kin.vis = ((9*10^-8)*Temp)+10^-5

D = (C*k_B*Temp)/(3*3.1416*dyn.vis*dp)

Sc = (kin.vis/D)

FSc = (Sc^(1/3))/2.9

Egb = (Sc^(-2/3)/14.5)*{1/6*log(1+FSc)^2/(1-FSc+FSc^2)+1/sqrt(3)*atan((2*FSc-
1)/sqrt(3))+3.1416/6*sqrt(3)}^-1

Eg = Egb

Vd = Vdrift+1/(Ra+(1/(Eg*u_star)))

quantile(Vd, c(.05, 0.10, .50, 0.95))
```

Codes for Monte Carlo uncertainty evaluation for Kouznetsov and Sofiev (2012) parameterization

```
#Dry deposition parameterization by Kouznetsov and Sofiev (2012)

#Uncertainty test: Grass

set.seed(5)

C1 = 0.2789

C2 = 3.115

C3 = 5.145*10^-11

C4 = -1.399

RH = replicate(10000,runif(100,0.76,0.84))

dp_a =2.0

dp_i = dp_a*10^-6

rd = dp_i/2

r_w = {(C1*rd^C2)/(C3*rd^C4-log10(RH))+rd^3}^(1/3)

dp = r_w*2

#Correction factor, C

k_B = 1.38*10^-23

Temp = (273.15+25)

P = 101325

d_air = 3.7208*10^-10

lambda = (k_B*Temp)/(sqrt(2)*3.1416*P*d_air^2)

C = 1+(2*lambda/dp)*(1.257+0.4*exp(-0.55*dp/lambda))

dyn.vis = 1.89*10^-5

rho = 1500

Tau = (rho*(dp)^2*C)/(18*dyn.vis)

V_s = Tau*9.81

u_star = replicate(10000,runif(100,0.27,0.33))

a  = 2*10^-3

kin.vis = 1.68*10^-5

D = (C*k_B*Temp)/(3*3.1416*dyn.vis*dp)
```

```
Sc = (kin.vis/D)

Re_star = (u_star*a)/kin.vis

# Compute V_diff (velocity for diffusion)

V_diff = 2*(Re_star^(-0.5))*Sc^(-2/3)

# Compute V_int (velocity for interception)

V_int = 80*u_star*((dp/a)^2)*(Re_star^(0.5))

# Compute V_imp

C_S = 0.003

C_R = 0.3

LAI = replicate(10000,runif(100,3.8,4.2))

CsCR = (C_S+C_R/LAI)^0.5

u.Uh = 0.3

u_star.by.U_h = min(u.Uh, CsCR)

#Compute Re_c

Re_c = ((u_star.by.U_h)^-1)^2*Re_star

# Calculate St

St = (Tau*u_star)/a

# Calculate St_e

St_e = St - Re_c^(-0.5)

eta_impSt.e1 = exp((-0.1/(St_e - 0.15 ) )-(1/sqrt(St_e -0.15)))

eta_impSt.e2 = 0

eta_impSt.e = ifelse(St_e>0.15,eta_impSt.e1,eta_impSt.e2)

V_imp = ((2*u_star.by.U_h)/u_star)*eta_impSt.e*(St-u_star.by.U_h*Re_star^-0.5)

# Dry deposition velocity

Vd = V_diff+V_int+V_imp+V_s

quantile(Vd, c(.05, 0.10, .50, 0.95))


#Dry deposition parameterization by Kouznetsov and Sofiev (2012)

#Uncertainty test: Coniferous forest
```

```
set.seed(5)

C1 = 0.2789

C2 = 3.115

C3 = 5.145*10^-11

C4 = -1.399

RH = replicate(10000,runif(100,0.76,0.84))

dp_a = 2.0

dp_i = dp_a*10^-6

rd = dp_i/2

r_w = {(C1*rd^C2)/(C3*rd^C4-log10(RH))+rd^3}^(1/3)

dp = r_w*2

#Correction factor, C

k_B = 1.38*10^-23

Temp =  273.15+25

P = 101325

d_air = 3.7208*10^-10

lambda = (k_B*Temp)/(sqrt(2)*3.1416*P*d_air^2)

C = 1+(2*lambda/dp)*(1.257+0.4*exp(-0.55*dp/lambda))

dyn.vis = 1.891*10^-5

rho = 1500

Tau = (rho*(dp)^2*C)/(18*dyn.vis)

V_s = Tau*9.81

u_star = replicate(10000,runif(100,0.27,0.33))

a  =  0.7*10^-3

kin.vis = 1.683*10^-5

D = (C*k_B*Temp)/(3*3.1416*dyn.vis*dp)

Sc = (kin.vis/D)

Re_star = (u_star*a)/kin.vis

# Compute V_diff (velocity for diffusion)
```

```
V_diff = 2*(Re_star^(-0.5))*Sc^(-2/3)

# Compute V_int (velocity for interception)

V_int = 80*u_star*((dp/a)^2)*(Re_star^(0.5))

# Compute V_imp

C_S = 0.003

C_R = 0.3

LAI = replicate(10000,runif(100,5.7,6.3))

CsCR = (C_S+C_R/LAI)^0.5

u.Uh = 0.3

u_star.by.U_h = min(u.Uh, CsCR)

#Compute Re_c

Re_c = ((u_star.by.U_h)^-1)^2*Re_star

# Calculate St

St = (Tau*u_star)/a

# Calculate St_e

St_e = St - Re_c^(-0.5)

eta_impSt.e1 = exp((-0.1/(St_e - 0.15 ) )-(1/sqrt(St_e -0.15)))

eta_impSt.e2 = 0

eta_impSt.e = ifelse(St_e>0.15,eta_impSt.e1,eta_impSt.e2)

V_imp = ((2*u_star.by.U_h)/u_star)*eta_impSt.e*(St-u_star.by.U_h*Re_star^-0.5)

# Dry deposition velocity

Vd = V_diff+V_int+V_imp+V_s

quantile(Vd, c(.05, 0.10, .50, 0.95))


#Dry deposition parameterization by Kouznetsov and Sofiev (2012)

#Uncertainty test: Deciduous forest

set.seed(5)

C1 = 0.2789

C2 = 3.115
```

```
C3 = 5.145*10^-11

C4 = -1.399

RH = replicate(10000,runif(100,0.76,0.84))

dp_a = 2.0

dp_i = dp_a*10^-6

rd = dp_i/2

r_w = {(C1*rd^C2)/(C3*rd^C4-log10(RH))+rd^3}^(1/3)

dp = r_w*2

#Correction factor, C

k_B = 1.38*10^-23

Temp = (273.15+25)

P = 101325

d_air = 3.7208*10^-10

lambda = (k_B*Temp)/(sqrt(2)*3.1416*P*d_air^2)

C = 1+(2*lambda/dp)*(1.257+0.4*exp(-0.55*dp/lambda))

dyn.vis = 1.89*10^-5

rho = 1500

Tau = (rho*(dp)^2*C)/(18*dyn.vis)

V_s = Tau*9.81

u_star = replicate(10000,runif(100,0.27,0.33))

a  = 7*10^-3

kin.vis = 1.68*10^-5

D = (C*k_B*Temp)/(3*3.1416*dyn.vis*dp)

Sc = (kin.vis/D)

Re_star = (u_star*a)/kin.vis

# Compute V_diff (velocity for diffusion)

V_diff = 2*(Re_star^(-0.5))*Sc^(-2/3)

# Compute V_int (velocity for interception)

V_int = 80*u_star*((dp/a)^2)*(Re_star^(0.5))
```

```
# Compute V_imp

C_S = 0.003

C_R = 0.3

LAI = replicate(10000,runif(100,9.5,10.5))

CsCR = (C_S+C_R/LAI)^0.5

u.Uh = 0.3

u_star.by.U_h = min(u.Uh, CsCR)

#Compute Re_c

Re_c = ((u_star.by.U_h)^-1)^2*Re_star

# Calculate St

St = (Tau*u_star)/a

# Calculate St_e

St_e = St - Re_c^(-0.5)

eta_impSt.e1 = exp((-0.1/(St_e - 0.15 ) )-(1/sqrt(St_e -0.15)))

eta_impSt.e2 = 0

eta_impSt.e = ifelse(St_e>0.15,eta_impSt.e1,eta_impSt.e2)

V_imp = ((2*u_star.by.U_h)/u_star)*eta_impSt.e*(St-u_star.by.U_h*Re_star^-0.5)

# Dry deposition velocity

Vd = V_diff+V_int+V_imp+V_s

quantile(Vd, c(.05, 0.10, .50, 0.95))


#Dry deposition parameterization by Kouznetsov and Sofiev (2012)

#Uncertainty test: Smooth surface (water)

set.seed(5)

C1 = 0.2789

C2 = 3.115

C3 = 5.415*10^-11

C4 = -1.399

dp_i = 0.5
```

```
dp = dp_i*10^-6

rho = 1500

RH = replicate(10000,runif(100,0.76,0.84))

Temp = 25+273.15

u_star = replicate(10000,runif(100,0.27,0.33))

z0_1 = 0.021*(u_star)^3.32

z0_2 = 0.00098*(u_star)^1.65

z0 = ifelse(u_star<= 0.16, z0_1, z0_2)

L = replicate(10000,runif(100,45,55))

kin.vis = ((9*10^-8)*Temp)+10^-5

dyn.vis = ((5*10^-8)*Temp)+4*10^-6

d_air = 3.7208*10^-10

k_B = 1.38*10^-23

P = 101325

lambda = (k_B*Temp)/(sqrt(2)*3.1416*P*d_air^2)

C = 1+((2*lambda/dp)*(1.257+0.4*exp(-0.55*dp/lambda)))

tau_p = (rho*(dp)^2*C)/(18*dyn.vis)

D = (C*k_B*Temp)/(3*3.1416*dyn.vis*dp)

v_s = 9.81*tau_p

taup = (tau_p*u_star^2)/(kin.vis)

Sc = (kin.vis/D)

vsplus = v_s/u_star

rplus = (dp*u_star)/(2*kin.vis)

R_s = 0

Rsplus = u_star*R_s

z_meas = 8/100

zpmax = (z_meas*u_star)/(kin.vis)

MOplus = (kin.vis)/(u_star*L)

#Fixed parameters
```

```
Zbuf = 3

Ztf = 18                              #turbophoretic sublayer height

taultf = 5                            #Lagrangian time in turbophoretic layer

Nutp_Ztf= (0.4*(Ztf)^3)/(Ztf^2+200)  #Dimensionless eddy viscosity of air

It_Ztf = (2.5*log10(Ztf ))-(100/Ztf^2)

It_Zbuf = (2.5*log10(Zbuf))-(100/Zbuf^2)

S = Sc^(1/3)

Zl = 20/S

fTmp = 2.5/Sc

fTmp1 = (fTmp^3/27+(fTmp*(100+5*sqrt(8*fTmp/27)+400)))^(1/3)

Zl_1 = fTmp1+((fTmp*fTmp)/(9*fTmp1))+(1/3)*fTmp

fTmp_1 = (Zl_1^2)/(Zl_1^2+200)

fTmp_2 = 1.2*(fTmp_1)-0.8*fTmp_1^2

fTmp1_1 = 1/(Sc*fTmp_2)

fTmp_3 = 1/Sc

x_1 = Zl_1 - fTmp1_1

x_2 = Zl_1

x_3 = Zl_1+fTmp1_1

Nutp_x_1 = (0.4*x_1^3)/(x_1^2+200)

Nutp_x_2 = (0.4*x_2^3)/(x_2^2+200)

Nutp_x_3 = (0.4*x_3^3)/(x_3^2+200)

fIvd = Rsplus+(Zl_1-fTmp1_1)*Sc+0.3333*fTmp1_1*(1/fTmp_3+((0.4*x_1^3)/(x_1^2+200)))+

4/(fTmp_3+((0.4*x_2^3)/(x_2^2+200)))+1/(fTmp_3+((0.4*x_3^3)/(x_3^2+200)))

x_4 = zpmax

x_5 = Zl_1 + fTmp1_1

It_x_4 = 2.5*log10(x_4) - 100/(x_4^2)

It_x_5 = 2.5*log10(x_5) - 100/(x_5^2)

#Now calculate fu_Psi(zpmax*MOplus)

s = 2.35*(zpmax*MOplus+abs(zpmax*MOplus))
```

```
u1 = 0.5*(abs(zpmax*MOplus)-zpmax*MOplus)

u = -4*u1/(2.65*sqrt(u1*sqrt(u1))+1)

fu_Psi = s+u

fTmp_4 = It_x_4 - It_x_5 + 2.5*fu_Psi

fIvd_1 = fIvd+0.5*(fTmp_4+abs(fTmp_4))

fu_vdplus_smooth_1 = 1/fIvd_1

Il_input1= Zl*S/7.92

Il_input2= rplus*S/7.92

Il_1 = -0.16667*log10(Il_input1^2-Il_input1+1)+0.57735*atan((2*Il_input1-1)*0.57735)+

0.3333*log10(Il_input1+1)

Il_2 = -0.16667*log10(Il_input2^2-Il_input2+1)+0.57735*atan((2*Il_input2-1)*0.57735)+

0.3333*log10(Il_input2+1)

R = 7.92*S^2*(Il_1-Il_2)

R_1 = 0.5*(R+abs(R))

Zl_2 = 0.5*(rplus+Zl+abs(rplus-Zl))

It_Zbuf = 2.5*log10(Zbuf) - (100/(Zbuf^2))

It_Zl_2 = 2.5*log10(Zl_2) - (100/(Zl_2^2))

R1 = It_Zbuf - It_Zl_2

R_2 = R_1+0.5*(R1+abs(R1))

fTmp_5 = vsplus*R_2

fTmp_6 = exp(-fTmp_5)

fIvd_2  = Rsplus*fTmp_6+(1-fTmp_6)/vsplus

fIvd_3 = Rsplus+R_2

fIvd_23 = ifelse(abs(fTmp_5)>0.001, fIvd_2, fIvd_3 )

V  = 0.81*taup/(Ztf-Zbuf)/(1+taup/taultf) + vsplus   #chcek for sign of vsplus

It_Ztf = 2.5*log10(Ztf) - 100/(Ztf^2)

R_3  = ((It_Ztf)-(It_Zbuf))*(1+taup/taultf)

fTmp_7 = V*R_3

fTmp_8 = exp(-fTmp_7)
```

```
fIvd_4 = (fIvd_23*fTmp_8)+(1-fTmp_8)/V

fIvd_5 = fIvd_3+R_3

fIvd_45 = ifelse(abs(fTmp_7)>0.001, fIvd_4, fIvd_5)

#Now calculations for the Lagrangian turbophoretic layer

Ztf2 = 2*taup

V_1 = 0.4+vsplus

R_4 = 0.1667*((1+taup/(0.5*Ztf))/(Nutp_Ztf)+4*(1+taup/(0.25*(Ztf+Ztf2)))/

((0.4*(0.5*(Ztf+Ztf2))^3)/((0.5*(Ztf+Ztf2))^2+200))+(1+taup/(0.5*Ztf2))/

((0.4*Ztf2 ^3)/(Ztf2^2+200)))*(Ztf2-Ztf)

fTmp_9 = V_1*R_4

fTmp_10 = exp(-fTmp_9)

fIvd_6 = fIvd_45*fTmp_10 + (1-fTmp_10)/V_1

fIvd_7 = fIvd_45+R_3

fIvd_67 = ifelse(abs(fTmp_9) > 0.001, fIvd_6, fIvd_7)

Ztf2_2 = Ztf

fIvd67_Ztf2 = ifelse(Ztf2>Ztf, fIvd_67, Ztf2_2)

#Following calculations are for aerodynamic layer

It_zpmax = 2.5*log10(zpmax) - 100/(zpmax^2)

Ztf22 = ifelse(Ztf2>Ztf, Ztf2, Ztf2_2)

It_Ztf22  = 2.5*log10(Ztf22) - 100/(Ztf22^2)

R_5 = It_zpmax - It_Ztf22  + 2.5*fu_Psi

R_6 = 0.5*(R_5+abs(R_5))

fTmp_11  = vsplus*R_6

fTmp_12 = exp(-fTmp_11)

fIvd_4567 = ifelse(Ztf2>Ztf, fIvd_67,fIvd_45)

fIvd_8 = (fIvd_4567* fTmp_12)+(1-fTmp_12)/vsplus

fIvd_9 = fIvd_4567 + R_6

fIvd_10 = ifelse(abs(fTmp_11) > 0.001, fIvd_8, fIvd_9)

fu_vdplus_smooth_3 = 1/fIvd_10
```

```
fu_vdplus_smooth = ifelse(Zl>Zbuf, fu_vdplus_smooth_1, fu_vdplus_smooth_3)

Vd_smooth = fu_vdplus_smooth*u_star

quantile(Vd_smooth, c(.05, 0.10, .50, 0.95))


#Dry deposition parameterization by Kouznetsov and Sofiev (2012)

#Uncertainty test: Ice/snow

set.seed(5)

C1 = 0.2789

C2 = 3.115

C3 = 5.415*10^-11

C4 = -1.399

RH = replicate(10000,runif(100,0.76,0.84))

dp_a = 2.0

dp_i = dp_a*10^-6

rd = dp_i/2

r_w = {(C1*rd^C2)/(C3*rd^C4-log10(RH))+rd^3}^(1/3)

dp = r_w*2

#Correction factor, C

k_B = 1.38*10^-23

Temp = 273.15+0

P = 101325

d_air = 3.7208*10^-10

lambda = (k_B*Temp)/(sqrt(2)*3.1416*P*d_air^2)

C = 1+(2*lambda/dp)*(1.257+0.4*exp(-0.55*dp/lambda))

dyn.vis = ((5*10^-8)*Temp)+4*10^-6

rho =  1500

Tau = (rho*(dp)^2*C)/(18*dyn.vis)

V_s = Tau*9.81

# Need to compute Sc, Re_star
```

```
u_star = replicate(10000,runif(100,0.27,0.33))

#u_star = replicate(10000,runif(100,0.27,0.33))

a  =  0.5*10^-3

kin.vis = ((9*10^-8)*Temp)+10^-5

D = (C*k_B*Temp)/(3*3.1416*dyn.vis*dp)

Sc = (kin.vis/D)

Re_star = (u_star*a)/kin.vis

# Compute V_diff (velocity for diffusion)

V_diff = 2*(Re_star^(-0.5))*Sc^(-2/3)

# Compute V_int (velocity for interception)

V_int = 80*u_star*((dp/a)^2)*(Re_star^(0.5))

# Compute V_imp

C_S = 0.003

C_R = 0.3

LAI = 0

CsCR = (C_S+C_R/LAI)^0.5

u.Uh = 0.3

u_star.by.U_h = min(u.Uh, CsCR)

#Compute Re_c

Re_c = ((u_star.by.U_h)^-1)^2*Re_star

# Calculate St

St = (Tau*u_star)/a

# Calculate St_e

St_e = St - Re_c^(-0.5)

eta_impSt.e1 = exp((-0.1/(St_e - 0.15 ) )-(1/sqrt(St_e -0.15)))

eta_impSt.e2 = 0

eta_impSt.e = ifelse(St_e>0.15,eta_impSt.e1,eta_impSt.e2)

V_imp = (2*u_star.by.U_h*eta_impSt.e*(St-(u_star.by.U_h*Re_star^-0.5)))*u_star

# Dry deposition velocity
```

```
Vd = V_diff+V_int+V_imp+V_s

quantile(Vd, c(.05, 0.10, .50, 0.95))
```

Codes for Monte Carlo uncertainty evaluation for Zhang and He (2014) parameterization

```
#Dry deposition parameterization by Zhang and He (2014)

#Uncertainty test: Grass

set.seed(5)

C1 = 0.2789

C2 = 3.115

C3 = 5.145*10^-11

C4 = -1.399

RH = replicate(10000,runif(100,0.76,0.84))

dp_a = 2.0

dp_i = dp_a*10^-6

rd = dp_i/2

r_w = {(C1*rd^C2)/(C3*rd^C4-log10(RH))+rd^3}^(1/3)

dp = r_w*2

#Correction factor, C

k_B = 1.38*10^-23

Temp = (273.15+25)

P = 101325

d_air = 3.7208*10^-10

lambda = (k_B*Temp)/(sqrt(2)*3.1416*P*d_air^2)

C = 1+(2*lambda/dp)*(1.257+0.4*exp(-0.55*dp/lambda))

dyn.vis = 1.89*10^-5

rho = 1500

Tau = (rho*(dp)^2*C)/(18*dyn.vis)

V_g = Tau*9.81

Rg = 1/V_g
```

```
u_star = replicate(10000,runif(100,0.27,0.33))

a1 = 5.4*10^-3

z = 5

L = replicate(10000,runif(100,45,55))

x = z/L

# Compute stability function (shi_H)

shi_H.1 = 2*log(0.5*{1+(1-16*x)^0.5})

shi_H.2 = -5*x

shi_H =ifelse(x <= 0, shi_H.1 , shi_H.2)

zR = 3.5

z0 = replicate(10000,runif(100,0.03,0.05))

k_c = 0.41

Ra = (log(zR/z0)-shi_H)/(k_c*u_star)

# Calculate Vds = 1/Rs

# For PM2.5

Vds_PM2.5 = (a1*u_star)

Rds_PM2.5 = (1/Vds_PM2.5)

#For PM2.5-10

#b1=

#b2=

#b3 =

#c1=

#c2 =

#c3 =

#k = c1*u_star+c2*u_star^2+c3*u_star^3

#LAI = replicate(10000,runif(100,3.8,4.2))

#LAImax =

#Vds_PM10 = (b1*u_star+b2*u_star^2+b3*u_star^3)*exp(k*(LAI/LAImax)-1)

#Vds_PM10 = (b1*u_star+b2*u_star^2+b3*u_star^3)
```

```
#Rds_PM10 = 1/Vds_PM10

# For PM10+

#d1=

#d2=

#d3 =

#f1=

#f2 =

#f3 =

#k = f1*u_star+f2*u_star^2+f3*u_star^3

#LAI =

#LAImax =

#Vds_10plus = (d1*u_star+d2*u_star^2+d3*u_star^3)*exp(k*(LAI/LAImax)-1)

#Vds_10plus = (d1*u_star+d2*u_star^2+d3*u_star^3)

#Rds_PM2.5 = (1/Vds_PM2.5)

#Compute Vd

Vd = 1/Rg+(1/(Ra+Rds_PM2.5))

quantile(Vd, c(.05, 0.10, .50, 0.95))


#Dry deposition parameterization by Zhang and He (2014)

#Uncertainty test: Coniferous forest

set.seed(5)

C1 = 0.2789

C2 = 3.115

C3 = 5.145*10^-11

C4 = -1.399

RH = replicate(10000,runif(100,0.76,0.84))

dp_a = 2.0

dp_i = dp_a*10^-6

rd = dp_i/2
```

```
r_w = {(C1*rd^C2)/(C3*rd^C4-log10(RH))+rd^3}^(1/3)

dp = r_w*2

#Correction factor, C

k_B = 1.38*10^-23

Temp = (273.15+25)

P = 101325

d_air = 3.7208*10^-10

lambda = (k_B*Temp)/(sqrt(2)*3.1416*P*d_air^2)

C = 1+(2*lambda/dp)*(1.257+0.4*exp(-0.55*dp/lambda))

dyn.vis = 1.89*10^-5

rho = 1500

Tau = (rho*(dp)^2*C)/(18*dyn.vis)

V_g = Tau*9.81

Rg = 1/V_g

u_star = replicate(10000,runif(100,0.27,0.33))

a1 = 4.3*10^-3

z = 35

L = replicate(10000,runif(100,45,55))

x = z/L

# Compute stability function (shi_H)

shi_H.1 = 2*log(0.5*{1+(1-16*x)^0.5})

shi_H.2 = -5*x

shi_H =ifelse(x <= 0, shi_H.1 , shi_H.2)

zR = 30

z0 = replicate(10000,runif(100,0.9,1.5))

k_c = 0.41

Ra = (log(zR/z0)-shi_H)/(k_c*u_star)

# Calculate Vds = 1/Rs

# For PM2.5
```

```
Vds_PM2.5 = (a1*u_star)

Rds_PM2.5 = (1/Vds_PM2.5)

#For PM2.5-10

#b1=

#b2=

#b3 =

#c1=

#c2 =

#c3 =

#k = c1*u_star+c2*u_star^2+c3*u_star^3

#LAI =

#LAImax =

#Vds_PM10 =
(b1*u_star+b2*u_star^2+b3*u_star^3)*exp(k*(LAI/LAImax)-
1)

#Vds_PM10 = (b1*u_star+b2*u_star^2+b3*u_star^3)

#Rds_PM10 = 1/Vds_PM10

# For PM10+

#d1=

#d2=

#d3 =

#f1=

#f2 =

#f3 =

#k = f1*u_star+f2*u_star^2+f3*u_star^3

#LAI =

#LAImax =

#Vds_10plus =
(d1*u_star+d2*u_star^2+d3*u_star^3)*exp(k*(LAI/LAImax)-
1)

#Vds_10plus = (d1*u_star+d2*u_star^2+d3*u_star^3)
```

```
Rds_PM10plus = (1/Vds_PM2.5)

#Compute Vd

Vd = 1/Rg+(1/(Ra+Rds_PM2.5))

quantile(Vd, c(.05, 0.10, .50, 0.95))


#Dry deposition parameterization by Zhang and He (2014)

#Uncertainty test: Deciduous forest

set.seed(5)

C1 = 0.2789

C2 = 3.115

C3 = 5.145*10^-11

C4 = -1.399

RH = replicate(10000,runif(100,0.76,0.84))

dp_a = 2.0

dp_i = dp_a*10^-6

rd = dp_i/2

r_w = {(C1*rd^C2)/(C3*rd^C4-log10(RH))+rd^3}^(1/3)

dp = r_w*2

#Correction factor, C

k_B = 1.38*10^-23

Temp = (273.15+25)

P = 101325

d_air = 3.7208*10^-10

lambda = (k_B*Temp)/(sqrt(2)*3.1416*P*d_air^2)

C = 1+(2*lambda/dp)*(1.257+0.4*exp(-0.55*dp/lambda))

dyn.vis = 1.89*10^-5

rho = 1500

Tau = (rho*(dp)^2*C)/(18*dyn.vis)

V_g = Tau*9.81 # m/s
```

```
Rg = 1/V_g

u_star = replicate(10000,runif(100,0.54,0.66))

a1 = 4.3*10^-3

z = 35

L = replicate(10000,runif(100,45,55))

x = z/L

# Compute stability function (shi_H)

shi_H.1 = 2*log(0.5*{1+(1-16*x)^0.5})

shi_H.2 = -5*x

shi_H =ifelse(x <= 0, shi_H.1 , shi_H.2)

zR = 50

z0 = replicate(10000,runif(100,1.125, 1.875))

k_c = 0.41

Ra = (log(zR/z0)-shi_H)/(k_c*u_star)

#Calculate Vds = 1/Rs

# For PM2.5

Vds_PM2.5 = (a1*u_star)

Rds_PM2.5 = (1/Vds_PM2.5)

# For PM2.5-10

#b1=

#b2=

#b3 =

#c1=

#c2 =

#c3 =

#k = c1*u_star+c2*u_star^2+c3*u_star^3

#LAI =

#LAImax =
```

```
#Vds_PM10 =
(b1*u_star+b2*u_star^2+b3*u_star^3)*exp(k*(LAI/LAImax)-
1)

#Rds_PM10 = 1/Vds_PM10

# For PM10+

#d1= -2.2

#d2= 3.9*10^1

#d3 = -6.7

#f1= 6.2

#f2 = -1.2*10^1

#f3 = 6.1

#k = f1*u_star+f2*u_star^2+f3*u_star^3

#LAI =

#LAImax =

#Vds_10plus =
(d1*u_star+d2*u_star^2+d3*u_star^3)*exp(k*(LAI/LAImax)-
1)

#Rds_10plus = (1/Vds_10plus)

#Compute Vd

Vd = 1/Rg+(1/(Ra+Rds_PM2.5))

quantile(Vd, c(.05, 0.10, .50, 0.95))



#Dry deposition parameterization by Zhang and He (2014)

#Uncertainty test: Water

set.seed(5)

C1 = 0.2789

C2 = 3.115

C3 = 5.415*10^-11

C4 = -1.399

RH = replicate(10000,runif(100,0.76,0.84))

dp_a =2.0
```

```
dp_i = dp_a*10^-6

rd = dp_i/2

r_w = {(C1*rd^C2)/(C3*rd^C4-log10(RH))+rd^3}^(1/3)

dp = r_w*2

#Correction factor, C

k_B = 1.38*10^-23

Temp = 273.15+25

P = 101325

d_air = 3.7208*10^-10

lambda = (k_B*Temp)/(sqrt(2)*3.1416*P*d_air^2)

C = 1+(2*lambda/dp)*(1.257+0.4*exp(-0.55*dp/lambda))

dyn.vis = ((5*10^-8)*Temp)+4*10^-6

rho = 1500

Tau = (rho*(dp)^2*C)/(18*dyn.vis)

V_g = Tau*9.81

Rg = 1/V_g

a1 = 6.9*10^-3

z = 8/100

L = replicate(10000,runif(100,45,55))

x = z/L

# Compute stability function (shi_H)

shi_H.1 = 2*log(0.5*{1+(1-16*x)^0.5})

shi_H.2 = -5*x

shi_H =ifelse(x <= 0, shi_H.1 , shi_H.2)

zR = 5

u_star = replicate(10000,runif(100,0.27,0.33))

z0_1 = 0.021*(u_star)^3.32

z0_2 = 0.00098*(u_star)^1.65

z0 = ifelse(u_star<= 0.16, z0_1, z0_2)
```

```
k_c = 0.41

Ra = (log(zR/z0)-shi_H)/(k_c*u_star)

# Calculate Vds = 1/Rs

#For PM2.5

Vds_PM2.5 = (a1*u_star)

Rds_PM2.5 = (1/Vds_PM2.5)

# For PM2.5-10

#b1= 2.6*10^-1

#b2= -1.3*10^0

#b3 = 3.0*10^0

#c1= 1.8

#c2 = -2.0*10^-1

#c3 = -5.3*10^-1

#k = c1*u_star+c2*u_star^2+c3*u_star^3

#LAI =

#LAImax =

#Vds_PM10 =
(b1*u_star+b2*u_star^2+b3*u_star^3)*exp(k*(LAI/LAImax)-
1)

#Rds_PM10 = 1/Vds_PM10

#For PM10+

#d1= -

#d2=

#d3 =

#f1=

#f2 =

#f3 =

#k = f1*u_star+f2*u_star^2+f3*u_star^3

#LAI =

#LAImax =
```

```
#Vds_PM10Plus =
(d1*u_star+d2*u_star^2+d3*u_star^3)*exp(k*(LAI/LAImax)-
1)

#Rds_PM10Plus = (1/Vds_PM10Plus)

#Compute Vd

Vd = 1/Rg+(1/(Ra+Rds_PM2.5))

quantile(Vd, c(.05, 0.10, .50, 0.95))



#Dry deposition parameterization by Zhang and He (2014)

#Uncertainty test: Ice/Water

set.seed(5)

C1 = 0.2789

C2 = 3.115

C3 = 5.415*10^-11

C4 = -1.399

RH = replicate(10000,runif(100,0.76,0.84))

dp_a = 2.0

dp_i = dp_a*10^-6

rd = dp_i/2

r_w = {(C1*rd^C2)/(C3*rd^C4-log10(RH))+rd^3}^(1/3)

dp = r_w*2

#Correction factor, C

k_B = 1.38*10^-23

Temp = 273.15+0

P = 101325

d_air = 3.7208*10^-10

lambda = (k_B*Temp)/(sqrt(2)*3.1416*P*d_air^2)

C = 1+(2*lambda/dp)*(1.257+0.4*exp(-0.55*dp/lambda))

dyn.vis = ((5*10^-8)*Temp)+4*10^-6

rho = 1500
```

```
Tau = (rho*(dp)^2*C)/(18*dyn.vis)

V_g = Tau*9.81

Rg = 1/V_g

a1 = 4.3*10^-3

z = 5

L = replicate(10000,runif(100,45,55))

x = z/L

# Compute stability function (shi_H)

shi_H.1 = 2*log(0.5*{1+(1-16*x)^0.5})

shi_H.2 = -5*x

shi_H =ifelse(x <= 0, shi_H.1 , shi_H.2)

zR = 10

u_star = replicate(10000,runif(100,0.27,0.33))

z0 = replicate(10000,runif(100,0.0075,0.0125))

k_c = 0.41

Ra = (log(zR/z0)-shi_H)/(k_c*u_star)

# Calculate Vds = 1/Rs#For PM2.5

Vds_PM2.5 = (a1*u_star)

Rds_PM2.5 = (1/Vds_PM2.5)

# For PM2.5-10

#b1=

#b2=

#b3 =

#c1=

#c2 =

#c3 =

#k = c1*u_star+c2*u_star^2+c3*u_star^3

#LAI =

# LAImax =
```

```
#Vds_PM10 = (b1*u_star+b2*u_star^2+b3*u_star^3)*exp(k*(LAI/LAImax)-1)

#Rds_PM10 = 1/Vds_PM10

# For PM10+

#d1=

#d2=

#d3 =

#f1=

#f2 =

#f3 =

#k = f1*u_star+f2*u_star^2+f3*u_star^3

#LAI =

#LAImax =

#Vds_PM10Plus = (d1*u_star+d2*u_star^2+d3*u_star^3)*exp(k*(LAI/LAImax)-1)

#Rds_PM10Plus = (1/Vds_PM10Plus)

#Compute Vd

Vd = 1/Rg+(1/(Ra+Rds_PM2.5))

quantile(Vd, c(.05, 0.10, .50, 0.95))
```

Codes for Monte Carlo uncertainty evaluation for Zhang and Shao (2014) parameterization

```
#Dry deposition parameterization by Zhang and Shao (2014)

#Uncertainty test: Plant (Grass, coniferous, and deciduous forests)

set.seed(5)

C1 = 0.2789

C2 = 3.115

C3 = 5.145*10^-11

C4 = -1.399

RH = replicate(10000,runif(100,0.76,0.84))

dp_a = 2.0

dp_i = dp_a*10^-6
```

```
rd = dp_i/2

r_w = {(C1*rd^C2)/(C3*rd^C4-log10(RH))+rd^3}^(1/3)

dp = r_w*2

#Correction factor, C

k_B = 1.38*10^-23

Temp = (273.15+15)

P = 101325

d_air = 3.7208*10^-10

lambda = (k_B*Temp)/(sqrt(2)*3.1416*P*d_air^2)

C = 1+(2*lambda/dp)*(1.257+0.4*exp(-0.55*dp/lambda))

dyn.vis = 1.841*10^-5

rho = 1500

Tau = (rho*(dp_i)^2*C)/(18*dyn.vis)

Tau_wet = (rho*(dp)^2*C)/(18*dyn.vis)

Wt = Tau*9.81

Vg = Wt

Vg_wet = Tau_wet*9.81

u_star = replicate(10000,runif(100,0.27,0.33))

k =  0.41

z =  1

zd = 0.20

h_c = 0.23

z0 = replicate(10000,runif(100,0.0015, 0.0025))

B1 = 0.45

Sc_T = (1+(Vg^2/u_star^2))^0.5

Ra = (Sc_T/(k*u_star))*(log((z-zd)/(h_c-zd)))

Rg = 1/Vg

U_h = replicate(10000,runif(100,3.88,4.12))

kin.vis = 1.593*10^-5
```

```
d_c = 0.005

D = (C*k_B*Temp)/(3*3.1416*dyn.vis*dp)

Sc = (kin.vis/D)

Re_h = (U_h*d_c)/(kin.vis)

nB = 0.5

C_B = 0.467

E_B = C_B*Sc^(-2/3)*Re_h^(nB-1)

#Compute impaction collection efficiency (E_IM)

beta_IM = 0.6

St_h = (Tau*u_star)/d_c

E_IM = (St_h/(St_h+beta_IM))^2

#Compute interception efficiency (E_IN)

Ain = 150

E_IN = Ain*u_star*(10^(-St_h))*(2*dp/d_c)

#Compute R

b = 2

R = exp(-b*sqrt(St_h))

#Compute w_dm

B2 = 3

w_dm = (u_star/U_h*h_c)       #For rough surface

#compute Tau_c/Tau (ratio of stress)

Beta = 200

C1 = 6

C2 = 0.1

lambda_FAI = 0.4

n_FAI = (lambda_FAI)/(h_c*d_c)

q = (3.1416*d_c^2)/4

eta_BAI = n_FAI*q

lambda_FAIe = ((lambda_FAI)/(1-eta_BAI)^C2)*exp((-C1*lambda_FAI)/(1-eta_BAI)^C2)
```

```
Tau_c_BY_Tau = (Beta*lambda_FAIe)/(1+Beta*lambda_FAIe)

#Compute Rs

E = E_B+E_IM+E_IN

Tau_wetplus = (Tau_wet*u_star^2)/kin.vis

Cd = 1/6

Rs = (R*w_dm*((E*Tau_c_BY_Tau/Cd)+(1+Tau_c_BY_Tau)*Sc^-1+10^(-3/Tau_wetplus))+Vg_wet)^-1

#Compute Vd

Vd = (Rg+((Rs-Rg)/exp(Ra/Rg)))^-1

quantile(Vd, c(.05, 0.10, .50, 0.95))


#Dry deposition parameterization by Zhang and Shao (2014)

#Uncertainty test: Water

set.seed(5)

C1 = 0.2789

C2 = 3.115

C3 = 5.415*10^-11

C4 = -1.399

RH = replicate(10000,runif(100,0.76,0.84))

dp_a = 2.0

dp_i = dp_a*10^-6

rd = dp_i/2

r_w = {(C1*rd^C2)/(C3*rd^C4-log10(RH))+rd^3}^(1/3)

dp = r_w*2

#Correction factor, C

k_B = 1.38*10^-23

Temp = 273.15+25

P = 101325

d_air = 3.7208*10^-10

lambda = (k_B*Temp)/(sqrt(2)*3.1416*P*d_air^2)
```

```
C = 1+(2*lambda/dp)*(1.257+0.4*exp(-0.55*dp/lambda))

dyn.vis = ((5*10^-8)*Temp)+4*10^-6

rho = 1500

Tau = (rho*(dp_i)^2*C)/(18*dyn.vis)

Tau_wet = (rho*(dp)^2*C)/(18*dyn.vis)

Wt = Tau*9.81

Vg = Wt

Vg_wet = Tau_wet*9.81

u_star = replicate(10000,runif(100,0.27,0.33))

k =  0.41

z0 = 0.3/1000

z = 8/100

U_h = replicate(10000,runif(100,4.85,5.15))

zd = 0

h_c = 30*z0

B1 = 0.45

Sc_T = (1+(Vg^2/u_star^2))^0.5

Ra = (B1*Sc_T/k*u_star)*log(z/z0)         # For smooth surface

Rg = 1/Vg

# Calculate surface resistance (Rs)

kin.vis = ((9*10^-8)*Temp)+10^-5

d_c = 0.005

D = (C*k_B*Temp)/(3*3.1416*dyn.vis*dp)

Sc = (kin.vis/D)

Re_h = (U_h*d_c)/(kin.vis)

nB = 0.5

C_B = 0.467

E_B = C_B*Sc^(-2/3)*Re_h^(nB-1)

#Compute impaction collection efficiency (E_IM)
```

```
beta_IM = 0.6

St_h = (Tau*u_star)/d_c

E_IM = (St_h/(St_h+beta_IM))^2

#Compute interception efficiency (E_IN)

Ain = 100

E_IN = Ain*u_star*(10^(-St_h))*(2*dp/d_c)

#Compute R

b = 2

R = exp(-b*sqrt(St_h))

#Compute w_dm

B2 = 3

w_dm = B2*u_star                              #For smooth surface

#compute Tau_c/Tau (ratio of stress)

Beta = 200

C_1 = 6

C_2 = 0.1

lambda_FAI = 0.538

n_FAI = (lambda_FAI)/(h_c*d_c)

q = (3.1416*d_c^2)/4

eta_BAI = n_FAI*q

lambda_FAIe = ((lambda_FAI)/(1-eta_BAI)^C_2)*exp((-C_1*lambda_FAI)/(1-eta_BAI)^C_2)

Tau_c_BY_Tau = (Beta*lambda_FAIe)/(1+Beta*lambda_FAIe)

#Compute Rs

E = E_B+E_IM+E_IN

Tau_wetplus = (Tau_wet*u_star^2)/kin.vis

Cd = 1/6

Rs = (R*w_dm*((E*Tau_c_BY_Tau/Cd)+(1+Tau_c_BY_Tau)*Sc^-1+10^(-3/Tau_wetplus))+Vg_wet)^-1

#Compute Vd

Vd = (Rg+((Rs-Rg)/exp(Ra/Rg)))^-1
```

```
quantile(Vd, c(.05, 0.10, .50, 0.95))
```

Codes for Sobol' sensitivity test for Zhang et al. (2001) parameterization

```
#Dry deposition parameterization by Zhang et al. (2001)

#Sobol sensitivity test: Grass (the code is similar for other LUCs)

#Change LUC dependent parameters for other LUCs

#Change sensitivity ranges for other LUCs

set.seed(5)

library(sensitivity)

library(boot)

C1 = 0.2789

C2 = 3.115

C3 = 5.415*10^-11

C4 = -1.399

dp_i = 10

dp_d = dp_i*10^-6

rd = dp_d/2

k_B = 1.38*10^-23

Temp = 273.15+25

P = 101325

d_air = 3.72*10^-10

lambda = (k_B*Temp)/(sqrt(2)*3.1416*P*d_air^2)

dyn.vis = ((5*10^-8)*Temp)+4*10^-6

z = 2

zR = 3.5

k_c = 0.41

e_0 = 3

R1 = 1

kin.vis = ((9*10^-8)*Temp)+10^-5
```

```
gamma = 0.54

alpha = 1.2

beta =  2

A = 2/1000

model <- function (X) ((((X[,2])*(2*{(C1*rd^C2)/(C3*rd^C4-
log10(X[,1]))+rd^3}^(1/3))^2*9.81*(1+(2*lambda/(2*{(C1*rd^C2)/(C3*rd^C4-
log10(X[,1]))+rd^3}^(1/3)))*(1.257+0.4*exp(-0.55*((2*{(C1*rd^C2)/(C3*rd^C4-
log10(X[,1]))+rd^3}^(1/3)))/lambda))))/(18*dyn.vis)))+

  (1/((((log(zR/(X[,4]))+5*z/(X[,3])))/(k_c*(X[,5])))))+

        (1/{(e_0*(X[,5]))*

              ((((kin.vis/(((1+(2*lambda/(2*{(C1*rd^C2)/(C3*rd^C4-
log10(X[,1]))+rd^3}^(1/3)))*(1.257+0.4*exp(-0.55*(2*{(C1*rd^C2)/(C3*rd^C4-
log10(X[,1]))+rd^3}^(1/3))/lambda)))*k_B*Temp)/(3*3.1416*dyn.vis*(2*{(C1*rd^C2)/(C3*rd^C4-
log10(X[,1]))+rd^3}^(1/3))))))^(-gamma))+

                ({{{{{(X[,2])*(2*{(C1*rd^C2)/(C3*rd^C4-
log10(X[,1]))+rd^3}^(1/3))^2*9.81*(1+(2*lambda/(2*{(C1*rd^C2)/(C3*rd^C4-
log10(X[,1]))+rd^3}^(1/3)))*(1.257+0.4*exp(-0.55*((2*{(C1*rd^C2)/(C3*rd^C4-
log10(X[,1]))+rd^3}^(1/3)))/lambda))))/(18*dyn.vis))*(X[,5]))/(9.81*A))/(alpha+(((((X[,2])*(2*
{(C1*rd^C2)/(C3*rd^C4-log10(X[,1]))+rd^3}^(1/3))^2*9.81*(1+(2*lambda/(2*{(C1*rd^C2)/(C3*rd^C4-
log10(X[,1]))+rd^3}^(1/3)))*(1.257+0.4*exp(-0.55*((2*{(C1*rd^C2)/(C3*rd^C4-
log10(X[,1]))+rd^3}^(1/3)))/lambda))))/(18*dyn.vis))*(X[,5]))/(9.81*A)))}^beta)+

                (0.5*((2*{(C1*rd^C2)/(C3*rd^C4-log10(X[,1]))+rd^3}^(1/3))/A)^2))*R1})))




N <- 100000

x1 = runif(1*N,0.1,1.0)           #RH

x2 = runif(1*N,1500,2000)         #rho

x3 = runif(1*N,10,100)            #L

x4 = runif(1*N,0.02,0.10)         #z0

x5 = runif(1*N,0.1,0.5)           #u_star

x_1 = runif(1*N,0.1,1.0)          #RH

x_2 = runif(1*N,1500,2000)        #rho

x_3 = runif(1*N,10,100)           #L

x_4 = runif(1*N,0.02,0.10)        #z0

x_5 = runif(1*N,0.1,0.5)          #u_star
```

```
Y1 = matrix(c(x1,x2,x3,x4,x5), nrow=N)

X1 = data.frame(matrix(Y1,nrow=N))

Y2 = matrix(c(x_1,x_2,x_3,x_4,x_5), nrow=N)

X2 = data.frame(matrix(Y2, nrow=N))

a = sobol2007(model = model, X1 = X1, X2= X2, nboot = 2000, conf = 0.95);a
```

Codes for Sobol' sensitivity test for the Petroff and Zhang (2010) parameterization

```
#Dry deposition parameterization by Petroff and Zhang (2010)

#Sobol sensitivity test: Grass (the code is similar for other LUCs)

#Change LUC dependent parameters for other LUCs

#Change sensitivity ranges for other LUCs

set.seed(5)

library(sensitivity)

library(boot)

C1 = 0.2789

C2 = 3.115

C3 = 5.415*10^-11

C4 = -1.399

dp_i = 10

dp_d = dp_i*10^-6

rd = dp_d/2

k_B = 1.38*10^-23

Temp = 273.15+25

P = 101325

d_air = 3.7208*10^-10

lambda = (k_B*Temp)/(sqrt(2)*3.1416*P*d_air^2)

dyn.vis = ((5*10^-8)*Temp)+4*10^-6

kin.vis = ((9*10^-8)*Temp)+10^-5

Vphor = 0
```

```
z = 2

zR = 3.5

k_c = 0.41

cd = 1/6

kx = 0.216

C_IT = 0.056

L_obs = 0.01

C_B = 0.996

C_IN = 0.162

C_IM = 0.081

beta_IM = 0.47

model <- function (X) ((((((X[,2])*(2*({(C1*rd^C2)/(C3*rd^C4-
log10(X[,1]))+rd^3}^(1/3)))^2*(1+(2*lambda/(2*({(C1*rd^C2)/(C3*rd^C4-
log10(X[,1]))+rd^3}^(1/3))))*(1.257+0.4*exp(-0.55*(2*({(C1*rd^C2)/(C3*rd^C4-
log10(X[,1]))+rd^3}^(1/3)))/lambda))))/(18*dyn.vis))*9.81)+Vphor)+1/(((log(zR/(X[,4]))+(5*(z/(
X[,3])))))/(k_c*(X[,5])))+1/((X[,5])*(((((kin.vis/(((1+(2*lambda/(2*({(C1*rd^C2)/(C3*rd^C4-
log10(X[,1]))+rd^3}^(1/3))))*(1.257+0.4*exp(-0.55*(2*({(C1*rd^C2)/(C3*rd^C4-
log10(X[,1]))+rd^3}^(1/3)))/lambda)))*k_B*Temp)/(3*3.1416*dyn.vis*(2*({(C1*rd^C2)/(C3*rd^C4-
log10(X[,1]))+rd^3}^(1/3)))))))^(-
2/3)/14.5)*{1/6*log(1+((((kin.vis/(((1+(2*lambda/(2*({(C1*rd^C2)/(C3*rd^C4-
log10(X[,1]))+rd^3}^(1/3))))*(1.257+0.4*exp(-0.55*(2*({(C1*rd^C2)/(C3*rd^C4-
log10(X[,1]))+rd^3}^(1/3)))/lambda)))*k_B*Temp)/(3*3.1416*dyn.vis*(2*({(C1*rd^C2)/(C3*rd^C4-
log10(X[,1]))+rd^3}^(1/3)))))))^(1/3))/2.9))^2/(1-
((((kin.vis/(((1+(2*lambda/(2*({(C1*rd^C2)/(C3*rd^C4-
log10(X[,1]))+rd^3}^(1/3))))*(1.257+0.4*exp(-0.55*(2*({(C1*rd^C2)/(C3*rd^C4-
log10(X[,1]))+rd^3}^(1/3)))/lambda)))*k_B*Temp)/(3*3.1416*dyn.vis*(2*({(C1*rd^C2)/(C3*rd^C4-
log10(X[,1]))+rd^3}^(1/3)))))))^(1/3))/2.9)+((((kin.vis/(((1+(2*lambda/(2*({(C1*rd^C2)/(C3*rd^
C4-log10(X[,1]))+rd^3}^(1/3))))*(1.257+0.4*exp(-0.55*(2*({(C1*rd^C2)/(C3*rd^C4-
log10(X[,1]))+rd^3}^(1/3)))/lambda)))*k_B*Temp)/(3*3.1416*dyn.vis*(2*({(C1*rd^C2)/(C3*rd^C4-
log10(X[,1]))+rd^3}^(1/3)))))))^(1/3))/2.9)^2)+1/sqrt(3)*atan((2*((((kin.vis/(((1+(2*lambda/(2
*({(C1*rd^C2)/(C3*rd^C4-log10(X[,1]))+rd^3}^(1/3))))*(1.257+0.4*exp(-
0.55*(2*({(C1*rd^C2)/(C3*rd^C4-
log10(X[,1]))+rd^3}^(1/3)))/lambda)))*k_B*Temp)/(3*3.1416*dyn.vis*(2*({(C1*rd^C2)/(C3*rd^C4-
log10(X[,1]))+rd^3}^(1/3)))))))^(1/3))/2.9)-1)/sqrt(3))+3.1416/6*sqrt(3)}^-1) + (2.5*10^-
3*0.14*((((((X[,2])*(2*({(C1*rd^C2)/(C3*rd^C4-
log10(X[,1]))+rd^3}^(1/3)))^2*(1+(2*lambda/(2*({(C1*rd^C2)/(C3*rd^C4-
log10(X[,1]))+rd^3}^(1/3))))*(1.257+0.4*exp(-0.55*(2*({(C1*rd^C2)/(C3*rd^C4-
log10(X[,1]))+rd^3}^(1/3)))/lambda))))/(18*dyn.vis))*(X[,5])^2)/kin.vis))^2)

)*{(1+((X[,6])*((((X[,9])/(exp(({(kx*(X[,6]))/(12*k_c^2*(1-
(X[,8])/(X[,7]))^2)}^(1/3)*(1+5*(z/(X[,3])))^(2/3)*{((X[,7])-
(X[,8]))/((X[,3]))})*((z)/(X[,7])-
1))))/(X[,5]))*((C_B*(((kin.vis/(((1+(2*lambda/(2*({(C1*rd^C2)/(C3*rd^C4-
log10(X[,1]))+rd^3}^(1/3))))*(1.257+0.4*exp(-0.55*(2*({(C1*rd^C2)/(C3*rd^C4-
log10(X[,1]))+rd^3}^(1/3)))/lambda)))*k_B*Temp)/(3*3.1416*dyn.vis*(2*({(C1*rd^C2)/(C3*rd^C4-
log10(X[,1]))+rd^3}^(1/3)))))))^(-2/3))*(((((X[,9])/(exp(({(kx*(X[,6]))/(12*k_c^2*(1-
(X[,8])/(X[,7]))^2)}^(1/3)*(1+5*(z/(X[,3])))^(2/3)*{((X[,7])-
(X[,8]))/((X[,3]))})*((z)/(X[,7])-1))))*L_obs)/(kin.vis))^(-
1/2)))+(C_IN*((2*({(C1*rd^C2)/(C3*rd^C4-
log10(X[,1]))+rd^3}^(1/3)))/L_obs)*(2+log(4*L_obs/(2*({(C1*rd^C2)/(C3*rd^C4-
```

```
log10(X[,1]))+rd^3}^(1/3))))))+(C_IM*((((((X[,2])*(2*({(C1*rd^C2)/(C3*rd^C4-
log10(X[,1]))+rd^3}^(1/3)))^2*(1+(2*lambda/(2*({(C1*rd^C2)/(C3*rd^C4-
log10(X[,1]))+rd^3}^(1/3))))*(1.257+0.4*exp(-0.55*(2*({(C1*rd^C2)/(C3*rd^C4-
log10(X[,1]))+rd^3}^(1/3)))/lambda))))/(18*dyn.vis)
)*((X[,9])/(exp(({(kx*(X[,6]))/(12*k_c^2*(1-
(X[,8])/(X[,7]))^2)}^(1/3)*(1+5*(z/(X[,3])))^(2/3)*{((X[,7])-
(X[,8]))/((X[,3]))})*((z)/(X[,7])-1)))))/L_obs)/((((((X[,2])*(2*({(C1*rd^C2)/(C3*rd^C4-
log10(X[,1]))+rd^3}^(1/3)))^2*(1+(2*lambda/(2*({(C1*rd^C2)/(C3*rd^C4-
log10(X[,1]))+rd^3}^(1/3))))*(1.257+0.4*exp(-0.55*(2*({(C1*rd^C2)/(C3*rd^C4-
log10(X[,1]))+rd^3}^(1/3)))/lambda))))/(18*dyn.vis)
)*((X[,9])/(exp(({(kx*(X[,6]))/(12*k_c^2*(1-
(X[,8])/(X[,7]))^2)}^(1/3)*(1+5*(z/(X[,3])))^(2/3)*{((X[,7])-
(X[,8]))/((X[,3]))})*((z)/(X[,7])-1)))))/L_obs)+(beta_IM)))^2))+(2.5*10^-
3*C_IT*(((((X[,2])*(2*({(C1*rd^C2)/(C3*rd^C4-
log10(X[,1]))+rd^3}^(1/3)))^2*(1+(2*lambda/(2*({(C1*rd^C2)/(C3*rd^C4-
log10(X[,1]))+rd^3}^(1/3))))*(1.257+0.4*exp(-0.55*(2*({(C1*rd^C2)/(C3*rd^C4-
log10(X[,1]))+rd^3}^(1/3)))/lambda))))/(18*dyn.vis))*(X[,5])^2)/kin.vis)^2)

)*(X[,7])/(((0.41*((X[,7])-(X[,8])))/((1+5*(z/(X[,3])))*((X[,7])-
(X[,8]))/((X[,3])))))))/((((((kin.vis/(((1+(2*lambda/(2*({(C1*rd^C2)/(C3*rd^C4-
log10(X[,1]))+rd^3}^(1/3))))*(1.257+0.4*exp(-0.55*(2*({(C1*rd^C2)/(C3*rd^C4-
log10(X[,1]))+rd^3}^(1/3)))/lambda)))*k_B*Temp)/(3*3.1416*dyn.vis*(2*({(C1*rd^C2)/(C3*rd^C4-
log10(X[,1]))+rd^3}^(1/3)))))))^(-
2/3)/14.5)*{1/6*log(1+((((kin.vis/(((1+(2*lambda/(2*({(C1*rd^C2)/(C3*rd^C4-
log10(X[,1]))+rd^3}^(1/3))))*(1.257+0.4*exp(-0.55*(2*({(C1*rd^C2)/(C3*rd^C4-
log10(X[,1]))+rd^3}^(1/3)))/lambda)))*k_B*Temp)/(3*3.1416*dyn.vis*(2*({(C1*rd^C2)/(C3*rd^C4-
log10(X[,1]))+rd^3}^(1/3)))))))^(1/3))/2.9))^2/(1-
((((kin.vis/(((1+(2*lambda/(2*({(C1*rd^C2)/(C3*rd^C4-
log10(X[,1]))+rd^3}^(1/3))))*(1.257+0.4*exp(-0.55*(2*({(C1*rd^C2)/(C3*rd^C4-
log10(X[,1]))+rd^3}^(1/3)))/lambda)))*k_B*Temp)/(3*3.1416*dyn.vis*(2*({(C1*rd^C2)/(C3*rd^C4-
log10(X[,1]))+rd^3}^(1/3)))))))^(1/3))/2.9)+((((kin.vis/(((1+(2*lambda/(2*({(C1*rd^C2)/(C3*rd^
C4-log10(X[,1]))+rd^3}^(1/3))))*(1.257+0.4*exp(-0.55*(2*({(C1*rd^C2)/(C3*rd^C4-
log10(X[,1]))+rd^3}^(1/3)))/lambda)))*k_B*Temp)/(3*3.1416*dyn.vis*(2*({(C1*rd^C2)/(C3*rd^C4-
log10(X[,1]))+rd^3}^(1/3)))))))^(1/3))/2.9)^2)+1/sqrt(3)*atan((2*((((kin.vis/(((1+(2*lambda/(2
*({(C1*rd^C2)/(C3*rd^C4-log10(X[,1]))+rd^3}^(1/3))))*(1.257+0.4*exp(-
0.55*(2*({(C1*rd^C2)/(C3*rd^C4-
log10(X[,1]))+rd^3}^(1/3)))/lambda)))*k_B*Temp)/(3*3.1416*dyn.vis*(2*({(C1*rd^C2)/(C3*rd^C4-
log10(X[,1]))+rd^3}^(1/3)))))))^(1/3))/2.9)-1)/sqrt(3))+3.1416/6*sqrt(3)}^-1) + (2.5*10^-
3*0.14*((((((X[,2])*(2*({(C1*rd^C2)/(C3*rd^C4-
log10(X[,1]))+rd^3}^(1/3)))^2*(1+(2*lambda/(2*({(C1*rd^C2)/(C3*rd^C4-
log10(X[,1]))+rd^3}^(1/3))))*(1.257+0.4*exp(-0.55*(2*({(C1*rd^C2)/(C3*rd^C4-
log10(X[,1]))+rd^3}^(1/3)))/lambda))))/(18*dyn.vis))*(X[,5])^2)/kin.vis))^2))*(X[,7])/((0.41*(
(X[,7])-(X[,8])))/((1+5*(z/(X[,3])))*((X[,7])-(X[,8]))/((X[,3]))))

)-({(kx*(X[,6]))/(12*k_c^2*(1-(X[,8])/(X[,7]))^2)}^(1/3)*(1+5*(z/(X[,3])))^(2/3)*{((X[,7])-
(X[,8]))/((X[,3]))})/2)*tanh(((((kx*(X[,6]))/(12*k_c^2*(1-
(X[,8])/(X[,7]))^2)}^(1/3)*(1+5*(z/(X[,3])))^(2/3)*{((X[,7])-
(X[,8]))/((X[,3]))})^2/4+(X[,6])*((((X[,9])/(exp(({(kx*(X[,6]))/(12*k_c^2*(1-
(X[,8])/(X[,7]))^2)}^(1/3)*(1+5*(z/(X[,3])))^(2/3)*{((X[,7])-
(X[,8]))/((X[,3]))})*((z)/(X[,7])-
1))))/(X[,5]))*((C_B*(((kin.vis/(((1+(2*lambda/(2*({(C1*rd^C2)/(C3*rd^C4-
log10(X[,1]))+rd^3}^(1/3))))*(1.257+0.4*exp(-0.55*(2*({(C1*rd^C2)/(C3*rd^C4-
log10(X[,1]))+rd^3}^(1/3)))/lambda)))*k_B*Temp)/(3*3.1416*dyn.vis*(2*({(C1*rd^C2)/(C3*rd^C4-
log10(X[,1]))+rd^3}^(1/3)))))))^(-2/3))*(((((X[,9])/(exp(({(kx*(X[,6]))/(12*k_c^2*(1-
(X[,8])/(X[,7]))^2)}^(1/3)*(1+5*(z/(X[,3])))^(2/3)*{((X[,7])-
(X[,8]))/((X[,3]))})*((z)/(X[,7])-1))))*L_obs)/(kin.vis))^(-
1/2)))+(C_IN*((2*({(C1*rd^C2)/(C3*rd^C4-
log10(X[,1]))+rd^3}^(1/3)))/L_obs)*(2+log(4*L_obs/(2*({(C1*rd^C2)/(C3*rd^C4-
log10(X[,1]))+rd^3}^(1/3))))))+(C_IM*((((((X[,2])*(2*({(C1*rd^C2)/(C3*rd^C4-
log10(X[,1]))+rd^3}^(1/3)))^2*(1+(2*lambda/(2*({(C1*rd^C2)/(C3*rd^C4-
log10(X[,1]))+rd^3}^(1/3))))*(1.257+0.4*exp(-0.55*(2*({(C1*rd^C2)/(C3*rd^C4-
log10(X[,1]))+rd^3}^(1/3)))/lambda))))/(18*dyn.vis)
)*((X[,9])/(exp(({(kx*(X[,6]))/(12*k_c^2*(1-
(X[,8])/(X[,7]))^2)}^(1/3)*(1+5*(z/(X[,3])))^(2/3)*{((X[,7])-
(X[,8]))/((X[,3]))})*((z)/(X[,7])-1)))))/L_obs)/((((((X[,2])*(2*({(C1*rd^C2)/(C3*rd^C4-
```

```
log10(X[,1]))+rd^3}^(1/3)))^2*(1+(2*lambda/(2*({(C1*rd^C2)/(C3*rd^C4-
log10(X[,1]))+rd^3}^(1/3))))*(1.257+0.4*exp(-0.55*(2*({(C1*rd^C2)/(C3*rd^C4-
log10(X[,1]))+rd^3}^(1/3)))/lambda))))/(18*dyn.vis)
)*((X[,9])/(exp(({(kx*(X[,6]))/(12*k_c^2*(1-
(X[,8])/(X[,7]))^2)}^(1/3)*(1+5*(z/(X[,3])))^(2/3)*{((X[,7])-
(X[,8]))/((X[,3]))})*((z)/(X[,7])-1)))))/L_obs)+(beta_IM)))^2))+(2.5*10^-
3*C_IT*(((((X[,2])*(2*({(C1*rd^C2)/(C3*rd^C4-
log10(X[,1]))+rd^3}^(1/3)))^2*(1+(2*lambda/(2*({(C1*rd^C2)/(C3*rd^C4-
log10(X[,1]))+rd^3}^(1/3))))*(1.257+0.4*exp(-0.55*(2*({(C1*rd^C2)/(C3*rd^C4-
log10(X[,1]))+rd^3}^(1/3)))/lambda))))/(18*dyn.vis))*(X[,5])^2)/kin.vis)^2)

)*(X[,7])/(((0.41*((X[,7])-(X[,8])))/((1+5*(z/(X[,3])))*((X[,7])-
(X[,8]))/((X[,3])))))))^0.5))/(((((kx*(X[,6]))/(12*k_c^2*(1-
(X[,8])/(X[,7]))^2)}^(1/3)*(1+5*(z/(X[,3])))^(2/3)*{((X[,7])-
(X[,8]))/((X[,3]))})^2/4+((X[,6])*((((X[,9])/(exp(({(kx*(X[,6]))/(12*k_c^2*(1-
(X[,8])/(X[,7]))^2)}^(1/3)*(1+5*(z/(X[,3])))^(2/3)*{((X[,7])-
(X[,8]))/((X[,3]))})*((z)/(X[,7])-
1))))/(X[,5]))*((C_B*(((kin.vis/(((1+(2*lambda/(2*({(C1*rd^C2)/(C3*rd^C4-
log10(X[,1]))+rd^3}^(1/3))))*(1.257+0.4*exp(-0.55*(2*({(C1*rd^C2)/(C3*rd^C4-
log10(X[,1]))+rd^3}^(1/3)))/lambda)))*k_B*Temp)/(3*3.1416*dyn.vis*(2*({(C1*rd^C2)/(C3*rd^C4-
log10(X[,1]))+rd^3}^(1/3)))))))^(-2/3))*(((((X[,9])/(exp(({(kx*(X[,6]))/(12*k_c^2*(1-
(X[,8])/(X[,7]))^2)}^(1/3)*(1+5*(z/(X[,3])))^(2/3)*{((X[,7])-
(X[,8]))/((X[,3]))})*((z)/(X[,7])-1))))*L_obs)/(kin.vis))^(-
1/2)))+(C_IN*((2*({(C1*rd^C2)/(C3*rd^C4-
log10(X[,1]))+rd^3}^(1/3)))/L_obs)*(2+log(4*L_obs/(2*({(C1*rd^C2)/(C3*rd^C4-
log10(X[,1]))+rd^3}^(1/3))))))+(C_IM*((((((X[,2])*(2*({(C1*rd^C2)/(C3*rd^C4-
log10(X[,1]))+rd^3}^(1/3)))^2*(1+(2*lambda/(2*({(C1*rd^C2)/(C3*rd^C4-
log10(X[,1]))+rd^3}^(1/3))))*(1.257+0.4*exp(-0.55*(2*({(C1*rd^C2)/(C3*rd^C4-
log10(X[,1]))+rd^3}^(1/3)))/lambda))))/(18*dyn.vis)
)*((X[,9])/(exp(({(kx*(X[,6]))/(12*k_c^2*(1-
(X[,8])/(X[,7]))^2)}^(1/3)*(1+5*(z/(X[,3])))^(2/3)*{((X[,7])-
(X[,8]))/((X[,3]))})*((z)/(X[,7])-1)))))/L_obs)/((((((X[,2])*(2*({(C1*rd^C2)/(C3*rd^C4-
log10(X[,1]))+rd^3}^(1/3)))^2*(1+(2*lambda/(2*({(C1*rd^C2)/(C3*rd^C4-
log10(X[,1]))+rd^3}^(1/3))))*(1.257+0.4*exp(-0.55*(2*({(C1*rd^C2)/(C3*rd^C4-
log10(X[,1]))+rd^3}^(1/3)))/lambda))))/(18*dyn.vis)
)*((X[,9])/(exp(({(kx*(X[,6]))/(12*k_c^2*(1-
(X[,8])/(X[,7]))^2)}^(1/3)*(1+5*(z/(X[,3])))^(2/3)*{((X[,7])-
(X[,8]))/((X[,3]))})*((z)/(X[,7])-1)))))/L_obs)+(beta_IM)))^2))+(2.5*10^-
3*C_IT*(((((X[,2])*(2*({(C1*rd^C2)/(C3*rd^C4-
log10(X[,1]))+rd^3}^(1/3)))^2*(1+(2*lambda/(2*({(C1*rd^C2)/(C3*rd^C4-
log10(X[,1]))+rd^3}^(1/3))))*(1.257+0.4*exp(-0.55*(2*({(C1*rd^C2)/(C3*rd^C4-
log10(X[,1]))+rd^3}^(1/3)))/lambda))))/(18*dyn.vis))*(X[,5])^2)/kin.vis)^2)

)*(X[,7])/(((0.41*((X[,7])-(X[,8])))/((1+5*(z/(X[,3])))*((X[,7])-
(X[,8]))/((X[,3])))))))^0.5)}/{(1+((X[,6])*((((X[,9])/(exp(({(kx*(X[,6]))/(12*k_c^2*(1-
(X[,8])/(X[,7]))^2)}^(1/3)*(1+5*(z/(X[,3])))^(2/3)*{((X[,7])-
(X[,8]))/((X[,3]))})*((z)/(X[,7])-
1))))/(X[,5]))*((C_B*(((kin.vis/(((1+(2*lambda/(2*({(C1*rd^C2)/(C3*rd^C4-
log10(X[,1]))+rd^3}^(1/3))))*(1.257+0.4*exp(-0.55*(2*({(C1*rd^C2)/(C3*rd^C4-
log10(X[,1]))+rd^3}^(1/3)))/lambda)))*k_B*Temp)/(3*3.1416*dyn.vis*(2*({(C1*rd^C2)/(C3*rd^C4-
log10(X[,1]))+rd^3}^(1/3)))))))^(-2/3))*(((((X[,9])/(exp(({(kx*(X[,6]))/(12*k_c^2*(1-
(X[,8])/(X[,7]))^2)}^(1/3)*(1+5*(z/(X[,3])))^(2/3)*{((X[,7])-
(X[,8]))/((X[,3]))})*((z)/(X[,7])-1))))*L_obs)/(kin.vis))^(-
1/2)))+(C_IN*((2*({(C1*rd^C2)/(C3*rd^C4-
log10(X[,1]))+rd^3}^(1/3)))/L_obs)*(2+log(4*L_obs/(2*({(C1*rd^C2)/(C3*rd^C4-
log10(X[,1]))+rd^3}^(1/3))))))+(C_IM*((((((X[,2])*(2*({(C1*rd^C2)/(C3*rd^C4-
log10(X[,1]))+rd^3}^(1/3)))^2*(1+(2*lambda/(2*({(C1*rd^C2)/(C3*rd^C4-
log10(X[,1]))+rd^3}^(1/3))))*(1.257+0.4*exp(-0.55*(2*({(C1*rd^C2)/(C3*rd^C4-
log10(X[,1]))+rd^3}^(1/3)))/lambda))))/(18*dyn.vis)
)*((X[,9])/(exp(({(kx*(X[,6]))/(12*k_c^2*(1-
(X[,8])/(X[,7]))^2)}^(1/3)*(1+5*(z/(X[,3])))^(2/3)*{((X[,7])-
(X[,8]))/((X[,3]))})*((z)/(X[,7])-1)))))/L_obs)/((((((X[,2])*(2*({(C1*rd^C2)/(C3*rd^C4-
log10(X[,1]))+rd^3}^(1/3)))^2*(1+(2*lambda/(2*({(C1*rd^C2)/(C3*rd^C4-
log10(X[,1]))+rd^3}^(1/3))))*(1.257+0.4*exp(-0.55*(2*({(C1*rd^C2)/(C3*rd^C4-
log10(X[,1]))+rd^3}^(1/3)))/lambda))))/(18*dyn.vis)
```

```
)*((X[,9])/(exp(({{(kx*(X[,6]))/(12*k_c^2*(1-
(X[,8])/(X[,7]))^2)}^(1/3)*(1+5*(z/(X[,3])))^(2/3)*{((X[,7])-
(X[,8]))/((X[,3]))}}*((z)/(X[,7])-1)))))/L_obs)+(beta_IM)))^2))+(2.5*10^-
3*C_IT*(((((X[,2])*(2*({(C1*rd^C2)/(C3*rd^C4-
log10(X[,1]))+rd^3}^(1/3)))^2*(1+(2*lambda/(2*({(C1*rd^C2)/(C3*rd^C4-
log10(X[,1]))+rd^3}^(1/3))))*(1.257+0.4*exp(-0.55*(2*({(C1*rd^C2)/(C3*rd^C4-
log10(X[,1]))+rd^3}^(1/3)))/lambda))))/(18*dyn.vis))*(X[,5])^2)/kin.vis)^2)

)*(X[,7])/(((0.41*((X[,7])-(X[,8])))/((1+5*(z/(X[,3])))*((X[,7])-
(X[,8]))/((X[,3])))))+({(kx*(X[,6]))/(12*k_c^2*(1-
(X[,8])/(X[,7]))^2)}^(1/3)*(1+5*(z/(X[,3])))^(2/3)*{((X[,7])-
(X[,8]))/((X[,3]))}}/2)*tanh(((((kx*(X[,6]))/(12*k_c^2*(1-
(X[,8])/(X[,7]))^2)}^(1/3)*(1+5*(z/(X[,3])))^(2/3)*{((X[,7])-
(X[,8]))/((X[,3]))}}^2/4+((X[,6])*((((X[,9])/(exp(({(kx*(X[,6]))/(12*k_c^2*(1-
(X[,8])/(X[,7]))^2)}^(1/3)*(1+5*(z/(X[,3])))^(2/3)*{((X[,7])-
(X[,8]))/((X[,3]))}}*((z)/(X[,7])-
1))))/(X[,5]))*((C_B*(((kin.vis/(((1+(2*lambda/(2*({(C1*rd^C2)/(C3*rd^C4-
log10(X[,1]))+rd^3}^(1/3))))*(1.257+0.4*exp(-0.55*(2*({(C1*rd^C2)/(C3*rd^C4-
log10(X[,1]))+rd^3}^(1/3)))/lambda)))*k_B*Temp)/(3*3.1416*dyn.vis*(2*({(C1*rd^C2)/(C3*rd^C4-
log10(X[,1]))+rd^3}^(1/3)))))))^(-2/3))*(((((X[,9])/(exp(({(kx*(X[,6]))/(12*k_c^2*(1-
(X[,8])/(X[,7]))^2)}^(1/3)*(1+5*(z/(X[,3])))^(2/3)*{((X[,7])-
(X[,8]))/((X[,3]))}}*((z)/(X[,7])-1))))*L_obs)/(kin.vis))^(-
1/2)))+(C_IN*((2*(({(C1*rd^C2)/(C3*rd^C4-
log10(X[,1]))+rd^3}^(1/3)))/L_obs)*(2+log(4*L_obs/(2*({(C1*rd^C2)/(C3*rd^C4-
log10(X[,1]))+rd^3}^(1/3))))))+(C_IM*((((((X[,2])*(2*({(C1*rd^C2)/(C3*rd^C4-
log10(X[,1]))+rd^3}^(1/3)))^2*(1+(2*lambda/(2*({(C1*rd^C2)/(C3*rd^C4-
log10(X[,1]))+rd^3}^(1/3))))*(1.257+0.4*exp(-0.55*(2*({(C1*rd^C2)/(C3*rd^C4-
log10(X[,1]))+rd^3}^(1/3)))/lambda))))/(18*dyn.vis)
)*((X[,9])/(exp(({(kx*(X[,6]))/(12*k_c^2*(1-
(X[,8])/(X[,7]))^2)}^(1/3)*(1+5*(z/(X[,3])))^(2/3)*{((X[,7])-
(X[,8]))/((X[,3]))}}*((z)/(X[,7])-1)))))/L_obs)/((((((X[,2])*(2*({(C1*rd^C2)/(C3*rd^C4-
log10(X[,1]))+rd^3}^(1/3)))^2*(1+(2*lambda/(2*({(C1*rd^C2)/(C3*rd^C4-
log10(X[,1]))+rd^3}^(1/3))))*(1.257+0.4*exp(-0.55*(2*({(C1*rd^C2)/(C3*rd^C4-
log10(X[,1]))+rd^3}^(1/3)))/lambda))))/(18*dyn.vis)
)*((X[,9])/(exp(({(kx*(X[,6]))/(12*k_c^2*(1-
(X[,8])/(X[,7]))^2)}^(1/3)*(1+5*(z/(X[,3])))^(2/3)*{((X[,7])-
(X[,8]))/((X[,3]))}}*((z)/(X[,7])-1)))))/L_obs)+(beta_IM)))^2))+(2.5*10^-
3*C_IT*(((((X[,2])*(2*({(C1*rd^C2)/(C3*rd^C4-
log10(X[,1]))+rd^3}^(1/3)))^2*(1+(2*lambda/(2*({(C1*rd^C2)/(C3*rd^C4-
log10(X[,1]))+rd^3}^(1/3))))*(1.257+0.4*exp(-0.55*(2*({(C1*rd^C2)/(C3*rd^C4-
log10(X[,1]))+rd^3}^(1/3)))/lambda))))/(18*dyn.vis))*(X[,5])^2)/kin.vis)^2)

)*(X[,7])/(((0.41*((X[,7])-(X[,8])))/((1+5*(z/(X[,3])))*((X[,7])-
(X[,8]))/((X[,3])))))))^0.5))/(((((kx*(X[,6]))/(12*k_c^2*(1-
(X[,8])/(X[,7]))^2)}^(1/3)*(1+5*(z/(X[,3])))^(2/3)*{((X[,7])-
(X[,8]))/((X[,3]))}}^2/4+((X[,6])*((((X[,9])/(exp(({(kx*(X[,6]))/(12*k_c^2*(1-
(X[,8])/(X[,7]))^2)}^(1/3)*(1+5*(z/(X[,3])))^(2/3)*{((X[,7])-
(X[,8]))/((X[,3]))}}*((z)/(X[,7])-
1))))/(X[,5]))*((C_B*(((kin.vis/(((1+(2*lambda/(2*({(C1*rd^C2)/(C3*rd^C4-
log10(X[,1]))+rd^3}^(1/3))))*(1.257+0.4*exp(-0.55*(2*({(C1*rd^C2)/(C3*rd^C4-
log10(X[,1]))+rd^3}^(1/3)))/lambda)))*k_B*Temp)/(3*3.1416*dyn.vis*(2*({(C1*rd^C2)/(C3*rd^C4-
log10(X[,1]))+rd^3}^(1/3)))))))^(-2/3))*(((((X[,9])/(exp(({(kx*(X[,6]))/(12*k_c^2*(1-
(X[,8])/(X[,7]))^2)}^(1/3)*(1+5*(z/(X[,3])))^(2/3)*{((X[,7])-
(X[,8]))/((X[,3]))}}*((z)/(X[,7])-1))))*L_obs)/(kin.vis))^(-
1/2)))+(C_IN*((2*(({(C1*rd^C2)/(C3*rd^C4-
log10(X[,1]))+rd^3}^(1/3)))/L_obs)*(2+log(4*L_obs/(2*({(C1*rd^C2)/(C3*rd^C4-
log10(X[,1]))+rd^3}^(1/3))))))+(C_IM*((((((X[,2])*(2*({(C1*rd^C2)/(C3*rd^C4-
log10(X[,1]))+rd^3}^(1/3)))^2*(1+(2*lambda/(2*({(C1*rd^C2)/(C3*rd^C4-
log10(X[,1]))+rd^3}^(1/3))))*(1.257+0.4*exp(-0.55*(2*({(C1*rd^C2)/(C3*rd^C4-
log10(X[,1]))+rd^3}^(1/3)))/lambda))))/(18*dyn.vis)
)*((X[,9])/(exp(({(kx*(X[,6]))/(12*k_c^2*(1-
(X[,8])/(X[,7]))^2)}^(1/3)*(1+5*(z/(X[,3])))^(2/3)*{((X[,7])-
(X[,8]))/((X[,3]))}}*((z)/(X[,7])-1)))))/L_obs)/((((((X[,2])*(2*({(C1*rd^C2)/(C3*rd^C4-
log10(X[,1]))+rd^3}^(1/3)))^2*(1+(2*lambda/(2*({(C1*rd^C2)/(C3*rd^C4-
log10(X[,1]))+rd^3}^(1/3))))*(1.257+0.4*exp(-0.55*(2*({(C1*rd^C2)/(C3*rd^C4-
```

```
log10(X[,1]))+rd^3}^(1/3)))/lambda))))/(18*dyn.vis)
)*((X[,9])/(exp(({(kx*(X[,6]))/(12*k_c^2*(1-
(X[,8])/(X[,7]))^2)}^(1/3)*(1+5*(z/(X[,3])))^(2/3)*{((X[,7])-
(X[,8]))/((X[,3]))})*((z)/(X[,7])-1)))))/L_obs)+(beta_IM)))^2))+(2.5*10^-
3*C_IT*(((((X[,2])*(2*({(C1*rd^C2)/(C3*rd^C4-
log10(X[,1]))+rd^3}^(1/3)))^2*(1+(2*lambda/(2*({(C1*rd^C2)/(C3*rd^C4-
log10(X[,1]))+rd^3}^(1/3))))*(1.257+0.4*exp(-0.55*(2*({(C1*rd^C2)/(C3*rd^C4-
log10(X[,1]))+rd^3}^(1/3)))/lambda))))/(18*dyn.vis))*(X[,5])^2)/kin.vis)^2)

)*(X[,7])/(((0.41*((X[,7])-(X[,8])))/((1+5*(z/(X[,3])))*((X[,7])-
(X[,8]))/((X[,3]))))))))^0.5)}))))



N <- 100000

x1 = runif(1*N,0.1,1.0)           #RH

x2 = runif(1*N,1500,2000)         #rho

x3 = runif(1*N,10,100)            #L

x4 = runif(1*N,0.02,0.10)         #z0

x5 = runif(1*N,0.1,0.5)           #u_star

x6 = runif(1*N,1,4)               #LAI

x7 = runif(1*N,0.15,0.77)         #h

x8 = runif(1*N,0.10,0.49)         #d

x9 = runif(1*N,1,5)               #U



x_1 = runif(1*N,0.1,1.0)           #RH

x_2 = runif(1*N,1500,2000)         #rho

x_3 = runif(1*N,10,100)            #L

x_4 = runif(1*N,0.02,0.10)         #z0

x_5 = runif(1*N,0.1,0.5)           #u_star

x_6 = runif(1*N,1,4)               #LAI

x_7 = runif(1*N,0.15,0.77)         #h

x_8 = runif(1*N,0.10,0.49)         #d

x_9 = runif(1*N,1,5)               #U



Y1 = matrix(c(x1,x2,x3,x4,x5,x6,x7,x8,x9), nrow=N)

X1 = data.frame(matrix(Y1, nrow=N))
```

```
Y2 = matrix(c(x_1,x_2,x_3,x_4,x_5,x_6,x_7,x_8,x_9), nrow=N)

X2 = data.frame(matrix(Y2, nrow=N))

a = sobol2007(model = model, X1 = X1, X2=X2, nboot = 2000, conf= 0.95);a
```

Codes for Sobol' sensitivity test for Kouznetsov and Sofiev (2012) parameterization

```
#Dry deposition parameterization by Kouznetsov and Sofiev (2012)

#Sobol sensitivity test: Grass (the code is similar for other LUCs)

#Change LUC dependent parameters for other LUCs

#Change sensitivity ranges for other LUCs

set.seed(5)

library(sensitivity)

library(boot)

C1 = 0.2789

C2 = 3.115

C3 = 5.415*10^-11

C4 = -1.399

dp_a = 10

dp_i = dp_a*10^-6

rd = dp_i/2

k_B = 1.38*10^-23

Temp = 273.15+25

P = 101325

d_air = 3.7208*10^-10

lambda = (k_B*Temp)/(sqrt(2)*3.1416*P*d_air^2)

dyn.vis = ((5*10^-8)*Temp)+4*10^-6

kin.vis = ((9*10^-8)*Temp)+10^-5

a  =  2*10^-3

kin.vis = ((9*10^-8)*Temp)+10^-5

C_S = 0.003
```

```
C_R = 0.3

u.Uh = 0.3

eta_impSt.e2 = 0

model<-function(X) ((2*((((X[,3])*a)/kin.vis)^(-
0.5))*(((kin.vis/(((1+(2*lambda/(2*({{C1*rd^C2)/(C3*rd^C4-
log10(X[,1]))+rd^3}^(1/3))))*(1.257+0.4*exp(-0.55*(2*({{C1*rd^C2)/(C3*rd^C4-
log10(X[,1]))+rd^3}^(1/3)))/lambda)))*k_B*Temp)/(3*3.1416*dyn.vis*(2*({{C1*rd^C2)/(C3*rd^C4-
log10(X[,1]))+rd^3}^(1/3))))))))^(-2/3))+(80*(X[,3])*(((2*({{C1*rd^C2)/(C3*rd^C4-
log10(X[,1]))+rd^3}^(1/3)))/(a))^2)*((((X[,3])*a)/kin.vis)^(0.5)))+(((2*((C_S+C_R/(X[,4]))^0.5
))/(X[,3]))*(ifelse(((((((X[,2])*(2*({{C1*rd^C2)/(C3*rd^C4-
log10(X[,1]))+rd^3}^(1/3)))^2*(1+(2*lambda/(2*({{C1*rd^C2)/(C3*rd^C4-
log10(X[,1]))+rd^3}^(1/3))))*(1.257+0.4*exp(-0.55*(2*({{C1*rd^C2)/(C3*rd^C4-
log10(X[,1]))+rd^3}^(1/3)))/lambda))))/(18*dyn.vis))*(X[,3]))/a) -
(((((C_S+C_R/(X[,4]))^0.5))^-1)^2*(((X[,3])*a)/kin.vis))^(-0.5))>0.15,(exp((-
0.1/(((((((X[,2])*(2*({{C1*rd^C2)/(C3*rd^C4-
log10(X[,1]))+rd^3}^(1/3)))^2*(1+(2*lambda/(2*({{C1*rd^C2)/(C3*rd^C4-
log10(X[,1]))+rd^3}^(1/3))))*(1.257+0.4*exp(-0.55*(2*({{C1*rd^C2)/(C3*rd^C4-
log10(X[,1]))+rd^3}^(1/3)))/lambda))))/(18*dyn.vis))*(X[,3]))/a) -
(((((C_S+C_R/(X[,4]))^0.5))^-1)^2*(((X[,3])*a)/kin.vis))^(-0.5)) - 0.15 ) )-
(1/sqrt(((((((X[,2])*(2*({{C1*rd^C2)/(C3*rd^C4-
log10(X[,1]))+rd^3}^(1/3)))^2*(1+(2*lambda/(2*({{C1*rd^C2)/(C3*rd^C4-
log10(X[,1]))+rd^3}^(1/3))))*(1.257+0.4*exp(-0.55*(2*({{C1*rd^C2)/(C3*rd^C4-
log10(X[,1]))+rd^3}^(1/3)))/lambda))))/(18*dyn.vis))*(X[,3]))/a) -
(((((C_S+C_R/(X[,4]))^0.5))^-1)^2*(((X[,3])*a)/kin.vis))^(-0.5))-
0.15)))),(eta_impSt.e2)))*((((((X[,2])*(2*({{C1*rd^C2)/(C3*rd^C4-
log10(X[,1]))+rd^3}^(1/3)))^2*(1+(2*lambda/(2*({{C1*rd^C2)/(C3*rd^C4-
log10(X[,1]))+rd^3}^(1/3))))*(1.257+0.4*exp(-0.55*(2*({{C1*rd^C2)/(C3*rd^C4-
log10(X[,1]))+rd^3}^(1/3)))/lambda))))/(18*dyn.vis))*(X[,3]))/a)-
((C_S+C_R/(X[,4]))^0.5)*(((X[,3])*a)/kin.vis)^-0.5))+((((X[,2])*(2*({{C1*rd^C2)/(C3*rd^C4-
log10(X[,1]))+rd^3}^(1/3)))^2*(1+(2*lambda/(2*({{C1*rd^C2)/(C3*rd^C4-
log10(X[,1]))+rd^3}^(1/3))))*(1.257+0.4*exp(-0.55*(2*({{C1*rd^C2)/(C3*rd^C4-
log10(X[,1]))+rd^3}^(1/3)))/lambda))))/(18*dyn.vis))*9.81))



N <- 100000

x1 = runif(1*N,0.1,1.0)            #RH

x2 = runif(1*N,1500,2000)          #rho

x3 = runif(1*N,0.1,0.5)            #u_star

x4 = runif(1*N,1,4)                #LAI

x_1 = runif(1*N,0.1,1.0)           #RH

x_2 = runif(1*N,1500,2000)         #rho

x_3 = runif(1*N,0.1,0.5)           #u_star

x_4 = runif(1*N,1,4)               #LAI

Y1 = matrix(c(x1,x2,x3,x4), nrow=N)

X1 = data.frame(matrix(Y1,nrow=N))
```

```
Y2 = matrix(c(x_1,x_2,x_3,x_4), nrow=N)

X2 = data.frame(matrix(Y2, nrow=N))

a = sobol2007(model = model, X1 = X1, X2=X2, nboot = 2000, conf = 0.95);a
```

Codes for Sobol' sensitivity test for Zhang and He (2014) parameterization

```
#Dry deposition parameterization by Zhang and He (2014)

#Sobol sensitivity test: Grass (the code is similar for other LUCs)

#Change LUC dependent parameters for other LUCs

#Change sensitivity ranges for other LUCs

set.seed(5)

library(sensitivity)

library(boot)

C1 = 0.4809

C2 = 3.082

C3 = 3.110*10^-11

C4 = -1.428

dp_a = 1

dp_i = dp_a*10^-6

rd = dp_i/2

k_B = 1.38*10^-23

Temp = 273.15+25

P = 101325

d_air = 3.7208*10^-10

lambda = (k_B*Temp)/(sqrt(2)*3.1416*P*d_air^2)

dyn.vis = ((5*10^-8)*Temp)+4*10^-6

z = 2

zR = 3.5

k_c = 0.41

# For PM2.5-10

b1= -7.9*10^-2
```

```
b2= 1.0*10^0

b3 = 6.6*10^-1

c1= 5.1*10^0

c2 = -4.2*10^0

c3 = 9.9*10^-1

LAImax = 4

model<- function(X) (1/(1/((((X[,2])*((2*({(C1*rd^C2)/(C3*rd^C4-
log10(X[,1]))+rd^3}^(1/3))))^2*(1+(2*lambda/(2*({(C1*rd^C2)/(C3*rd^C4-
log10(X[,1]))+rd^3}^(1/3))))*(1.257+0.4*exp(-0.55*(2*({(C1*rd^C2)/(C3*rd^C4-
log10(X[,1]))+rd^3}^(1/3)))/lambda))))/(18*dyn.vis))*9.81))+(1/(((log(zR/(X[,5]))-
(ifelse((z/(X[,4])) <= 0, (2*log(0.5*{1+(1-16*(z/(X[,4])))^0.5})),(-
5*(z/(X[,4])))))))/(k_c*(X[,3])))+(1/((b1*(X[,3])+b2*(X[,3])^2+b3*(X[,3])^3)*(exp((c1*(X[,3])+c
2*(X[,3])^2+c3*(X[,3])^3)*(X[,6])/LAImax)-1))))))



N <- 100000

x1 = runif(1*N,0.1,1.0)          #RH

x2 = runif(1*N,1500,2000)        #rho

x3 = runif(1*N,0.1,0.5)          #u_star

x4 = runif(1*N,10,100)           #L

x5 = runif(1*N,0.02,0.10)        #z0

x6 = runif(1*N,1,4)              #LAI

x_1 = runif(1*N,0.1,1.0)          #RH

x_2 = runif(1*N,1500,2000)        #rho

x_3 = runif(1*N,0.1,0.5)          #u_star

x_4 = runif(1*N,10,100)           #L

x_5 = runif(1*N,0.02,0.10)        #z0

x_6 = runif(1*N,1,4)              #LAI

Y1 = matrix(c(x1,x2,x3,x4,x5,x6), nrow=N)

X1 = data.frame(matrix(Y1,nrow=N))

Y2 = matrix(c(x_1,x_2,x_3,x_4,x_5,x_6), nrow=N)

X2 = data.frame(matrix(Y2, nrow=N))

a = sobol2007(model = model, X1 = X1, X2=X2, nboot = 2000, conf = 0.95);a
```

Codes for Sobol' sensitivity test for Zhang and Shao (2014) parameterization

```
#Dry deposition parameterization by Zhang and Shao (2014)

#Sobol sensitivity test: Grass (the code is similar for other LUCs)

#Change LUC dependent parameters for other LUCs

#Change sensitivity ranges for other LUCs

set.seed(5)

library(sensitivity)

library(boot)

C1 = 0.2789

C2 = 3.115

C3 = 5.415*10^-11

C4 = -1.399

dp_a = 10

dp_i = dp_a*10^-6

rd = dp_i/2

k_B = 1.38*10^-23

Temp = 273.15+25

P = 101325

d_air = 3.7208*10^-10

lambda = (k_B*Temp)/(sqrt(2)*3.1416*P*d_air^2)

dyn.vis = ((5*10^-8)*Temp)+4*10^-6

kin.vis = ((9*10^-8)*Temp)+10^-5

Temp = 273.15+25

k =  0.41

z =  1

zd = 0.20

z0 = 0.3/1000

h_c = 0.3*z0

B1 = 0.45
```

```
d_c = 0.005

nB = 0.5

C_B = 0.467

beta_IM = 0.6

Ain = 150

b = 2

B2 = 3

Beta = 200

C_1 = 6

C_2 = 0.1

lambda_FAI = 0.4

n_FAI = (lambda_FAI)/(h_c*d_c)

q = (3.1416*d_c^2)/4

eta_BAI = n_FAI*q

lambda_FAIe = ((lambda_FAI)/(1-eta_BAI)^C_2)*exp((-C_1*lambda_FAI)/(1-eta_BAI)^C_2)

Tau_c_BY_Tau = (Beta*lambda_FAIe)/(1+Beta*lambda_FAIe)

Cd = 1/6

model<- function(X) ((((1/(((((X[,2])*(dp_i)^2*(1+(2*lambda/(2*({(C1*rd^C2)/(C3*rd^C4-
log10(X[,1]))+rd^3}^(1/3))))*(1.257+0.4*exp(-0.55*(2*({(C1*rd^C2)/(C3*rd^C4-
log10(X[,1]))+rd^3}^(1/3)))/lambda))))/(18*dyn.vis))*9.81)))+(((((exp(-
b*sqrt(((((X[,2])*(dp_i)^2*(1+(2*lambda/(2*({(C1*rd^C2)/(C3*rd^C4-
log10(X[,1]))+rd^3}^(1/3))))*(1.257+0.4*exp(-0.55*(2*({(C1*rd^C2)/(C3*rd^C4-
log10(X[,1]))+rd^3}^(1/3)))/lambda))))/(18*dyn.vis))*(X[,3]))/d_c)))*(((X[,3])/(X[,4])*h_c)
)*(((((C_B*((kin.vis/(((1+(2*lambda/(2*({(C1*rd^C2)/(C3*rd^C4-
log10(X[,1]))+rd^3}^(1/3))))*(1.257+0.4*exp(-0.55*(2*({(C1*rd^C2)/(C3*rd^C4-
log10(X[,1]))+rd^3}^(1/3)))/lambda)))*k_B*Temp)/(3*3.1416*dyn.vis*(2*({(C1*rd^C2)/(C3*rd^C4
-log10(X[,1]))+rd^3}^(1/3)))))))^(-2/3)*(((X[,4])*d_c)/(kin.vis))^(nB-
1))+(((((((X[,2])*(dp_i)^2*(1+(2*lambda/(2*({(C1*rd^C2)/(C3*rd^C4-
log10(X[,1]))+rd^3}^(1/3))))*(1.257+0.4*exp(-0.55*(2*({(C1*rd^C2)/(C3*rd^C4-
log10(X[,1]))+rd^3}^(1/3)))/lambda))))/(18*dyn.vis))*(X[,3]))/d_c)/((((((X[,2])*(dp_i)^2*(1
+(2*lambda/(2*({(C1*rd^C2)/(C3*rd^C4-log10(X[,1]))+rd^3}^(1/3))))*(1.257+0.4*exp(-
0.55*(2*({(C1*rd^C2)/(C3*rd^C4-
log10(X[,1]))+rd^3}^(1/3)))/lambda))))/(18*dyn.vis))*(X[,3]))/d_c)+beta_IM))^2)+(Ain*(X[,3]
)*(10^((-((((X[,2])*(dp_i)^2*(1+(2*lambda/(2*({(C1*rd^C2)/(C3*rd^C4-
log10(X[,1]))+rd^3}^(1/3))))*(1.257+0.4*exp(-0.55*(2*({(C1*rd^C2)/(C3*rd^C4-
log10(X[,1]))+rd^3}^(1/3)))/lambda))))/(18*dyn.vis))*(X[,3]))/d_c)))*(2*(2*(2*({(C1*rd^C2)/(C3
*rd^C4-
log10(X[,1]))+rd^3}^(1/3)))/d_c))))*(Tau_c_BY_Tau/Cd))+(1+Tau_c_BY_Tau)*((kin.vis/(((1+(2*l
ambda/(2*({(C1*rd^C2)/(C3*rd^C4-log10(X[,1]))+rd^3}^(1/3))))*(1.257+0.4*exp(-
0.55*(2*({(C1*rd^C2)/(C3*rd^C4-
log10(X[,1]))+rd^3}^(1/3)))/lambda)))*k_B*Temp)/(3*3.1416*dyn.vis*(2*({(C1*rd^C2)/(C3*rd^C4
-log10(X[,1]))+rd^3}^(1/3)))))))^-1+10^((-3/(((((X[,2])*((2*({(C1*rd^C2)/(C3*rd^C4-
log10(X[,1]))+rd^3}^(1/3))))^2*(1+(2*lambda/(2*({(C1*rd^C2)/(C3*rd^C4-
```

```
log10(X[,1]))+rd^3}^(1/3))))*(1.257+0.4*exp(-0.55*(2*({(C1*rd^C2)/(C3*rd^C4-
log10(X[,1]))+rd^3}^(1/3)))/lambda))))/(18*dyn.vis))*(X[,3])^2)/kin.vis))))+((((X[,2])*((2*
({(C1*rd^C2)/(C3*rd^C4-
log10(X[,1]))+rd^3}^(1/3))))^2*(1+(2*lambda/(2*({(C1*rd^C2)/(C3*rd^C4-
log10(X[,1]))+rd^3}^(1/3))))*(1.257+0.4*exp(-0.55*(2*({(C1*rd^C2)/(C3*rd^C4-
log10(X[,1]))+rd^3}^(1/3)))/lambda))))/(18*dyn.vis))*9.81))^-1)-
(1/(((((X[,2])*(dp_i)^2*(1+(2*lambda/(2*({(C1*rd^C2)/(C3*rd^C4-
log10(X[,1]))+rd^3}^(1/3))))*(1.257+0.4*exp(-0.55*(2*({(C1*rd^C2)/(C3*rd^C4-
log10(X[,1]))+rd^3}^(1/3)))/lambda))))/(18*dyn.vis))*9.81))))/(exp(((((1+(((((X[,2])*((2*({
(C1*rd^C2)/(C3*rd^C4-log10(X[,1]))+rd^3}^(1/3))))^2*(1+(2*lambda/(2*({(C1*rd^C2)/(C3*rd^C4-
log10(X[,1]))+rd^3}^(1/3))))*(1.257+0.4*exp(-0.55*(2*({(C1*rd^C2)/(C3*rd^C4-
log10(X[,1]))+rd^3}^(1/3)))/lambda))))/(18*dyn.vis))*9.81)^2/(X[,3])^2))^0.5)/(k*(X[,3])))*
(log((z-zd)/(h_c-zd))))/(1/(((((X[,2])*(dp_i)^2*(1+(2*lambda/(2*({(C1*rd^C2)/(C3*rd^C4-
log10(X[,1]))+rd^3}^(1/3))))*(1.257+0.4*exp(-0.55*(2*({(C1*rd^C2)/(C3*rd^C4-
log10(X[,1]))+rd^3}^(1/3)))/lambda))))/(18*dyn.vis))*9.81)))))))^-1)
```

```
N <- 100000

x1 = runif(1*N,0.1,1.0)            #RH

x2 = runif(1*N,1500,2000)          #rho

x3 = runif(1*N,0.1,0.5)            #u_star

x4 = runif(1*N,1,5)                #U

x_1 = runif(1*N,0.1,1.0)           #RH

x_2 = runif(1*N,1500,2000)         #rho

x_3 = runif(1*N,0.1,0.5)           #u_star

x_4 = runif(1*N,1,5)               #U

Y1 = matrix(c(x1,x2,x3,x4), nrow=N)

X1 = data.frame(matrix(Y1, nrow=N))

Y2 = matrix(c(x_1,x_2,x_3,x_4), nrow=N)

X2 = data.frame(matrix(Y2, nrow=N))

a = sobol2002(model = model, X1 = X1, X2=X2, nboot = 2000, conf= 0.95);a
```

2 CHAPTER 2: Improvement in atmosphere-terrestrial exchange parameterizations of gaseous elemental mercury for application in chemical transport models

Abstract

In chemical transport models (CTMs) for mercury (Hg), net elemental Hg^0 surface-atmosphere exchange is parameterized based on atmospheric dry deposition of Hg^0 and re-emission from terrestrial surfaces. Despite extensive use of the resistance-based Hg^0 deposition and subsequent re-emission approaches in models, there are gaps in performance evaluations of these implementations against field observations of net Hg^0 exchange. In this study, we evaluate performance of existing net exchange parameterizations (referred to here as the base model) by comparing modeled fluxes of Hg^0 to fluxes measured using micrometeorological techniques. Comparisons were performed with measurements conducted in two terrestrial ecosystems: a grassland site in Switzerland and an Arctic tundra site in Alaska, U.S. that spanned two seasons each: summer and winter. The base model included the dry deposition parameterization from Zhang et al. (2003) and the soil Hg^0 re-emission scheme from the global CTM GEOS-Chem by Song et al. (2015). Comparisons of modeled and measured Hg^0 fluxes showed large discrepancies for both sites, particularly in the summer months when the base model overestimated daytime net deposition by factors greater than 3 and 10, respectively. In addition, the base model was unable to capture a measured nighttime net Hg^0 deposition at both sites. In winter months, the base model showed insufficient diel variability in modeled fluxes compared to field measurements and was unable to capture a measured net deposition. To improve overall performance of Hg^0 exchange simulation, we conducted a step-wise model calibration, and recommend the following changes be made to the base model: (i) reduce stomatal uptake of Hg^0 over vegetated ecosystems (grassland and tundra here) by a factor 5-7; (ii) to increase nighttime net Hg^0 deposition, increase ground and cuticular uptake by reducing the respective resistance terms by factors of 3-4 and 2-4; and (iii) implement a new soil re-emission parameterization to produce larger simulated daytime and reduced nighttime emissions. We conclude that, in general, the use of resistance-based models combined with a soil re-emission flux parameterization is able to reproduce observed diel and seasonal Hg^0 exchange in terrestrial ecosystems. However, continued improvement through model testing against reliable ecosystem-level flux and foliar uptake data is needed.

2.1 Introduction

Atmosphere-surface exchange of gaseous elemental mercury (Hg^0) is an important component of the global Hg budget (Zhu et al., 2016; Eckley et al., 2016). Despite advances in Hg^0 exchange flux measurements and their incorporation in chemical transport models (CTMs; Kwon and Selin, 2016), there remain large uncertainties with regard to the magnitudes and mechanistic understanding of the bi-directional terrestrial surface-atmosphere exchange processes of Hg^0 (Agnan et al., 2016). Hg^0 is the dominant form (ca. 95%) of Hg in the atmosphere (Millhollen et al., 2006), and deposition of Hg^0 can contribute significantly to total Hg deposition, particularly over vegetated ecosystems (Obrist et al, 2018; Jiskra et al., 2018). For example, evidence from stable Hg isotope studies suggest that atmospheric Hg^0 contributes 57–94% of total Hg in ecosystems (Demers et al. 2013; Zheng et al. 2016; Enrico et al., 2016; Obrist et al. 2017; Jiskra et al. 2015; Wang et al. 2016a). Moreover, it is also estimated that up to 65% of total present-day Hg emissions to the atmosphere could be attributed to secondary emission (re-emission) of Hg^0 from previous deposition of Hg from terrestrial and aquatic surfaces ('legacy emissions'; Corbitt et al., 2011; Amos et al., 2013). Given the significance of atmospheric Hg^0 as a source and sink to terrestrial ecosystems, and a complex bi-directional exchange behavior that includes both deposition and emission processes, an adequate framework to parameterize atmosphere-surface exchange processes of Hg^0 in CTMs is critical.

In most CTMs, Hg^0 dry deposition to and emission from terrestrial surfaces are parameterized separately (i.e., de-coupled treatment). A resistance-based approach

(Wesely, 1989; Walmsley and Wesely, 1996; Wesely and Hicks, 2000; Zhang et al., 2003) is commonly used to model dry deposition. The resistance-based deposition algorithm is implemented in all major global CTMs including GLEMOS (Travnikov et al., 2009), GEOS-Chem (Selin et al., 2008; Song et al., 2015), GEM-MACH-Hg (Dastoor et al., 2015), ECHMERIT (Jung et al., 2009), and CAM-Chem (Lei et al., 2013). Similarly, regional models such as WRF-Chem (Gencarelli et al., 2017) also use the resistance-based approach for Hg^0 deposition. In addition, adaptation to a coupled bi-directional exchange parameterization is conducted as well, but is limited, as for example in the CMAQ modeling system (CMAQ-Hem and CCLM-CMAQ; Bash, 2010). Currently, there exist large uncertainties in modeling dry gaseous deposition using resistance-based algorithms (Wu et al., 2011). These uncertainties stem from lack of process-based understanding of Hg^0 deposition and emissions (Obrist et al., 2018), the model's inability to fully describe physiological processes involved such as vegetation stomatal responses to various environmental conditions (Wu et al., 2011), lack of consideration of terrain complexity (Hicks et al., 2016), and exclusion of fast, within-canopy chemical reactions (Wesely and Hicks, 2000). In an inter-comparison study of four resistance-based deposition models of reactive nitrogen species, Flechard et al. (2011) reported factors of 2 to 3 disagreement between the models. However, in addition to model inter-comparison, there is a need for evaluation of the existing and newly developed dry deposition parameterizations against field observations for a suite of atmospheric species (Zhang et al., 2009; Wu et al., 2011) and environmental settings, which for Hg^0 is largely lacking.

To estimate Hg^0 emissions to the atmosphere from soils and vegetative surfaces, several empirical models have been developed (Poissant and Casimir, 1998; Xu et al., 1999; Zhang et al., 2001; Lin and Tao, 2003; Bash et al., 2004; Gbor et al., 2006; Lin et al., 2010). These models are based primarily on measured field flux measurements and observed environmental drivers such as air and soil temperatures, solar radiation, soil moisture and soil Hg content (Zhu et al., 2016). Several of these formulations have been implemented in CTMs, with some modifications, to parameterize Hg^0 fluxes from terrestrial surfaces. For example, in GEOS-Chem (Song et al., 2015), soil re-emission is parameterized following Zhang et al. (2001), in which re-emission of Hg^0 is a function of incident solar radiation at the ground surface. Currently, due to knowledge gaps in a fundamental mechanistic understanding of Hg^0 exchange between air and soil and air and vegetation (Pirrone et al., 2013; Zhu et al., 2016), it is unfeasible to implement a fully mechanistic surface-atmosphere exchange parameterizations in CTMs.

In this study, we aim to test existing parameterizations of Hg^0 exchange implemented in CTMs by evaluation using high quality exchange flux measurements at the ecosystem-level (i.e., including both soil and vegetation exchanges) at two sites and two seasons. Our comparison includes the most commonly used dry gaseous Hg^0 deposition scheme from Zhang et al. (2003) and a soil re-emission scheme implemented in GEOS-Chem (Song et al., 2015). We evaluate model performance against measured whole-ecosystem net exchange fluxes of Hg^0 from a grassland in Switzerland and an Arctic tundra site in Alaska. The objectives of this study are to: (1) assess the performance of the current dry deposition and soil re-emission parameterizations in modeling net Hg^0 exchange fluxes; (2)

characterize which model parameters most strongly influence modeled fluxes and how their adjustment improves comparison with measured field fluxes; and (3) provide suggestions for future treatment and further development of Hg^0 atmosphere-terrestrial surface exchange parameterizations in CTMs for a variety of environmental settings.

2.2 Parameterizations of Hg^0 atmosphere-terrestrial exchange examined

The resistance-based model of Zhang et al. (2003) was used to model deposition flux of Hg^0 because this is the most up-to-date and widely used resistance-based deposition parameterization. The framework of the Zhang et al. (2003) model is similar to the resistance analogy proposed by Wesely (1989). In both models, three parallel resistances to gaseous deposition are assumed: aerodynamic, boundary or quasi-laminar, and surface resistances. The model of Zhang et al. (2003) uses leaf area index (LAI) to scale Hg^0 uptake by foliage and uses updated formulations for non-stomatal (e.g., cuticular) and ground deposition. The model allows selection of land use category (LUC) parameters that are specific for grassland (i.e., long grass) and tundra. The major resistance expressions in the Zhang et al. (2003) parameterization are described in section 2.2.1. To model soil re-emission of Hg^0, the parameterization used in the current GEOS-Chem (v-9-02) Hg model (Song et al., 2015) was applied. The soil re-emission modeling framework is described in section 2.2.2.

2.2.1 Modeling dry deposition of Hg^0

In global 3-D CTMs, the uptake of gaseous species at the surface is characterized by downward dry deposition flux (F_d) to be applied at the lowest model layer located at finite distance, z, from the surface. Vertical flux in the surface layer is assumed to be conserved for a species, and its dry deposition velocity (v_d) is calculated as $v_d = F_d(z)/C_z$, where C_Z is gaseous concentration at height z. In CTMs that use a resistance-based dry deposition parameterization, v_d for gaseous species such as Hg^0 is parameterized using the electrical resistance analogy (Zhang et al., 2003) as

$$v_d = \frac{1}{R_a+R_b+R_s}, \quad (1)$$

where R_a is the aerodynamic resistance, R_b is the quasi-laminar sublayer resistance, and R_s is the bulk surface resistance. The term R_s in Eq. (1) has two components: the stomatal resistance (R_{st}) and the non-stomatal resistance (R_{nst}). In the paper by Zhang et al. (2003), R_s is parameterized as

$$\frac{1}{R_s} = \frac{1-W_{st}}{R_{st}+R_m} + \frac{1}{R_{nst}}, \quad (2)$$

where W_{st} is the fraction of stomatal blockage under wet conditions. R_{st} is directly proportional to minimum stomatal resistance (r_{stmin}), which is a LUC-dependent parameter based on water vapor transfer to leaves under optimal conditions (Zhang et al., 2003). The R_{nst} term is parameterized by Zhang et al. (2003) as

$$\frac{1}{R_{nst}} = \frac{1}{R_{ac}+R_{gd}} + \frac{1}{R_{cut}}, \quad (3)$$

where R_{ac} is the in-canopy aerodynamic resistance, R_{gd} is the ground resistance, and R_{cut} is the cuticular resistance. R_{gd} and R_{cut} are gaseous species dependent parameters. For any species *i* (except SO_2 and O_3), Zhang et al. (2003) suggested the following scaling approach to calculate $R_x(i)$ $(e.g., R_x = R_{gd}\ or\ R_{cut})$:

$$\frac{1}{R_x(i)} = \frac{\beta}{R_x(O_3)} + \frac{\alpha}{R_x(SO_2)}, \quad (4)$$

where α and β are scaling factors for chemical species solubility and half-redox reactivity, respectively. For Hg^0, α = 0 and β = 0.1 (Wang et al., 2014). The expressions used for calculating individual resistance terms shown in Eqs. (2-3) and LUC-specific base resistance parameter values can be found in the paper by Zhang et al. (2003) and references therein.

2.2.2 Modeling re-emission of Hg^0

In GEOS-Chem (version 9-02; http://www.geos-chem.org), re-emission flux of Hg^0 from terrestrial surfaces (E_{soil}) is parameterized as a function of solar radiation and soil Hg concentration (Song et al., 2015) as

$$E_{soil} = \gamma C_{soil} \exp\left(1.1 \times 10^{-3} \times R_g\right), \quad (5)$$

where C_{soil} is the soil Hg concentration (ng g^{-1}) and R_g is the solar radiation flux at the ground (W m^{-2}). The scaling factor γ (1.2×10^{-2} g m^{-2} h^{-1}) is used to account for the global mass balance of the preindustrial model simulation. Selin et al. (2008) used the following

expression to calculate R_g as functions of solar radiation (SR) at top of canopy and leaf area index (LAI),

$$R_g = SR \exp\left(\frac{-\alpha LAI}{\cos\theta}\right), \quad (6)$$

where θ is the solar zenith angle and $\alpha = 0.5$ is an extinction coefficient assuming random leaf angle distributions.

2.3 Methods

2.3.1 Data description

Measured micrometeorological net exchange flux data of Hg^0 were collected from two ecosystems: grassland and tundra (long grass and tundra LUCs, respectively, in the Zhang et al., 2003 parameterization) were used for model evaluation. The data of Hg^0 exchange over a sub-alpine grassland site at Früebüel (47° 6′ 47'' N, 8° 32'16'' E, elevation of 1000 m) in central Switzerland were acquired from Fritsche et al. (2008). At this site, Hg^0 exchange fluxes were measured using the aerodynamic method over a full year (September 2005 to August 2006). The second site used for model evaluation was from Toolik Field Station (Obrist et al., 2017). This Arctic tundra site is located in the northern foothills of the Brooks Range, Alaska (68° 38' N, 149° 38' W, elevation of 760 m). Hg^0 flux exchange measurements were conducted using the aerodynamic method at the Toolik Field station site from September 2014 to September 2016. In this study, we used exchange flux and meteorological data for year 2016 from this site for model evaluation. For both sites, the data included hourly averages for atmospheric Hg^0 concentrations, Hg^0 net exchange

fluxes, and corresponding values for the following meteorological variables: wind speed, friction velocity, air temperature, surface soil temperature, solar radiation, atmospheric pressure, relative humidity, and Monin-Obukhov length. For analysis of 24-hour temporal patterns (further referred to as *diel variation),* the aforementioned measured variables were averaged for hourly values for July and August (at both sites) and for December (grassland site) and January (tundra site). In addition, to reduce noise in measured flux variability and better track the diel patterns of Hg^0 fluxes, a 5-hour moving average filter was used for measured Hg^0 fluxes. This filtering was done due to the large variability in measured ½-hourly averaged flux data, which stems from difficulties in measuring small exchange fluxes against a large background concentration (see, e.g., Fritsche et al., 2008; Obrist et al., 2017). For soil Hg^0 emission model simulations, we used measured soil Hg concentrations of 100.8 ng g^{-1} at the grassland and 100.0 ng g^{-1} at the tundra site.

2.3.2 Model evaluation and calibration

To evaluate the performance of the base parameterizations (i.e., Zhang et al., 2003 and Song et al., 2015), LUC-specific (i.e., long grass or tundra) simulations were performed. Hourly averaged meteorological and atmospheric concentration data from the grassland and tundra sites were used as model inputs. To account for seasonal variability in modeling analysis, simulations were conducted for typical summer and winter meteorological conditions for each of the two ecosystems, which included July and August for summer measurements and December for winter measurements at the grassland site and January

for the tundra site. Agreement between the measured and modeled exchange fluxes was evaluated using degree of agreement (*d*), calculated using Eq. (7):

$$d = 1 - \frac{\sum_{i=1}^{n}(O_i - M_i)^2}{\sum_{i=1}^{n}(|O_i| + |M_i|)^2}, \quad (7)$$

where O_i is the observed net flux, M_i the modeled net flux, and n the number of observations. A *d*-value of 1 indicates perfect agreement between observed and modeled net flux.

Based on the performance of the base model, systematic adjustments to the default model parameters were performed through application of adjustment factors. This modulation of specific model parameters serves as model calibration, with the main objective to increase the overall agreement between the modeled and measured exchange fluxes (i.e., to maximize the *d*-value using Eq. 7) and to assess which model settings result in the most relevant changes (both in magnitude and direction) of the net exchange fluxes. Model response (referred to as the adjusted model) to these adjustments are assessed and discussed in detail, and suggestions are made to improve the treatment of net exchange processes of Hg^0 in CTMs. To optimize the base model, a step-wise manual calibration was performed in the following order: (i) reduction in modeled stomatal uptake of Hg^0, (ii) increase in modeled non-stomatal uptake of Hg^0, and (iii) revision to soil Hg^0 re-emission parameters. Because only three parameters in the base dry deposition model were selected for calibration, a manual step-wise method, as opposed to a sophisticated numerical optimization tool such as random-hyper parameter optimization (Bergstra et al., 2012) or Bayesian optimization (Snoek et al., 2012), was deemed a reasonable choice.

2.4 Results and discussion

In sections 2.4.1 and 2.4.2, measured ecosystem-level atmosphere-terrestrial surface exchange fluxes of Hg^0 from both sites are compared with modeled net exchange fluxes using the base parameterizations. Based on the evaluation results obtained using the base model configuration, a step-wise model parameter calibration was performed to assess the changes in net exchange behavior of Hg^0 as a function of modulating certain default model parameters in sections 2.4.3 and 2.4.4. In section 2.4.5, growing season vegetation Hg uptake was calculated based on base and adjusted model parameterizations of Hg^0 dry deposition and compared to observed Hg accumulation in plant leaves at the grassland and tundra sites as an additional model constraint.

2.4.1 Evaluation of modeled net exchange fluxes in summer using the base model

2.4.1.1 *Temperate grassland site at Früebüel, Switzerland*

The hourly averaged modeled (blue lines in Figure 1) and measured (black dotted lines) net exchange fluxes of Hg^0 (F_{net}) for the summer months using the base model with the default dry deposition and re-emission parameterizations are shown in Fig. 1 (panel A: July 2006; panel B: August 2006). At this site, a leaf area index (LAI) of 5.0 m^2 m^{-2} was used for July and August month simulations derived from monthly averaged MODerate resolution Imaging Spectroradiometer (MODIS) -Terra (ORNL DAAC, 2017).

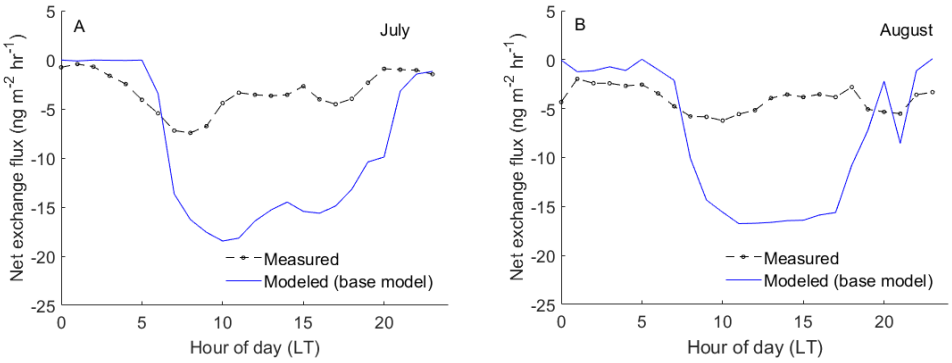

Figure 1. Comparison of averaged diel variations of measured (black) and modeled (blue; base model) net exchange fluxes of Hg^0 at the grassland site (Früebüel, Switzerland) in summer (LT = local time): A) July 2006 and B) August 2006.

Diel Hg^0 exchange (Fig. 1) of modeled F_{net} was primarily controlled by the surface resistance term (R_s in Eq. 1) of the dry deposition model, which includes both stomatal and non-stomatal uptake. Of the two deposition pathways, stomatal uptake dominated over non-stomatal uptake. Increased net deposition of Hg^0 in the daytime compared to nighttime deposition was attributed primarily to stomatal uptake during daytime (R_{st} term in Eq. 2). Comparison between measured and modeled F_{net} in Fig. 1 suggests that while the base model was able to capture an observed diel pattern of fluxes, it considerably overestimated net deposition of Hg^0 during daytime. In addition, the measurements showed a significant nighttime deposition of Hg^0 during summer nights in the range of – 0.44 to –5.51 ng m^{-2} hr^{-1} (for both months), which the model was unable to reproduce and instead predicted nighttime fluxes near zero (i.e., neither net deposition nor net emission).

In July (Fig. 1A), measured F_{net} showed bimodal peaks in deposition at 1100 and 1400 LT. An observed decline in measured net deposition at approximately 1300 LT can be caused by leaf stomatal closure, or alternatively by increased soil Hg^0 emissions during midday when solar radiation and soil surface temperature peak (both of which are positively

correlated to soil Hg^0 emissions; Agnan et al., 2016), reducing mid-day net dry Hg^0 deposition. The base model was able to reproduce the observed bimodal flux distribution during daytime, albeit with a small time lag of 1 to 2 hours. However, the absolute differences in measured and modeled F_{net} are large (10.81 ng m^{-2} hr^{-1}) throughout daytime. For example, mean measured and modeled daytime F_{net} (0700 to 2000 LT) were -4.17 ng m^{-2} hr^{-1} and -14.98 ng m^{-2} hr^{-1}, respectively, showing that the base model overestimated measured deposition by a factor of >3.5. In addition, at nighttime (2100 to 0600 LT), the base model largely failed to reproduce an observed net deposition, resulting in model underestimation of nighttime net deposition by a factor of 2. On a daily basis (daytime and nighttime), the base model overestimated the measured F_{net} (i.e., net deposition) by a factor of ca. 2 in July (daily sum measured F_{net} of -77.49 ng m^{-2} day^{-1} versus -219.32 ng m^{-2} day^{-1} predicted by the base model).

In August, modeled and measured F_{net} exhibited patterns similar to July, with a few differences (Fig. 1B): (i) the base model showed a unimodal pattern of net exchange, and (ii) a midday decline in net exchange due to possible stomatal closure was not evident in the modeled F_{net}, which was in relatively good accord with observations. Consistent with the July simulation, however, the base model overestimated measured daytime (0700 to 2000 LT) F_{net} by a factor of >2.5 and underestimated measured nighttime (2100 to 0600 LT) F_{net} by a factor >2. On a daily basis, the base model overestimated measured F_{net} by a factor of ca. 3 (daily sum of measured F_{net} of -97.46 ng m^{-2} day^{-1} versus -191.53 ng m^{-2} day^{-1} predicted by the base model).

2.4.1.2 *Arctic tundra site at Toolik Field Station, Alaska*

Comparison between the hourly averaged modeled and measured F_{net} for the summer months (July and August of 2016) at the tundra site is shown in Fig. 2. At this site, average LAIs of 1.5 and 2.0 $m^2\ m^{-2}$ (ORNL, 2017) were used for July and August base model simulations, respectively. Although measured fluxes exhibit a net Hg^0 emission during midday in July (Fig. 2A), average daytime (0400 to 2300 LT) fluxes showed a small net deposition (−0.11 ng $m^{-2}\ hr^{-1}$). The modeled net deposition flux was substantially higher throughout daytime (-2.96 ng $m^{-2}\ hr^{-1}$). In the short nighttime period (0000 to 0300 LT), measured F_{net} was dominated by a strong Hg^0 deposition (mean of -2.62 ng $m^{-2}\ hr^{-1}$), which the base model was unable to reproduce (i.e., mean of -0.46 ng $m^{-2}\ hr^{-1}$). Comparison between measured and modeled fluxes at nighttime shows that the base model underestimated measured net deposition by a factor >5.5.

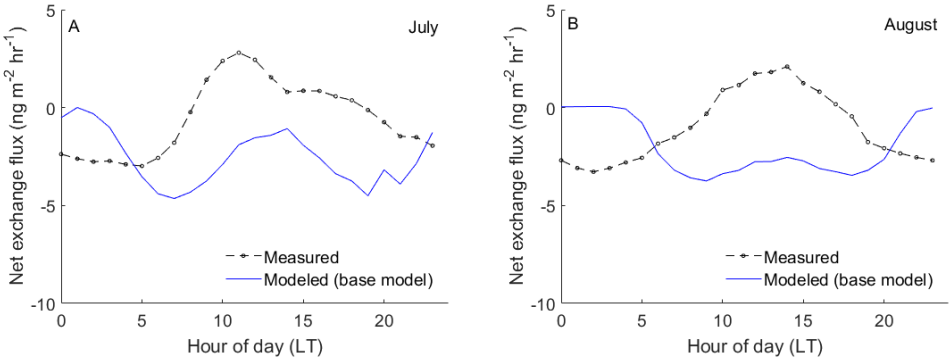

Figure 2. Comparison of averaged diel variations of measured and modeled (base model) net exchange fluxes of Hg^0 at the Arctic tundra site (Toolik Field station, Alaska, U.S.) in summer: A) July 2016 and B) August 2016.

In August (Fig. 2B), measured F_{net} during daytime (0600 to 2200 LT) exhibited a small net deposition (-0.23 ng $m^{-2}\ hr^{-1}$), yet a bi-modal diel trend was evident again, with net

deposition during the early and later parts of the day and net Hg^0 emission during midday. Consistent with the July simulation (Fig. 2A), the base model over-predicted daytime net deposition by a factor of 12 in August, and was unable reproduce a shift from net deposition to net emission during midday. Also similar to the July simulation, the measured net exchange at nighttime (2300 to 0500 LT) in August (Fig. 2B) exhibited a substantial Hg^0 deposition (-2.89 ng m^{-2} hr^{-1}), which the base model underestimated by a factor >30.

2.4.2 Evaluation of modeled net exchange fluxes in winter using the base model

Overall, in winter, Fig. 3A shows that measured F_{net} of the temperate grassland showed a net Hg^0 deposition in the range of -0.23 to -5.29 ng m^{-2} hr^{-1} during nighttime (1800 to 0800 LT) and diel patterns during daytime showed a small net Hg^0 emission (ca. 1.4 ng m^{-2} hr^{-1}) in the afternoon (1400 to 1600 LT). In winter at the tundra site (Figure 3B), measured F_{net} exhibited a small net deposition for most of the day with no clear differences between nighttime and daytime fluxes and with hourly fluxes ranging from –1.11 ng m^{-2} hr^{-1} (small net deposition) to 0.95 ng m^{-2} hr^{-1} (small net emission). As illustrated in Fig. 3, modeled F_{net} fluxes at both sites largely lack diel flux patterns. Note that for winter months, we assumed a LAI of ~0 (i.e., no active vegetation activity), but did not implement any processes within the snow cover. At both sites, the base model was unable to reproduce a small measured net deposition and consistently produced a small rate of net Hg^0 emissions during both daytime and nighttime. In winter months, cumulative modeled net daily emissions at the grassland and tundra sites were 18.90 and 23.36 ng m^{-2} day^{-1}, respectively.

In contrast, measured net daily depositions were -34.67 and -5.17 ng m^{-2} day^{-1}, respectively, at the two sites.

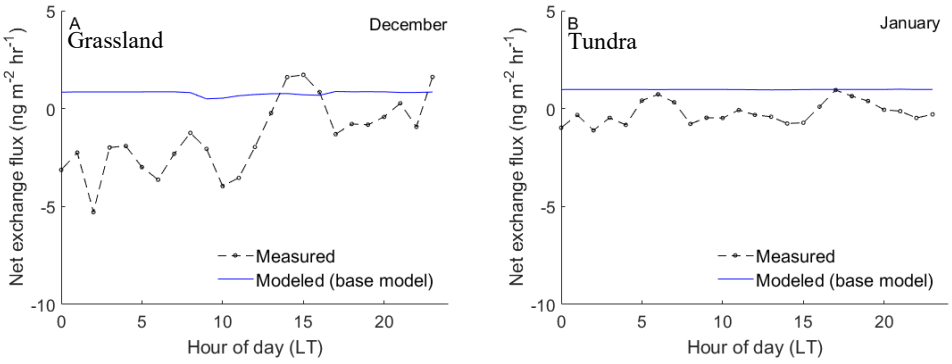

Figure 3. Comparison of averaged diel variations of measured (black) and modeled (blue) (base model) net exchange fluxes of Hg^0 in winter: A) temperate grassland site (December 2005) and B) Arctic tundra site (January 2016).

The measurement-model comparisons shown in Figs. 2 and 3 suggest that in order to improve the performance of modeled exchange, three major components in the coupled (i.e., deposition and emission) models need to be addressed. First, net nighttime Hg^0 deposition observed at both sites is largely lacking in model simulations, suggesting that the current Hg^0 deposition scheme, which is strongly driven by stomatal Hg^0 uptake, needs to implement a stronger deposition pathway via non-stomatal pathways that are active during the night (i.e., cuticular, R_{cut}, and ground, R_{gd}, resistance terms in Eq. 3). Second, the modeled leaf Hg^0 uptake needs to be reduced substantially (i.e., increased stomatal resistance R_{st} term in Eq. 2) as daytime deposition is over-predicted in the modeled F_{net} by a factor of up to 26 (e.g., in July at the Arctic tundra site). Third, further improvement in model vs. measurement agreement can be reached by adjusting the soil Hg^0 re-emission scheme. In section 2.4.3, we examine and discuss resulting flux responses of adjusting the

corresponding resistance parameters, R_{st}, R_{cut}, and R_{gd}, which directly affect the three main processes highlighted above.

2.4.3 Model response to adjusted deposition parameterization (summer)

2.4.3.1 *Model response to reduced stomatal uptake*

As discussed, modeled diel flux patterns in the default dry Hg^0 deposition model rely heavily on stomatal Hg^0 uptake, which generally accounts for over 90% of the daytime Hg^0 deposition and results in over-prediction of measured deposition by factors of 3 to 26, as illustrated above. In the Zhang et al. (2003) dry deposition parameterization, a set of default parameter values were suggested for the minimal stomatal resistance (r_{stmin}) for different LUCs, including a default value r_{stmin} of 100 s m^{-1} for long grass. To reduce the stomatal uptake of Hg^0 at daytime, we performed a set of sensitivity tests by allowing the default r_{stmin} value to vary over a wide range (e.g., 100 to 800 s m^{-1}) and examining the corresponding responses to the modeled net exchange fluxes. These sensitivity tests served as the first step in model calibration. For the grassland site, we found that an increase in the default r_{stmin} value by a factor of seven led to significant reduction of daytime Hg^0 deposition and reasonably good agreement between the measured and modeled daytime fluxes, as illustrated by Fig. 4A.

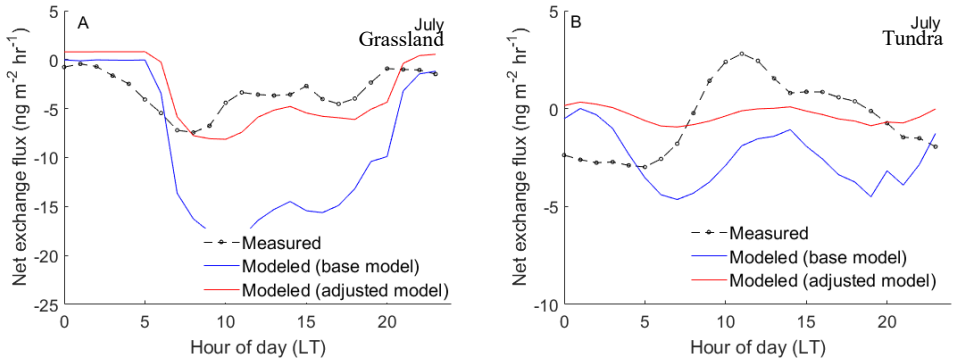

Figure 4. Model response to reduced stomatal uptakes of Hg^0 and comparison of modeled and measured net exchange fluxes of Hg^0 in July: A) temperate grassland site and B) Arctic tundra site.

The default parameter value for r_{stmin} was 150 s m^{-1} for the tundra LUC following Zhang et al.'s (2003) parameterization. Using a similar model calibration approach through sensitivity testing as in the first step, by allowing r_{stmin} to vary from 150 to 1050 s m^{-1}, we identified that a five-fold increase in the default r_{stmin} (i.e., to 750 s m^{-1}) led to an improved performance of the modeled Hg^0 deposition during the daytime (Fig. 4B). Any further increase in the r_{stmin} value caused worsening of model performance in the nighttime (Fig. 4B). Hence, comparisons between base model and adjusted model simulations with increased stomatal resistance by factors of 7 (for the temperate grassland) and 5 (for the Arctic tundra) suggest that the dry deposition model is extremely sensitive to changes in r_{stmin}. Reducing the modeled stomatal uptake of Hg^0 substantially improved the agreement between measured and modeled net exchange fluxes during the daytime for both ecosystems in summer months (model simulation plots in August for both grassland and tundra are shown in Fig. S1). For example, at the grassland site, daytime net Hg^0 deposition using the adjusted r_{stmin} parameterization deviated on average by 2.14 ng m^{-2} hr^{-1} from

measured fluxes, while deviations from the unadjusted model averaged 9.81 ng m^{-2} hr^{-1}. At the tundra site, daytime net Hg^0 deposition with the adjusted parameters deviated on average by 1.36 ng m^{-2} hr^{-1} from measured fluxes compared to 3.16 ng m^{-2} hr^{-1} for the base model.

A consequence of adjustment of r_{stmin} values was that model performance worsened at night at both sites compared to the base model. This finding suggests that while increased stomatal resistance leads to improvements in daytime fluxes and improved diel patterns, other resistance terms that are independent of stomatal behavior such as ground and cuticular resistances need to be revised to achieve better flux agreement at night, as described in the following section.

2.4.3.2 *Model response to increased ground and cuticular uptake, and reduced stomatal uptake*

In both the temperate grassland and Arctic tundra sites, measured F_{net} exhibited a net Hg^0 deposition during nighttime, which the base model and the stomatal-adjusted model were largely unable to reproduce. Increased nighttime Hg^0 deposition (i.e., in the absence of significant stomatal uptake) can be achieved either through increasing the ground (R_{gd}) and/or cuticular (R_{cut}; i.e., to the leaf surface) uptake of Hg^0, or by reducing soil re-emission fluxes (section 2.4.3.3). We first increased the ground and cuticular uptake along with the implemented reduced stomatal uptake described above, and show the resulting changes in model behavior in Fig. 5.

For the grassland site, we calibrated the model by adjusting the default parameters for cuticular resistance (dry) (R_{cutdO3}) and ground resistance (dry) R_{gdO3}, which in the base model were 4000 and 200 s m^{-1} (LUC: long grass), respectively (Zhang et al. (2003)). Note that the values for these resistance parameters are based on ozone (O_3) assuming dry conditions. The model was calibrated through a series of sensitivity tests using the following ranges: 500-4000 s m^{-1} and 50-200 s m^{-1} for R_{cutdO3} and R_{gdO3}, respectively. We found that reductions in the default parameter values R_{cutdO3} and R_{gdO3} by factors greater than four still resulted in only negligible improvements in nighttime model performance (Fig. 5A). However, such increases substantially worsened the daytime model performance for both summer months. Thus, we applied a factor of four reduction in the base model values for both of these parameters (R_{cutdO3} and R_{gdO3}).

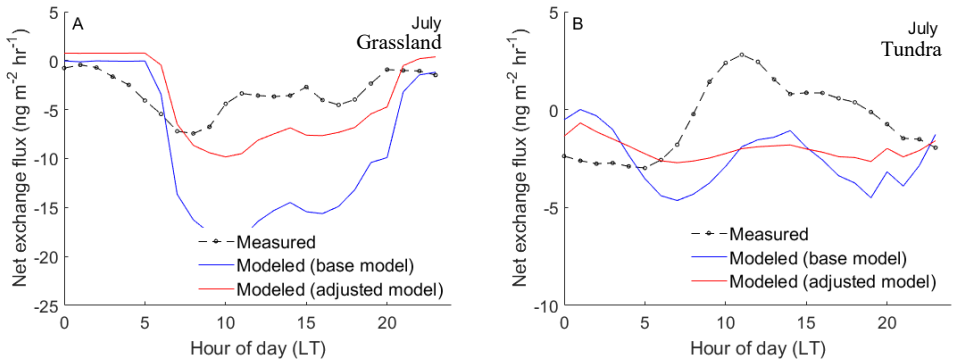

Figure 5. Model response to increased cuticular and ground uptake, and reduced stomatal uptake, of Hg^0, and comparison of modeled and measured net exchange fluxes of Hg^0: A) temperate grassland site and B) Arctic tundra site.

Similarly, for the tundra site, we calibrated the model by first testing the sensitivity of the default parameters for R_{cutdO3} and R_{gdO3}, which were 8000 and 500 s m^{-1}, respectively, in the Zhang et al. (2003) model. A series of sensitivity tests were performed using the

following ranges: 500-8000 s m^{-1} and 50-200 s m^{-1} for R_{cutdO3} and R_{gdO3}, respectively. From the model calibration results, we determined that factors of two and three decreases in R_{cutdO3} and R_{gdO3}, respectively, in the base values of each of these parameters (R_{cutdO3} and R_{gdO3}) produced an exchange flux pattern that exhibited small net nighttime deposition (Fig. 5B). Using the same adjustment factors for R_{cutdO3} and R_{gdO3}, model simulation plots in August for both grassland and tundra are shown in Fig. S2.

Collectively, these findings suggest that adjustments of resistance parameters alone (i.e., stomatal, cuticular, and ground) cannot satisfactorily reproduce measured fluxes, even though the increased stomatal resistance led to a large improvement in modeled daytime fluxes. However, we note that after revision of these resistance parameters, the mean modeled dry deposition velocity (v_d) for Hg^0 at the grassland site was 0.12 cm s^{-1}, which falls within the range of suggested v_d values for Hg^0 deposition (0.10-0.40 cm s^{-1}) over vegetative surfaces (Zhang et al., 2009).

2.4.3.3 *Model response to revised soil Hg^0 re-emission and dry deposition parameterizations*

In many studies, secondary emission of Hg^0 is parameterized as an exponential function of solar radiation and surface temperature in order to simulate re-emission from soil and other surfaces (Carpi and Lindberg, 1997; Moore and Carpi, 2005; Zhang et al., 2001; Agnan et al., 2016). Based on field measurements, we now also understand that nighttime soil Hg^0 re-emission are low and often negligibly small. Yet, based on the results shown above, we also stipulate that implementing a larger daytime soil emission would improve the

agreement between modeled and measured exchange fluxes. We achieve both of these requirements by also implementing a new soil Hg^0 emission parameterization, which is based on a statistical relationship (Eq. 8) between soil Hg^0 flux ($E_{soil\_new}, ng\ m^{-2}\ hr^{-1}$), solar radiation ($R_{g'}, Wm^{-2}$) and soil Hg concentration ($C_{soil}, \mu g\ g^{-1}$) derived using surface-air exchange flux data from Eckely et al. (2016). Assuming that the diurnal variation in soil re-emission flux of Hg^0 follows a symmetrical sine-curve relationship, we applied a sinusoidal function to better reproduce the observed diel pattern in exchange fluxes. The resulting expression is

$$E_{soil\_new} = 10^{[0.709+0.119\log(C_{soil})+0.137\log(R_{g'})]} \times a^{-1} sin\frac{\pi t}{D}. \quad (8)$$

In Eq. (8), D is duration (in hour) between sunrise and sunset, and t is time (in hour) of daylight hours. The sinusoidal function (based on a sine-curve light distribution pattern) is consistent with the canopy light attenuation formulation provided by Liu (1996). To avoid double-counting solar position in Eq. (8), we estimated the solar radiation at the ground ($R_{g'}$) without normalizing the exponential term by solar zenith angle as done previously, as shown in Eq. (6). The suggested expression for $R_{g'}$ is

$$R_{g'} = SR \exp(-\alpha LAI). \quad (9)$$

This model portion was calibrated by once again applying a series of sensitivity tests to determine the value of the coefficient a that produced the best-fit modeled soil flux values as compared to measured soil Hg^0 flux values at both sites. Following Eq. (8), we simulated net exchange fluxes using reduced nighttime and increased daytime soil Hg^0 re-

emission for summer months at the grassland and tundra sites. For both sites in summer, we found that a value of *a* of 1.5 produced the best agreement between the modeled and measured F_{net} (Fig. 6). The major outcome of modifying the soil re-emission parameterization was that a substantial improvement in model ability to reproduce the observed diel pattern in F_{net} was achieved. This improved ability was achieved through the combination of largely eliminating nighttime soil re-emission and substantially increasing daytime emissions.

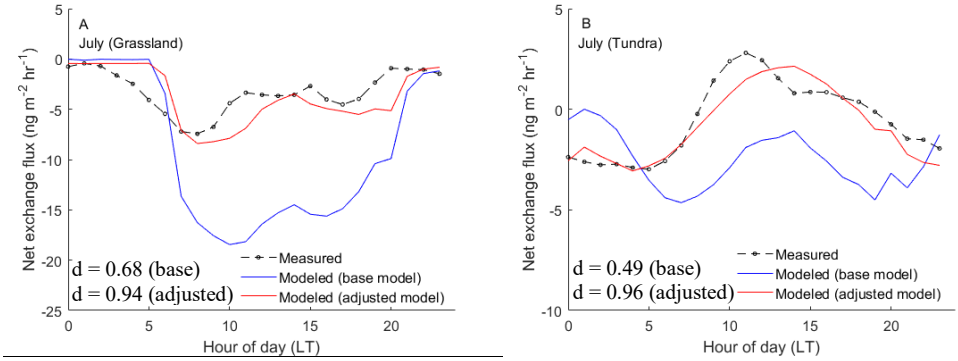

Figure 6. Model response to reduced nighttime and increased daytime soil re-emission and revised resistance parameters, and comparison of modeled and measured net exchange fluxes of Hg^0 in July: A) temperate grassland site and B) Arctic tundra site.

As a result of the adjustment in Hg^0 emission fluxes, the ratio between modeled and measured daily sum of fluxes at the temperate grassland site decreased from factors of ca. 3 to 1.1 (improved model) in July (Fig. 6A; mean modeled net fluxes of -3.72 vs. measured fluxes of -3.23 ng m^{-2} hr^{-1}). Similarly, for August (Fig. S3A), the ratio between the modeled and measured fluxes was within a factor of 1.2. Degree of agreement (*d*) values between modeled fluxes and observations also support the improvement in model performance (i.e., 0.94 vs. 0.68, and 0.96 vs. 0.72 for July and August, respectively). The improvement in

both the ratios and the *d*-values demonstrates that revising the soil re-emission function can significantly improve the agreement between modeled and measured Hg^0 fluxes (see Table 1).

For the Arctic tundra site, we found that the ratio between the modeled and measured fluxes decreased from factors about 4.5 (base model) to 1.3 (improved model) in July (Fig. 6B). For August (Fig. S3B), the ratio between the modeled (improved model) and measured exchange fluxes was 0.96. The *d*-values (base vs. adjusted models) were 0.96 vs. 0.49, and 0.97 vs. 0.35 for July and August, respectively. Table 2 presents the statistical summary of this comparison.

Table 1. Mean measured and modeled F_{net} (ng m^{-2} hr^{-1}) at the grassland site.

Month	**Measured**	**Modeled (base)**	**Modeled (improved)**
		Mean F_{net} (daytime)	
July	-4.17	-14.98	-5.81
August	-4.66	-12.62	-5.36
December	-0.98	0.69	-1.44
		Mean F_{net} (nighttime)	
July	-1.91	-0.96	-0.79
August	-3.22	-1.48	-1.81
December	-1.72	0.85	-1.42
		Mean F_{net} (daily)	
July	-3.23	-9.14	-3.72
August	-4.06	-7.98	-3.88
December	-1.44	0.79	-.1.43

Table 2. Mean measured and modeled F_{net} (ng m^{-2} hr^{-1}) at the Arctic tundra site.

Month	Measured	Modeled (base)	Modeled (improved)
		Mean F_{net} (daytime)	
July	-0.11	-2.96	-0.45
August	-0.23	-2.79	-0.44
January	-0.56	0.96	-0.23
		Mean F_{net} (nighttime)	
July	-2.62	-0.46	-2.37
August	-2.89	-0.10	-2.45
January	-0.15	0.98	-0.22
		Mean F_{net} (daily)	
July	-0.53	-2.54	-0.77
August	-1.01	-2.01	-1.03
January	-0.22	0.97	-0.23

2.4.4 Model response to revised dry deposition and soil re-emission parameterizations in winter

For winter months, we performed the same adjustments for the dry deposition model for both respective LUCs and show results of these adjustments in Fig. 7. The results indicate that in winter months with sub-zero air temperature and snow on the ground, revisions of these resistance terms of dry deposition had no discernable effect on improving the agreement between measured and modeled exchange fluxes. However, the modeled fluxes of both the base simulation and the adjusted simulation largely replicated a generic lack of strong diel patterns in measured Hg^0 fluxes.

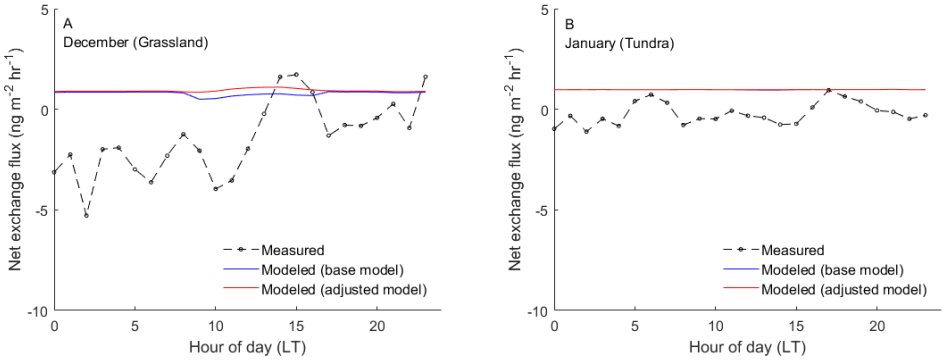

Figure 7. Model response to reduced nighttime and increased daytime soil re-emission and revised resistance parameters, and comparison of modeled and measured net exchange fluxes of Hg^0 in July: A) temperate grassland site and B) Arctic tundra site.

However, neither simulation replicates the observed net Hg^0 flux under snow cover. We suggest adding a net soil Hg^0 sink in soils and completely eliminating emissions from ecosystems under snow, as can be inferred from experimental studies (Obrist et al. 2017; Obrist et al., 2014). We also recommend de-coupling wintertime fluxes from variability imposed by solar radiation and temperature. Figure 8 shows that turning off soil re-emission (both at day- and nighttime) at both sites and adding a net soil Hg^0 sink on the order of 1 ng m^{-2} hr^{-1} at the grassland site led to the best agreement between measured and modeled net Hg^0 fluxes. Even still, the agreement between modeled and measured fluxes at both sites is not very good, possibly due to small fluxes during the winter, when stable atmospheric conditions make such measurements challenging (Obrist et al., 2017).

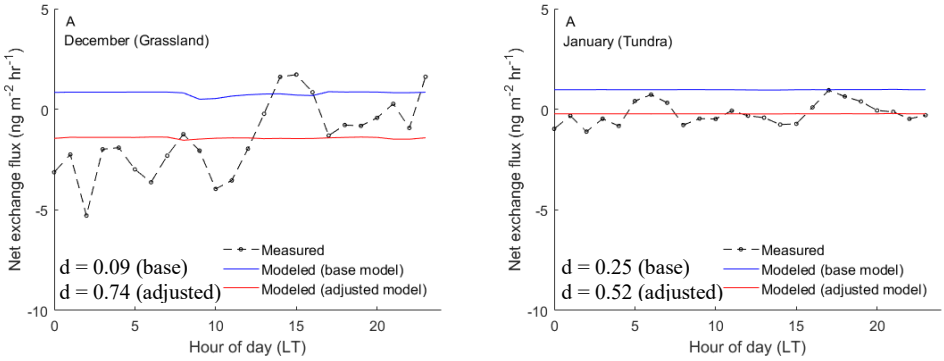

Figure 8. Model response to reduced soil re-emission and revised resistance parameters, and comparison of modeled and measured net exchange fluxes of Hg^0 at the: A) grassland site in December 2005 and B) tundra site in January 2016.

2.4.5 Seasonal mercury accumulation in leaves estimated using the deposition model

In addition to constraining modeled net Hg^0 deposition fluxes with measured field fluxes, an additional verification can be achieved by comparing foliar Hg uptake between modelled stomatal and non-stomatal uptake and measured leaf Hg contents from the field. Several studies have documented that during the growing season, net Hg uptake occurs in leaves resulting in increasing leaf Hg content over time (Risch et al., 2017; Rutter et al., 2011; Rea et al., 2002). Other studies, in particular using stable isotope analysis, have confirmed that foliar Hg is primarily derived from atmospheric Hg^0 uptake (Demers et al., 2013; Enrico et al., 2016).

To evaluate how implemented changes in stomatal and cuticular leaf resistance terms impact plant Hg^0 accumulation, and hence total Hg tissue concentrations, we estimated seasonal (April to August) Hg accumulation in vegetation at the grassland site for both

base and adjusted model parameterizations. The following expression was used to estimate the leaf Hg concentration (C_{Hgleaf}):

$$C_{Hgleaf}\left(\frac{ng}{g}\right) = F_{dep(st+cut)} \times t_L \times SLA \times \frac{1}{LAI}, \quad (9)$$

where $F_{dep(st+cut)}$ is the net dry deposition flux of Hg^0 (ng m^{-2} day^{-1}) due to leaf uptake via stomatal and cuticular pathways, t_L is the duration of the growing season in days, and SLA is the specific leaf surface area (leaf surface area per mass: m^2 g^{-1}). We used an *SLA* value of 0.017 m^2 g^{-1} for *Dactylis glomerata* (Arredondo and Schnyder, 2003) in Eq. (9). *Dactylis glomerata* is one of the dominant plant species at the Früebüel grassland site. For the Arctic tundra site, we used an *SLA* value of 0.014 m^2 g^{-1} for *Batula nana* (van Wijk et al., 2005), which is one of the dominant shrub vegetation types. In addition, monthly averaged LAI values obtained from MODIS-Terra database (ORNL DAAC, 2017) for each growing season month were used. To calculate deposition fluxes, the average measured atmospheric Hg^0 concentration (Fritsche et al., 2008) for each growing season month was used.

Comparison between seasonal Hg accumulation using the base model and the adjusted model (Fig. 9) supports the findings shown earlier that the base model parameterization strongly overestimates Hg^0 uptake. In fact, at the grassland site, the estimated tissue Hg concentrations would yield a value of 164 ng g^{-1}, which is much higher than leaf Hg concentrations commonly measured across ecosystems in temperate regions (21-78 ng g^{-1}; Wang et al., 2016b). In contrast, using the adjusted deposition model parameterization with increased stomatal resistance (i.e., reduced leaf Hg^0 uptake), estimated growing season

tissue Hg concentrations of 76 ng g^{-1}. This estimated value is comparable to commonly reported leaf and litterfall tissue concentrations across ecosystems in temperate regions. Similarly, at the tundra site, the base model over-predicts the leaf-tissue Hg concentration by a factor >2.5. At this site, the adjusted model-predicted growing-season (May-August) leaf Hg concentration (28.66 ng g^{-1}) is in good agreement with the measured tissue Hg concentration (25.02 ng g^{-1}, D. Obrist, personal communication).

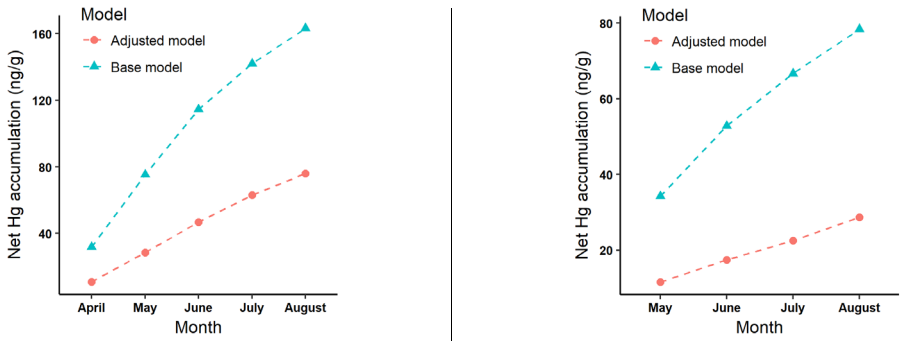

Figure 9. Growing season Hg accumulation in (A) *Dactylis glomerata* at the grassland site and (B) shrub vegetation (dominated by *Betula nana*) at the tundra site using base and adjusted dry deposition models.

2.5 Conclusions

This paper presents an evaluation of resistance-based dry gaseous deposition and soil Hg^0 re-emission parameterizations using direct comparison to micrometeorological flux measurements from two ecosystems. To our knowledge, this is the first direct performance evaluation of commonly used Hg^0 net exchange parameterizations in CTMs with direct ecosystem-level flux measurements. In this work, we evaluated how the major resistance terms (including both stomatal and non-stomatal resistance terms) affect modeled Hg^0 exchange and how they can be best parameterized to simulate measured exchange fluxes.

The base model configuration overestimates net Hg deposition by factors of 3-4 in summer, leading to unreasonably high tissue concentrations during the growing season, and does not provide replication of strong diel variation with net nighttime deposition and daytime net Hg^0 volatilization. We found that the largest source of deviation from measurements was caused by a strong overestimation of stomatal leaf Hg uptake, and that modeled Hg^0 fluxes responded most strongly to modulation of the stomatal uptake term.

By adjusting resistance terms and implementing a revised soil Hg^0 re-emission parameterization, both diel patterns and magnitudes of fluxes were replicated well within the current resistance-based modeling framework. Increases in stomatal and non-stomatal resistance terms that reduce plant Hg uptake and increased nighttime Hg deposition, along with revision of the soil re-emission parameterization, produced good agreement between measured and modeled exchange fluxes, particularly in summer months. As an independent model evaluation, modeled estimated growing season foliar accumulation using the adjusted model parameters was in much better agreement with observed foliar Hg contents in both ecosystems. Continued improvement in model parameterizations is needed for better agreement in winter months, when deposition dominates the overall exchange between the surface and the atmosphere. Because stomatal uptake generally accounts for over 90% of total Hg^0 deposition during daytime as shown, for example, for the grassland site in Fig. S4, the model calibration was performed by adjusting the stomatal resistance term (e.g., r_{stmin}) first, followed by adjusting the non-stomatal resistance terms R_{cutdO3} and R_{gdO3}. One could argue that increasing soil Hg^0 re-emission as the first step of model calibration followed by adjustment to the resistance parameters in the deposition model

could lead to improved agreement between modeled and measured net exchange fluxes as well. However, this approach requires a large increase in soil Hg^0 re-emission, which would fall outside the measured ranges of Hg^0 emission fluxes from background ecosystems (Eckely et al., 2016; Agnan et al., 2016). We stress that the physiological accuracy of the adjusted resistance parameter values should be viewed in the context of the intended application of those parameters in this work, to better reproduce the observed net exchange fluxes through applying adjustment factors to the base parameter values.

Based on our findings, we make the following generic recommendations for improvement in modeling Hg^0 exchange using resistance-based approaches. 1) We suggest that stomatal resistance be increased several times to reduce bias in overestimating Hg uptake. In the ecosystems we studied (long grass and tundra LUCs), the best performance was achieved through reduction by a factor of 5 (tundra) to 7 (grasslands); 2) cuticular uptake and ground uptake should be increased by reducing their respective resistance terms. This increase results in higher nighttime Hg^0 deposition, which is supported by field observations and is currently not well predicted by the base model. In the ecosystems we studied, reductions in cuticular resistance by factors of 4 (grassland) and 2 (tundra), and reductions of ground resistance by factors of 4 (grassland) and 3 (tundra) provided the best results. 3) Finally, the soil re-emission parameterization currently adapted in GEOS-Chem should be revised to increase diel variability in Hg^0 fluxes and to set fluxes at nighttime to zero. We implemented these features by combining an equation for a sinusoidal response to solar radiation by vegetation and a statistically-derived soil flux model that is consistent with

experimental flux measurements performed over background soils. Other soil flux models sensitive to solar radiation might also achieve the same results.

Although the two LUCs studied here together comprise 48% (40% grassland and 8% tundra) of terrestrial land surface on Earth (Iversen et al., 2015; Foley et al., 2005), reliable ecosystem-level exchange flux data are currently not available for most other LUCs (in particular forests; Agnan et al., 2016). That said, we would expect the above generic recommendations for improving base model performance to be applicable to other ecosystems having background atmospheric Hg^0 concentrations (e.g., 1.0 to 1.7 ng m^{-3}; Agnan et al., 2016), with tests for applicability including both modeled seasonal Hg plant uptake and comparison with foliar Hg concentration data. Further tests include large-scale model comparison with regional atmospheric Hg^0 deposition patterns across ecosystems. Although current understanding does not allow us to develop a fully mechanistic approach to model net Hg^0 exchange, application of resistance-based models here is supported by experimental field data, including observations of stomatal and non-stomatal (Stamenkovic and Gustin, 2009), and soil (Agnan et al., 2016), Hg^0 uptake. Coupling modeled deposition with a soil re-emission model based on an observed strong response to solar radiation is also experimentally supported (Eckley et al., 2016; Lin et al., 2010). A potential limitation of our approach is that we modeled net deposition to plants, as opposed to gross deposition corrected by a fractional re-emission loss. Such a fractional re-emission loss from plant surfaces has experimental support from both flux measurements and stable isotope data (Demers et al., 2013; Enrico et al., 2016). This fractional re-emission loss is also incorporated into some global models for Hg such as GEOS-Chem (Song et a., 2015).

However, the degree of re-emission from plant surfaces is poorly quantified (Graydon et al., 2008), and the approach of modeling net Hg^0 deposition taken here resulted in satisfactory comparisons with both observed net exchange fluxes and foliar accumulation.

A supplemental information (S.I.) (section 2.7) is provided after the references. The S.I. section includes the figures of modeled vs. measured net exchange fluxes in August at the grassland and tundra sites.

2.6 References

Agnan, Y., Le Dantec, T., Moore, C.W., Edwards, G.C., Obrist, D., 2016. New Constraints on Terrestrial Surface-Atmosphere Fluxes of Gaseous Elemental Mercury Using a Global Database. Environ Sci Technol 50, 507-524.

Amos, H.M., Jacob, D.J., Streets, D.G., Sunderland, E.M., 2013. Legacy impacts of all-time anthropogenic emissions on the global mercury cycle. Global Biogeochemical Cycles 27, 410-421.

Arredondo, J.T., Schnyder, H., 2003. Components of leaf elongation rate and their relationship to specific leaf area in contrasting grasses. New Phytologist 158, 305-314.

Bash, J.O., 2010. Description and initial simulation of a dynamic bidirectional air-surface exchange model for mercury in Community Multiscale Air Quality (CMAQ) model. Journal of Geophysical Research 115.

Bash, J.O., Miller, D.R., 2009. Growing season total gaseous mercury (TGM) flux measurements over an Acer rubrum L. stand. Atmospheric Environment 43, 5953-5961.

Bash, J.O., Miller, D.R., Meyer, T.H., Bresnahan, P.A., 2004. Northeast United States and Southeast Canada natural mercury emissions estimated with a surface emission model. Atmospheric Environment 38, 5683-5692.

Bergstra, J., Bengio, Y., 2012. Random search for hyper-parameter optimization. Journal of Machine Learning Research 13, 281-305.

Carpi, A., Lindberg, S.E., 1998. Application of a Teflon™ dynamic flux chamber for quantifying soil mercury flux: tests and results over background soil. Atmospheric Environment 32, 873-882.

Corbitt, E.S., Jacob, D.J., Holmes, C.D., Streets, D.G., Sunderland, E.M., 2011. Global source–receptor relationships for mercury deposition under present-day and 2050 emissions scenarios. Environmental science & technology 45, 10477-10484.

Dastoor, A., Ryzhkov, A., Durnford, D., Lehnherr, I., Steffen, A., Morrison, H., 2015. Atmospheric mercury in the Canadian Arctic. Part II: Insight from modeling. Science of The Total Environment 509, 16-27.

Demers, J.D., Blum, J.D., Zak, D.R., 2013. Mercury isotopes in a forested ecosystem: Implications for air-surface exchange dynamics and the global mercury cycle. Global Biogeochemical Cycles 27, 222-238.

Eckley, C.S., Tate, M.T., Lin, C.J., Gustin, M., Dent, S., Eagles-Smith, C., Lutz, M.A., Wickland, K.P., Wang, B., Gray, J.E., Edwards, G.C., Krabbenhoft, D.P., Smith, D.B., 2016. Surface-air mercury fluxes across Western North America: A synthesis of spatial trends and controlling variables. Sci Total Environ 568, 651-665.

Enrico, M., Roux, G.l.L., Marusczak, N., Heimbürger, L.-E., Claustres, A., Fu, X., Sun, R., Sonke, J.E., 2016. Atmospheric mercury transfer to peat bogs dominated by gaseous elemental mercury dry deposition. Environmental science & technology 50, 2405-2412.

Ericksen, J., Gustin, M., Schorran, D., Johnson, D., Lindberg, S., Coleman, J., 2003. Accumulation of atmospheric mercury in forest foliage. Atmospheric Environment 37, 1613-1622.

Foley, J.A., DeFries, R., Asner, G.P., Barford, C., Bonan, G., Carpenter, S.R., Chapin, F.S., Coe, M.T., Daily, G.C., Gibbs, H.K., 2005. Global consequences of land use. science 309, 570-574.

Flechard, C.R., Nemitz, E., Smith, R.I., Fowler, D., Vermeulen, A.T., Bleeker, A., Erisman, J.W., Simpson, D., Zhang, L., Tang, Y.S., Sutton, M.A., 2011. Dry deposition of reactive nitrogen to European ecosystems: a comparison of inferential models across the NitroEurope network. Atmospheric Chemistry and Physics 11, 2703-2728.

Fleck, J., Grigal, D., Nater, E., 1999. Mercury uptake by trees: an observational experiment. Water, Air, & Soil Pollution 115, 513-523.

Frescholtz, T.F., Gustin, M.S., Schorran, D.E., Fernandez, G.C., 2003. Assessing the source of mercury in foliar tissue of quaking aspen. Environmental Toxicology and Chemistry 22, 2114-2119.

Fritsche, J., Obrist, D., Zeeman, M., Conen, F., Eugster, W., Alewell, C., 2008. Elemental mercury fluxes over a sub-alpine grassland determined with two micrometeorological methods. Atmospheric Environment 42, 2922-2933.

Gbor, P., Wen, D., Meng, F., Yang, F., Zhang, B., Sloan, J., 2006. Improved model for mercury emission, transport and deposition. Atmospheric Environment 40, 973-983.

Gencarelli, C.N., Bieser, J., Carbone, F., De Simone, F., Hedgecock, I.M., Volker, M., Travnikov, O., Yang, X., Pirrone, N., 2017. Sensitivity model study of regional mercury dispersion in the atmosphere. Atmospheric Chemistry and Physics 17, 627.

Graydon, J.A., St. Louis, V.L., Hintelmann, H., Lindberg, S.E., Sandilands, K.A., Rudd, J.W., Kelly, C.A., Hall, B.D., Mowat, L.D., 2008. Long-term wet and dry deposition of total and methyl mercury in the remote boreal ecoregion of Canada. Environmental science & technology 42, 8345-8351.

Grigal, D., 2002. Inputs and outputs of mercury from terrestrial watersheds: a review. Environmental Reviews 10, 1-39.
Gustin, M.S., Lindberg, S.E., Weisberg, P.J., 2008. An update on the natural sources and sinks of atmospheric mercury. Applied Geochemistry 23, 482-493.

Hicks, B.B., Saylor, R.D., Baker, B.D., 2016. Dry deposition of particles to canopies—A look back and the road forward. Journal of Geophysical Research: Atmospheres 121.

Iversen, C.M., Sloan, V.L., Sullivan, P.F., Euskirchen, E.S., McGuire, A.D., Norby, R.J., Walker, A.P., Warren, J.M.,

Wullschleger, S.D., 2015. The unseen iceberg: plant roots in arctic tundra. New Phytologist 205, 34-58

Jiskra, M., Sonke, J., Obrist, D., et al., 2018. Vegetation mercury pump controls seasonal variations in global atmospheric mercury. Nature Geoscience, in press.

Jiskra, M., Wiederhold, J.G., Skyllberg, U., Kronberg, R.M., Hajdas, I., Kretzschmar, R., 2015. Mercury deposition and re-emission pathways in boreal forest soils investigated with Hg isotope signatures. Environ Sci Technol 49, 7188-7196.

Jung, G., Hedgecock, I., Pirrone, N., 2009. ECHMERIT V1. 0–a new global fully coupled mercury-chemistry and transport model. Geoscientific Model Development 2, 175-195.

Kwon, S.Y., Selin, N.E., 2016. Uncertainties in Atmospheric Mercury Modeling for Policy Evaluation. Current Pollution Reports 2, 103-114.

Lei, H., Liang, X.-Z., Wuebbles, D., Tao, Z., 2013. Model analyses of atmospheric mercury: present air quality and effects of transpacific transport on the United States. Atmospheric Chemistry and Physics 13, 10807-10825.

Liu, D. L., 1996. Incorporating diurnal light variation and canopy light attenuation into analytical equations for calculating daily gross photosynthesis. Ecological modelling 93, 175-189.

Lin, C.-J., Gustin, M.S., Singhasuk, P., Eckley, C., Miller, M., 2010. Empirical models for estimating mercury flux from soils. Environmental science & technology 44, 8522-8528.

Lin, X., Tao, Y., 2003. A numerical modelling study on regional mercury budget for eastern North America. Atmospheric Chemistry and Physics 3, 535-548.

Lindberg, S., Bullock, R., Ebinghaus, R., Engstrom, D., Feng, X., Fitzgerald, W., Pirrone, N., Prestbo, E., Seigneur, C., 2007. A synthesis of progress and uncertainties in attributing the sources of mercury in deposition. AMBIO: a Journal of the Human Environment 36, 19-33.

Millhollen, A.G., Gustin, M.S., Obrist, D., 2006. Foliar mercury accumulation and exchange for three tree species. Environmental science & technology 40, 6001-6006.

Obrist, D., Agnan, Y., Jiskra, M., Olson, C.L., Colegrove, D.P., Hueber, J., Moore, C.W., Sonke, J.E., Helmig, D., 2017. Tundra uptake of atmospheric elemental mercury drives Arctic mercury pollution. Nature 547, 201-204.

Obrist, D., Kirk, J.L., Zhang, L., Sunderland, E.M., Jiskra, M., Selin, N.E., 2018. A review of global environmental mercury processes in response to human and natural perturbations: Changes of emissions, climate, and land use. Ambio, 1-25.

Obrist, D., Pokharel, A.K., Moore, C., 2014. Vertical profile measurements of soil air suggest immobilization of gaseous elemental mercury in mineral soil. Environmental science & technology 48, 2242-2252.

ORNL DAAC. 2017. MODIS Collection 6 Land Products Global Subsetting and Visualization Tool. ORNL DAAC, Oak Ridge, Tennessee, USA. Accessed March 28, 2017.

Pirrone, N., Aas, W., Cinnirella, S., Ebinghaus, R., Hedgecock, I.M., Pacyna, J., Sprovieri, F., Sunderland, E.M., 2013. Toward the next generation of air quality monitoring: Mercury. Atmospheric Environment 80, 599-611.

Rea, A., Lindberg, S., Scherbatskoy, T., Keeler, G.J., 2002. Mercury accumulation in foliage over time in two northern mixed-hardwood forests. Water, Air, & Soil Pollution 133, 49-67.

Risch, M.R., DeWild, J.F., Gay, D.A., Zhang, L., Boyer, E.W., Krabbenhoft, D.P., 2017. Atmospheric mercury deposition to forests in the eastern USA. Environ Pollut 228, 8-18.

Rutter, A.P., Schauer, J.J., Shafer, M.M., Creswell, J., Olson, M.R., Clary, A., Robinson, M., Parman, A.M., Katzman, T.L., 2010. Climate sensitivity of gaseous elemental mercury dry deposition to plants: impacts of temperature, light intensity, and plant species. Environmental science & technology 45, 569-575.

Selin, N.E., Jacob, D.J., Yantosca, R.M., Strode, S., Jaeglé, L., Sunderland, E.M., 2008. Global 3-D land-ocean-atmosphere model for mercury: Present-day versus preindustrial cycles and anthropogenic enrichment factors for deposition. Global Biogeochemical Cycles 22, n/a-n/a.

Smith-Downey, N.V., Sunderland, E.M., Jacob, D.J., 2010. Anthropogenic impacts on global storage and emissions of mercury from terrestrial soils: Insights from a new global model. Journal of Geophysical Research 115.

Snoek, J., Larochelle, H., Adams, R.P., 2012. Practical bayesian optimization of machine learning algorithms, Advances in neural information processing systems, pp. 2951-2959.

Song, S., Selin, N.E., Gratz, L.E., Ambrose, J.L., Jaffe, D.A., Shah, V., Jaeglé, L., Giang, A., Yuan, B., Kaser, L., Apel, E.C., Hornbrook, R.S., Blake, N.J., Weinheimer, A.J., Mauldin Iii, R.L., Cantrell, C.A., Castro, M.S., Conley, G., Holsen, T.M., Luke, W.T., Talbot, R., 2016. Constraints from observations and modeling on atmosphere–surface exchange of mercury in eastern North America. Elementa: Science of the Anthropocene 4, 000100.

Song, S., Selin, N.E., Soerensen, A.L., Angot, H., Artz, R., Brooks, S., Brunke, E.-G., Conley, G., Dommergue, A., Ebinghaus, R., 2015. Top-down constraints on atmospheric mercury emissions and implications for global biogeochemical cycling. Atmospheric Chemistry and Physics 15, 7103-7125.

Stamenkovic, J., Gustin, M.S., 2009. Nonstomatal versus stomatal uptake of atmospheric mercury. Environmental science & technology 43, 1367-1372.

Travnikov, O., Jonson, J., Andersen, A., Gauss, M., Gusev, A., Rozovskaya, O., Simpson, D., Sokovyh, V., Valiyaveetil, S., Wind, P., 2009. Development of the EMEP global modelling framework: Progress report. EMEP/MSC-E Technical Report 7/2009, Meteorological Synthesizing Centre–East (MSC-E), Moscow, Russia.

Van Wijk, M.T., Williams, M., Shaver, G.R., 2005. Tight coupling between leaf area index and foliage N content in arctic plant communities. Oecologia 142, 421-427.

Vivanco, M.G., Bessagnet, B., Cuvelier, C., Theobald, M.R., Tsyro, S., Pirovano, G., Aulinger, A., Bieser, J., Calori, G., Ciarelli, G., Manders, A., Mircea, M., Aksoyoglu, S., Briganti, G., Cappelletti, A., Colette, A., Couvidat, F., D'Isidoro, M., Kranenburg, R., Meleux, F., Menut, L., Pay, M.T., Rouïl, L., Silibello, C., Thunis, P., Ung, A., 2017. Joint analysis of deposition fluxes and atmospheric concentrations of inorganic nitrogen and sulphur compounds predicted by six chemistry transport models in the frame of the EURODELTAIII project. Atmospheric Environment 151, 152-175.

Walmsley, J.L., Wesely, M.L., 1996. Modification of coded parameterizations of surface resistances to gaseous dry deposition. Atmospheric Environment 30, 1181-1188.

Wang, X., Bao, Z., Lin, C.J., Yuan, W., Feng, X., 2016a. Assessment of Global Mercury Deposition through Litterfall. Environ Sci Technol 50, 8548-8557.

Wang, X., Luo, J., Yin, R., Yuan, W., Lin, C.-J., Sommar, J., Feng, X., Wang, H., Lin, C., 2016b. Using mercury isotopes to understand mercury accumulation in the montane forest floor of the eastern tibetan plateau. Environmental science & technology 51, 801-809.

Weiss, A., Norman, J., 1985. Partitioning solar radiation into direct and diffuse, visible and near-infrared components. Agricultural and Forest meteorology 34, 205-213.

Wesely, M., 1989. Parameterization of surface resistances to gaseous dry deposition in regional-scale numerical models. Atmospheric Environment (1967) 23, 1293-1304.

Wesely, M., Hicks, B., 2000. A review of the current status of knowledge on dry deposition. Atmospheric environment 34, 2261-2282.

Wu, Z., Wang, X., Chen, F., Turnipseed, A.A., Guenther, A.B., Niyogi, D., Charusombat, U., Xia, B., William Munger, J., Alapaty, K., 2011. Evaluating the calculated dry deposition velocities of reactive nitrogen oxides and ozone from two community models over a temperate deciduous forest. Atmospheric Environment 45, 2663-2674.

Xu, X., Yang, X., Miller, D.R., Helble, J.J., Carley, R.J., 1999. Formulation of bi-directional atmosphere-surface exchanges of elemental mercury. Atmospheric Environment 33, 4345-4355.

Zhang, L., Brook, J., Vet, R., 2003. A revised parameterization for gaseous dry deposition in air-quality models. Atmospheric Chemistry and Physics 3, 2067-2082.

Zhang, L., Moran, M.D., Makar, P.A., Brook, J.R., Gong, S., 2002. Modelling gaseous dry deposition in AURAMS: a unified regional air-quality modelling system. Atmospheric Environment 36, 537-560.

Zhang, L., Wright, L.P., Blanchard, P., 2009. A review of current knowledge concerning dry deposition of atmospheric mercury. Atmospheric Environment 43, 5853-5864.

Zheng, W., Obrist, D., Weis, D., Bergquist, B.A., 2016. Mercury isotope compositions across North American forests. Global Biogeochemical Cycles 30, 1475-1492.

Zhu, W., Lin, C.-J., Wang, X., Sommar, J., Fu, X., Feng, X., 2016. Global observations and modeling of atmosphere–surface exchange of elemental mercury: a critical review. Atmospheric Chemistry and Physics 16, 4451-4480.

2.7 Supplemental information

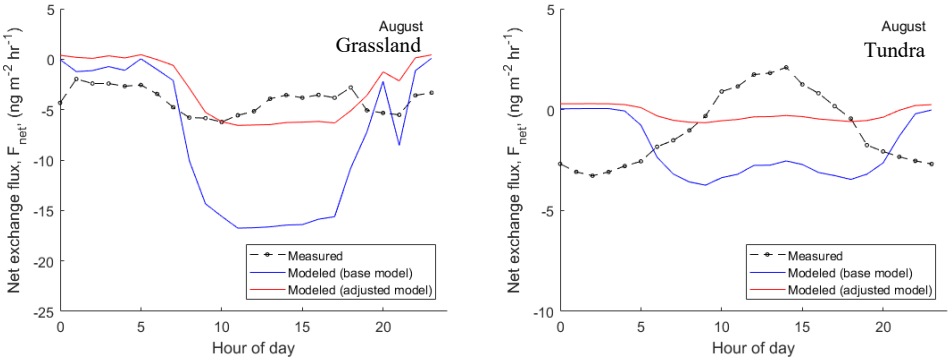

Figure S1. Model response to reduced stomatal uptakes of Hg^0 and comparison of modeled and measured net exchange fluxes of Hg^0 in August: A) temperate grassland site and B) Arctic tundra site.

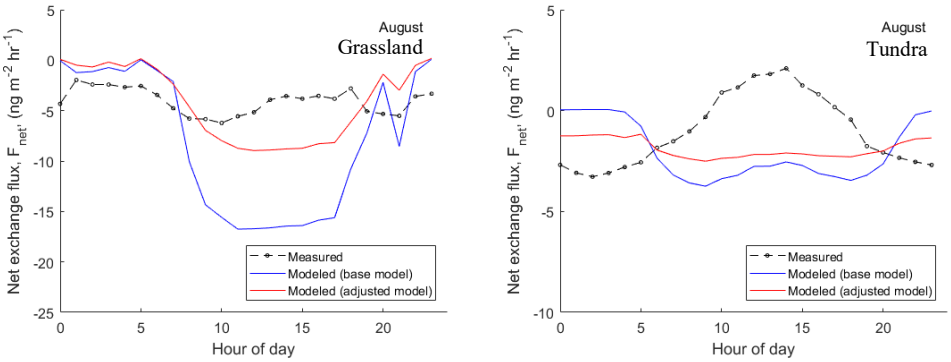

Figure S2. Model response to decreased cuticular and ground uptake, and reduced stomatal uptake, of Hg^0, and comparison of modeled and measured net exchange fluxes of Hg^0 in August: A) temperate grassland site and B) Arctic tundra site.

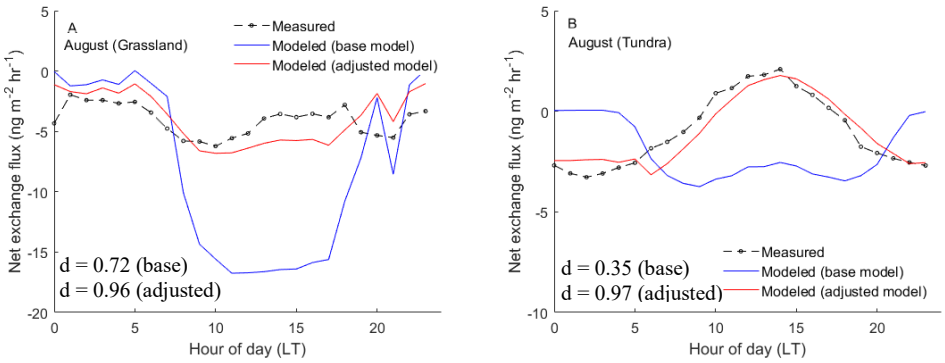

Figure S3. Model response to reduced nighttime and increased daytime soil re-emission and revised resistance parameters, and comparison of modeled and measured net exchange fluxes of Hg^0 in August: A) temperate grassland site and B) Arctic tundra site.

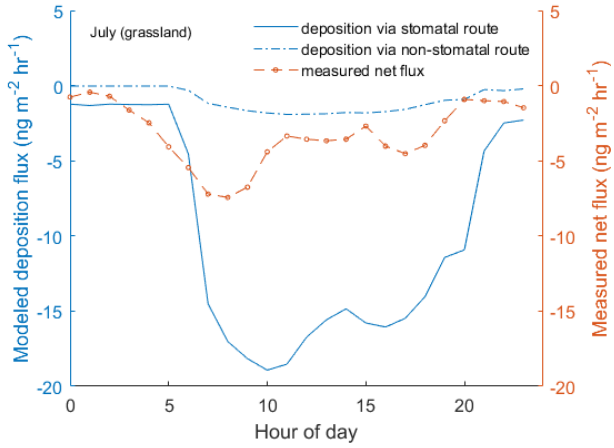

Figure S4. Contributions of stomatal and non-stomatal uptake of Hg^0 using the base model in July at the temperate grassland.

3 CHAPTER 3: Application of a multimedia model to investigate recovery of Lake Superior from historical polychlorinated biphenyl (PCB) contamination

Abstract

Polychlorinated biphenyl (PCB) compounds are of major concern in the Laurentian Great Lakes because of their toxicity and historical use, primarily as additives to oils and industrial fluids, and discharge from industrial sources. Following the ban on production in the U.S. in 1979, atmospheric concentrations of PCBs in the Lake Superior region decreased rapidly. Subsequently, PCB concentrations in the lake surface water also reached near equilibrium as the atmospheric levels of PCBs declined. However, previous studies on long-term PCB concentrations and trends in top predatory fish suggested that an initial decline of PCB concentrations in fish has leveled off in Lake Superior. In this study, a dynamic multimedia model was developed with the objective to investigate the observed leveling off of PCB concentrations in Lake Superior lake trout. The model structure consists of two water layers (the epilimnion and the hypolimnion), and the surface mixed sediment layer, with atmospheric deposition as the primary external pathway of PCB input to the lake. The model was applied for different PCB congeners exhibiting a range in hydrophobicity and volatility. Using this model, we compare the long-term trends in predicted PCB concentrations in different environmental media with relevant available measurements for Lake Superior. The modeling results suggest that rates of PCB decline in Lake Superior lake trout (half-life, $t_{1/2} \approx 21$ to 92 years) are slower than rates of decline in air ($t_{1/2} \approx 12$ years), water ($t_{1/2} \approx 12$ years), and sediment ($t_{1/2} \approx 17$ years). However, the model predictions are not consistent with observed trends in lake trout PCB concentrations for 1990-2013, with $t_{1/2} > 90$ years. The combination of the weak of role of sediment resuspension in elevating PCB levels in water, as predicted by the model, and the substantially longer time for recovery in lake trout as indicated by monitoring data leads us to suggest that food web changes in the lake may be affecting trends in PCB concentrations in lake trout.

3.1 Introduction

Following their production, which began in 1930 in the United States (U.S.), polychlorinated biphenyl (PCB) compounds were primarily used in packing plants, paper mills, electric equipment manufacturers, tanneries, machine shops, and foundries in the U.S. Great Lakes region (Jeremiason et al., 1994; Hornbuckle et al., 2006). Despite the fact that new usages of PCBs were halted in 1976 (Hornbuckle et al., 2006) followed by complete production ban in 1979 in the U.S., PCBs continue to disseminate globally through repeated cycles of atmosphere-surface exchange (Perlinger et al., 2016).

Because of this cycling, PCBs have been detected even in remote locations (e.g. Isle Royale, Lake Superior and the Arctic Ocean) with very little to no history of PCB usage (Swain et al., 1977; Sobek and Gustafsson, 2014). Lake Superior, the largest of the five Great Lakes, is sensitive to persistent and semi-volatile hydrophobic organic pollutants such as PCBs because of its large surface area and long water residence time (Eisenreich et al., 1981). More specifically, PCBs are of great concern in Lake Superior aquatic systems because these compounds tend to bioaccumulate in the aquatic food chain (Swackhamer and Hites, 1988) and pose health risks to wildlife and humans through fish consumption (Stow, 1995; Humphrey et al., 2000).

Although at present PCBs are not being actively used in the U.S., they are still being emitted into the atmosphere in the Great Lakes basin through volatilization from waste disposal sites or burning of products containing high concentrations of PCBs (Hornbuckle

et al., 2006; Sun et al., 2006). In addition, secondary emissions (via surface-air exchange) also contribute to background atmospheric levels of PCBs (e.g., Rowe and Perlinger, 2012). Given its large surface area coupled with a lack of industrial sources in the basin, atmospheric deposition is likely to be the major route of entry for PCBs in Lake Superior (Strachan and Eisenreich, 1988; Eisenreich and Hollod, 1979; Jeremiason et al., 1994). Following atmospheric deposition (wet and dry), PCBs accumulate in water and lake sediments, and every trophic level of the aquatic food web (Eisenreich and Hollod, 1979; Houde et al., 2008).

Temporal trend analysis (1992-2010) of atmospheric PCB concentration data collected at Eagle Harbor in Michigan, one of the Lake Superior air monitoring locations monitored by the Integrated Atmospheric Deposition Network (IADN), revealed that atmospheric concentrations tend to respond rapidly (half-life, $t_{1/2}$ = 13.0±2.8 years) to changes in PCB emissions (Salamova et al., 2013). Previous studies (e.g., Jeremiason et al., 1994) showed that the measured PCB concentrations Lake Superior waters also declined rapidly ($t_{1/2}$ = 3.5 years) from 1980 to 1992 as a direct consequence of reduced atmospheric emissions. In contrast, temporal trend analysis (1999-2009) of fish PCB concentration data from several Lake Superior locations indicated a lack of statistically significant declining concentration trend in top predatory fish (Chang et al., 2012). Lin (2016) analyzed seven Lake Superior fish concentration data sets from 1978-2013 produced by three state and two federal agencies and found no statistically significant declining trends in fish PCB concentrations in five of the seven data sets from 1995-2013. The study by Lin (2016) found that the fish PCB concentrations declined rapidly in the late 1970s and 1980s;

however, in recent years, concentrations in Lake Superior fish have leveled off. This recent leveling off of PCB concentrations in Lake Superior fish was also observed independently in other studies (e.g., David et al., 1996; Bhavsar et al., 2007).

To explain the lag in fish response to declining atmospheric and water PCB concentrations, and the current leveling off of observed fish PCB concentrations, a couple of hypotheses have been proposed. Some researchers (e.g., Smith, 2000) hypothesized that recycling of PCBs from sediments to water could be the cause of the observed slow recovery in fish in Lake Superior. A second hypothesis was that changes in lake food chain and climatic influences lead to the slower response in biota as compared to lake water (Lake Erie, Hebert et al., 2006; Lake Ontario, Gewurtz et al., 2011). However, both of these hypotheses are yet to be tested.

In this study, we developed a dynamic coupled air-water-sediment model for Lake Superior with the primary objective to examine whether or not sediment resuspension fluxes of PCBs can adequately explain the lag in biota response despite a consistent decline in the atmospheric concentration of PCBs. Other objectives of this study were to compare and contrast environmental transport and fate of PCB congeners of varying thermodynamic properties based on their modeled and observed temporal trends in water and sediment concentrations, and to apply a simplified fish bioaccumulation model together with predicted aqueous concentrations to estimate the likely delay in fish recovery from legacy PCB inputs that can be attributed to sediment resuspension and bioaccumulation.

3.2 Methods

3.2.1 Site description

Of the five Laurentian Great Lakes, Lake Superior is the largest in terms of both volume (12,100 km^3) and surface area (82,100 km^2; Spence et al., 2011). The mean depth of the lake is ca. 150 m (Xue et al., 2017) and water residence time is ca. 180 years (Quinn, 1992). The lake receives ca. two-thirds of its water inputs from precipitation (2,071 $m^3\ s^{-1}$), while the watershed contributes, on average, ca. 1,620 $m^3\ s^{-1}$ (Lenters, 2004). Both over-lake air and surface water temperatures exhibit strong seasonal variability, which is evident from the time-series of mean monthly over-lake air temperature (from 1948 to 2014) and surface water temperature (from 1950 to 2015) shown in Fig. 1. The long-term record of wind speed data (from 1948 to 2011) measured over the lake surface also exhibit strong seasonality (Fig. 1) with a mean speed of 6 m s^{-1}, while the mean difference between wind speed in winter and summer months is ca. 3.5 m s^{-1}.

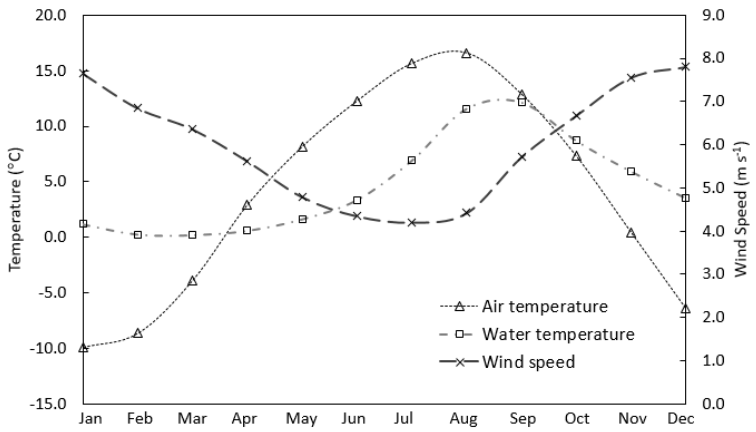

Figure 1. Mean monthly over-water air and surface water temperatures, and wind speed for Lake Superior (data source: https://coastwatch.glerl.noaa.gov/statistic/).

Lake Superior is generally dimictic (Assel, 1986). Thermal layers in lake waters begin to form in spring (April) and the lake becomes completely vertically stratified in middle to late July (Bennett, 1978; Ullman et al., 1998: from Urban et al., 2005) until September. During spring and fall, waters freely circulate from the surface to the bottom. In winter, ice cover forms on Lake Superior, with large inter-annual variability (Wang et al., 2012).

3.2.2 Model inputs

3.2.2.1 *Congener-specific atmospheric PCB concentrations*

The coupled air-water-sediment model (described in section 3.2.3) was driven by atmospheric concentrations of six PCB congeners (Congeners 18, 52, 118, 153, 180, and 194; their physicochemical properties are listed in Table S1) over the period 1930 to 2013. This time span conforms to the onset of commercial production of PCBs and the most recently measured PCB concentration data in air reported by the IADN for the Eagle Harbor, Michigan site. To reconstruct the historical atmospheric PCB concentrations from 1930 to 1989, we utilized the PCB emissions inventory from Breivik et al. (2007). This inventory provides country-specific emissions of 22 individual PCB congeners (from 1930 to 2000) including the six congeners selected for this study. Of the 22 congeners listed in the Breivik et al. (2007) emission inventory, 17 congeners have been routinely monitored at the Eagle Harbor site by the IADN since 1990. Total emissions of these 17 congeners in the U.S. from 1930 to 2000 are shown in Fig. 2A. Using these two data sets (i.e., the Breivik inventory and the IADN concentration measurements), we estimated the total (n = 17 congeners) PCB emissions in the U.S. and the total (n = 17) atmospheric PCB

concentrations from 1990 to 2000. Following these estimates, the ratios between total concentrations and total emissions were calculated for each year from 1990 to 2000. Because the resulting ratios exhibit a wide range (e.g., 1.6 to 12.6 pg m^{-3} yr $tons^{-1}$), the lower bound estimate was used to calculate the total (n = 17) atmospheric PCB concentrations using the emission inventory for years 1930 to 1989 using Eq. (1).

$$\sum_{n=17} C_{PCB} = \sum_{n=17} E_{PCB} \left(\frac{tons}{year}\right) \times 1.6 \left(\frac{pg}{m^3}\frac{year}{tons}\right), \quad (1)$$

where $\sum_{n=17} C_{PCB}$ is the sum of total (n = 17) atmospheric PCB concentrations and $\sum_{n=17} E_{PCB}$ is the sum of total (n = 17) atmospheric emissions for each year from 1930 to 1989.

For the selected six congeners, the ratio between congener-specific to total (n = 17) concentrations was calculated using the data measured by the IADN from 1990 to 2000. Because the resulting ratios exhibited large ranges, geometric means were calculated for each of the six congeners. These congener-specific ratios were multiplied by $\sum_{n=17} C_{PCB}$ to estimate the corresponding congener-specific concentrations from 1930 to 1989 for the U.S. Reconstructing congener-specific concentration profiles in this manner assumes that the ratio: $\frac{\sum_{n=17} C_{PCB}}{\sum_{n=17} E_{PCB}}$ = 1.6 pg m^{-3} yr $tons^{-1}$ was constant throughout over the period of 1930 to 1989. For 1990-2013, we used atmospheric PCB concentrations measured by the IADN as input to the model. The concentration profiles of six congeners from 1930-2013 are shown in Fig. 2B.

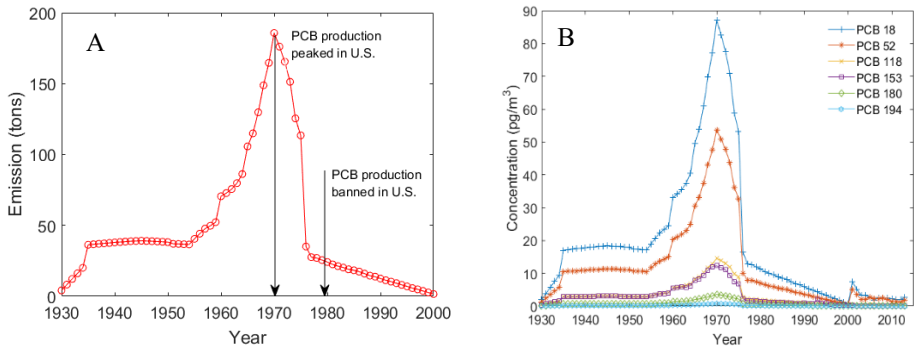

Figure 2. (A). Historic emissions of 17 PCB congeners in the U.S. from 1930-2000. (B). Atmospheric concentration profiles of six PCB congeners from 1930-2013.

3.2.2.2 *Lake and meteorological parameters*

The physical attributes of Lake Superior that were used in this study are listed in Table 1. The mean monthly over-lake air temperature, lake surface temperature, and over-lake wind speed data from 1948-2014 were obtained from the meteorological databases of NOAA-Great Lakes Environmental Research Laboratory. The data points for each of these parameters were fitted using simple sinusoidal functions to enable data interpolation for a daily time step. In addition, mean monthly ice-cover data for Lake Superior was used to adequately represent the influence of lake ice coverage. Data for vertical diffusion coefficient across the thermocline were obtained from McCarthy (2016). These data points were fitted using a simple sinusoidal function to enable data interpolation for a daily time step. Table 2 lists the monthly mean meteorological parameter values used as inputs in this modeling study. The mean monthly ice coverage (the percentage of the total lake surface area) data from 1973 to 2002 are also provided in Table 2 (Assel, 2003).

Table 1. Lake parameter values used in the Lake Superior PCB model.

Parameter	Value	Units
Lake volume, V	12,230	km^3
Lake Surface area, A_0	82,100	km^2
Throughflow of water (including precipitation), Q_{total}	116	$km^3\ yr^{-1}$
Mean precipitation rate into the lake, Q_{prec}	65	$km^3\ yr^{-1}$
Watershed runoff into the lake, Q_{wa}	51	$km^3\ yr^{-1}$
The depth of epilimnion, h_E	20	m
The depth of hypolimnion, h_H	110	m
The depth of thermocline, h_{th}	20	m
Mass fraction of organic matter in atmospheric particles, f_{om}	0.20	
Total suspended particulate matter concentration in air, TSP	10	$\mu g\ m^{-3}$
Aerosol particle scavenging efficiency of precipitation, W_p	50,000	
Total suspended solids in both water columns, TSS	0.0004	$kg\ m^{-3}$
Mass fraction of organic carbon in suspended solids (in water layers), f_{oc}	0.20	
Mean particle settling velocity in water columns, V_s	394	$m\ yr^{-1}$
Aqueous boundary layer thickness in sediment layer, t_{bl}	0.05	cm
Sediment mixed layer depth, z_{mix}	1	cm
The density of solids in sediment, ρ_s	2,500	$kg\ m^{-3}$
The porosity of the sediment layer, ϕ	0.90	
Sediment resuspension rate, μ_{res}	0.25	$kg\ m^{-2}\ yr^{-1}$
Preservation factor of organic carbon in sediment layer, β	0.10	
Mass fraction of organic carbon in sediment layer, f_{ocs}	0.06	

Table 2. Mean monthly meteorological variables and ice coverage for Lake Superior.

Month	Over-water air temperature (°C)	Surface water temperature (°C)	Wind Speed ($m\ s^{-1}$)	Percent ice coverage
January	-9.9	1.2	7.6	18
February	-8.6	0.3	6.8	43
March	-3.9	0.2	6.4	44
April	2.9	0.6	5.6	12
May	8.2	1.6	4.8	1
June	12.3	3.4	4.4	0
July	15.6	6.9	4.2	0
August	16.6	11.6	4.4	0
September	12.9	12.2	5.7	0
October	7.3	8.7	6.7	0
November	0.5	5.9	7.6	0
December	-6.4	3.5	7.8	2

3.2.3 Model description

To simulate the historical to present-day (i.e., 1930-2013) concentrations of six PCB congeners in Lake Superior, a three-box model was developed. This modeling framework includes lake stratification; the lake is divided into the surface layer (epilimnion), the deep-water layer (hypolimnion), and a surface mixed sediment layer (SMSL), which is in contact with the hypolimnion. Atmospheric deposition of PCBs was the primary input to the model lake. Because of its remote location and small number of point sources of PCBs (Jeremiason et al., 1994), the contribution from the Lake Superior watershed was assumed to be negligible. The conceptual schematic of the model lake is shown in Fig. 3.

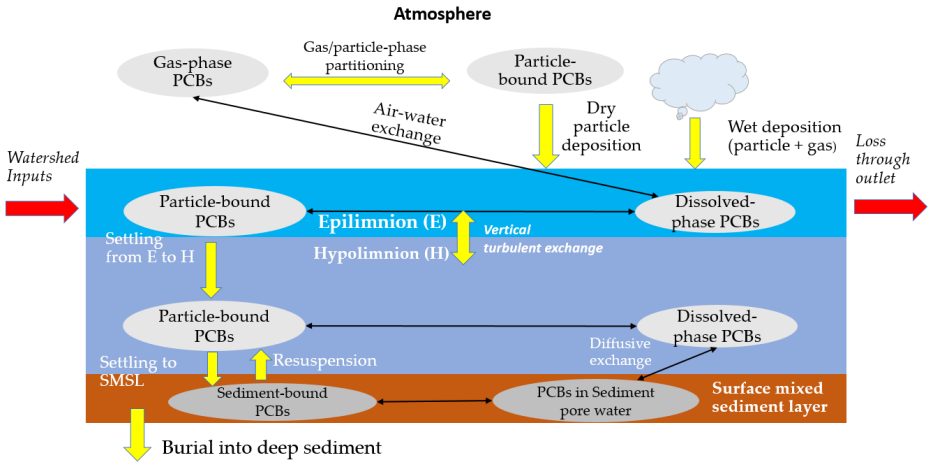

Figure 3. Structure of the multimedia PCB model for Lake Superior.

The mass balance equations for epilimnion, hypolimnion, and surficial sediment layer are

$$\frac{dC_wE}{dt} = J_t - \left(k_{wE} + k_{aw_{TE}} + k_{sE} + k_{exE}\right)C_wE + k_{exE}C_wH\ , \tag{2}$$

$$\frac{dC_wH}{dt} = -(k_{sH} + k_{exH} + k_{sedex})C_wH + \left(k_{sH_{star}} + k_{exH}\right)C_wE + (k_{sedex}/f_{wH}/K_d^{sc})C_s\ , \tag{3}$$

$$\frac{dC_s}{dt} = (m^{-1}V_sf_{sH} + m^{-1}v_{sedex})C_wH - (V_sr_{sw}\beta m^{-1} + v_{sedex}{f_{wH}}^{-1}K_d^{sc^{-1}}m^{-1})C_s\ , \tag{4}$$

where C_wE, C_wH, and C_s are the PCB concentrations in the epilimnion, hypolimnion, and SMSL, respectively. Total PCB inputs to the lake (J_t) consist of net air-water exchange flux (J_{aw}), dissolved wet deposition flux (J_{dwet}), dry particle deposition flux (J_{pdry}), and wet particle deposition flux (J_{pwet}). Hence, J_t is expressed as

$$J_t = J_{aw} + J_{dwet} + J_{pdry} + J_{pwet}. \tag{5}$$

The net air-water exchange flux was calculated according to Schwarzenbach et al. (2003) as

$$J_{aw} = v_{a/w} C_a (1 - \phi)(A_o - \frac{A_o IC}{100})/V_E/K_{aw}, \quad (6)$$

where $v_{a/w}$ is air-water (epilimnion) exchange velocity, C_a is atmospheric concentration of a PCB congener, A_o is surface area of the lake, V_E is volume of the epilimnion, K_{aw} is temperature-corrected dimensionless Henry's law constant, IC is the monthly averaged ice coverage (%), and ϕ is the fraction of PCB congener sorbed to particles. Using the gas-particle partitioning approach by Harner and Shoeib (2002), ϕ was calculated as

$$\phi = \frac{K_P TSP}{(K_P TSP + 1)}, \quad (7)$$

where TSP is the total suspended particulate concentration in the atmosphere, and K_P is the particle-gas partition coefficient, which was calculated as

$$\log(K_P) = \log(K_{oa}) + \log(f_{om}) - 11.91, \quad (8)$$

where K_{oa} is the congener-specific temperature corrected octanol-air partition coefficient, and f_{om} is the fraction of organic matter on atmospheric particles. The wet deposition flux for gas-phase PCB congeners was calculated as

$$J_{dwet} = Q_{pr} C_a (1 - \phi)/V_E/K_{aw}, \quad (9)$$

where Q_{pr} is precipitation flow rate into the lake. The dry particle deposition flux was calculated as

$$J_{pdry} = \frac{C_a \phi v_d f_d A_o}{V_E}, \quad (10)$$

where v_d is the dry particle deposition velocity, and f_d is the fraction of time it is not raining or snowing (0.9). The wet particle deposition flux was calculated as

$$J_{pwet} = \frac{W_p Q_{pr} C_a \phi}{V_E}. \quad (11)$$

The rate constants in Eqs. (2-4) are defined as follows:

Flushing rate of the epilimnion, $k_{wE} = \frac{Q}{V_E}$, where Q is the total outflow rate from the lake.

Air-water exchange rate, $k_{aw_{TE}} = f_{wE} \frac{v_{a/w}}{h_E}$, (12)

where h_E is depth of the epilimnion, and f_{wE} is fraction dissolved in epilimnion, which was calculated as

$$f_{wE} = \frac{1}{1 + r_{sw} K_{dE}},$$

where r_{sw} is the solid-to-water phase ratio, and K_{dE} is the distribution coefficient of suspended solids in the epilimnion. Equation (13) was used to calculate K_{dE}.

$$K_{dE} = K_{ocE} f_{oc}, \quad (13)$$

where f_{oc} is fraction of organic carbon content of suspended solids (in the epilimnion and hypolimnion), and the partition coefficient between organic carbon and water (in the epilimnion), K_{ocE}, was calculated as

$$K_{ocE} = 10^{(0.74\log(K_{ow_{TE}})+0.15)}, \quad (14)$$

where $K_{ow_{TE}}$ is the temperature-corrected (in epilimnion) octanol-water partition coefficient for different PCB congeners. An expression similar to f_{wE} was used to calculate the fraction dissolved in hypolimnion (f_{wH}), while K_d was calculated using the relevant properties of the hypolimnion.

The removal rate of particles from the epilimnion (k_{sE}) was calculated as

$$k_{sE} = \frac{V_s}{h_E}(1 - f_{wE}), \quad (15)$$

where V_s is the particle settling velocity from water to sediment, and h_E is the depth of epilimnion.

The exchange rate (loss from epilimnion by mixing across thermocline), k_{exE}, and loss from the hypolimnion by mixing across thermocline (k_{exH}) were calculated as

$$k_{exE} = \frac{v_{ex}}{h_E}, \quad (16)$$

$$k_{exH} = \frac{v_{ex}}{h_H}, \quad (17)$$

where v_{ex} is exchange velocity across thermocline, which was calculated as

$$v_{ex} = \frac{E_{th}}{h_{th}}, \quad (18)$$

where E_{th} is vertical diffusion coefficient across thermocline, and h_{th} is thermocline thickness. The rate of particle-bound PCB removal from hypolimnion (k_{sH}) was calculated as

$$k_{sH} = \frac{V_s}{h_H}(1 - f_{wH}), \tag{19}$$

The sediment-water exchange rate, k_{sedex} was calculated using

$$k_{sedex} = \frac{v_{sedex}}{h_H} \tag{20}$$

where v_{sedex} is sediment exchange velocity. Equation (21) was used to calculate v_{sedex}.

$$v_{sedex} = f_{wH}(v_{seddiff} + K_d^{sc}\mu_{res}) \tag{21}$$

In Eq. (21), the terms $v_{seddiff}$, K_d^{sc}, and μ_{res} are the diffusive exchange velocity between the SMSL and the hypolimnion, the distribution coefficient in SMSL, and the sediment resuspension rate, respectively. The expressions for calculating these terms are provided below (Eqs. 22-23).

$$v_{seddiff} = \frac{D_{PCBi}^{w}}{\delta_{bl}}, \tag{22}$$

where D_{PCBi}^{w} is the molecular diffusivity of congener in water (hypolimnion), and δ_{bl} is the aqueous boundary layer thickness in SMSL.

$$K_d^{sc} = K_{ocH} f_{ocs}, \tag{23}$$

where f_{ocs} is the mass fraction of organic carbon of SMSL.

The sediment mixed layer mass per area (m) was calculated as

$$m = z_{mix}(1 - \varphi_{sc})\rho_{sc}, \quad (24)$$

where z_{mix} is sediment mixed layer depth, φ_{sc} is porosity of sediment, and ρ_{sc} is density of sediment. Eqs. (2-4) were solved numerically using MATLAB® solver *ODE45*, which yielded the concentrations (C_wE, C_wH, and C_s) at a daily time step from 1930 to 2013.

3.2.4 Model validation

3.2.4.1 *Data sets of measured PCB concentrations in water*

To compare the congener-specific modeled PCB concentrations in epilimnion water (i.e., C_wE) with measured concentrations, we used the following data sets: measurements from 1986 reported by Baker and Eisenreich (1990), measurements conducted in fall 2002 and spring 2003 reported by Zhu (2003), the 1996-97 measurements reported by IADN (Galarneau et al., 2000; Buehler et al., 2001), and 2006 measurements from the Great Lakes Aquatic Contaminants Survey (GLACS; USEPA GLNPO, 2009). Together, these sources reported measured aqueous concentrations for congeners 18, 52, 118, 180, and 194.

3.2.4.2 *Data sets of measured PCB concentrations in sediment*

Reliable data of congener-specific measured PCB concentrations from surficial sediment in Lake Superior are very limited. Moreover, measurements from recent years (e.g., after 2002) are lacking. To evaluate the modeled sediment concentrations (C_s), we used two data sets of PCB concentrations in sediments in Lake Superior in 1986 (Baker and Eisenreich,

1989) and 2002 (Li et al., 2009), respectively. These sources reported concentrations of congeners 18, 52, 118, and 180 measured across various Lake Superior sediment core locations.

3.2.5 Uncertainty analysis

Large uncertainties are associated with several input parameters relating to lake characteristics and thermodynamic properties of individual PCB congeners. To assess the influence of these uncertainties on the modeled concentrations, four parameters (V_s, z_{mix}, K_{ow}, and K_{aw}) were varied over plausible ranges. These four parameters can be categorized into two groups: PCB thermodynamic properties (K_{ow} and K_{aw}) and lake characteristics (V_s and z_{mix}). These PCB thermodynamic properties were chosen because of large uncertainties, primarily due to different measurement and estimation techniques used for the determination of their values (Mackay et al., 1997). In addition, we assumed lake-wide averaged values for certain lake characteristics (e.g., V_s and z_{mix}). However, in reality these parameters are likely to be spatially variable. To evaluate the uncertainty in modeled water and sediment concentrations, a one-at-a-time sensitivity analysis was performed using both high and low values of each of these four parameters, while keeping the other three parameters fixed at their base values (i.e., base scenario). The results obtained through this approach were used to determine which parameter contributes the largest uncertainty, in terms of magnitude, in the modeled aqueous and sediment concentrations from the base case scenario. A second objective of performing the uncertainty analysis was to estimate

the resulting half-lives of total (n = 6) PCBs in water and sediment for each parameter-setting scenario (i.e., base case and upper and lower bound cases).

3.2.6 Modeling of PCB concentrations in fish

To provide an estimate of the time response of PCB concentrations in fish as a function of declining water concentrations, we applied a simple first-order bioaccumulation model. This model is based on the assumption that the rate of change in PCB concentrations in predatory fish (e.g., lake trout) is a function of two rate constants: (i) the PCB uptake rate via ingestion of diet (prey; k_D), and (ii) the mortality rate (k_E) of predatory fish. The generic form of the time-varying bioaccumulation model is:

$$\frac{dC_{fish}}{dt} = k_D C_D - k_E C_{fish}, \quad (25)$$

where C_{fish} and C_D are the PCB concentrations in the target predatory fish (e.g., lake trout) and in the prey (diet) item in the food web, respectively. The dietary uptake clearance rate constant k_D is a linear function of the dietary chemical transfer efficiency (E_D), the feeding rate (G_D), and the weight of the organism (W_B; Arnot and Gobas, 2004). Equations (26) – (28) were used to calculate each of these terms.

$$k_D = \frac{E_D G_D}{W_B}. \quad (26)$$

To provide an estimate of congener specific dietary PCB transfer efficiency, E_D was calculated as a function of K_{ow} using Eq. (27).

$$E_D = (3.0 \times 10^{-7} K_{ow} + 2.0)^{-1}. \quad (27)$$

To estimate the feeding rates in cold-water fish species, Arnot and Gobas (2004) suggested the following bioenergetic relationship based on studies of lake trout.

$$G_D = 0.022W_B^{0.85} \exp(0.06T), \quad (28)$$

where T is the water temperature in °C.

Assuming a first-order rate of decline in the modeled concentrations in hypolimnion water, C_wH was expressed as

$$\frac{dC_wH}{dt} = -k_{wH}C_wH. \quad (29)$$

The concentration of any given PCB congener can be determined by integrating Eq. (29) as

$$C_wH = C_wH_{(t=0)}e^{-k_{wH}t}, \quad (30)$$

where k_{wH} is the first-order rate of constant (yr^{-1}) at which the PCB concentrations in the hypolimnion decrease, and $C_wH_{(t=0)}$ is the concentration at time, t = 0. We used a congener-specific bioaccumulation factors (BAF; ratio of concentration of PCB congener in the organism to the concentration of PCB congener in water) to determine the concentrations in zooplankton (trophic level 2). Following this step, using the relationships between trophic magnification factor (TMF) and trophic level (TL) developed for the lake trout food web from North American lakes by Houde et al. (2008), we transformed the individual congener-specific trophic level 2 concentrations to trophic level 4 concentrations (C_D). The transformed form of Eq. (25) is written as:

$$\frac{dC_{fish}}{dt} = k_D \frac{BAF_i}{\alpha} C_w H - k_E C_{fish}. \quad (31)$$

Substituting Eq. (30) into Eq. (31) yields

$$\frac{dC_{fish}}{dt} + k_E C_{fish} = k_D \frac{BAF_i}{\alpha} C_w H_{(t=0)} e^{-k_{wH} t}. \quad (32)$$

The solution to Eq. (32) is

$$C_{fish} = \frac{\frac{BAF_i}{\alpha} k_D k_{wH} C_w H_{(t=0)}}{k_E - k_{wH}} (e^{-k_{wH} t} - e^{-k_E t}) \quad (33)$$

where $\alpha = \frac{10^{(logTMF_i \times TL_2)}}{10^{(logTMF_i \times TL_4)}}$

Here, TL_i values were taken as $TL_2 = 2$ and $TL_4 = 4$. TMF_i values of various PCB congeners were taken from the paper by Houde et al. (2008). BAF_i values of individual PCB congeners related to K_{ow} values were based on water and zooplankton PCB concentration data (Borgå et al., 2006). Using a timestep of a day, the simulations were performed from 1990 to 2013 to estimate the total (n = 6) fish PCB concentrations. Subsequently, the $t_{1/2}$ in fish was determined for the same period and compared with available measured $t_{1/2}$ fish data.

3.3 Results and discussion

To enable an understanding of the role of sediment recycling in modifying PCB concentrations in water layers, the simulations were performed by i) allowing sediment resuspension and ii) turning-off sediment resuspension into the hypolimnion. Using the

assembled measurements of congener-specific PCB concentrations in water and sediments, the model simulation results were compared (sections 3.3.1 and 3.3.2, respectively). Temporal trends in the total (n = 6) modeled PCB concentrations in water and surficial sediments were analyzed and compared with the measured atmospheric and fish PCB concentrations trends in section 3.3.3. The results from model parameter uncertainty tests are discussed in section 3.3.4. Finally, the predicted fish PCB concentration trend was converted into half-life ($t_{1/2}$) in fish and compared with the $t_{1/2}$ estimated using fish PCB concentration monitoring data from across Lake Superior (section 3.3.5).

3.3.1 PCB concentrations in water

The modeled $C_w E$, both with and without particle resuspension fluxes from the sediment layer (i.e., SMSL) to epilimnion waters is shown by the solid black and dashed red lines, respectively, in Figs. 4 (A-F). These results suggest that particle resuspension from the SMSL has a small effect on PCB concentrations in the water, especially for the low to medium molecular weight (MW) congeners (i.e., congeners with three to six chlorine atoms such as PCBs 18 to 153). However, for the high MW congeners (congeners with more than six chlorine atoms), especially PCB 194 in the set of six congeners that were modeled, particle resuspension had a noticeable effect in increasing the aqueous concentration. This finding is not surprising because, of the six congeners, PCB 194 has the largest sediment resuspension flux due to its large solid-water distribution coefficient (K_d) and consequent high fraction associated with particulates in the lake.

The measured and modeled concentrations (annual or seasonal mean) for six PCB congeners are contrasted in Figs. 4 (A-F). Since differences between modeled C_wE and C_wH were small, the following results and discussion focus on the epilimnion only. In general, the ratio between the modeled and measured aqueous concentrations fell within factors of 0.2 to 3.7 (Table 3). For Congeners 18, 118, and 180 the model under-predicted the concentrations measured in 1986 (Baker and Eisenreich, 1989) by factors of 3.5 to 4.6. Large uncertainties associated with these measurements are noticeable from Figs. 4 (A, C, and E). In contrast, the model over-predicted the measured concentrations from 1996 and 1997 by factors of 1.2 to 3.6 for Congeners 18 and 52. Model-predicted seasonally averaged C_wE were in good agreement with the measured concentrations of Congeners 18 and 52 by Zhu (2003) (the ratios between the modeled and measured concentrations were within 0.3 to ~1.0). The available measurements from the most recent year (GLACS, 2006) for Congeners 18, 52, 118, 180, and 194 exhibited relatively good agreement as the modeled C_wE fell within the reported uncertainty ranges of the measured PCB concentrations (the ratio between the modeled and measured concentrations ranged from 1.2 to 3.6).

Table 3. Comparison between modeled and measured PCB concentrations in water.

Data source	Year	Congener	Measured concentration, (pg/L) [mean±sd]	Modeled concentration (epiliminon), (pg/L) [mean]	Modeled concentration (hypolimnion), (pg/L) [mean]
Baker and Eisenreich (1990)	1986	PCB 18	33.8±15.5	7.34	7.59
		PCB 118	21.9±11.0	6.32	6.56
		PCB 180	23.1±23.7	5.61	5.85
IADN data (Galarneau et al., 2000; Buehler et al., 2001)	1996	PCB 18	2.50	4.43	4.60
		PCB 52	4.80	5.82	6.07
	1997	PCB 18	1.50	4.05	4.20
		PCB 52	1.38	5.07	5.27
Zhu (2003)	Fall 2002	PCB 18	13.4±6.91	4.95	5.69
		PCB 52	19.2±10.9	5.10	5.72
	Spring 2003	PCB 18	4.79±1.13	4.96	4.87
		PCB 52	8.12±1.16	5.26	5.32
GLACS	2006	PCB 18	1.81±1.12	2.47	2.59
		PCB 52	1.47±1.88	5.14	5.15
		PCB 118	0.86±1.22	1.49	1.54
		PCB 180	0.61±1.10	2.20	2.29
		PCB 194	0.72±1.21	0.88	0.95

In general, the long-term trends in the modeled PCB concentrations (C_wE) were in accord with the trends of historic production and atmospheric emissions of the six PCB congeners (Fig. 2) with few exceptions. Firstly, even though the U.S. production of PCBs peaked in 1970, the highest modeled C_wE exhibited a time lag of 2 to 5 years (Fig. 4). This observed

time lag could result from an error in estimating the historic concentrations using a constant concentration to emission ratio based on present-day ratios. Another possible explanation for this time lag could pertain to secondary emissions (e.g., emissions of previously deposited PCBs from terrestrial and aquatic surfaces), that were not explicitly included in this study. Secondly, after the U.S. ban on PCB production in 1979, the concentrations in the water column declined more rapidly for the low MW congeners (e.g., Congeners 18, 52 with three to four chlorine atoms) than those of the high MW congeners (e.g., Congeners 180, 194 having seven or more chlorine atoms). This finding is not surprising because the low MW congeners undergo relatively faster air-water exchange as compared to the high MW congeners, resulting in a more rapid decline in aqueous concentrations. Overall, the declining temporal trends (1979-2013) in modeled PCB concentrations as shown in Figs. 4 (A-F) suggest that the U.S. ban on PCB production in 1979 has been effective in reducing the PCB burden in Lake Superior water. However, the present-day (2013) PCB concentrations in water are yet to reach the early 1930s levels for all six PCB congeners.

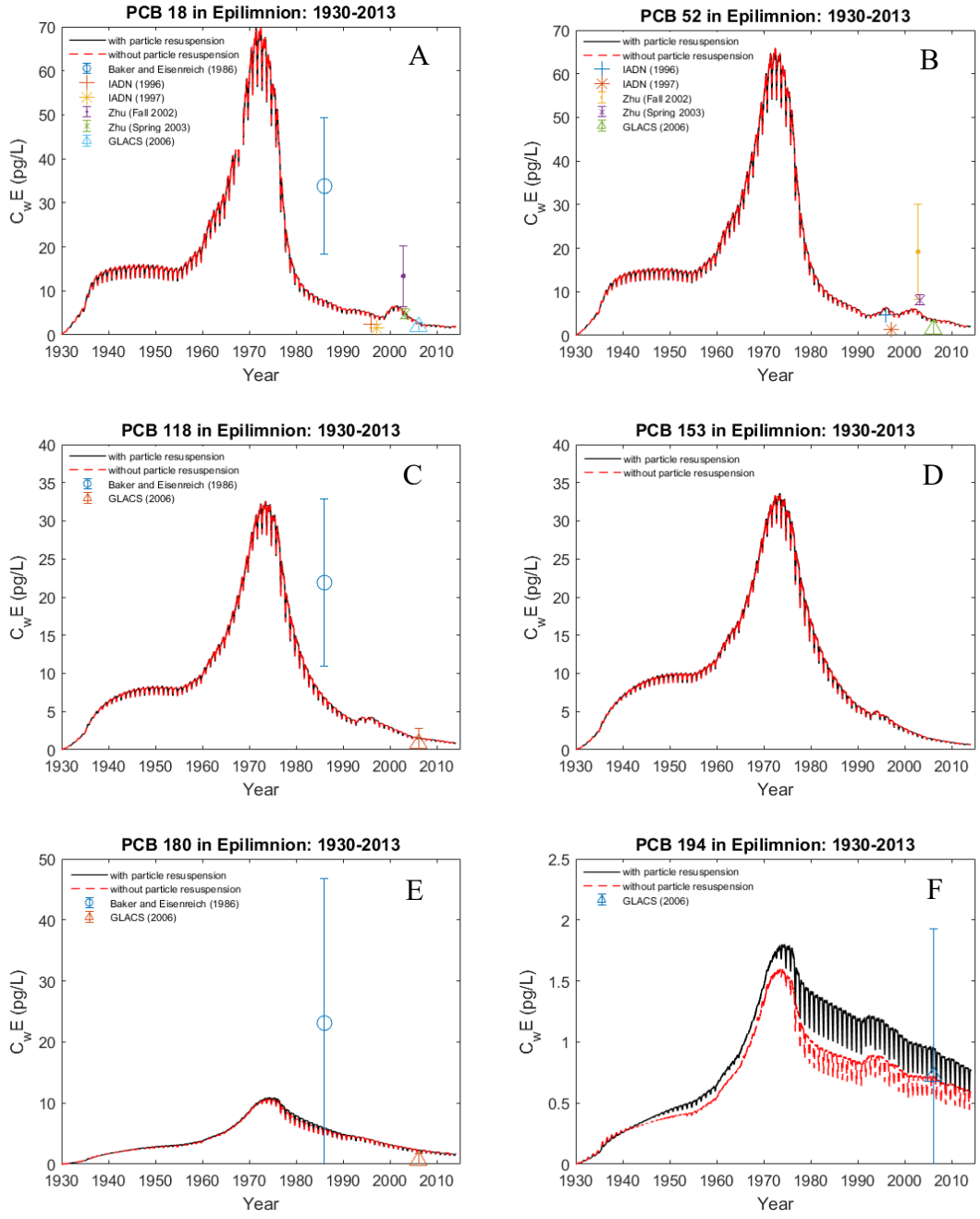

Figure 4. Simulated historical congener-specific PCB concentrations in water (epilimnion), $C_w E$ and comparison with measurements. The vertical lines indicate the uncertainty (in terms of standard deviation) in measured concentrations.

3.3.2 PCB concentrations in surficial sediment

It is evident from Figs. 5 (A-G) that sediment resuspension exhibited a noticeable effect on the modeled C_s as chlorination increases (e.g., PCB 18 in Fig. 5A vs. PCB 194 in Fig. 5G). This finding suggests that the high MW congeners are more sensitive to sediment recycling. Moreover, the increased sensitivity to sediment recycling as a function of increasing MW as evident from Figs. 5(A-E, G) is consistent with the physicochemical properties of the six PCB congeners (Table S1). In general, the high MW PCB congeners exhibit higher hydrophobicity (large K_{ow} and K_d values), thus stronger sorption to particles that eventually settle to sediments from waters (followed by recycling back to water). Therefore, when sediment resuspension was turned off, the resulting net sediment-water exchange flux of particle-bound PCBs yielded relatively high modeled C_s. Using the model results shown in Figs. 5(F-G), it was estimated that from 1979-2013, particle resuspension recycled to the water column ca. 20% of the PCB settling flux of PCBs 180 and 194. In contrast, the weak role of sediment resuspension for the low MW congeners is supported by their relatively weak hydrophobicity (low K_{ow} and K_d values). Typically, the K_{ow} values for high MW congeners (e.g., PCB 194) are up to three orders of magnitude higher than that of low MW congeners (e.g., PCB 18 or 52).

The rates of decline in PCB concentrations in the SMSL were controlled partially by the physicochemical properties of the congeners. Figure 5(A-G) shows that after the U.S. production ban in 1979, the modeled C_s of the low MW congeners declined relatively fast. It is likely that repeated sediment-water exchange of the low MW congeners tended to cause them to desorb into the water column and subsequently emit back into the

atmosphere, which resulted in their relatively faster decline in the SMSL (Hornbuckle et al., 2006). In contrast, concentrations of PCBs 180 and 194 declined at a slower rate since 1979 to 2013.

Because the sediment concentration data sets (i.e., Baker and Eisenreich, 1989 and Li et al., 2009) consisted of sediment core measurements collected across various locations in Lake Superior, these measurements were grouped based on proximity of the sampling locations. For example, sediment cores collected from the station 1383 (Baker-St. 1383) by Baker and Eisenreich (1989) were in closer proximity to sampling point Superior 12 (SU-12) than to sampling point Superior 08 (SU-08) by Li et al. (2009). Figure 5 shows the modeled PCB concentrations for six congeners in SMSL with corresponding measurements (except Congeners 153 and 194) for years 1986 and 2002. Together, Fig. 5(A-C and E-F) indicate that the model underestimated the measured C_s at all measurement locations. Of the four congeners, the best agreement between the model and measurements was found for PCB 180 in 1986 (ratio of modeled to measured concentrations = 0.75, Fig. 5E, Table 4). In general, for PCB 180, the modeled C_s were in good agreement with measurements (Fig. 5(E-F), Table 4). However, for low to medium MW congeners (18, 52, 118), the model largely under-predicted (by up to two orders of magnitude) the measured C_s. It is not entirely evident what might have caused this large disagreement. However, measurements for multiple locations within the same data set varied by up to one order of magnitude (e.g., measured C_s of Congeners 52 and 118 from Li et al., 2009 and Baker and Eisenreich, 1989, as shown in Fig. 5B and 5C, respectively). This large variability in measured sediment concentrations suggests strong site dependency (e.g., depositional vs.

non-depositional zones within the lake), which makes it challenging to reproduce these observed concentrations using the model of lake-wide average rates.

Table 4. Comparison between modeled and measured PCB concentrations in SMSL.

Data source	Year	Congener	Measured Concentration (ng/kg) [mean]	Modeled Concentration (ng/kg) [mean]
Baker and Eisenreich (1989) Core: St. 1383	1986	PCB 18	30	6
		PCB 118	1000	82
		PCB 180	470	352
Li et al. (2009) SU-12	2002	PCB 18	472	6
		PCB 52	445	11
		PCB180	390	173
Baker and Eisenreich (1989) Core: St. 1387	1986	PCB 18	90	6
		PCB 118	930	82
		PCB 180	710	352
Li et al. (2009) SU-08	2002	PCB 18	No data	6
		PCB 52	972	11
		PCB180	1093	173

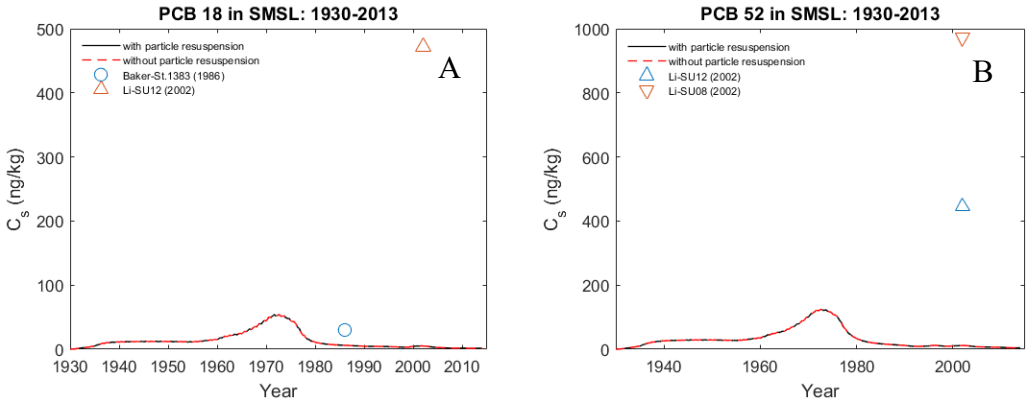
PCB 18 in SMSL: 1930-2013
with particle resuspension
without particle resuspension
Baker-St.1383 (1986)
Li-SU12 (2002)
A
C_s (ng/kg)
Year

PCB 52 in SMSL: 1930-2013
with particle resuspension
without particle resuspension
Li-SU12 (2002)
Li-SU08 (2002)
B
C_s (ng/kg)
Year

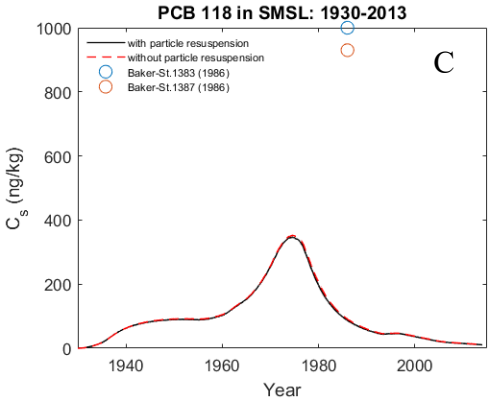
PCB 118 in SMSL: 1930-2013
with particle resuspension
without particle resuspension
Baker-St.1383 (1986)
Baker-St.1387 (1986)
C
C_s (ng/kg)
Year

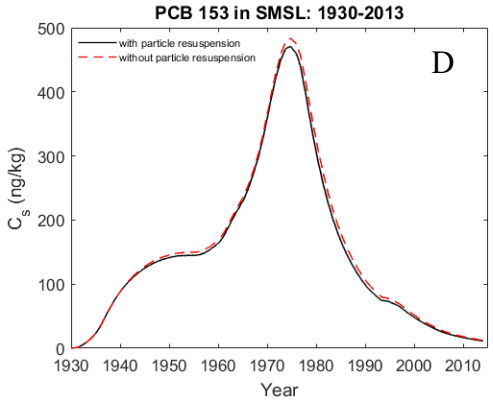
PCB 153 in SMSL: 1930-2013
with particle resuspension
without particle resuspension
D
C_s (ng/kg)
Year

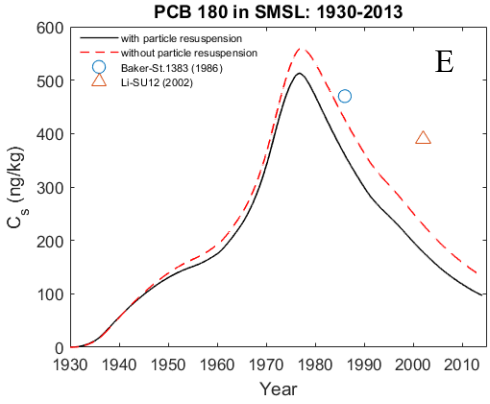
PCB 180 in SMSL: 1930-2013
with particle resuspension
without particle resuspension
Baker-St.1383 (1986)
Li-SU12 (2002)
E
C_s (ng/kg)
Year

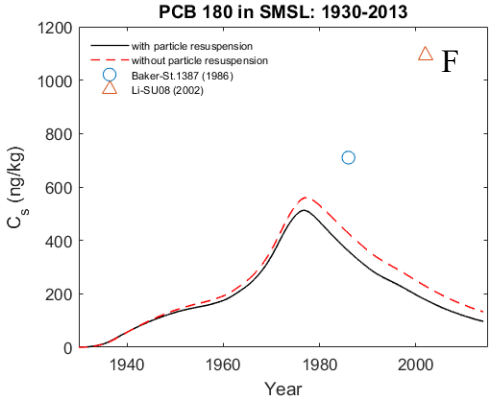
PCB 180 in SMSL: 1930-2013
with particle resuspension
without particle resuspension
Baker-St.1387 (1986)
Li-SU08 (2002)
F
C_s (ng/kg)
Year

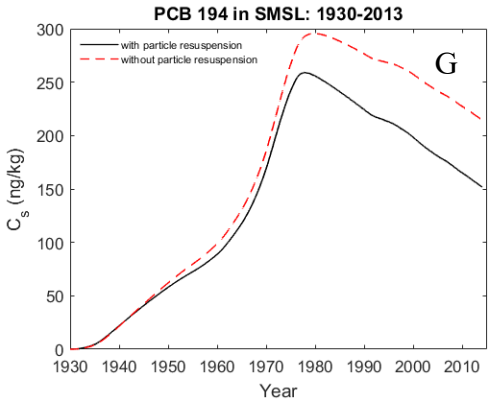

Figure 5. Simulated historical congener-specific PCB concentrations in SMSL, $C_{s,}$ and comparison with measurement (denoted by the symbols).

The results indicate that simulated PCB concentrations increased by seven to nine orders of magnitude as compared to early-1930s levels. The time lag between the highest modeled concentrations and the peak U.S. production year (1970) was from three to eight years. Even though sediment concentrations for Congeners 18, 52, 118, and 153 decreased rapidly after the PCB production ban in 1979, the present-day (2013) concentrations are yet to reach levels at or below the levels of the early 1930s. The modeled concentrations of the high MW congeners PCB 180 and 194 exhibited a relatively slow decline in the SMSL and their present-day concentrations are at or above 1960-levels.

We invoke a few possible explanations for the disagreement between the modeled and measured water and sediment concentrations. First, the model applied herein was intended to provide lake-wide average concentrations; thus, it is challenging to capture the large spatial variability in PCB concentrations that is evident in the measurement studies. Second, several input parameters in the model have large uncertainties; therefore, selected values of those parameters could partially affect the degree of overall model vs. measurement agreement. Third, our modeling framework stems primarily from the concept

of mass balance, where we applied rate constants to explain the lake and sediment processes for a relatively long period (1930-2013). This approach to modeling lakes is relatively simpler than using complex hydrodynamic models, which are often more realistically configured. Some researchers (e.g., Bennington et al., 2010) have argued that large-scale circulation models are better suited for modeling contaminant fate and transport in Lake Superior.

3.3.3 Comparison of temporal trends of PCB concentrations in air, water, sediment, and fish

To provide a relative comparison of how fast concentrations in the water layers (epilimnion and hypolimnion), sediment layer (SMSL), and fish are changing compared to atmospheric concentrations of PCBs, we fitted the annual mean modeled concentration data using a simple first-order rate model as

$$\ln(concentration) = a_0 + at, \tag{34}$$

where *concentration* is the total (n = 6) PCB concentrations in air, water layers, SMSL, and fish, a is the first-order rate constant with units of years^{-1} and a_0 is the intercept. We used PCB concentrations in air and modeled concentrations in waters, sediment, and fish from 1990-2013 to perform the trend analyses. From the regression results obtained using Eq. (34), half-lives of total (n = 6) PCB congeners in four environmental compartments and fish were estimated using

$$t_{1/2} = \frac{-\ln(2)}{a}. \tag{35}$$

The PCB concentration decline in all four environmental compartments and fish and the estimated half-lives are shown in Figure 6. For all cases, the regressions are statistically significant at $p < 0.05$. As illustrated in Fig. 6A, the concentration of $\sum_{n=6} PCB$ in the atmosphere has been declining with $t_{1/2} \approx 12$ years. This estimate is consistent with the reported $t_{1/2} = 12.2 \pm 3$ years for total PCB concentrations from 1991 to 2010 in Lake Superior air by Salamova et al. (2013). From 1990 to 2013, the decline in PCBs in the water layer (epilimnion or hypolimnion) was ca. 6 % per year (first-order rate constant of -0.06 yr^{-1}), which results in a $t_{1/2} \approx 12$ years. However, at present, the rate of decline in water is slower as compared to the rate derived from multiple measurement data sets from 1980 to 1996 (22 % per year = first-order rate constant of -0.25 yr^{-1}; Smith, 2000). The absence of virtually any lag between the PCB half-lives in Lake Superior air and water suggests (Fig. 6A) that aqueous concentrations will strongly reflect the future changes in atmospheric PCB inputs to the lake.

Unlike lake water, lake sediments have been responding at a slower rate, ca. 4 % decline in $\sum_{n=6} PCB$ concentrations per year (first-order rate constant of -0.04 yr^{-1}) with a $t_{1/2}$ = 17.6 years. This rate of decline is consistent with rates derived using sediment core measurements. For example, measurements from 1977 to 1990 (Looney, 1984; Eisenreich, 1987; Baker, 1988; Jeremiason, 1993) produced a range of $t_{1/2}$ from ca. 6 to 23 years (first-order rate constant from -0.11 yr^{-1} to -0.03 yr^{-1}).

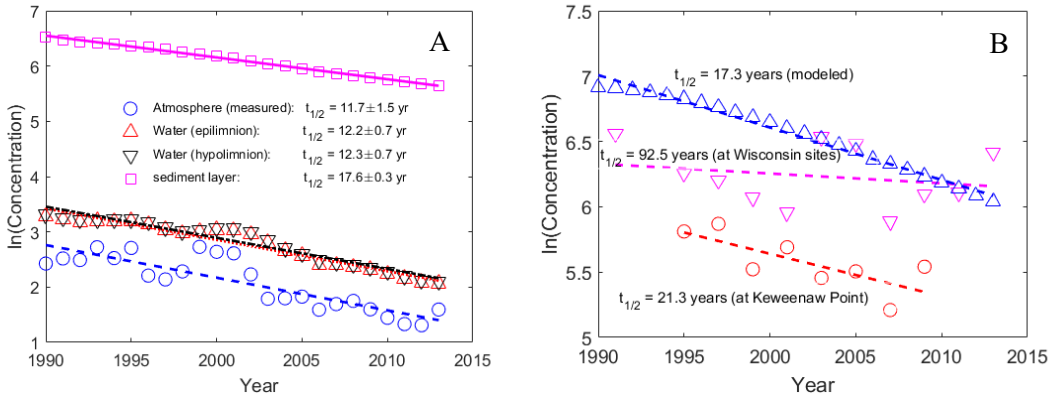

Figure 6. (A). Half-lives of total (n = 6) PCBs in various media in Lake Superior and (B). Comparison between half-lives in fish using modeled (in blue) and measured PCB concentrations at two sites: Keweenaw Point, MI (in red), and Wisconsin sites (in purple). The data points for the Wisconsin sites represent arithmetic mean of the measured fish PCB concentrations in each year at multiple sampling locations in Lake Superior.

The PCB concentrations in top predator fish (e.g., lake trout) data have been regarded as a useful indicator of contamination and long-term trends in the aquatic system (Hites and Forti, 2005; Chang et al., 2012). Several monitoring agencies (U.S. Environmental Protection Agency, Environment and Climate Change Canada, Michigan Department of Environmental Quality, Minnesota Department of Natural Resources, and Wisconsin Department of Natural Resources) have assembled long-term (e.g., 1978-2013) lake trout PCB concentration data collected from various locations in Lake Superior. These data sets offer an opportunity to perform a long-term trend analysis on fish PCB concentrations to examine whether or not any significant declining trend is evident. Using data sets for seven fish monitoring locations across Lake Superior, Lin (2016) performed statistical trend analyses for years 1996 to 2013, and found no statistically significant temporal trends in PCB concentrations in lake trout at five locations. Fish concentration data from only two locations (Keweenaw Point, MI and Wisconsin sites) exhibited slow but statistically

significant declining trends over the period 1991 to 2013 (Table 5). In Fig. 6B, total (n = 6) lake trout PCB concentrations from 1990 to 2013 modeled using Eq. (33) are compared with the measured fish PCB concentrations at the two Lake Superior monitoring locations having significant half-lives. We note that the set of congeners in the total measured and modeled fish PCB concentrations are not identical. Because the fish concentration data sets did not include congener-specific concentrations, it was not possible to perform a comparison between the measured and modeled fish concentrations using the six congeners modeled in this study. It is evident from Fig. 6B that the model predicted decline was not consistent with the observed decline in fish PCB concentrations. The model-estimated $t_{1/2}$ was ca. 17 years, while measurements suggest an upper bound $t_{1/2}$ of 92.5 years at the Wisconsin sites.

Table 5. Summary of temporal trends in fish PCB concentrations in Lake Superior.

Location	Time period	Data source[2]	Half-life, $t_{1/2}$ (yrs)
----	1990-2013	This study	~17
Keweenaw Point	1995-2009	U.S. EPA	~21
WI sites	1991-2013	WI-DNR	~92
Keweenaw Bay	1995-2009	MDEQ	No significant trend[1]
Apostle Islands	1996-2008	U.S. EPA	No significant trend[1]
MN sites	1996-2010	MN-DNR	No significant trend[1]
Thunder Bay	1997-2013	ECCC	No significant trend[1]
Whitefish Bay	1997-2013	ECCC	No significant trend[1]

[1]From Lin (2016).
[2]U.S. EPA = United States Environmental Protection Agency, MDEQ = Michigan Department of Environmental Quality, WI-DNR = Wisconsin Department of Natural Resources, MN-DNR = Minnesota Department of Natural Resources, ECCC = Environment and Climate Change Canada.

Collectively, the trend analysis results in Fig. 6 suggest that fish PCB concentrations in Lake Superior are declining at a much slower rate than that of air, water, and sediment. The coupled water-sediment model cannot explain this slow recovery in lake trout

concentrations observed in the monitoring data. Given the weak role of sediment resuspension as illustrated by the model simulations (sections 3.3.1 and 3.3.2), the lack of significant declining trends in fish concentrations at most sampling locations, and the substantially large difference between measured and modeled $t_{1/2}$ in fish, factors other than sediment recycling appear to be causing the delay in fish recovery. One factor that may influence the observed temporal trends in PCB concentrations is changes in food web dynamics in Lake Superior. Previous studies focused in the Laurentian Great Lakes (e.g., Gewurtz et al., 2011; Hebert et al., 2000; 2006) suggested that the trajectories of persistent and bioaccumulative contaminants in upper trophic level biota could be altered by changes in lake food webs. However, testing this hypothesis is beyond the scope of this study.

3.3.4 Uncertainty analysis

A major objective of performing the uncertainty analysis was to examine how uncertainties in four selected parameter values affect the resulting half-lives of total PCBs estimated for water and sediment. Following this approach, one could compare the relative magnitude of these half-lives with the observed $t_{1/2}$ of fish. In this way, the uncertainty analysis also serves as an additional tool to test the hypothesis that sediment recycling is contributing to the current observed leveling off of fish PCB concentrations in Lake Superior. Additionally, the uncertainty analysis results enable us to further examine the relative (dis)agreement between the modeled and measured water/sediment concentrations. Model sensitivity runs were performed using the lower and upper bound values of the four selected

parameters (V_s, z_{mix}, K_{ow}, and K_{aw}) from their uncertainty ranges and were compared with the base case simulations.

3.3.4.1 *Uncertainties in modeled water (epilimnion) concentrations*

The resulting changes in the modeled PCB concentrations in the epilimnion in regard to uncertainties in V_s are shown Fig. S1(A-F). These results indicated that the low to medium MW congeners (PCBs 18, 52, 118, and 153) were less sensitive to the uncertainties in V_s. In contrast, as expected, the two high MW congeners (PCB 180 and 194) were more sensitive to changes in V_s. The trajectories of water concentrations as shown in Fig. S1(E-F) indicate an increase and a decrease in V_s from its base value resulting in lower and higher C_wE, respectively. For high MW congeners the particle settling flux from the water layers to the sediment was a dominant process because of their large K_d values. Likewise, as particle-bound PCBs settled through the water layer, their total concentrations in water decreased. Fig. S2(A-F) show the trajectories of C_wE resulting from the uncertainty range of z_{mix}. In general, the response of the model to changing z_{mix} values was similar to that of changing V_s (i.e., low to medium MW congeners were less sensitive to z_{mix} as compared to the high MW ones, and an increase and a decrease in z_{mix} from its base value resulted in lower and higher C_wE, respectively). Of the four parameters tested, the model simulations were the most sensitive to the thermodynamic properties (K_{ow} and K_{aw}) of PCBs, as can be seen from Figs. S3(A-F) and S4(A-F). Increasing the K_{ow} value for a PCB congener tended to increase its hydrophobicity, which also increased its fraction sorbed in water layers. This enhanced partitioning between the dissolved and sorbed phases resulted

in increased settling of PCBs from waters to sediment, which in turn reduced PCB concentrations in water (Fig. S3(A-F)). Uncertainties in K_{aw} have a strong effect on the trajectories of C_wE. As can be seen from Fig. S4(A-F), the low MW congeners (e.g., PCBs 18 and 52) were very sensitive to K_{aw} values. A 3-fold decrease in K_{aw} from its base value resulted in a ca. 3-fold increase in the modeled C_wE. Similarly, a 3-fold increase in K_{aw} from its base value resulted in a ca. 3-fold decrease in the modeled C_wE. This high sensitivity of the model to K_{aw} is consistent with the fundamental process of PCB air-water exchange; a higher K_{aw} indicates a greater tendency toward loss via volatilization, resulting in low water concentrations.

For each sensitivity simulation, the half-lives of total (n = 6) PCB concentrations were calculated. The $t_{1/2}$ in the epilimnion varied from 9.8 to 13.5 years, while the $t_{1/2}$ for the base case was 12.2 years. In the hypolimnion, $t_{1/2}$ varied from 11.3 to 13.8 years. Collectively, these estimates suggest that the $t_{1/2}$ derived from the base-case simulations was precise.

3.3.4.2 *Uncertainties in the modeled SMSL concentrations*

For low to medium MW congeners (PCBs 18, 52, 118, and 153), the uncertainties in V_s exhibited a small effect on the modeled C_s (Fig. S5(A-D)). C_s for PCBs 180 and 194 were the most sensitive to changes in V_s (Fig. S5(E-F)). For these two congeners, particle-settling flux to the sediment layer (which increased as V_s increased) dominated over the resuspension fluxes. For example, for the upper bound of V_s, the simulated C_s increased by 7-16% for PCBs 194 and 180. Fig. S6(A-F) show the resulting modeled C_s for three z_{mix}

values. The uncertainty in z_{mix} had a large influence on C_s as MW increased (for z_{mix} = 0.1 cm, 60% increase in the modeled C_s for PCB 180, 180% increase in C_s for PCB 194). The model was most sensitive to K_{ow} and K_{aw} as can be seen from Fig. S7(A-F). The resulting half-lives for each sensitivity simulation were calculated for the SMSL and are presented in Table 6. The resulting $t_{1/2}$ ranged from 11.1 to 20.9 years (base $t_{1/2}$ = 17.6).

Following model uncertainty analysis, the simulated aqueous and sediment concentrations were interpreted to provide further insight into the relative (dis)agreement between the model and measurements. One can see from the model runs if these parameter uncertainties can explain the difference. It is evident that a very high value of z_{mix}, K_{ow}, or K_{aw} is not supported by the measurements. However, the lower range of the parameter value could provide an improved agreement; however, the model vs. measurement discrepancy is large.

From the uncertainty analysis, we determined the ranges in $t_{1/2}$ for water (11.3 to 13.8 years) and for sediment (11.1 to 20.9 years). These half-lives were well below the $t_{1/2}$ (measured) for fish as illustrated in Fig. 6B. This finding indicates that, within the range of uncertainty in model prediction, the $t_{1/2}$ of the model is lower than that calculated from the fish measurements. Therefore, we posit that factors other than sediment recycling such as changes in food web dynamics are responsible for sustaining the PCB concentrations in lake trout in Lake Superior.

Table 6. Half-lives of total PCBs in Lake Superior water and sediment.

		In epilimnion		In hypolimnion		In sediment layer	
Scenario	Value	$t_{1/2}$ (yr)	Uncertainty (±yr)	$t_{1/2}$ (yr)	Uncertainty (±yr)	$t_{1/2}$ (yr)	Uncertainty (±yr)
Base	**----**	**12.2**	**0.7**	**12.3**	**0.7**	**17.6**	**0.3**
Low V_s	0.5 m d^{-1}	12.1	0.7	12.2	0.7	16.6	0.3
High V_s	1.5 m d^{-1}	12.2	0.7	12.4	0.7	17.8	0.3
Low z_{mix}	0.1 cm	11.2	0.7	11.3	0.7	11.1	0.2
High z_{mix}	2.0 cm	12.8	0.7	12.9	0.7	19.5	0.3
Low K_{ow}	Base K_{ow}/3	11.7	0.7	11.8	0.7	14.3	0.3
High K_{ow}	3×Base K_{ow}	13.0	0.7	13.1	0.7	20.4	0.2
Low K_{aw}	Base K_{aw}/3	13.8	0.5	13.8	0.5	20.9	0.2
High K_{aw}	3×Base K_{aw}	9.5	0.7	11.3	0.7	14.4	0.3

Together, the range in half-lives obtained through uncertainty analysis were lower than the half-life of fish PCB concentrations at the Keweenaw Point and sites. This finding strengthens the hypothesis that sediment resuspension does not control the observed PCB levels in fish. It further supports the hypothesis that changes in food web dynamics are a likely factor in sustaining the current PCB levels in top predatory fish.

3.4 Conclusions

We applied a coupled atmosphere-water-sediment model to investigate the long-term (1930-2013) behavior of PCBs in Lake Superior. The findings point out that the U.S. ban on PCB production in 1979 has been effective in reducing atmospheric concentrations of

PCBs, which was followed by reductions in water and sediment concentrations of PCBs in Lake Superior. The trajectories of model-predicted water and sediment concentrations of six PCB congeners exhibiting a wide a range in MW and thermodynamic properties indicated that concentrations of low-MW congeners declined relatively quickly after the PCB production ban. However, these concentrations are yet to reach early 1930-levels.

There are several limitations to our modeling approach. First, we did not include secondary emissions while estimating the congener-specific concentrations of the six congeners. Second, recycling of PCBs associated with carbon cycling was not included in the multimedia model. Third, we did not include fish population dynamics; instead, bioaccumulation factors were used to project the PCB concentrations in the fish diet.

The temporal trend analyses from 1990 to 2013 indicated that the PCB concentrations in the atmosphere and the water are declining at about the same rate ($t_{1/2} \approx 12$ years). However, the estimated $t_{1/2}$ in the sediment lags that in the water by ca. five years, suggesting a slower recovery from legacy PCB inputs. A simplified approach was taken to predict the biota (predatory fish) concentrations using the model-predicted aqueous concentrations, which resulted in a $t_{1/2} \approx 17$ years in top predatory fish. This modeled $t_{1/2}$ was not supported by available long-term (1990-2013) fish PCB concentration measurements in Lake Superior, which produced a $t_{1/2} > 90$ years. This mismatch between modeled and observed time to recovery in fish negates the hypothesis that recycling of PCBs from sediments is controlling the current trajectory of fish PCB concentrations in Lake Superior. We suggest that other factors, such as changes in food web dynamics, as

pointed out by some earlier studies (e.g., Gewurtz et al., 2011; Hebert et al., 2006), may be affecting trajectories of top predator fish PCB concentrations in the lake.

A supplemental information (S.I.) (section 3.6) is provided after the references. The S.I. section includes the table of PCB physiochemical properties and the figures from uncertainty analysis presented in section 3.3.4.

3.5 References

Assel, R.A., 1986. Fall and winter thermal structure of Lake Superior. Journal of Great Lakes Research 12, 251-262.

Assel, R.A., 2003. NOAA Atlas: An Electronic Atlas of Great Lakes Ice Cover, Winters 1973-2002. Great Lakes Environmental Research Laboratory.

Baker, J.E., 1988. The particle-mediated geochemistry of hydrophobic organic contaminants in large lakes. University of Minnesota.

Baker, J.E., Eisenreich, S.J., 1989. PCBs and PAHs as tracers of particulate dynamics in large lakes. Journal of Great Lakes Research 15, 84-103.

Baker, J.E., Eisenreich, S.J., 1990. Concentrations and fluxes of polycyclic aromatic hydrocarbons and polychlorinated biphenyls across the air-water interface of Lake Superior. Environmental Science & Technology 24, 342-352.

Bennett, E.B., 1978. Characteristics of the thermal regime of Lake Superior. Journal of Great Lakes Research 4, 310-319.

Bennington, V., McKinley, G.A., Kimura, N., Wu, C.H., 2010. General circulation of Lake Superior: Mean, variability, and trends from 1979 to 2006. Journal of Geophysical Research: Oceans 115.

Bhavsar, S.P., Jackson, D.A., Hayton, A., Reiner, E.J., Chen, T., Bodnar, J., 2007. Are PCB levels in fish from the Canadian Great Lakes still declining? Journal of Great Lakes Research 33, 592-605.

Borgå, K., Fisk, A.T., Hargrave, B., Hoekstra, P.F., Swackhamer, D., Muir, D.C., 2005. Bioaccumulation factors for PCBs revisited. Environmental science & technology 39, 4523-4532.

Borgmann, U., Whittle, D., 1992. Bioenergetics and PCB, DDE, and mercury dynamics in Lake Ontario lake trout (Salvelinus namaycush): a model based on surveillance data. Canadian Journal of Fisheries and Aquatic Sciences 49, 1086-1096.

Breivik, K., Sweetman, A., Pacyna, J.M., Jones, K.C., 2007. Towards a global historical emission inventory for selected PCB congeners—a mass balance approach: 3. An update. Science of the Total Environment 377, 296-307.

Buehler, S., Hafner, W., Basu, I., Audette, C.V., Brice, K.A., Chan, C., Froude, F., Galarneau, E., Hulting, M.L., Jantunen, L., 2001. Atmospheric deposition of toxic substances to the Great Lakes: IADN results through 1998. Rep. EPA 905-R-01 7.

Chang, F., Pagano, J.J., Crimmins, B.S., Milligan, M.S., Xia, X., Hopke, P.K., Holsen, T.M., 2012. Temporal trends of polychlorinated biphenyls and organochlorine pesticides in Great Lakes fish, 1999–2009. Science of the total environment 439, 284-290.

David, S., Hesselberg, R., Rodgers, P.W., Feist, T.J., 1996. Contaminant trends in lake trout and walleye from the Laurentian Great Lakes. Journal of Great Lakes Research 22, 884-895.

Eisenreich, S.J., 1987. The chemical limnology of nonpolar organic contaminants: polychlorinated biphenyls in Lake Superior. ACS Publications.

Eisenreich, S.J., Hollod, G.J., Johnson, T.C., 1979. Accumulation of polychlorinated biphenyls (PCBs) in surficial Lake Superior sediments. Atmospheric deposition. Environmental Science & Technology 13, 569-573.

Eisenreich, S.J., Looney, B.B., Thornton, J.D., 1981. Airborne organic contaminants in the Great Lakes ecosystem. Environmental Science & Technology 15, 30-38.

Galarneau, E., Audette, C., Bandemehr, A., Basu, I., Bidleman, T., Brice, K., Burniston, D., Chan, C., Froude, F., Hites. R., Hulting, M., Neilson, M., Orr, D., Simcik, M., Strachan, W., Hoff, R., 2000. Atmospheric deposition of toxic substances to the Great Lakes: IADN results to 1996. Rep. EPA 905-R-00004.

Gewurtz, S.B., Backus, S.M., Bhavsar, S.P., McGoldrick, D.J., de Solla, S.R., Murphy, E.W., 2011. Contaminant biomonitoring programs in the Great Lakes region: review of approaches and critical factors. Environmental Reviews 19, 162-184.

Hebert, C.E., Arts, M.T., Weseloh, D.C., 2006. Ecological tracers can quantify food web structure and change. Environmental science & technology 40, 5618-5623.

Hebert, C.E., Hobson, K.A., Shutt, J.L., 2000. Changes in food web structure affect rate of PCB decline in herring gull (Larus argentatus) eggs. Environmental science & technology 34, 1609-1614.

Hites, R., Forti, T., 2005. Program Review of the Great Lakes Fish Monitoring Program (GLFMP).

Hornbuckle, K.C., Carlson, D.L., Swackhamer, D.L., Baker, J.E., Eisenreich, S.J., 2006. Polychlorinated biphenyls in the Great Lakes, Persistent Organic Pollutants in the Great Lakes. Springer, pp. 13-70.

Houde, M., Muir, D.C., Kidd, K.A., Guildford, S., Drouillard, K., Evans, M.S., Wang, X., Whittle, D.M., Haffner, D., Kling, H., 2008. Influence of lake characteristics on the biomagnification of persistent organic pollutants in lake trout food webs. Environmental toxicology and chemistry 27, 2169-2178.

Humphrey, H., Gardiner, J.C., Pandya, J.R., Sweeney, A.M., Gasior, D.M., McCaffrey, R.J., Schantz, S.L., 2000. PCB congener profile in the serum of humans consuming Great Lakes fish. Environmental health perspectives 108, 167.

Jeremiason, J.D., Hornbuckle, K.C., Eisenreich, S.J., 1994. PCBs in Lake Superior, 1978-1992: decreases in water concentrations reflect loss by volatilization. Environmental science & technology 28, 903-914.

Lenters, J.D., 2004. Trends in the Lake Superior water budget since 1948: A weakening seasonal cycle. Journal of Great Lakes Research 30, 20-40.

Li, A., Rockne, K.J., Sturchio, N., Song, W., Ford, J.C., Wei, H., 2009. PCBs in sediments of the Great Lakes–Distribution and trends, homolog and chlorine patterns, and in situ degradation. Environmental Pollution 157, 141-147.

Lin, H., 2016. Temporal trends and spatial variabilities of PCB concentrations in lake trout from Lake Superior from 1995 to 2013. Michigan Technological University.

Looney, B.B., 1984. Dynamic behavior of chlorinated organics in Lake Superior: sediment, water and air interactions.

McCarthy, S.M., 2016. Modeling the physical and biogeochemical processes in Lake Superior using LAKE2K. Michigan Technological University.

Mackay, D., Shiu, W.Y., Ma, K.-C., 1997. Illustrated handbook of physical-chemical properties of environmental fate for organic chemicals. CRC press.

Perlinger, J.A., Gorman, H.S., Norman, E.S., Obrist, D., Selin, N.E., Urban, N.R., Wu, S., 2016. Measurement and Modeling of Atmosphere-Surface Exchangeable Pollutants (ASEPs) To Better Understand their Environmental Cycling and Planetary Boundaries. ACS Publications.

Quinn, F.H., 1992. Hydraulic residence times for the Laurentian Great Lakes. Journal of Great Lakes Research 18, 22-28.

Rowe, M., Perlinger, J.A., 2012. Micrometeorological measurement of hexachlorobenzene and polychlorinated biphenyl compound air-water gas exchange in Lake Superior and comparison to model predictions. Atmospheric Chemistry and Physics 12, 4607-4617.

Salamova, A., Pagano, J.J., Holsen, T.M., Hites, R.A., 2013. Post-1990 temporal trends of PCBs and organochlorine pesticides in the atmosphere and in fish from Lakes Erie, Michigan, and Superior. Environmental science & technology 47, 9109-9114.

Schwarzenbach, R. P., Gschwend, P. M. and Imboden, D. M., 2003. Environmental Organic Chemistry, John Wiley & Sons, Inc., Hoboken, NJ, USA.

Shoeib, M., Harner, T., 2002. Using measured octanol-air partition coefficients to explain environmental partitioning of organochlorine pesticides. Environmental toxicology and chemistry 21, 984-990.

Smith, D.W., 2000. Analysis of rates of decline of PCBs in different Lake Superior media. Journal of Great Lakes Research 26, 152-163.

Sobek, A., Gustafsson, O.r., 2014. Deep water masses and sediments are main compartments for polychlorinated biphenyls in the Arctic Ocean. Environmental science & technology 48, 6719-6725.

Spence, C., Blanken, P., Hedstrom, N., Fortin, V., Wilson, H., 2011. Evaporation from Lake Superior: 2: Spatial distribution and variability. Journal of Great Lakes Research 37, 717-724.

Stow, C.A., 1995. Factors associated with PCB concentrations in Lake Michigan fish. Environmental science & technology 29, 522-527.

Sun, P., Basu, I., Hites, R.A., 2006. Temporal trends of polychlorinated biphenyls in precipitation and air at Chicago. Environmental science & technology 40, 1178-1183.

Swackhamer, D.L., Hites, R.A., 1988. Occurrence and bioaccumulation of organochlorine compounds in fishes from Siskiwit Lake, Isle Royale, Lake Superior. Environmental science & technology 22, 543-548.

Swackhamer, D.L., Skoglund, R., 1993. Bioaccumulation of PCBs by algae: kinetics versus equilibrium. Environmental Toxicology and Chemistry 12, 831-838.

Swain, W.R., 1978. Chlorinated organic residues in fish, water, and precipitation from the vicinity of Isle Royale, Lake Superior. Journal of Great Lakes Research 4, 398-407.

Ullman, D., Brown, J., Cornillon, P., Mavor, T., 1998. Surface temperature fronts in the Great Lakes. Journal of Great Lakes Research 24, 753-775.

Urban, N., Auer, M., Green, S.A., Lu, X., Apul, D., Powell, K., Bub, L., 2005. Carbon cycling in Lake Superior. Journal of Geophysical Research: Oceans 110.

U.S. EPA GLNPO (2009). “Great Lakes Aquatic Contaminants Survey Final Report.”

Wang, J., Bai, X., Hu, H., Clites, A., Colton, M., Lofgren, B., 2012. Temporal and spatial variability of Great Lakes ice cover, 1973–2010. Journal of Climate 25, 1318-1329.

Xue, P., Pal, J.S., Ye, X., Lenters, J.D., Huang, C., Chu, P.Y., 2017. Improving the simulation of large lakes in regional climate modeling: Two-way lake–atmosphere coupling with a 3D hydrodynamic model of the Great Lakes. Journal of Climate 30, 1605-1627.

3.6 Supplemental information

Table S1. Physicochemical properties of six PCB congeners.

Congener	*Molecular formula*	*MW*[1] (g mol^{-1})	*MV*[2] (cm^3 mol^{-1})	log K_{oa}^{3}	log K_{ow}^{4}	K_{aw}^{5}
PCB 18	$C_{12}H_7Cl_3$	257.5	247.3	7.6	5.1	4.9×10^{-3}
PCB 52	$C_{12}H_6Cl_4$	292	268.2	8.3	5.6	3.2×10^{-3}
PCB 118	$C_{12}H_5Cl_5$	326.4	289.1	9.4	6.4	1.5×10^{-3}
PCB 153	$C_{12}H_4Cl_6$	360.9	310	9.7	6.6	1.3×10^{-3}
PCB 180	$C_{12}H_3Cl_7$	395.3	330.9	10.5	7.1	6.9×10^{-4}
PCB 194	$C_{12}H_2Cl_8$	429.8	351.8	11.2	7.7	4.6×10^{-4}

[1]*Molecular weight (MW) (Shiu and Mackay, 1986).*
[2]*Le Bas molar volume (MV) (Shiu and Mackay, 1986).*
[3,4,5]*Octanol-air partition coefficient (K_{oa}), octanol-water partition coefficient (K_{ow}), dimensionless Henry's law constant (K_{aw}) at 25°C calculated using Poly-Parameter Linear Free Energy Relationships (Environmental Organic Chemistry, 3rd Edition, Schwarzenbach et al., 2016).*

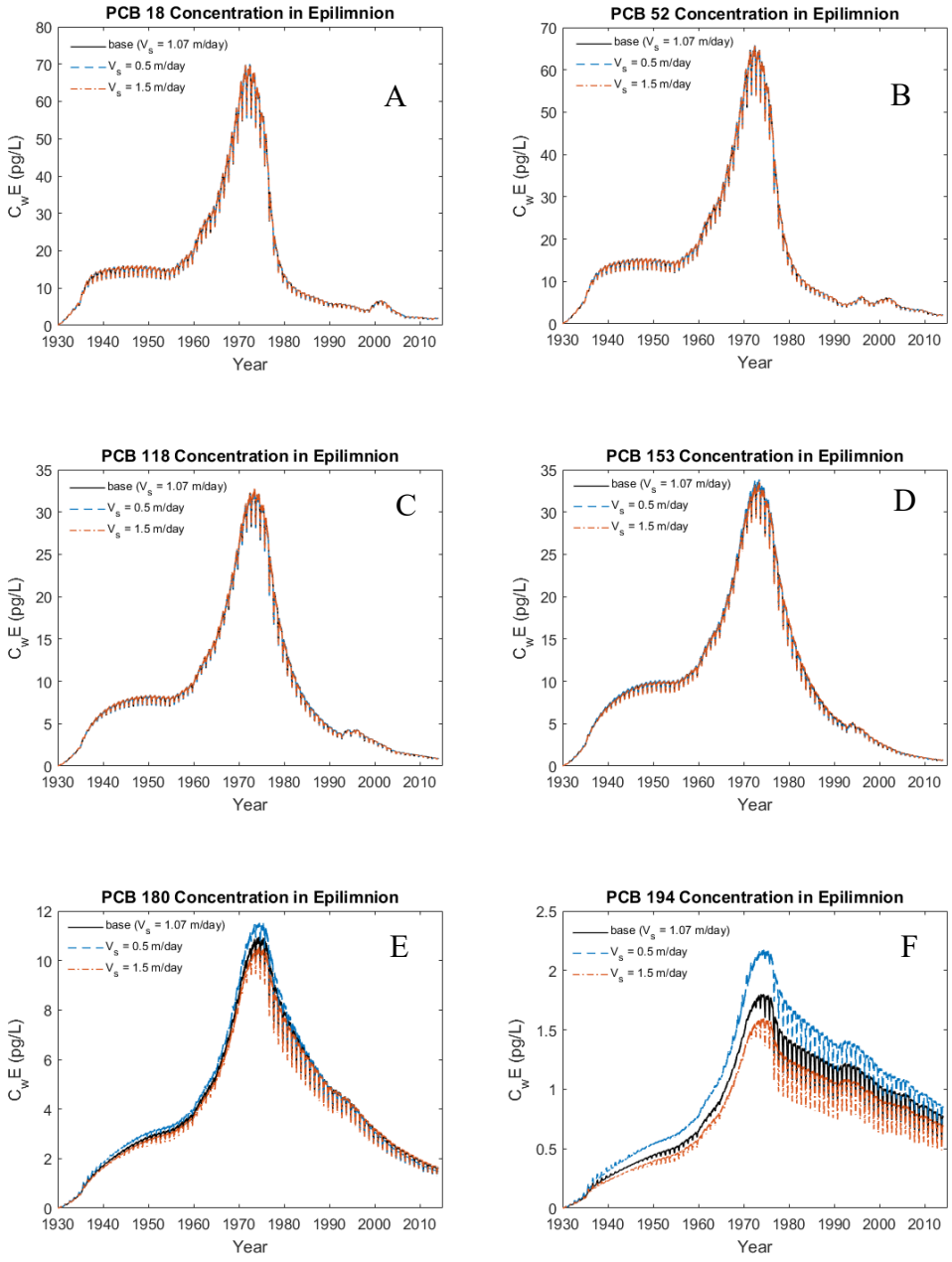

Figure S1. Sensitivity of modeled epilimnion PCB concentrations ($C_w E$) to particle settling velocity (V_s).

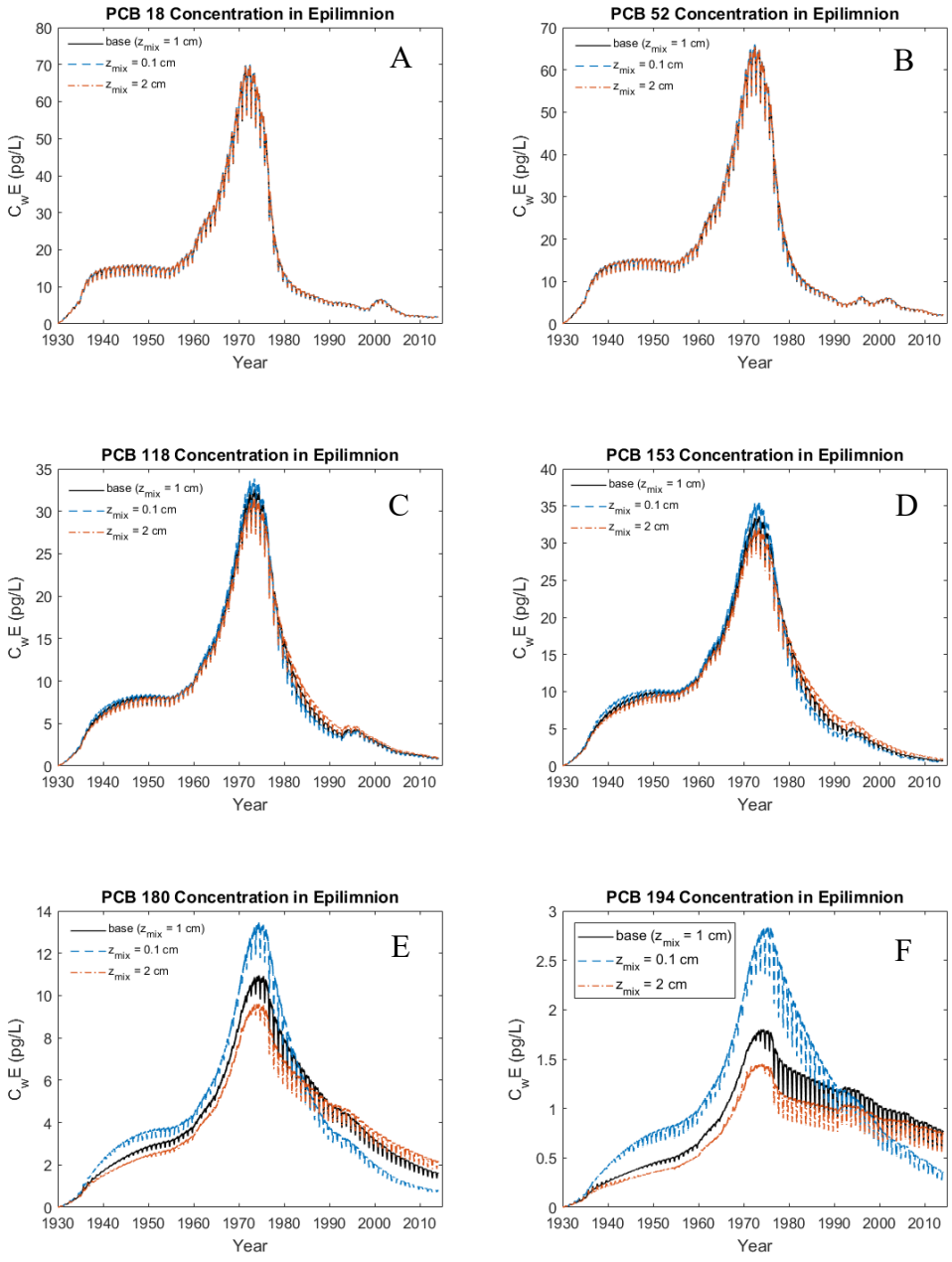

Figure S2. Sensitivity of modeled epilimnion PCB concentrations (C_wE) to sediment mixed layer depth (z_{mix}).

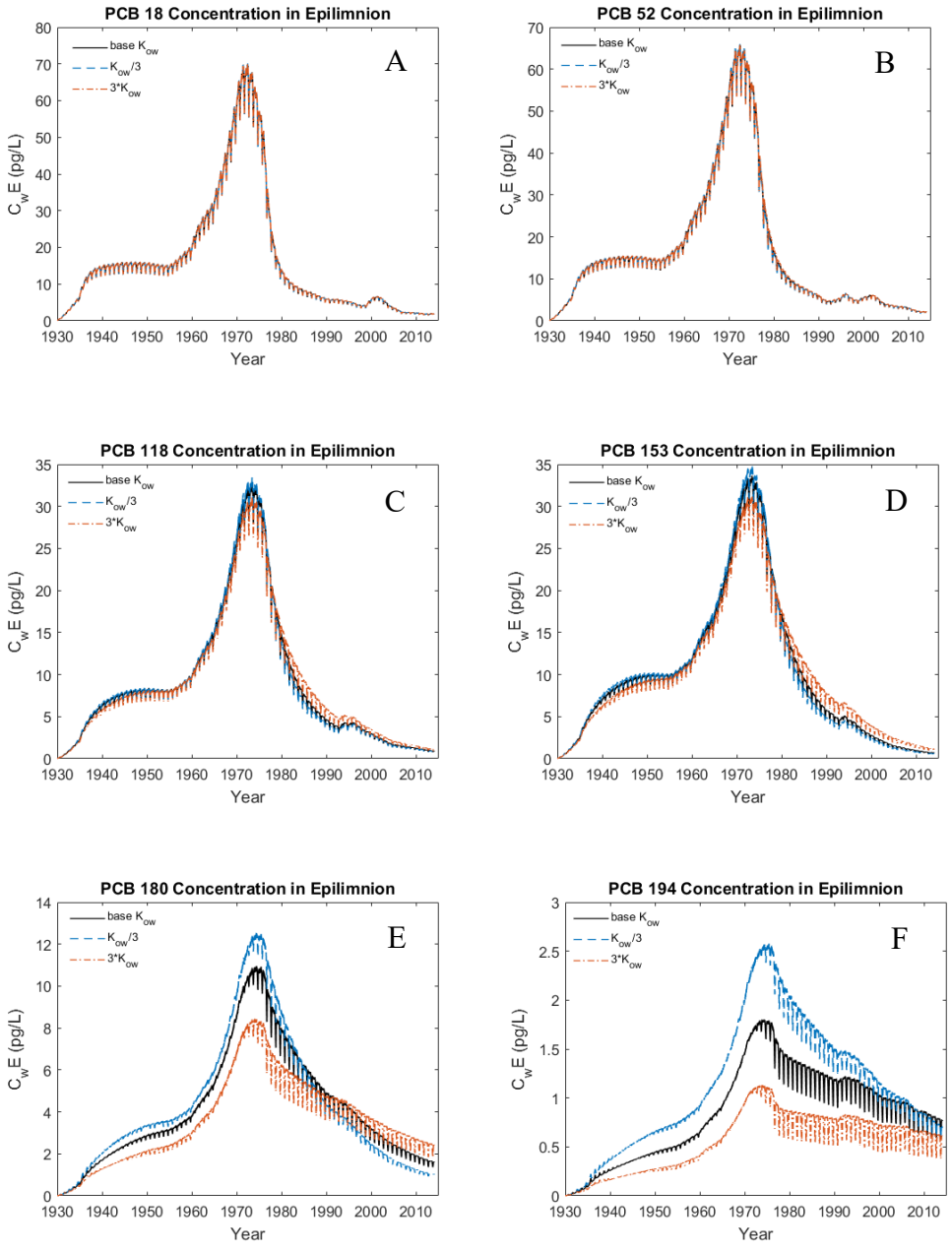

Figure S3. Sensitivity of modeled epilimnion PCB concentrations (C_wE) to octonal-water partition coefficient (K_{ow}).

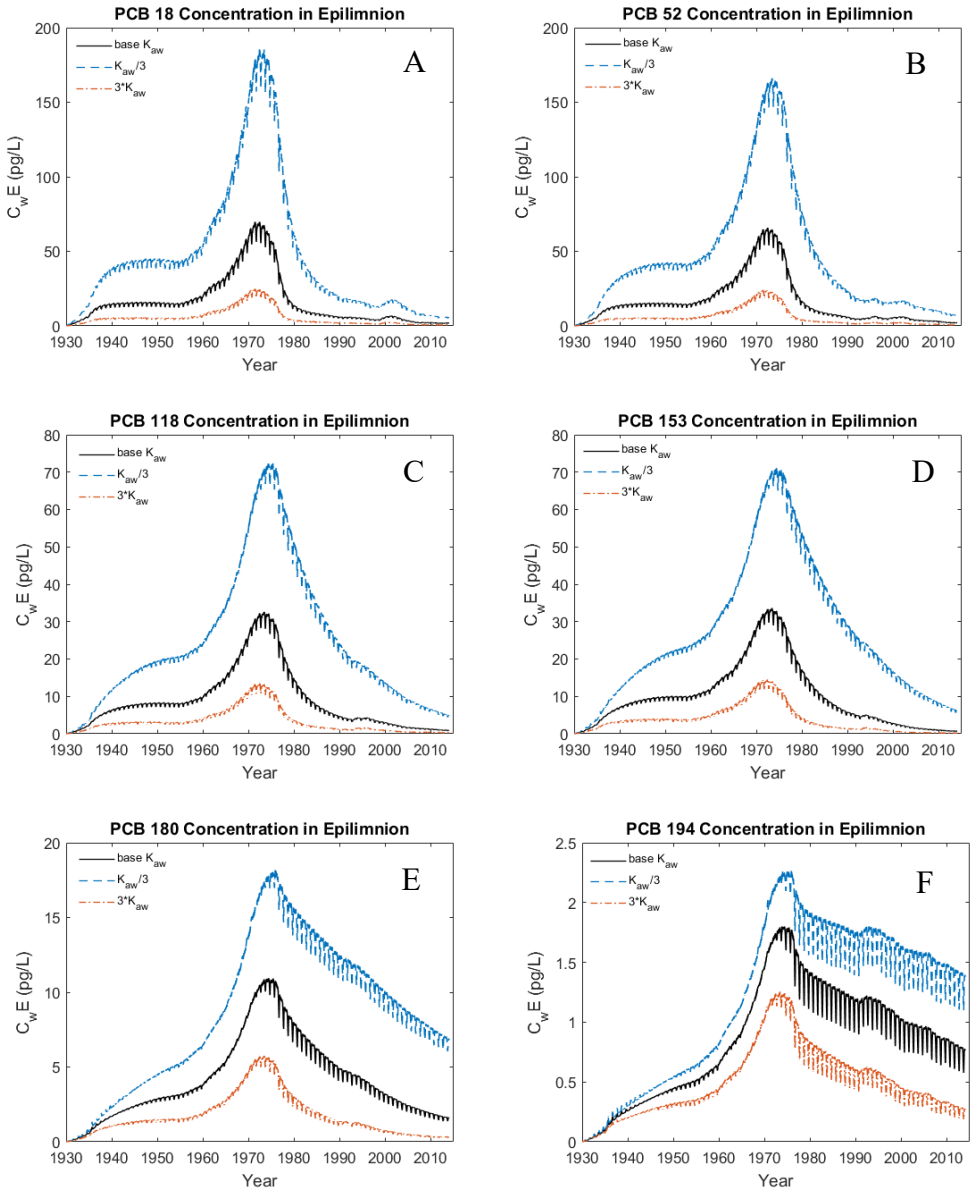

Figure S4. Sensitivity of modeled epilimnion PCB concentrations (C_wE) to dimensionless Henry's law constant (K_{aw}).

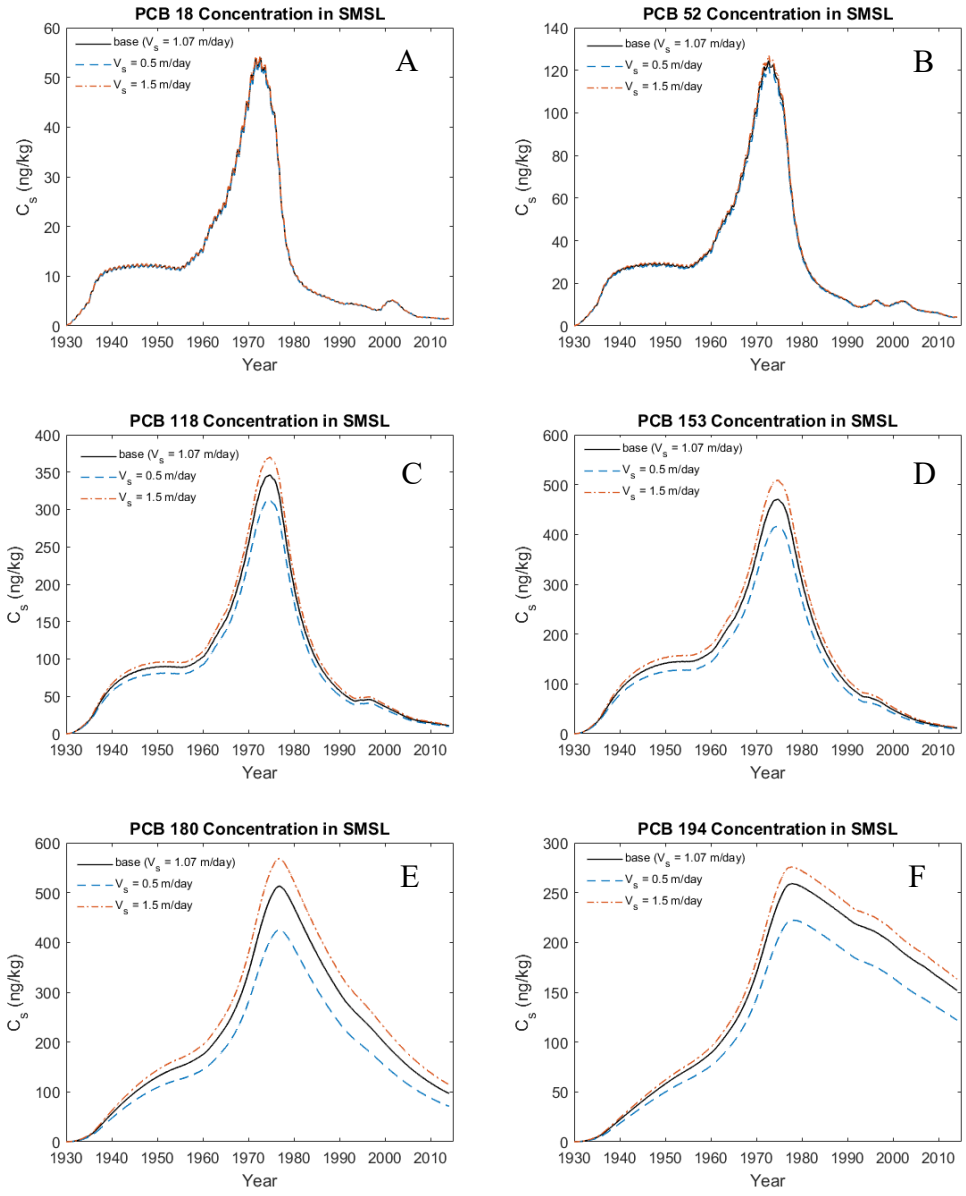

Figure S5. Sensitivity of modeled sediment layer PCB concentrations (C_s) to particle settling velocity (V_s).

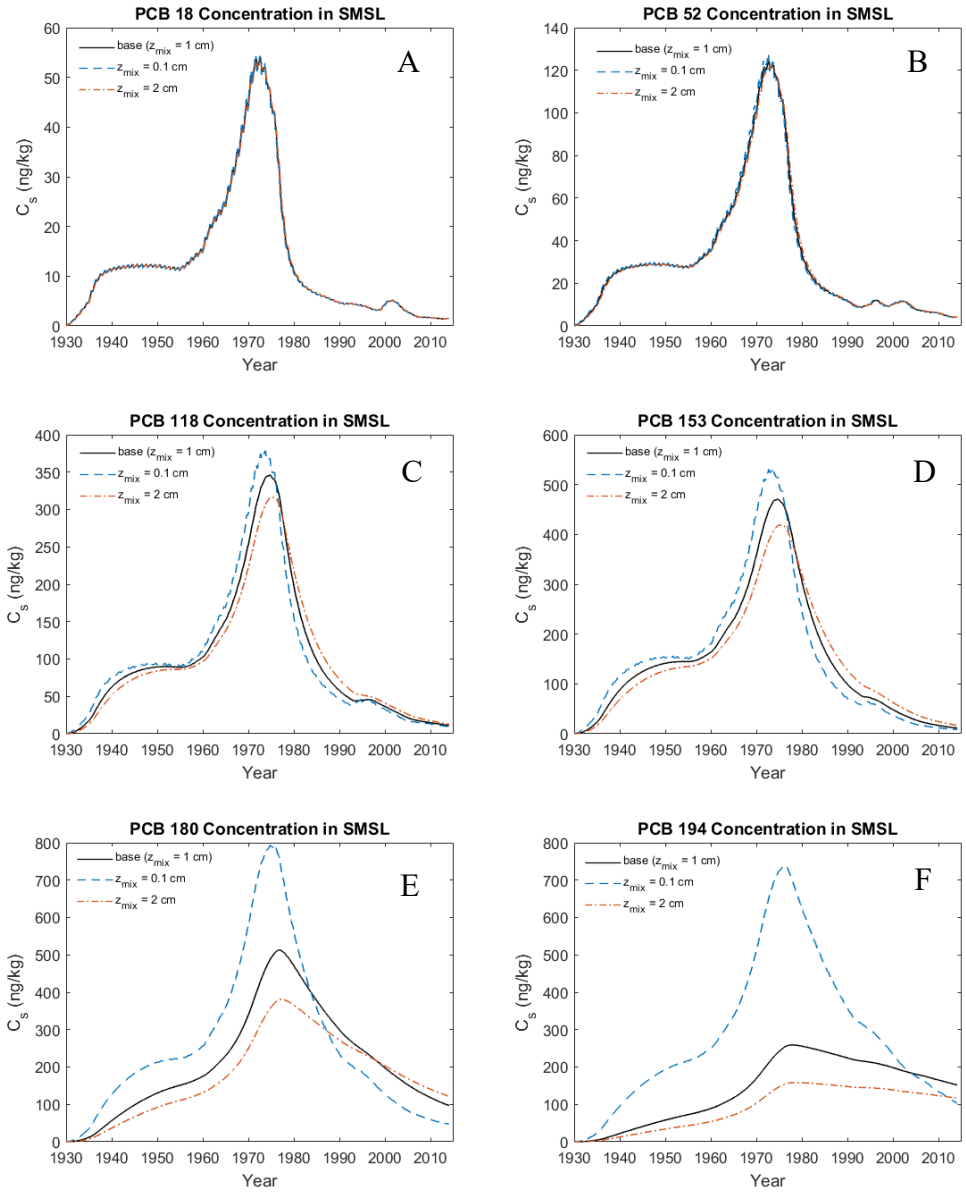

Figure S6. Sensitivity of modeled sediment layer PCB concentrations (C_s) to sediment mixed layer depth (z_{mix}).

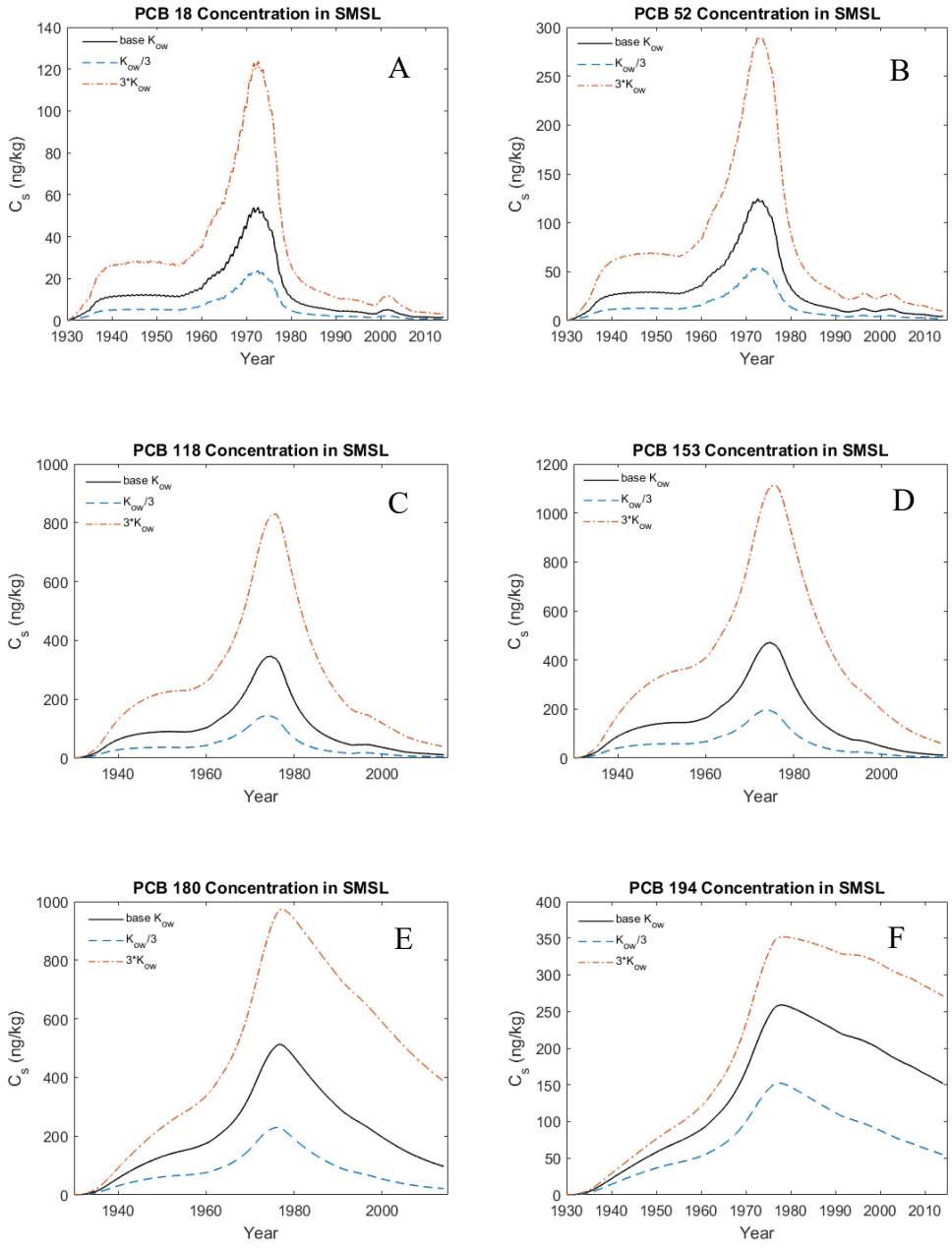

Figure S7. Sensitivity of modeled sediment layer PCB concentrations (C_s) to octonal-water partition coefficient (K_{ow}).

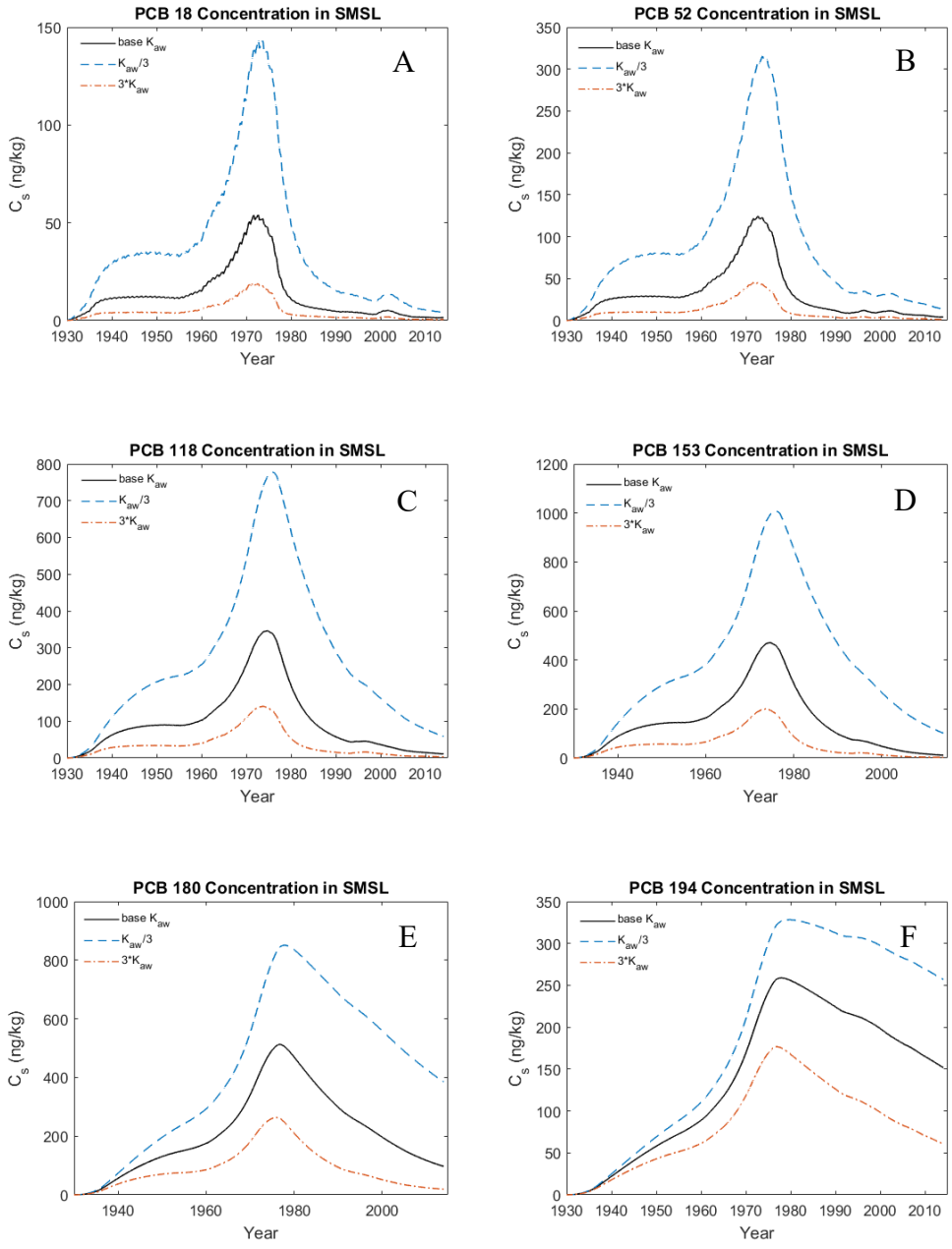

Figure S8. Sensitivity of modeled sediment layer PCB concentrations (C_s) to dimensionless Henry's law constant (K_{aw}).

3.7 References (supplemental information)

Shiu, W.Y., Mackay, D., 1986. A critical review of aqueous solubilities, vapor pressures, Henry's law constants, and octanol–water partition coefficients of the polychlorinated biphenyls. Journal of Physical and Chemical Reference Data 15, 911-929.

Schwarzenbach, R. P., Gschwend, P. M. and Imboden, D. M., 2016. Environmental Organic Chemistry, John Wiley & Sons, Inc., Hoboken, NJ, USA.

Appendix

Copyright Transfer Agreement for Chapter 1 from Copernicus Publications.

Serving Scientists since 1985

Copernicus Publications
The Innovative Open Access Publisher

You publish. We care.

Co-founder of CASPA Member of STM

About us
Meetings
Publications
Services
Open-access journals
For authors
- Services for authors
- Article processing charges
- Financial support
- Licence & copyright
- Manuscript preparation
- Proofreading guidelines
- Obligations for authors
- General terms

For reviewers
Software updates
Launch YOUR journal
Open science
Online system
Customers
Facts & figures
News & press
Career
Contact us

User ID
Password
New User Lost Login?

ORCID Member Organization

We support the Deutschland STIPENDIUM

General terms

While Copernicus Publications welcomes any original scientific work for publication, we expect the following:

- The work submitted for publication has not been published before, except in the form of abstracts, preprints, published lectures, theses, proceedings-type publications, or discussion papers that have not undergone full journal peer-review, and it is not under consideration for peer-reviewed publication elsewhere.
- The authors are aware that their submission will be automatically checked for plagiarism. In their own interest, they should avoid dubious cases (e.g. exact copies of site or method descriptions) by using quotation marks and citing the original work.
- Its publication has been approved by all author(s) and, tacitly or explicitly, by the responsible authorities and/or the institutes where the work has been carried out.
- If and when the manuscript is accepted for peer-reviewed publication, it may be re-used under the terms of the Creative Commons Attribution 4.0 License but not submitted for peer-reviewed publication elsewhere.
- The authors have secured the right to reproduce any material in his/her/their work that has already been published elsewhere.
- The authors agree to the Licence and Copyright Agreement.
- The authors agree to the article processing charges valid on the date of manuscript submission (receipt of electronic files).
- The authors agree to and have obeyed the General Obligations for Authors.
- From submission to publication, the authors of a manuscript are formally represented by the registered contact author(s). After publication, the authors of a manuscript are formally represented by the corresponding author(s) specified in the published paper.
- The authors are aware that discussion papers remain permanently archived, accessible and citeable.
- With regard to the evaluation of manuscripts, the editors and the referees will follow their guidelines as summarized in the General Obligations for Editors and the General Obligations for Referees.
- The journals' editorial boards reserve the right to remove referee reports and any other comments if they contain personal insults.
- The use of general descriptive names, trade names, trademarks, etc., in the articles of this journal, even if not specifically identified, does not imply that these names are not protected by the relevant laws and regulations.
- The members of the journals' editorial boards try to guide the review process as carefully as possible but cannot take legal responsibility for the outcome and aftermath of acceptance or rejection.
- While the advice and information in this journal is believed to be true and accurate at the date each article is published, neither the authors, the editors, nor Copernicus Publications can accept any legal responsibility for any errors or omissions that may be made. Copernicus Publications makes no guarantee, expressed or implied, with respect to the material contained herein.